Preparation, Characterization, and Evaluation of Photocatalytic Properties of a Novel $NaNbO_3$/ Bi_2WO_6 Heterostructure Photocatalyst for Water Treatment

Yu Qiao

Thesis submitted to the University of Ottawa
in partial fulfillment of the requirements for the
Master of Applied Science degree in Chemical Engineering

uOttawa

Department of Chemical and Biological Engineering
Faculty of Engineering
University of Ottawa

Abstract

Semiconductor-based heterogeneous photocatalysis, as one of the advanced oxidation processes that makes use of semiconductors and inexhaustible solar light, has recently been extensively studied and applied to water decontamination. However, due to low light absorption efficiencies and severe electron-hole recombination, modifications on semiconductor structures are required in order to enhance their photocatalytic performance. Heterogeneous photocatalyst composites, taking advantage of the improved light absorption efficiency as well as the facilitated electron-hole separation at the interface between different semiconductors, have been proven to be a promising strategy. In this study, novel $NaNbO_3/Bi_2WO_6$ photocatalyst composites with a type-II heterogeneous alignment were successfully prepared via a facile wet impregnation method. The as-prepared photocatalysts were characterized by powder X-ray diffraction (XRD), scanning electron microscopy (SEM), high-resolution transmission electron microscopy (HRTEM), X-ray photoelectron spectroscopy (XPS), diffuse reflectance UV-Vis spectroscopy (DRS), photocurrent (PC) and electrochemical impedance spectroscopy (EIS) analyses. The 30 wt% $NaNbO_3/Bi_2WO_6$ composite exhibited the best performance for degrading an RhB (rhodamine B) aqueous solution under visible light irradiation ($\lambda > 410$ nm), which was ca. 40 times and ca. 2.5 times that of the pristine $NaNbO_3$ and Bi_2WO_6, respectively. The improved photocatalytic activity may be attributed to the enhanced electron-hole separation efficiency in Bi_2WO_6 with the assistance of $NaNbO_3$, as well as the dye-sensitization effect of RhB itself. Radical quenching experiments revealed that h^+ played the predominant role, and $O_2^{\bullet-}$ functioned as well to some degree. The produced intermediates during the reaction and RhB degradation pathway were speculated and investigated as well. The excellent stability and reusability were verified by repetitively running for five times. Based on experimental results, a plausible functioning mechanism was proposed. Effects of several operation parameters on the catalyst performance including initial RhB concentration, catalyst dosage, reaction temperature and initial pH were also discussed. This study provides solid evidence for $NaNbO_3$ to be a promising candidate for photocatalysis and gives out a novel photocatalytic mechanism of Bi_2WO_6-based type-II heterostructures.

Acknowledgment

First and foremost, I would like to express my sincere and deepest gratitude to my supervisor, Dr. Jason Zhang, for providing me the opportunity to pursue a Master's degree in chemical engineering at the University of Ottawa, as well as his guidance for the last two and half years.

I appreciate the Natural Sciences and Engineering Research Council of Canada (NSERC) for providing research funding on this project.

I would also like to acknowledge Xiangchao Meng, a senior member of our group, for his suggestions at the beginning of this work and his help with material characterization. My thanks also to my colleagues, Zhiliang Yang, Zizhen Li, and Yuxuan Ren, for their company and understanding.

I am also grateful to Dr. Yun Liu and Dr. Alexander Mommers at the Centre for Catalysis Research and Innovation (CCRI) at the University of Ottawa, for their assistance and advice in material characterization.

At last, I would like to thank my parents for their unconditional and selfless love and support. Mr. and Mrs. Liu for making Ottawa a second home of mine. My friends for their friendship and care, as well as my teddy bear for his company for the last eleven years.

Table of Contents

List of Tables

List of Figures

Abbreviation

About Semiconductor Structure and Properties

SC	Semiconductor
CB	Conduction band
VB	Valence band
e^-	Photogenerated electrons
h^+	Photogenerated holes
HOMO	Highest occupied molecular orbital
LUMO	Lowest unoccupied molecular orbital
QD	Quantum dot
CCQD	Carbon-containing quantum dot
CQD	Carbon quantum dot
CNQD	g- C_3N_4 quantum dots
GQD	Graphene quantum dot
GO	Graphene oxide
rGO	Reduced graphene oxide
CNT	Carbon nanotube
MWCNT	Multiwalled carbon nanotubes
AQY	Apparent quantum yield
QY	Quantum yield
TOC	Total organic carbon
LSPR	Localized surface plasmon resonance
NIEL	New impurity energy level
NP	Nanoparticle
UCL	Upconverted luminescence

Organic Substrates

4-CP	Para-chlorophenol
4-NP	4-Nitrophenol
AF	Acid fuchsin
AB 14	Acid brown 14
AO10	Acid orange 10
AR 27	Acid red 27
BPA	Bisphenol A
CAP	Chloramphenicol
EFA	Enrofloxacin
EY	Eosin Y
IBP	Ibuprofen
MB	Methyl blue
MEG	Multiple-exciton-generation
MG	Malachite green
MO	Methyl orange
MR	Methyl red
MV	Methyl violet
NOR	Norfloxacin
PCP	Pentachlorophenol
RB5	Reactive black 5
RhB	Rhodamine B
RR	Reactive red
TC	Tetracycline hydrochloride
X-3B	Reactive Brilliant red X-3B

Light Sources

IR	Infrared radiation
NIR	Near-infrared radiation
UV	Ultraviolet
Vis	Visible light
LED	Light-emitting diode

Characterization Technologies

(HR)SEM	(High-resolution) scanning electron microscopy
(HR)TEM	(High-resolution) transmission electron microscopy
DRS	Diffuse reflectance UV-Vis spectroscopy
EDS	Energy-dispersive X-ray spectroscope
EIS	Electrochemical impedance spectroscopy
ESR	Electron spin resonance
Raman	Raman spectroscopy
FTIR	Fourier-transform infrared spectroscopy
PC	Photocurrent
PL	Photoluminescent
XPS	X-ray photoelectron spectroscopy (XPS)
XRD	X-ray diffraction

Scavengers for Quenching Experiment

AO	Ammonium oxalate
BQ	p-benzoquinone
EDTA	Ethylenediaminetetraacetate
IPA	Isopropanol
t-BuOH/TBA	Tert-butyl alcohol
TEA	Triethylamine

Other

AOP	Advanced oxidation process
CPC	Compound parabolic collector
DDW	Deionized water
NHE	Normal hydrogen electrode
PANI	Polyaniline
Ppy	Polyrrole
TEOA	Triethanolamine
NBO	Composite consists of sodium niobate and bismuth tungstate

Chapter I
Introduction

1.1 Background

Water is one of the most abundant resources of the world, covering 70% of the earth's surface. However, only 0.65% of the total water mass can be directly used by human beings [1]. Moreover, the uneven distribution and severe contamination make available water increasingly deficient [2,3]. Therefore, it is urgent to explore proper strategies for wastewater treatment.

Conventional contaminant treatments are usually based on biological (e.g., bacteria, fungi, plant extracts, etc.) and physical processes (e.g, adsorption, precipitation, laser pyrolysis, etc.) [4]. However, lots of organic pollutants are non-biodegradable, and physical treatments usually focus on concentrating and separating out the pollutants without decomposing or degrading them.

Recently, advanced oxidation processes (AOPs), defined as aqueous or gaseous oxidation processes making use of powerful oxidizing agents (primarily, but not exclusively, hydroxyl radicals, •OH) generated in situ to decontaminate water, have been extensively studied and applied to water purification [5]. Hydroxyl radical, with an oxidation potential of +2.8 eV vs. Normal Hydrogen Electrode (NHE), is such a strong oxidant (just behind Fluorine, +3.03 eV) that can be deemed non-selective towards organic molecules with rate constants on the order of $10^{-6}\sim10^{-9}\ M^{-1}s^{-1}$ [2,6]. Also, AOPs normally lead to the best yields in organic destruction when biological treatments are unfeasible [7].

As one of the AOPs, photocatalysis is capable of harnessing inexhaustible solar irradiation as the source of energy, and thus is known as a "green technology" [8]. Compared to homogeneous photocatalysis, catalysts in heterogeneous photocatalysis are easy to be separated after use, as well as retrieved and reused subsequently.

In 1972, Fujishima and Honda first discovered the photocatalytic activity on titanium dioxide (TiO_2) with respect to producing hydrogen by splitting water in a photoelectrochemical solar cell [9]. Since then, TiO_2 has attracted significant attention in photocatalysis due to its high activity, strong stability to light illumination, low price, and nontoxicity [4,10–12]. Yet, it was not until Pruden and Ollis realized a complete mineralization of trichloroethylene in aqueous solutions that photocatalysis began to extensively develop for water decontamination [13]. In the recent decade, a vast amount of semiconductors, such as ZnO [14], WO_3 [15], AgBr [16], Bi_2WO_6 [17], $SrTiO_3$ [18], etc., have demonstrated their efficiencies in degrading a wide range of organic pollutants into readily biodegradable compounds, which can be easily mineralized into CO_2, H_2O, and inorganic ions subsequently. Yet, the two primary challenges, low light absorption efficiency and poor electron/hole separation efficiency, inhibit their application in industries. In order to overcome the above problems, numerous strategies on photocatalyst modification have been proposed with respect to the physical, chemical, and energy-band structures of semiconductors. Type-II heterogeneous alignment takes advantage of the facilitated charge carrier transfer at the interface of different semiconductors, favoring the electron/hole separation, and thus is considered to be a promising modification approach.

As a member of perovskite alkaline niobates, $NaNbO_3$ has demonstrated its photocatalytic activity in water splitting [19], water treatment [20], as well as CO_2 reduction [21] under UV irradiation. However, its application is restrained under visible light irradiation due to its wide bandgap (~3.5 eV). Bi_2WO_6, on the other hand, is an extensively used visible-light responsive photocatalyst owing to its narrow bandgap (~2.7 eV), but severe recombination between the photogenerated electrons and holes limits its further use.

1.2 Objectives

In order to overcome the poor electron/hole separation in Bi_2WO_6 while maintaining its visible-light-responsivity, multiple objectives of this project are listed below:

i) Synthesis pure $NaNbO_3$ and Bi_2WO_6 samples via hydrothermal methods separately;

ii) Synthesis $NaNbO_3/Bi_2WO_6$ heterojunction composites via a facile wet impregnation method;

iii) Characterize the crystal structure, morphology, size, composition, element oxidation states, optical absorption properties, and electrochemical properties with XRD, SEM, HRTEM, XPS, UV-Vis DRS, PC, and EIS;

iv) Explore a potential functioning mechanism of the composites in the case of photocatalytic degradation of RhB aqueous solution under visible light irradiation;

v) Optimize the $NaNbO_3$ content in the composites;

vi) Investigate the effects of operation parameters, including initial RhB concentration, catalyst dosage, temperature, and initial pH, on photocatalytic performance.

1.3 Thesis Outline

The main body of this thesis consists of five parts: introduction, literature review, experimental results, conclusions, and appendix. Each of them was presented in their respective chapters, which are described as the following:

- **Chapter I: Introduction**

  This part briefly introduces the urgency of proper wastewater treatment, the development of photocatalysis, as well as the properties of $NaNbO_3$ and Bi_2WO_6.

- **Chapter II: Recent Meliorating Strategies on Semiconductor Photocatalysts for Organic Decontamination in Water: A Review**

This part provides a comprehensive literature review on semiconductor-based heterogeneous photocatalysis. The involved fundamentals and principles are discussed in detail at the beginning of the chapter. Further, considering the two primary challenges, which are low light absorption efficiency and poor electron/hole separation efficiency, recent attempts on the modification of semiconductors are thoroughly reviewed, with their functioning mechanisms interpreted at first. In the end, a brief conclusion of challenges that heterogenous photocatalysis is faced with at this stage is provided, and the prospective works that can be expected in the future is proposed as well.

- **Chapter III: Facile Synthesis of $NaNbO_3/Bi_2WO_6$ Heterojunction Composite with Enhanced Visible-Light-Driven Photocatalytic Performance towards RhB Degradation**

This chapter is written in journal article format, and covers the project scope and objectives. In this chapter, a series of novel $NaNbO_3/Bi_2WO_6$ heterogeneous photocatalyst composites with different $NaNbO_3$ content are successfully prepared and characterized. The functioning mechanism is investigated based on the photocatalytic degradation of RhB aqueous solution under visible light irradiation, which is quite different from previous reported heterostructure systems containing Bi_2WO_6 when it works as the electron reservoir and $O_2^{\bullet-}$ is one of the primary reactive species Further, effects of multiple operation parameters including the initial RhB concentration, catalyst dosage, reaction temperature and initial pH are also explored.

- **Chapter IV: Conclusions and Recommendations**

This part makes a general conclusion based on the work in this project, as well as suggestions on the future work.

- **Appendix A: Supporting Information of Chapter III**

- **Appendix B: Summary of Semiconductor Modification Strategies**

- **Appendix C: Effect of Operation Parameters on Heterogeneous Photocatalysis: A Brief Review**

- **Appendix D: Strategies Coupling Photocatalysis with Other Treatment: A Brief Summary**

- **Appendix E: Recent Development in Photoreactor Design: A Brief Review**

- **Appendix F: Previously Failed Attempts**

  This part summaries systems that have been tried but eventually failed. The involved principles and theories are stated, the expected effects are speculated, the experimental methods are described in detail, and the potential reasons for the failure are analyzed at last.

References

[1] M.A. Oturan, J.-J. Aaron, Advanced Oxidation Processes in Water/Wastewater Treatment: Principles and Applications. A Review, Crit. Rev. Environ. Sci. Technol. 44 (2014) 2577–2641. doi:10.1080/10643389.2013.829765.

[2] S. Malato, J. Blanco, A. Vidal, D. Alarcón, M.I. Maldonado, J. Cáceres, W. Gernjak, Applied studies in solar photocatalytic detoxification: an overview, Sol. Energy. 75 (2003) 329–336. doi:10.1016/j.solener.2003.07.017.

[3] S. Malato, P. Fernández-Ibáñez, M.I. Maldonado, J.J.J. Blanco, W. Gernjak, D.C. Alarcón, M.I. Maldonado, P. Fernández-Ibáñez, W. Gernjak, D.C. Alarcon, M.I. Maldonado, P. Fernandez-Ibanez, W. Gernjak, D.C. Alarcón, M.I. Maldonado, P. Fernández-Ibáñez, W. Gernjak, Photocatalytic decontamination and disinfection of water with solar collectors, Catal. Today. 122 (2007) 137–149. doi:10.1016/j.cattod.2007.01.034.

[4] V.C. Padmanaban, M.S. Giri Nandagopal, G. Madhangi Priyadharshini, N. Maheswari, G. Janani Sree, N. Selvaraju, Advanced approach for degradation of recalcitrant by nanophotocatalysis using nanocomposites and their future perspectives, Int. J. Environ. Sci. Technol. 13 (2016) 1591–1606. doi:10.1007/s13762-016-1000-9.

[5] W.H. Glaze, J.W. Kang, D.H. Chapin, The chemistry of water treatment processes involving ozone, hydrogen peroxide, and ultraviolet radiation, Ozone Sci. Eng. 9 (1987) 335–352. doi:10.1080/01919518708552148.

[6] T.-T. Lim, P.-S. Yap, M. Srinivasan, A.G. Fane, TiO2/AC Composites for Synergistic Adsorption-Photocatalysis Processes: Present Challenges and Further Developments for Water Treatment and Reclamation, Crit. Rev. Environ. Sci. Technol. 41 (2011) 1173–1230. doi:10.1080/10643380903488664.

[7] S. Esplugas, J. Gimenez, S. Contreras, E. Pascual, M. Rodriguez, Comparison of different advanced oxidation processes for phenol degradation, Water Res. 36 (2002) 1034–1042. doi:10.1016/S0043-1354(01)00301-3.

[8] Y. Chan, S. Pung, S. Sreekantan, F. Yeoh, Photocatalytic activity of β-MnO2 nanotubes grown on PET fibre

under visible light irradiation, J. Exp. Nanosci. 11 (2016) 603–618. doi:10.1080/17458080.2015.1102342.

[9] A. FUJISHIMA, K. HONDA, Electrochemical Photolysis of Water at a Semiconductor Electrode, Nature. 238 (1972) 37–38. doi:10.1038/238037a0.

[10] R. Daghrir, P. Drogui, D. Robert, Modified TiO2 For Environmental Photocatalytic Applications: A Review, Ind. Eng. Chem. Res. 52 (2013) 3581–3599. doi:10.1021/ie303468t.

[11] S.M. Gupta, M. Tripathi, A review of TiO2 nanoparticles, Chinese Sci. Bull. 56 (2011) 1639–1657. doi:10.1007/s11434-011-4476-1.

[12] S.G. Kumar, L.G. Devi, Review on Modified TiO2 Photocatalysis under UV/ Visible Light: Selected Results and Related Mechanisms on Interfacial Charge Carrier Transfer Dynamics, Phys. Chem. A. 115 (2011) 13211–13241. doi:10.1021/jp204364a.

[13] A.L. Pruden, D.F. Ollis, Photoassisted heterogeneous catalysis: The degradation of trichloroethylene in water, J. Catal. 82 (1983) 404–417. doi:10.1016/0021-9517(83)90207-5.

[14] M.J. Sampaio, M.J. Lima, D.L. Baptista, A.M.T. Silva, C.G. Silva, J.L. Faria, Ag-loaded ZnO materials for photocatalytic water treatment, Chem. Eng. J. (2016). doi:10.1016/j.cej.2016.05.105.

[15] G. Xi, J. Ye, Q. Ma, N. Su, H. Bai, C. Wang, In situ growth of metal particles on 3D urchin-like WO3 nanostructures, J. Am. Chem. Soc. 134 (2012) 6508–6511. doi:10.1021/ja211638e.

[16] H. Wang, J. Gao, T. Guo, R. Wang, L. Guo, Y. Liu, J. Li, Facile synthesis of AgBr nanoplates with exposed {111} facets and enhanced photocatalytic properties, Chem. Commun. 48 (2012) 275–277. doi:10.1039/C1CC16423F.

[17] C. Li, G. Chen, J. Sun, J. Rao, Z. Han, Y. Hu, W. Xing, C. Zhang, Doping effect of phosphate in Bi2WO6 and universal improved photocatalytic activity for removing various pollutants in water, Appl. Catal. B Environ. 188 (2016) 39–47. doi:10.1016/j.apcatb.2016.01.054.

[18] L.F. da Silva, W. Avansi, J. Andrés, C. Ribeiro, M.L. Moreira, E. Longo, V.R. Mastelaro, Long-range and short-range structures of cube-like shape SrTiO3 powders: microwave-assisted hydrothermal synthesis and photocatalytic activity, Phys. Chem. Chem. Phys. 15 (2013) 12386. doi:10.1039/c3cp50643f.

[19] H. Shi, X. Li, D. Wang, Y. Yuan, Z. Zou, J. Ye, NaNbO3 nanostructures: Facile synthesis, characterization, and their photocatalytic properties, Catal. Letters. 132 (2009) 205–212. doi:10.1007/s10562-009-0087-8.

[20] X. Li, Q. Li, L. Wang, The effects of NaNbO3 particle size on the photocatalytic activity for 2-propanol photodegradation, Phys. Chem. Chem. Phys. 15 (2013) 14282–9. doi:10.1039/c3cp51790j.

[21] H. Shi, T. Wang, J. Chen, C. Zhu, J. Ye, Z. Zou, Photoreduction of carbon dioxide over NaNbO3 nanostructured photocatalysts, Catal. Letters. 141 (2011) 525–530. doi:10.1007/s10562-010-0482-1.

Chapter II
Inorganic Semiconductor-Based Photocatalysis Used for Water Decontamination: A Review

2.1 Introduction

As an advanced oxidation process (AOP), heterogeneous photocatalysis, taking advantage of mild reaction conditions, minimal generation of secondary waste and a wide range of applications for environmental decontamination, has emerged as an important destructive treatment for organic pollutants in water. However, the low quantum efficiency and poor reaction rate limit its further use [1]. To overcome the above deficiencies, considerable efforts attempting to extend light absorption spectra and enhance charge carrier separation have been made.

Since heterogeneous photocatalysis was found to be effective on water decontamination, TiO_2 has been mostly researched not only because it is the origin, but also due to its high activity, strong stability, low price, and nontoxicity [2–6]. Yet, considering that studies and applications of TiO_2 have been comprehensively and thoroughly investigated and summarized [2–6], this part focuses on novel semiconductors emerged in the last decade, which have demonstrated their efficiency in degrading a wide range of organic pollutants to readily biodegradable compounds that can be mineralized into CO_2, H_2O, and inorganic ions subsequently.

Although many reviews focused on semiconductor-based photocatalytic water decontamination have been published, most of them concentrate on a specific topic, such as strategies extending light absorption spectra [7], TiO_2 -based photocatalysis [2–6], semiconductor oxide based photocatalysts [8], heterojunction photocatalysts [9–13], microsphere photocatalysts [14], semiconductor quantum dots [15], photodeposition [16], *etc*. The present review provides a comprehensive and systematic overview of novel semiconductor-based photocatalysis in water treatment developed in the recent decade, as well as a detailed introduction to the fundamentals and principles of photocatalysis.

In this review, fundamentals and principles of semiconductor-based heterogeneous photocatalysis are discussed in detail. Further, considering the two primary challenges in semiconductor-based photocatalysis, which are poor light absorption and low electron/hole separation efficiency, a systematic and comprehensive summary of photocatalyst modification strategies that have been made in the last decade is given, along with each of the theoretical background is stated. In the end, we provide a brief conclusion of challenges that heterogeneous photocatalysis is faced with at this stage, as well as prospective works that can be expected in the future

2.2 Fundamentals and Principles of Semiconductor-based Heterogeneous Photocatalysis

2.2.1 Semiconductor Properties for Photocatalysis

The energy structure of a given material consists of two energy bands: one is the valence band (VB) filled with valence electrons, and the other is the empty conduction band (CB). For semiconductors, there is an energy gap between the two bands, called the bandgap, in which electrons can transfer from the CB to the VB when triggered by external stimulations such as irradiation in photocatalysis.

The CB energy represents the reducing capacity of the semiconductor; the higher (more negative) the CB, the stronger reducing capacity of the semiconductor. Only species (electron acceptors) with lower reduction potential than that of the CB can be reduced. The VB energy, on the other hand, represents the oxidizing capacity; the lower (more positive) the location of the top, the

stronger oxidizing capacity of the semiconductor, and only species (electron donors) with an oxidation potential higher than this limitation can be oxidized. In other words, the difference between the energy bands of the semiconductor and the redox potential of the redox couple determines the possibility for a photocatalytic reaction to happen thermodynamically. Energy band positions and bandgaps of some commonly used semiconductor materials are given in Figure 1.

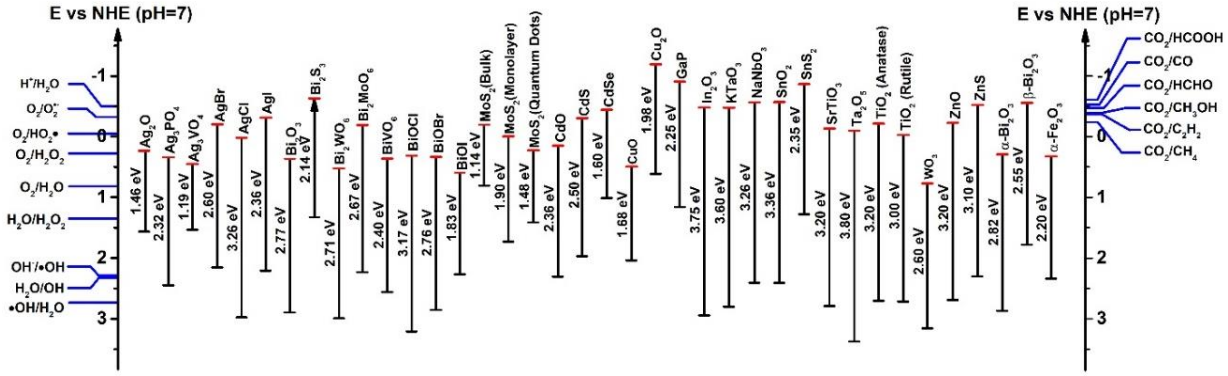

Figure 1 Absolute CB and VB energy potential values of various semiconductors and redox potential commonly used in photocatalysis with respect to the normal hydrogen energy (NHE) potential at pH=7.

The bandgap energy (E_g) determines the maximum light spectrum a semiconductor can absorb and use [17]. According to Plank relation describing the band-edge wavelength (λ) and bandgap energy (E_g) as shown by Equation (1) [18],

$$\lambda\,(\mathrm{nm}) = 1240/\mathrm{E_g}\,(\mathrm{eV}) \qquad (1)$$

the smaller the bandgap energy of a semiconductor, the longer the wavelength it can respond to. However, as the bandgap gets narrower, although the light-responsive region would be broader, decrease in redox capacities and faster recombination rates would also be inevitable. Therefore, the selected semiconductors should have proper bandgaps which balance the two considerations above.

For a crystalline semiconductor, its optical absorption near the band edge follows the formula proposed by Tauc [19]:

$$\alpha h\nu = A(h\nu - \mathrm{E_g})^{n/2} \qquad (2)$$

where α is the absorption coefficient, h is the Plank constant, ν is the light frequency, A is a constant, E_g is the band gap of the semiconductor, and n is determined by the type of optical transition of a semiconductor (n=1 for direct transition, and for indirect transition n=4). Therefore, the bandgap of a semiconductor can be calculated from the plot of $(\alpha h\nu)^{2/n}$ versus $(h\nu)$, as shown in Figure 2 [20].

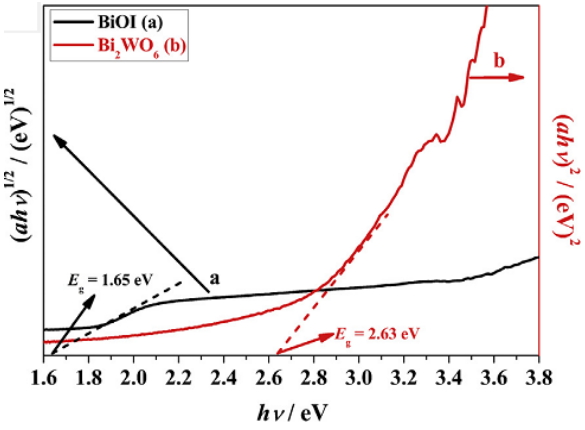

Figure 2 Plots of $(\alpha h\nu)^{1/2}$ and $(\alpha h\nu)^2$ versus hν of BiOI (indirect transition) and Bi_2WO_6, (direct transition) respectively. Adapted with permission from [20]. Copyright (2015) Elsevier.

To further estimate the band edge positions of a semiconductor at the point of zero charge, the following empirical formulas are usually used:

$$E_{CB} = \chi - E^e - 0.5\, E_g \quad (3)$$

$$E_{VB} = E_g + E_{CB} \quad (4)$$

where E_{CB} is the conduction band edge potential, E_{VB} is the valence band edge potential, χ is the electronegativity of the semiconductor (the geometric mean of the constituent atoms), E^e is the energy of free electrons on the hydrogen scale (~4.5 eV vs. NHE). [20]

Since photocatalytic activity is strongly impacted by experimental conditions such as light source, *pH*, temperature, etc., it is necessary to find a parameter comparing the efficiencies of different systems. Quantum efficiency, also known as quantum yield, is defined as the percentage of the number of the reacted electrons to the total number of the absorbed photons from the irradiation as shown in Equation (5), suggesting the quantitative relationship between photoproduct formation rates and spectral irradiation. [21]

$$\mathrm{QY}(\%) = \frac{\text{Number of reacted electrons}}{\text{Number of absorbed photons}} \times 100\% \quad (5)$$

However, it is infeasible to determine the absolute quantity of photons absorbed by a photocatalyst in a dispersed system due to light scattering [22]. Thus, the obtained quantum yield is actually the apparent quantum yield (AQY) [23] reflecting the uncertainty in photochemistry [21]. AQY is usually smaller than QY since the amount of incident photons is greater than that of absorbed photons.

$$\mathrm{AQY}(\%) = \frac{\text{Number of reacted electrons}}{\text{Number of incident photons}} \times 100\% \quad (6)$$

For studies in the stage of laboratory research, photocatalytic performance of photocatalysts is usually manifested by photocatalytic degradation efficiency, as indicated in Equation (7).

$$\mathrm{E}(\%) = \frac{\mathrm{C_o} - \mathrm{C}}{\mathrm{C_o}} \times 100\% \quad (7)$$

where, C_o and C are the initial substrate concentration and substrate concentration at any time, respectively.

The concentration of a chromatic substrate in photocatalytic experiments are usually converted to the absorbance at its characteristic peak. The linear relationship between absorbance and concentration is described by Beer-Lambert Law,

$$\mathrm{A} = \mathrm{a}(\lambda) * \mathrm{b} * \mathrm{C} \quad (8)$$

where A is the absorbance, $a(\lambda)$ is the wavelength-dependent coefficient, b is the path length of irradiation going through, C is the concentration.

2.2.2 Photocatalytic Degradation of Organic Substrates in Aqueous Systems

From a microscopic point of view, a photocatalytic degradation process can be divided into three steps: (i) light absorption; (ii) energy conversion (from light energy to electrochemical energy); and (iii) substrate degradation. Yet, it is more often indicated from the microscopic perspectives, as shown is Figure 3.

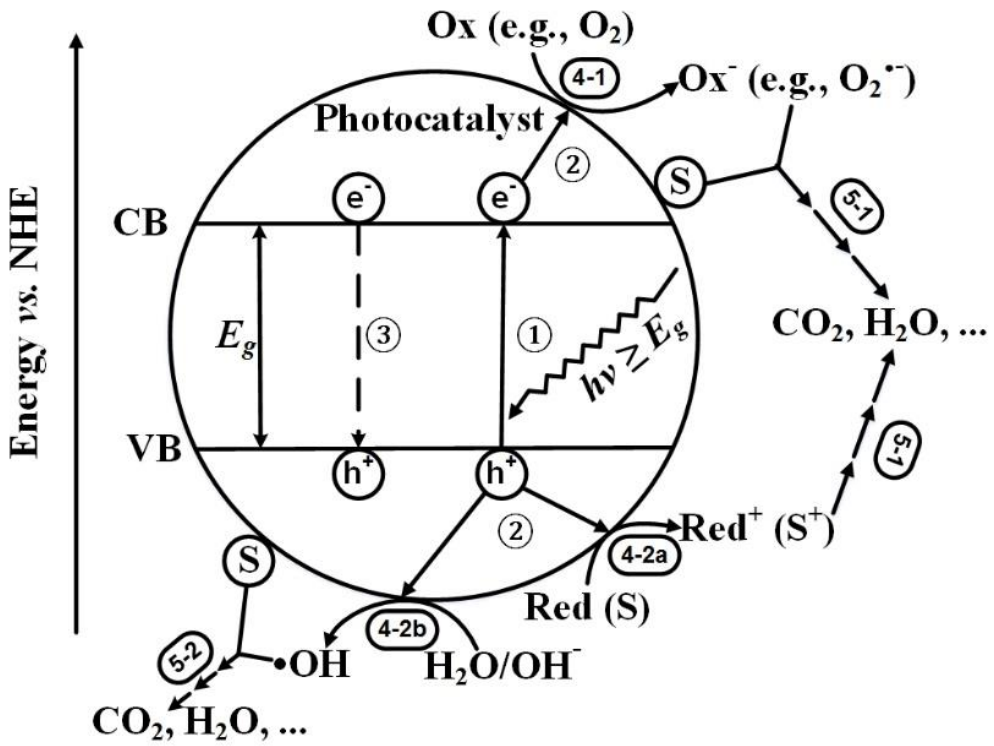

Figure 3 Photocatalytic process on semiconductors in aqueous systems. CB and VB represent conduction and valence band of the semiconductor, respectively; E_g represents the bandgap; hν represents the energy of irradiation; e^- and h^+ represent photogenerated electrons and holes, respectively; Ox and Red represent oxidative and reductive species, respectively; S represents substrate molecules.

When a semiconductor absorbs a photon with the energy greater than or equal to its bandgap energy (E_g), a valence electron would be triggered to migrate to the conduction band, leaving behind a hole on the valence band where the electron used to be (step 1). Electrons and holes generated in this way are powerful reductants and oxidants, respectively, and are almost non-selective to organic, inorganic, and microcontaminants [24]. The produced electron/hole pairs must separate in order to reach the semiconductor surface and take part in the subsequent reactions (step 2). On the other hand, recombination (step 3), as a rival of separation, is a spontaneous and thermodynamically inevitable process due to the Coulomb force between electrons and holes, prohibiting them from reacting with other species in the system. Electrons and holes that reached the semiconductor surface may oxidize the substrates directly (step 4-2a) or indirectly by producing reactive species such as superoxide radicals (step 4-1) and hydroxyl radicals (step 4-2b). After multiple steps, the original substrates will be decomposed and mineralized into H_2O, CO_2, and other simple inorganic ions eventually

2.2.3 Mechanism

Photocatalysis for water treatment is usually the oxidative degradation of the substrate pollutants. The mechanism can be classified into two groups according to the functioning reactive species: the direct mechanism is triggered by h_{VB}^{+}, while the indirect mechanism is induced by oxidative radicals generated from the interaction between e_{CB}^{-} or h_{VB}^{+} and other dissolved species in the system.

The direct oxidation mechanism is also called the hole oxidation mechanism, meaning the organic substrates are oxidized and degraded by photoinduced holes directly. This usually happens when the oxidizing potential of the semiconductor VB is lower than that of the $OH^{-}/\bullet OH$ redox pairs and stronger than that of the substrates.

The indirect oxidation mechanism is also called the free radical oxidation mechanism, meaning that the organic compounds are oxidized by oxidative radicals, which are normally but not limited to $\bullet OH$ and $O_2^{\bullet-}$.

The typical participation of holes is indicated by Equation (9-10), based on the oxidation potentials of the semiconductor VB and the redox pairs [25].

$$h_{VB}^{+} + H_2O \rightarrow \bullet OH + H^{+} \quad (9)$$

$$h_{VB}^{+} + OH^{-} \rightarrow \bullet OH \quad (10)$$

For photogenerated electrons, it may produce $O_2^{\bullet-}$ via Equation (11) or $\bullet OH$ going through more complicated processed as revealed by Equation (12) or (13) in acidic and basic environment, respectively [4,26].

$$e_{CB}^{-} + O_2 \rightarrow O_2^{\bullet-} \quad (11)$$

$$e_{CB}^{-} + O_2 \rightarrow O_2^{\bullet-}$$
$$O_2^{\bullet-} + H_2O \rightarrow H_2O_2,$$
$$O_2^{\bullet-} + e_{CB}^{-} + 2H^{+} \rightarrow H_2O_2 \text{ (Acid environment)} \quad (12)$$
$$H_2O_2 \rightarrow 2 \bullet OH$$

$$e_{CB}^{-} + O_2 \rightarrow O_2^{\bullet-}$$

$$O_2^{\bullet-} + H_2O \rightarrow OH^- + \bullet OOH \text{ (Basic environment)} \quad (13)$$

$$\bullet OOH + H^+ \rightarrow \bullet OH + OH^-$$

$$OH^- + h_{VB}^+ \rightarrow \bullet OH$$

In order to further investigate the mechanism of a photocatalytic system, it is necessary to determine the functioning reactive species.

By comparing the redox potential of band edges and reactive radicals, primary reactive radicals can be predicted theoretically. For example, during the decomposition of benzylic alcohols photocatalyzed by Bi_2MoO_6, since the reduction potential of CB (-0.33 eV) was more negative than that of $O_2/O_2^{\bullet-}$ (-0.28 eV), $O_2^{\bullet-}$ could be produced by reducing adsorbed O_2 with photogenerated electrons and further decompose the substrates afterwards. Due to the more positive oxidation potential of Bi_2MoO_6 VB compared to benzyl alcohol, holes were able to oxidize benzyl alcohol directly. Therefore, the degradation of benzylic alcohols was mainly carried out by $O_2^{\bullet-}$ and h^+. [27]

Table 1 Examples of several commonly used scavengers

Reactive Species	Scavenger	Ref.
h^+	Ethylenediaminetetraacetate (EDTA)	[30]
	Triethylamine (TEA)	[31]
•OH	Isopropanol (IPA)	[32]
	Tert-butyl alcohol (t-BuOH)	[30]
$O_2^{\bullet-}$*	p-benzoquinone (PBQ)	[33]
e^-*	Noble metal nanoparticles	[34]
	Bromate ions (BrO_3^-)	[26]

*: Scavenge of superoxide radicals is usually realized by electron scavengers.
**: Hydrogen peroxide and ozone act as both electron scavengers and hydroxyl radical providers.

A more perspicuous way is to apply the quenching experiment. Scavengers with respective to different reactive species are applied separately. The stronger the blocking effect towards photocatalysis, the more important role the corresponding reactive species plays. In general, h^+, $O_2^{\bullet-}$ and •OH are considered to be the main active groups involved in the photodegradation of

organic pollutants [28]. Examples of commonly used scavengers are exhibited in Table 1. In the study on light-driven removal of RhB over $SrTiO_3$ modified Bi_2WO_6 composites, photocatalytic activity was found to be greatly suppressed by the addition of EDTA and IPA, indicating the predominant effect of h^+ and •OH, respectively. Thus, it was deduced that part of holes generated on Bi_2WO_6 VB flowed to $SrTiO_3$ and oxidized RhB directly, while the rest of them stayed at the Bi_2WO_6 VB and produced •OH active species for RhB degradation by oxidizing OH^- ions. [29]

An ESR (electron spin resonance) test gives a more intuitive way to determine the primary reactive species. Species with the strongest captured ESR signal functions the most. In the BiOBr/guanine/UV system, UV-generated electrons and holes recombined without the formation of $\bullet OH$ nor $O_2^{\bullet-}$ in the absence of a substrate (Figure 4a and b). In contrast, the typical signals of the trapped DMPO $-\bullet OH$ and DMPO $-O_2^{\bullet-}$ were observed to increase with the irradiation time. In addition, compared to the stronger signals of DMPO $-O_2^{\bullet-}$, $\bullet OH$ payed an insignificant role. Also, considering the less positive oxidation potential of the BiOBr VB (2.25 eV) compared to the redox potentials of $H_2O/\bullet OH$ (2.27eV) and $OH^-/\bullet OH$ (2.7 eV) pairs, $\bullet OH$ was not produced by holes but derived from the reduction of the formed $O_2^{\bullet-}$ following Equation (12). [35]

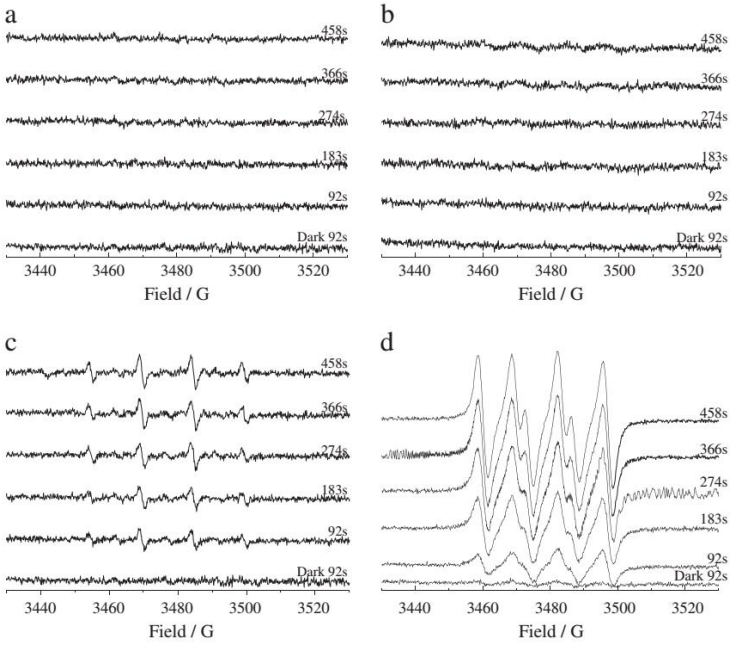

Figure 4 ESR signals of DMPO $-\bullet OH$ in aqueous solution (a and c) and DMPO $-O_2^{\bullet-}$ adducts in methanol solution (b and d) under UV light irradiation. a and b are in the absence of substrate; c and d are in the presence of guanine. Reaction conditions: guanine=10.0 mg/L, BiOBr=1.0 g/L and DMPO=0.4 mol/L. Reprinted with permission from [35]. Copyright (2014) Elsevier.

2.2.4 Kinetics

The kinetics of photocatalytic degradation of aqueous pollutants is still a subject of debate [36]. Most studies claim that the initial reaction rate follows the pseudo-first-order kinetics which is rationalized in terms of the modified Langmuir-Hinshelwood model to accommodate reactions occurring at a solid-liquid interface. The influence of initial concentration of the substrates on the degradation rate can be expressed via the following equation:

$$\mathrm{r} = -\frac{\mathrm{dC}}{\mathrm{dt}} = \mathrm{k_r}\theta_\mathrm{r} = \frac{\mathrm{k_r KC}}{1+\mathrm{KC}} \quad (14)$$

where, C is the substrate concentration at an arbitrary time, t is the reaction time, k_r is the reaction rate constant, θ_r is the fraction of catalyst surface area covered by the substrate, and K is the reactant adsorption equilibrium constant.

The values of the C and K are typically in the level ppm (mg/L), which makes *KC* much lower than 1. Therefore, the above equation can be simplified as:

$$-\frac{\mathrm{dC}}{\mathrm{dt}} = \mathrm{k_r KC} = \mathrm{K_{app} C} \quad (15)$$

where K_{app} is the apparent reaction rate constant. The term "reaction rate constant" will refer to apparent reaction rate constant of pseudo-first order reaction unless specifically stated. Integrating with the limits of $C = \mathrm{C_0}$ when $t = 0$ and $C = \mathrm{C}$ when $t = \mathrm{t}$, where C represents the concentration at any time, Equation (15) gives,

$$\ln\frac{\mathrm{C_0}}{\mathrm{C}} = \mathrm{K_{app} t} \quad (16)$$

Because of the intermediates produced during the reaction, evaluation of photocatalytic efficiency through monitoring of the disappearance rate of initial substrates is not reliable. In this case, the reaction kinetics may be different. Therefore, total organic carbon (TOC) is used as a more convincing parameter to replace the substrate concentration.

Considering that most studies focusing on the organic pollutant degradation upon semiconductor surface follow the pseudo-first-order mechanism, the reaction rate constants involved in this review are apparent reaction rate constants unless stated otherwise.

2.3 Modification of Photocatalysts

2.3.1 Introduction

As mentioned above, there are two main challenges in photocatalysis, low reaction rate and poor quantum efficiency [1]. Strategies focusing on modifying semiconductor nanoparticles can be summarized in two ways: the enhancement of light absorption and the inhibition of e^-/h^+ recombination.

Since photocatalysis was applied on water decontamination, wide bandgap semiconductors such as titanium dioxide (TiO_2) and zinc oxide (ZnO) have been most widely used. Although exhibiting promising photocatalytic performances, they only respond to UV irradiation, which is merely 3% of the total solar energy [37]. Plus, considering the inverse relation between the wavelength and energy of irradiation (Equation (1)), semiconductors with narrower band gaps have broader light absorption regions. Modification strategies narrowing down bandgaps include inducing impurity levels into the energy-band structures and taking advantage of the size effect, which usually occurs in quantum dots. Moreover, quantum dots have also been found to be capable of converting long-wavelength irradiation to short-wavelength light that can be used by the semiconductor on which they deposit. Another effective method to enhance absorbance is by using the localized surface plasmon resonance (LSPR) effect of noble metal nanoparticles to provide electrons for the subsequent photocatalytic processes. The LSPR effect may also improve light absorption efficiency by photon scattering or near-field electromagnetic enhancement.

As the competitor of surface redox reactions, recombination is detrimental to photocatalytic processes. The separation of electrons and holes not only decreases recombination, but also provides a higher chance for charge carriers to reach the semiconductors' surface and take part in the subsequent reactions with the substrates either directly or indirectly by producing reactive radicals such as $\bullet OH$ and $O_2^{\bullet -}$, etc.

Additionally, other modifications on semiconductors surface by means of enhancing the interactions between reactive species and adsorbed substrates, such as increasing the surface area

by reducing the particle size or exposing more reactive sites with the assistance of surface defects, are also responsible for the promoted photocatalytic performance.

In this section, attempts made for semiconductor modification in the last decade are systematically reviewed, starting with the interpretations of their principles and mechanisms.

2.3.2 Doping

Doping refers to the intentional introduction of impurities, which are usually ions or atoms, into the interior structures of a semiconductor. These impurities are also known as dopants. Depending on different dopants, doping can be classified as metal doping or non-metal doping. Some studies have also tried to co-dope metal and non-metal elements, or self-dope with dopants coming from the pristine semiconductor itself.

2.3.2.1 Metal Doping

Metal doping is achieved by substituting extrinsic metal ions for metal cations in the semiconductor lattice [38]. The size of the dopant and the original cation should be as close as possible in order to maintain a stable solid solution [38] and hence high solubility [39]. For instance, Cr^{3+} has similar ionic parameter as Zn^{2+}, suggesting that Cr^{3+} can easily penetrate into ZnO crystal lattice and substitute for Zn^{2+} in the crystal [38]. Valence is another parameter that has impact on the stability of doped semiconductors. Only when valences of the dopant and the original cation are the same can a continuous solid solution be formed. When Ti^{4+} was doped into WO_3 particles, the difference of valence between Ti^{4+} and W^{6+} led to the formation of a finite solid solution, and the solubility of Ti^{4+} dopant was approximately 10 mol% under the given experimental conditions [39]. Besides, since better adsorption of substrates on the catalyst surface facilitates its degradation, doping should be carried out near the semiconductor surface as well [40].

The most applied metals in metal doping are transition metals (e.g., Cr, W, Mn, Pd, Cu, Ti, Ag, etc.) and rare earth metals (e.g., Sn, Ga, Sm, Eu, etc.) due to their empty or partially filled atomic orbitals [40]. Some post-transition metal (Bi) [41] and alkali earth metal (Sr) [42] dopants are also able to enhance the photocatalytic performance of semiconductors. Two common mechanisms of

metal ion doping have been proposed and experimentally proven: (i) introduction of an impurity energy level; and (ii) increase of oxygen vacancies.

i) Introduction of Impurity Energy Level

When a foreign metal ion is doped in a semiconductor lattice, the hybridization of atomic orbitals between the conduction band electrons of the pristine semiconductor and the localized electrons of the metal ion dopant can lead to the formation of a new impurity energy level (NIEL) between valence and conduction bands [38]. These NIELs may function as electron trappers (Figure 5(a)), donors (Figure 5(b)), or both (Figure 5(c)) [36,40]. Meanwhile, a spatial charge layer will be generated on the semiconductor surface, facilitating electron transfer and inhibiting them from recombining with holes. [43] As a result, not only will the light absorption spectra be expanded, the electron/hole separation efficiency will be improved as well, thus leading to a better photocatalytic performance.

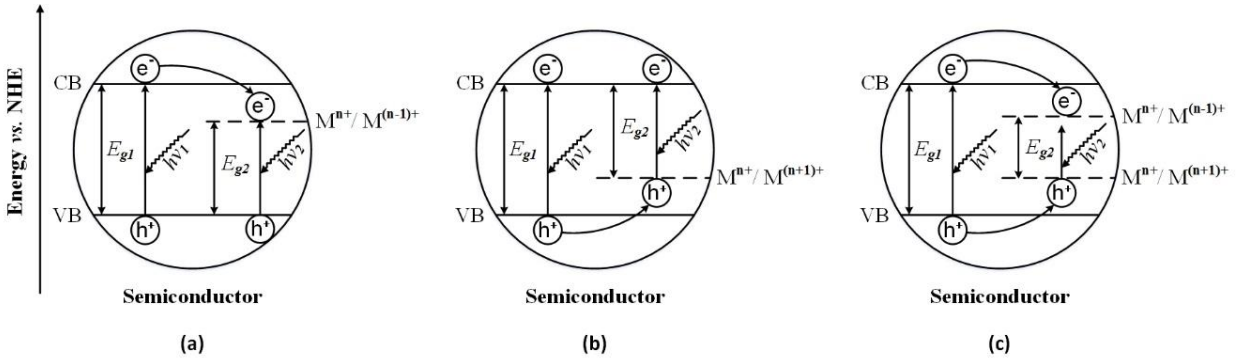

Figure 5 Transfer pathways of photogenerated carriers when an impurity functions as electron: (a) trappers, (b) donors, and (c) both. E_{g1} and E_{g2} represent the original bandgap before and after doping, respectively; $h\nu_1$ and $h\nu_2$ represent the minimum light energy that can be absorbed before and after doping, respectively; M^{n+}, $M^{(n-1)+}$ and $M^{(n+1)+}$ represent the ground state, reduction state, and oxidation state of the metal dopant, respectively.

Figure 6 reveals an increasing light absorption of ZnO in the visible region with the rising W dopant concentration [44]. In the case of Cr-doped ZnO, the sp-d exchange interactions between the produced CB electrons in ZnO and the localized d electrons in Cr^{3+} ions which substituted Zn^{2+} ions broadened the UV-Visible absorption spectra of non-visible-light-responsive ZnO to nearly the entire range of visible light spectrum. The s-d and p-d exchange interactions between Cr^{3+} and Zn^{2+} led to a negative and a positive correction to CB and VB, respectively. The TOC removal of MO was improved from 5.4% up to 58.7% under visible light irradiation. [38,45]

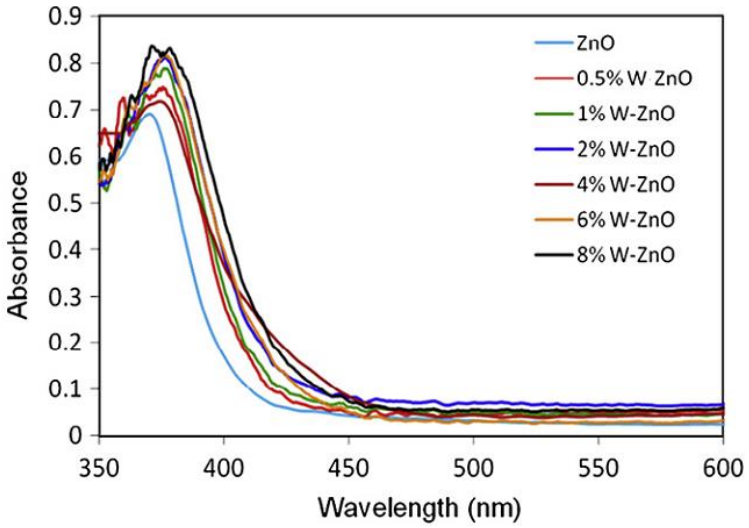

Figure 6 Diffuse reflectance spectra of synthesized ZnO nanoparticles and W-ZnO nanocomposites with different amounts of W. Reprinted with permission from [44]. Copyright (2013) Elsevier.

Metal dopants with partially filled atomic orbitals may act as electron acceptors. For instance, due to the partially filled 4f-orbitals, Sm^{3+} acted as a Lewis acid capturing e^- produced in $CuAlO_4$, which not only extended the light absorption spectra but facilitated electrpn/hole separation as well, and he degradation rate of MO was promoted from 65% to 85% as a result [46]. When the dopant works as electron donors, the situation is the opposite of that in the case of trapping electrons. Niishiro et al. found when Ni^{2+} was doped in $SrTiO_3$, E_g remarkably decreased from 3.2 eV to 1.6 eV, which was attributed to the electron transition from a donor level formed by Ni^{2+} 3d orbitals in the forbidden band to the CB of the $SrTiO_3$ host [47].

Group-I elements (Li, Na , and K) were found to function as both electron acceptors and donors simultaneously in ZnO [48]. By means of doping K^+, Zhong et al. realized a drastically enhanced photodegradation efficiency towards RhB on ZnO. In this system, two NIELs between CB and VB were carried out simultaneously by the K^+ dopants, leading to an obviously reduced bandgap energy and thus a greatly expanded light absorption spectra [49].

ii) Increase of Oxygen Vacancies

This phenomenon usually occurs when metal ions are introduced into metal oxide semiconductors. It has been reported that single oxygen vacancy (V_o^+) defects in metal oxides were capable of

trapping holes to form charged oxygen vacancy (V_o^{++}) defects (Equation (19)) [50], which would then react with OH^- to give out • OH [51]. The possible process is shown as follows:

$$\text{Semiconductor (Metal Oxide)} + h\nu \rightarrow e_{CB}^- + h_{VB}^+ \quad (17)$$

$$e_{CB}^- + O_2 \rightarrow O_2^{\bullet -} \quad (18)$$

$$V_o^+ + h_{VB}^+ \rightarrow V_o^{++} \quad (19)$$

$$V_o^{++} + OH^- \rightarrow \bullet OH \quad (20)$$

Moafi et al. doped W^{6+} into ZnO via a sol-gel method, reducing the bandgap of ZnO from 3.2 eV to 2.85 eV, and the degradation efficiency of MB within 1 h was promoted from 49% to 87% under UV-Vis irradiation. W^{6+} could either substitute for or be interstitially introduced into the ZnO lattice to produce oxygen vacancies which would accelerate the nanocrystallite growth of wurtzite ZnO. [44]

There is usually an optimal content of oxygen vacancies, above which the performance of the catalyst would deteriorate. On the basis Ni^{2+}-doped $SrTiO_3$, and with the consideration that the ionic radii of La^{3+} and Sr^{2+} are close, Jia et al. doped Ni^{2+} and La^{3+} into $SrTiO_3$ lattice simultaneously by isomorphically substituting La^{3+} for Sr^{2+} without producing a large lattice strain, where Ni^{2+} donated electrons while La^{3+} decreased oxygen vacancies to a favorable level and increased the surface area. A complete degradation of MB was obtained under incandescent lamp light irradiation for 14 h, which was only 19% on the pure $SrTiO_3$. [52]

iii) Other Effects

Metal ion dopants are also capable of increasing the specific surface area of the semiconductors, which provides more active sites for substrate adsorption and the subsequent degradation. Except for the commonly observed reduced particle size such as W^{6+}-doped ZnO [53], transition of semiconductors' crystal morphologies is another reason for the increased specific surface area as well as reactive sites. Li et al. reported a conversion in ZnO crystal lattice from lamellar into a granule structure with decreased particle size as the result of K^+ doping [49]. Wang et al. found the morphology of BiOBr transferred from the tetragonal matlockite structure to hierarchical flower-like and the specific surface area was 3 times higher as the results of doping Ti^{4+}.

Photocatalytic tests showed a nearly 100% degradation of RhB within 3 h with a 60% higher reaction constant. [54]

The degradation mechanism may also change when a semiconductor was doped by foreign metal ions. For example, as a thiazine dye, MB is easy to dimerize in aqueous solution. Voicu et al. claimed that pure ZnO equally degrades MB and its dimer $(MB)_2$, while W^{6+}-doped ZnO transformed MB to $(MB)_2$ before strongly degrading the latter. The degradation rate was promoted to 98.6% after doping while the bandgap energy almost remained the same. [55]

Dopant concentration has a direct impact on photocatalytic performance. In general, there is an optimal dopant concentration, at which the photocatalytic efficiency is the highest and declines before and afterwards. As shown in Figure 7, the highest activity of decomposing MO occurred on the 1.46wt% $Eu^{3+}/BiVO_4$ sample, and decreased as the Eu content continuously increased, although the visible light responsive kept rising. This may be due to the short-circuiting mechanism of the coupled reaction, which occurred only at Eu^{3+} content above a certain level. At high doping of europium, since Eu^{3+} was confined on the catalyst surface, there was a high possibility for the trapped electrons to recombine with the holes. The reduction of Eu^{3+} to Eu^{2+} by photogenerated electrons was expected to be faster than the photocatalytic oxidation reaction by oxygen. In that case, the excess Eu dopants might act as recombination centers or cover the active sites on $BiVO_4$ surface and thereby reduce the charge separation efficiency. [56] Similarly, when the concentration of Sr dopant was too high, except for the formed recombination centers between the CB and the VB in the Bi_2O_3 host, an impurity phase of $SrCO_3$ was also resulted, which might work as recombination and thus thwart photocatalysis. [42]

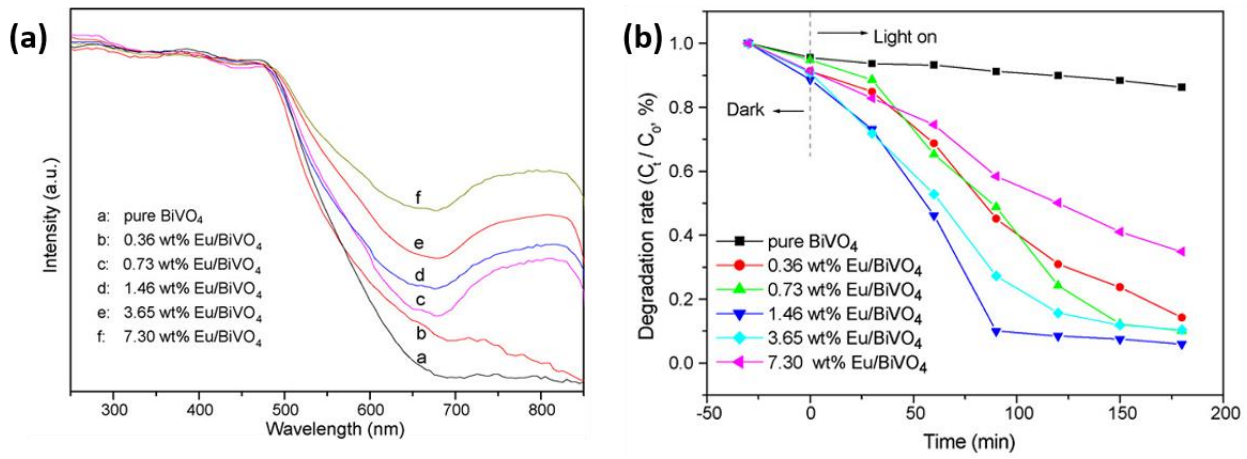

Figure 7 (a) UV–vis diffuses reflectance spectra of pure and $Eu/BiVO_4$ series catalysts; (b) the degradation rate between $\ln(C_0/C_t)$ and treatment time of as-prepared catalysts. Reprinted with permission from [56]. Copyright (2009) Elsevier.

2.3.2.2 Non-metal Doping

Although metal doping does improve photocatalytic efficiency, its drawbacks such as small adsorption and thermal instability are also notable [8,57]. In addition, it is inevitable for the metal ion dopants to dissolve in the solution, which may be more toxic than the pollutant substrates [58]. In order to avoid these deficiencies, non-metal doping has been investigated as an alternative strategy.

Nitrogen, as the most intensively studied non-metal dopant, is usually introduced into semiconductors containing oxygen as an atom by hybridizing O 2p orbital with N 2p orbital and functions as the electron donor, thus elevating the VB of the semiconductor [59,60].

Arunkumar and Vijayaraghavan doped N in $ZnSb_2O_6$ through facile urea assisted combustion synthesis, resulting in a reduction of 0.53 eV in the band gap of $ZnSb_2O_6$ and consequently a red-shift of the absorption edge by ~90 nm. The complete decomposition of RhB was realized in 75 min, compared to 180 min carried out by pure $ZnSb_2O_6$ [61]. Considering that it is also possible for non-metal dopants to work as recombination centers which may counteract or even override the positive effects, Meng et al. realized a decrement of 0.77 eV in the bandgap of $La_2Ti_2O_7$ by doping N, which debased the CB and rose the VB simultaneously without introducing an NIEL. Approximately 92% of MO was degraded under visible light, while pure $La_2Ti_2O_7$ was non-

visible-light-active. [62] Doping N into $BiVO_4$ lattice brought about not only a smaller E_g, but exposed more (040) facets as well. The doped composites exhibited twice as much activity as the pure $BiVO_4$. [59]

Interestingly, Chen et al. found N-doped ZnO prepared by the decomposition of zinc nitrate converted the conductivity of ZnO from n-type to p-type. Under UV irradiation, the N-doped ZnO had a higher photocatalytic reduction activity but a lower oxidation activity compared to pure ZnO, which was attributed to the narrow-deep acceptor levels induced by the redundant holes suffering from the mutual exclusion effect near the VB. As a result, h^+ transferred to the interior of the p-type ZnO while e^- moved to the surface, which was in favor of photoreduction while adverse to photooxidation. [63]

Carbon and sulfur have been applied as dopants in oxygen-containing compounds by substituting for O as anions due to their similar electronic shell structures as O's [64]. Meanwhile, oxygen vacancies may also be introduced, providing more active sites as well as electron traps and thus better photocatalytic efficiency.

Yu et al. synthesized C-doped BiOCl through a low temperature wet-chemical method with polyacrylamide (PAM) as both chelating and doping agents. From XRD results, the peak position of 0.2PAM BiOCl shifted slightly toward a lower 2θ value compared with 0PAM BiOCl, which was mainly ascribed to the large radius of C^{4-} versus that of O^{2-}, indicating that the C^{4-} ions were introduced into the BiOCl lattice by replacing O^{2-} with C^{4-}. On the other hand, peak shift towards higher 2θ value for 0.3PAM, 0.4PAM, and 0.5PAM BiOCl samples suggested that the C^{4-} ions occupy the interstitial site in the BiOCl lattice. Moreover, the binding energy peak at 282.68 eV shown in XPS results was ascribed to the generated Bi-C bond, indicating a successful substitution of O by C in the lattice of BiOCl as well. [65]

Sulfur possesses similar an electronic shell structure with oxygen and thus similar physical and chemical properties, making it a suitable substitute for oxygen. Ma et al. doped S into non-visible-light-responsive ZnO through a one-pot hydrothermal method with L-cysteine as the sulfur source. DRS results demonstrated a red-shifted absorption edge as S concentration increased. The intensity of the Photoluminescence (PL) peak remarkably decreased ascribing to electron trapping centers

brought about by the S dopants. This indicated a highly improved electron/hole separation efficiency, which was further demonstrated by EIS test and the improved RhB degradation efficiency. [64]

Iodine (I) is an element that can be doped at either the cation or the anion form with the formed NIELs trapping holes or electrons, respectively. Al-Hamdi introduced I^{5+} into SnO_2 lattice through a wet-chemical process and extended the light responsive region of SnO_2 to the visible region. Continuous states consisting of 5p and/or 5s orbitals of I^{5+} and the O 2p orbital of the VB were favorable for efficient trapping of holes at the I-induced states in SnO_2 nanoparticle. Doping also decreased a crystallite size. Phenol degradation rate with 1% iodine doped SnO_2 nanoparticles was over 10 times higher compared to the degradation achieved through undoped SnO_2 nanoparticles under the same irradiation. [66] Lin et al. synthesized a novel I^--doped BiOBr. The slightly lower shifted angles of the (102) and (110) peaks observed in the XRD pattern with increasing doped I^- amounts suggested that I^- ions were homogeneously incorporated into the BiOBr lattice by replacing a portion of Br^- ions, due to the larger ionic radius of I^- (2.2 Å) in comparison with that of Br^- (1.96 Å). SEM images exhibited that the particle structure of BiOBr transformed from solid microspheres to scattered flakes with broken microspheres, which carried out more active sites. Moreover, transient photocurrent responses became weaker after doping, indicating a facilitated electron/hole separation. As a result, a nearly complete degradation of MO under visible light was realized after doping, as compared to 55% over pure BiOBr. [67]

Boron (B) is usually doped at its oxidation state, B^{3+}, working as an electron trap. In B-doped $BiVO_4$, B^{3+} substituted for O^{2-} and caused more V^{4+} ions as well as oxygen vacancies, while no obvious change in morphology or crystal size was observed. All three species, B^{3+}, V^{4+}, and oxygen vacancies, were able to capture e^-, facilitating e^-/h^+ separation and thus photocatalysis. E_g was decreased owing to the NIEL introduced by B^{3+} dopants just beneath the CB, leading to a red shift in the light absorbance area. B^{3+} also rendered an acidic surface of $BiVO_4$, making it easier to adsorb polarized organic pollutants. The degradation efficiency of MB within 50 min under visible light irradiation was elevated up to 98% as the result of doping. [58]

Same as metal doping, the effect of non-metal doping strongly depends on dopant concentration as well. Increasing the dopant concentration within a specific range may be beneficial to

photocatalysis. However, given that doping is generally realized by ion implantation, excessive dopants may occupy the interstitial positions in the semiconductor lattice, which would reduce the light transparency or even deteriorate the thermostability of the pristine semiconductor, and thus hinder light absorption [58]. Additionally, it should be noticed that the doping level may be limited due to the difference in the radii of dopant ions and the ions they substitute for. The research on doping C^{4-} into BiOCl lattice is a good example, where the great difference in radius between C^{4-} and O^{2-} ions made the incorporation of C^{4-} difficult, and the optimal dosage of C^{4-} was 0.4g in the experimental setting, above which the excess C might aggregate and play the role of the recombination centers [65]. Ma et al. demonstrated a reducing bandgap energy of S^{2-}-doped SnO_2 when the dopant concentration went up (Table 2). However, the highest photocatalytic activity showed up on $S2-SnO_2$, suggesting a balance between the positive and negative effects carried out by high dopant concentration. [64]

Table 2 S content of the samples obtained from TG data and the estimated bandgap energy. Produced from data provided by [64].

Sample	S/at%	E_g/eV
SnO_2	-	3.61
$S1-SnO_2$	7.13	3.01
$S2-SnO_2$	15.28	2.63
$S3-SnO_2$	31.45	2.46

Considering that most non-metal-doped semiconductors are prepared or post-treated by calcination, the calcination temperature is another significant factor determining the photocatalytic performance of doped photocatalysts. Wang et al. synthesized N-doped Nb_2O_5 through annealing Nb_2O_5 particles under NH_3 atmosphere at the relatively low temperatures of 400 ^{0}C, 500 ^{0}C, and 600 ^{0}C, followed by a hydrothermal reaction. The increase of the annealing temperature led to a greater amount of doped N and thus better visible-light responsivity but worse photocatalytic performance. This is because the excessive N atoms doped into Nb_2O_5 lattice acted as recombination centers and thus inhibited photocatalysis. [60] In the research on F-doped TiO_2, it was proposed that the high calcination temperature not only caused a reduced particle size, which

further resulted in few reactive sites, but transferred TiO_2 from the high-active anatase to the low-active rutile as well, and thus an increased photocatalytic efficiency [68]. Wang's group doped N into the $BiVO_4$ lattice by calcining the N source (hexamethylene tetramine, $C_6H_{12}N_4$) and the $BiVO_4$ precursor between 350 and 550 ^{0}C for 5h. Results showed that the photocatalytic activity of N-doped $BiVO_4$ measured by deconposing MO increased when the calcination temperature elevated from 350 to 500 ^{0}C and then decreased as the temperature continuously rose. This was because high calcination temperature was good for the growth of N-doped $BiVO_4$ crystallinity, resulting in better photocatalytic performance. However, when the temperature was higher than 500 ^{0}C, further grain growth might be caused, potentially leading to lower photocatalytic activity. [69]

Hydrothermal treatment, as another way to realize doping, also has varying influences on the doping effect at different temperatures. Wang et al. investigated the reaction temperature on preparing N -doped $(BiO)_2CO_3$ by hydothermal treatment. XRD spectra exhibited that the relatively high temperature benefited the preferred crystal growth, which was also stable. However, from SEM images, the formed uniform $(BiO)_2CO_3$ hierarchical microflowers composed of 2D nanosheets under 150 and 180 ^{0}C were destroyed at 210 ^{0}C, and the best photocatalytic activity towards NO removal occurred at 180 ^{0}C. It was speculated that at low temperatures vetween 150 and 180 ^{0}C, the nanosheets could self-assemble to construct hierarchical microspheres. Nevertheless, the nanosheets could not be self-assembled as the treatment temperature increased to 210 ^{0}C due to the accelerating hydrothermal reaction and the increasing thickness, forming randomly and irregularly arranged lamina-like nanoplates. [70]

2.3.2.3 Metal and Non-metal Co-doping

Metal and non-metal doping may introduce recombination centers as long as new impurity energy levels are generated. In addition, decomposition of a photocatalyst itself is somehow inevitable when they are prepared or post-treated by calcination, which is a usual case in doping. Although sometimes decomposition may give out desirable surface defects and/or oxygen vacancies and thus in favor of substrate adsorption, the dopant concentration and calcination temperature should be controlled carefully to avoid damaging the semiconductor crystal lattice. Considering the limited dopant concentration and potential compensating defects incurred by metal or non-metal

doping, co-doping may be a better choice. F dopant was deemed to be responsible for the generation of excess reactive oxygen species caused by the free electrons created by the F^- incorporation into the regular O_2^- sites. The Mg dopants, on the other hand, decreased the crystallite size and thus increased the specific surface area, the amount of defect states and singly ionized oxygen vacancies, which generated more hydroxyl radicals. [71]

2.3.2.4 Self-doping

As mentioned above, the introduction of foreign impurities not only brings about undesirable thermal instability of photocatalysts, but also increases the difficulty of tuning the redoxidative species during photocatalysis [72]. Meanwhile, eliminating excessive dopants also increases the complexity of photocatalyst preparation. Besides, the potential impacts of dopant itself and the doping process on the environment are not often considered. Therefore, self-doping, where dopants come from the pristine semiconductor itself, was proposed. Compared to doping with exotic elements, self-doping maintains a more homogeneous texture while enhancing light absorption [73].

Ding et al. implemented Bi^{3+}-self doped $NaBiO_3$ through the hydrolysis of $NaBiO_3 \bullet 2H_2O$ in HNO_3 aqueous solutions, which promoted the degradation efficiency of both RhB and BPA within 40 min to nearly 100% under visible light irradiation, with a respective 3.1 and 2.6 times higher reaction rate constant compared to that over pure $NaBiO_3$. Bi^{3+} was introduced into $NaBiO_3$ crystals by replacing Bi^{5+} in the BiO_6 octahedra structure, accompanied with generated oxygen vacancies. These Bi^{3+} defects ($Vo - Bi^{3+}$) produced isolated states in the band gap and acted as electron donors. E_g was decreased from 2.45 to 1.68 eV. Therefore, the electronic transmission from the VB to $Vo - Bi^{3+}$ was deemed as the primary contribution to both the enhanced visible light absorption and the facilitated carrier separation. This process is exhibited in Equation (21), where the symbol □ represents an empty position originating from the release of O_2^- ions in the lattice. [73]

$$4Bi^{5+} + O^{2-} \rightarrow 4Bi^{5+} + 4e^-/\square + O_2 \rightarrow 2Bi^{5+} + (Bi^{3+} - \square - Bi^{3+}) + O_2 \quad (21)$$

In another research on Bi^{3+}-self-doping, dopants did not change redox potentials of the photogenerated carriers but promoted their separation in the $BiWO_6$ lattice by replacing W atoms

with Bi. The substituted Bi atoms had much smaller charges than the W atoms and other Bi atoms. In addition, electrons of oxygen atoms around a substituted Bi atom in the doped composite were also decreased compared to the pristine $BiWO_6$, suggesting a charge redistribution after doping. This redistribution changed the internal electric field of the photocatalyst, favoring electron/hole separation. As a result, the decolorization and TOC removal of pentachlorophenate in 5 h were promoted to 90% and 85%, respectively, with a 12 times higher reaction rate constant. The primary reactive species changed from h^+ to $O_2^{\bullet-}$ after doping. [72]

Self-doping may be influenced by dopant concentration as well. The most common impact of excessive dopants is the redundant defects, which are potential recombination centers retarding photocatalysis. In the research of I^--self-doped BiOI carried out by Zhang et al., both the photocatalytic activity and efficiency were decreased when the iodine content exceeded the optimal value as exhibited in Figure 8. [74]

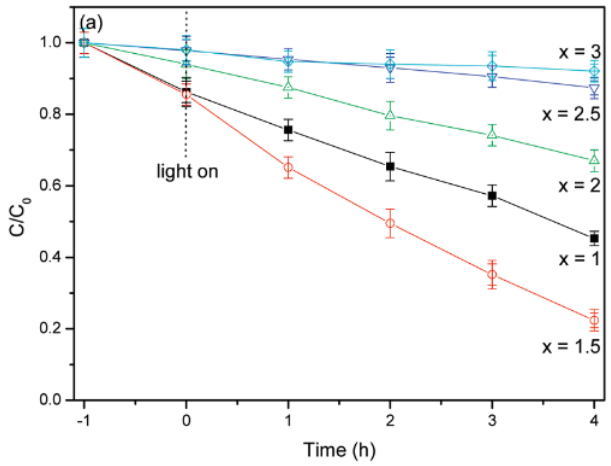

Figure 8 Variation on degradation efficiencies of $BiOI_x$ towards methyl orange under visible light irradiation. Reprinted with permission from [74]. Copyright (2010) American Chemical Society.

2.3.3 Metal Nanoparticle Loading (Deposition)

When metal nanoparticles (NPs) are loaded on the semiconductor surface, two possible phenomena may happen at the interface: the Schottky barrier and the localized surface plasmon resonance (LSPR) effect [75]. Schottky barrier leads to photogenerated electrons in the semiconductor flowing into the loaded metal NPs and therefore contributes to effective electron/hole separation. LSPR effect, on the other hand, facilitates light absorption and thus

reactive species generation in three ways: photon scattering, LSPR sensitization, and near-field electromagnetic enhancement [76]. These two phenomena may occur separately or function synergistically based on excitation conditions.

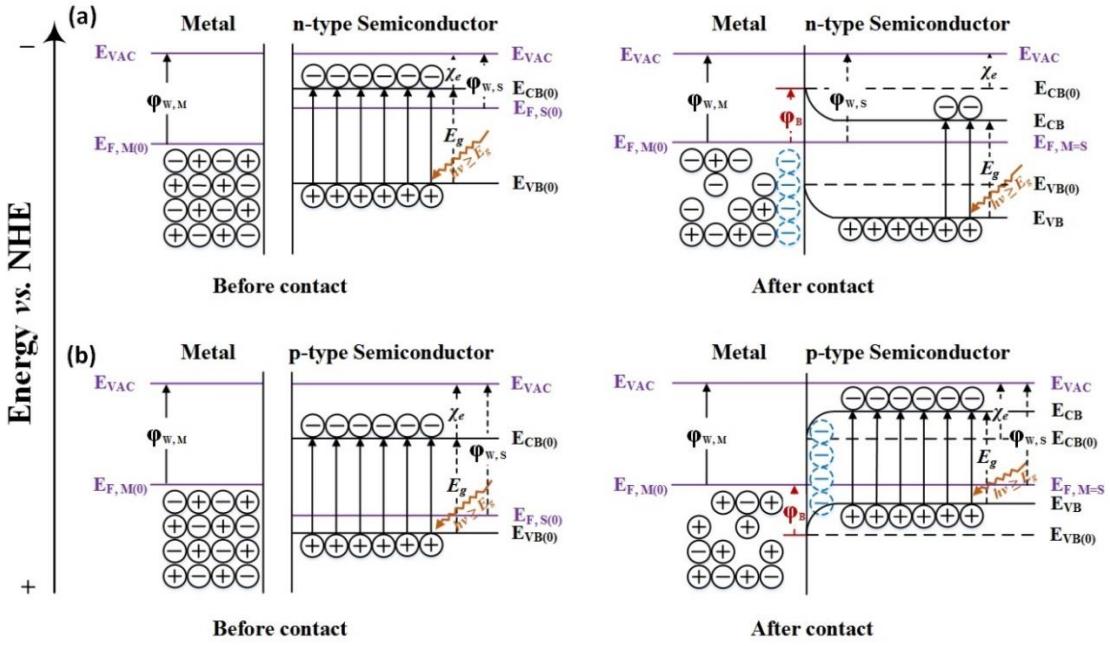

Figure 9 Charge carrier distribution before and after metal nanoparticles contact with n-type (a) and p-type (b) semiconductors. $E_{F,M(0)}$ refers to the vacuum level. $E_{F,M(0)}$ and $E_{F,S(0)}$ refer to the Fermi levels of metal and semiconductor before contact, respectively. $E_{F,M=S}$ refers to the newly reached equilibrated Fermi level. $E_{CB(0)}$ and $E_{VB(0)}$ refer to the energies of the conduction band and valence band before contact, respectively. E_{CB} and E_{VB} refer to the energies of the conduction band and valence band after contact, respectively. χ_e refers to the electron affinity. $\phi_{W,M}$ and $\phi_{W,S}$ refer to the work function of the metal and semiconductor, respectively. ϕ_B refers to the Schottky barrier.

For n-type semiconductors, their Fermi levels are generally higher than those of metals [75]. Therefore, when metal NPs are deposited onto an excited semiconductor, photogenerated electrons would migrate from the semiconductor to the metal until their Fermi levels reach an equilibrium. Thus, some electrons would accumulate on the metal side at the metal/semiconductor interface, while the holes would collect on the other side, forming a potential energy barrier, which is the so-called Schottky barrier. Schottky barrier blocks electrons transferred to the metal from flowing back to the semiconductor so that they can participate in the subsequent reactions with the substrates before recombining. On the contrary, for metal NPs/p-type semiconductor photocatalysts, metal usually works as the electron donor, and the charge distribution is on the

contrary to in the case of n-type semiconductors [34]. The charge carrier distribution in metal/n-type semiconductor and metal/p-type semiconductor components are indicated in Figure 9(a) and (b), respectively.

Metals have no bandgaps, so that conduction (free) electrons in metal NPs move freely. Therefore, when metal NPs are illuminated by light with the wavelength far exceeding the NPs' diameters, electrons can easily gain energy from the light [77]. This excites electrons in an NP redistribute to higher energy states from the lower levels, leading to a high density of electrons on one side and a low density on the other [75]. As a result, two electric fields with opposite directions inside and outside will be created, which is also called electron polarization, meanwhile oscillation of the metal surface electrons will be caused by their positive nuclei [75]. If the photon frequency matches the electron oscillation frequency, this phenomenon is called Localized Surface Plasmon Resonance (LSPR) [78]. So far, three mechanisms have been proposed to explain LSPR-enhanced photocatalysis: near-field electromagnetic enhancement, LSPR sensitization, and photon scattering [76].

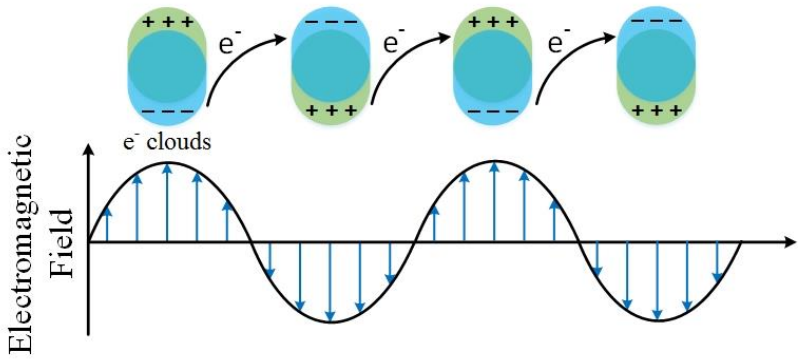

Figure 10 Localized Surface Plasmon Resonance (LSPR) effect on metal nanoparticles.

When there is a spectra overlap among the illumination source, the semiconductor absorption, and the metal NPs LSPR, an LSPR-induced electromagnetic field would form at the metal/semiconductor interface, which has the intensity of up to 100-10000 times that of the incident electric field of the semiconductor [79] . Since the e^-/h^+ pair generation rate is proportional to the local excitation light intensity, more active charge carriers will be produced, resulting in an enhanced photocatalytic activity [80]. Besides, the formed electromagnetic field is also capable of polarizing the nonpolar substrates and attracting charged and polarized substrates

due to Coulombic forces, which enhances substrate adsorption [81], and heats up the surrounding environment facilitating mass transfer and the surface redox reactions [82]. The intensity of the above near-field electromagnetic enhancement is the highest at the metal/semiconductor interface, and decays nearly exponentially with the distance between the metal and the semiconductor [83]. During decaying, e^- in the electron clouds formed in plasmon metal NPs can be injected to the semiconductor CB if they have sufficient energy to overcome the Schottky barrier, which is called "hot electron" [84,85]. The holes left behind in the metal nanocrystal have a mild oxidation ability, which can be utilized for chemoselective oxidation of some organic molecules [86]. When the size of metal particles increases, incident photons can be scattered by being reflected multiple times around the semiconductor before reaching its surface. This process not only prolongs the optical path lengths of the photons and thus improves the light absorption efficiency of the semiconductor, but leads to an enhanced electron/hole as well [87]. The relative contributions of absorption and scattering to the total optical excitation, described by Mie theory [88], strongly depends on the size of the metal NPs. Tcherniak et al. performed Mie theory calculated NP diameters ranging from 20 to 300 nm, and elucidated that the scattering cross-section became larger than the absorption cross-section for a NP size was larger than 102 nm as shown in Figure 9 [89]. Similarly, Christopher et al. indicated an effective scattering effect of Ag NPs on TiO_2 when the Ag size was between 30~100 nm [90].

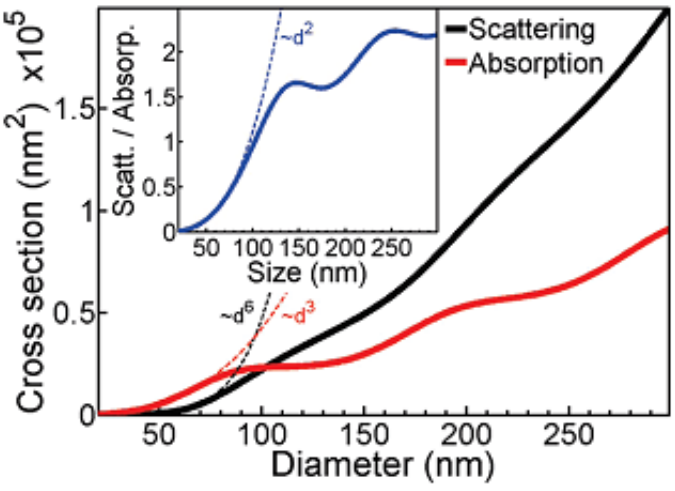

Figure 11 Mie theory prediction for scattering (black) and absorption (red) cross sections as function of NP size as a wavelength of 532 nm and with a medium index of refraction of 1.25. Inset: Ratio of scattering and absorption cross sections as a function of NP size. The dashed lines show how simplified power dependences are only accurate for NP sized below 80 nm. Reprinted with permission from [89]. Copyright (2010) American Chemical Society.

The earliest and most often applied metals loaded on semiconductors are noble metals, especially silver (Ag) and gold (Au).

In Ag-loaded AgI composites, Ag and AgI were simultaneously excited under visible light to form e^-/h^+ pairs. Due to the lower Fermi level of Ag compared to that of AgI, electrons produced by AgI flowed to Ag and then trapped by the adsorbed O_2 molecules to generate $O_2^{\bullet-}$ and $\bullet OH$. Degradation efficiency of RhB reached 97.4% within 20 min with a 1.6 times higher reaction rate constant compared to pure AgI. [91] Sampaio et al. reported a promoted decomposition efficiency towards phenol when Ag was deposited onto ZnO, where Ag NPs worked as the electron sink, and h^+ played the main role [92]. Yet, Jiang et al. reported that electrons flowed from Ag to AgBr after loading due to the lower Fermi level of p-type AgBr [34]. Daupor and Wongnawa found that light source influenced the mechanism of LSPR-assisted photocatalysis carried out by Ag/AgCl. Under UV irradiation, AgCl was excited and the generated electrons moved to the deposited Ag NPs as a result of Fermi level equilibrium. Under visible light, on the other hand, AgCl could not be triggered while Ag metal NPs were able to absorb photons from the irradiation through the intrinsic LSPR effect and produced e^-/h^+ pairs. The produced electrons transferred to the CB of AgCl and gave out reactive species $O_2^{\bullet-}$ by reducing O_2. The generated holes left in Ag NPs could take part in the photocatalytic process in two ways. One was to oxidize Cl^- ions to Cl^o atoms, which could oxidize orange G dye and then be reduced back to Cl^- ions. The other was to produce $\bullet OH$ from OH^-. [93]

Au NPs loading is also studied. When Bi_2O_3 was loaded with Au NPs, the RhB degradation efficiency was promoted from 26% to 80%. With respect to 2,4-dichlorophenol, not only did the degradation rate increase from 35% to 65%, the TOC removal rate was rose from 19% to 53% as well. The absorption shoulder center of Au/Bi_2O_3 composites located around 590 nm attributed to the LSPR effect of Au NPs, while there was no absorption observed in the region of 450~800 nm for pure Bi_2O_3. Results also revealed that the loaded Au NPs played a critical role in charge carrier separation by capturing the electrons from the CB of the excited Bi_2O_3. [94] In another study carried out on Au-loaded Bi_2O_3, the degradation rate constant of AO 10 was promoted to 1.8 times higher when Au was loaded [95]. The same effects have also been observed when Au NPs were loaded on WO_3 for decomposing diverse organics, including RhB, MO, MB, and AF

illuminated by visible light [96]. Yet, instead of accepting electrons, Au NPs functioned as electron donors in Au/Bi_2CuO_4 composites due to their higher Fermi level compared to that of Bi_2CuO_4. Results showed the maxima of absorbance was red-shifted to 593 eV, and the degradation rate of ceftiofur sodium was promoted up to 56% [97].

Other noble metals have also been investigated. The photocatalytic activity of Pt-loaded WO_3 was much better than that of N-doped TiO_2 under visible light and was almost comparable to TiO_2 under UV irradiation. The deposited Pt NPs were speculated to work as the electron pool and producer of $O_2^{\bullet-}$. [98] Yu et al. investigated the effects of three noble metals (Rh, Pd, and Pt) on the optical and photocatalytic performance for the degradation of AO II dye under visible light when they were loaded onto BiOX (Cl, Br, I) separately, and their efficiencies on BiOCl were in the order of $Rh > Pt > Pd$. They also found that the Pd and Pt over bismuth oxyhalides were at their metallic states while Rh existed as both metal and oxide species. [99]

However, the expensive cost, possible toxicity and complicated postprocessing (leaching) of noble metals limit their widely practical applications [40]. Therefore, some transition and post-transition metals were explored. For instance, Cu-loaded $BiVO_4$ revealed an enhanced catalytic efficiency compared with pure $BiVO_4$ towards MB degradation attributed to its broadened absorption region and narrowed bandgap carried out by Cu NPs [100]. Bi-loaded Bi_2WO_6 indicated an improved activity compared to pure Bi_2WO_6, which was mainly attributed to the formed Schottky barrier on the Bi/Bi_2WO_6 interface as well as the increased local electromagnetic field in the metallic Bi NPs, which improved both the electron-hole separation efficiency and light absorption ability were intensely improved. [101]

Yu et al. greatly promoted the degradation activity towards MO under visible light over Ag_3PO_4 by loading Ag NPs and Fe(III) cocatalysts simultaneously. The Ag NPs caused an obviously enhanced visible-light absorption due to its LSPR effect, producing more photogenerated carriers; the Fe(III) cocatalysts worked as effective active sites for the subsequent O_2 reduction, generating $O_2^{\bullet-}$ as well as hindering recombination. The reaction followed a pseudo-first-order mechanism, and the rate constant (K_{app}) of pure, Fe(III)-loaded, Ag-loaded and Fe(III)/Ag-coloaded Ag_3PO_4 was listed in Table 3. [102]

Table 3 Comparison of reaction rate constants of pure and loaded Ag_3PO_4. Produced from data provided by [102].

Sample	K_{app}/min^{-1}
Ag_3PO_4	0.024
Fe(III)-loaded Ag_3PO_4	0.03
Ag-loaded Ag_3PO_4	0.032
Fe(III)/Ag-loaded Ag_3PO_4	0.038

Wang et al. employed the synergetic effect of doping and loading and reduced the time of completely degrading RhB under daylight lamp from 3h to 1h by loading Ag onto the Ti-doped BiOBr surface. The irradiation activated both Ti-doped BiOBr and the loaded Ag NPs. The LSPR-induced electrons in Ag NPs flowed to the CB of Ti-doped BiOBr and were subsequently trapped by O_2 to form $O_2^{\bullet-}$. Meanwhile, Ag NPs that lost electrons transformed to its oxidation state Ag^{n+}, which was considered to be an active species oxidizing RhB and could subsequently return back to the ground state Ag. Moreover, the photogenerated holes could oxidize RhB both directly and indirectly by producing • OH. [103]

The contribution of the LSPR effect of metal NPs is found to primarily depend on their shape and size [77]. Specifically, surface geometry changes in the particle shape or size may cause a shift in the electric field density on the surface, impacting the oscillation frequency of electrons, and then generate different cross-sections for optical properties including absorption and scattering [104]. In general, sharp corners have red-shifted peaks compared to rounded structures with the similar sizes, since the sharp features tend to increase charge separation and reduce the restoring force for the dipole oscillation such that a reduction in resonance frequency or red-shift in wavelength is expected [105]. TEM images of Ag triangular nanoparticles revealed an obvious blue shift in the absorption shoulder peak when they became rounder [106]. Furthermore, hollowing out a metal nanostructure has also been proven to be a powerful means to dramatically red-shift the LSPR peak while maintaining a compact size by Wang et al. The solid Ag NPs had an LSPR speak at ~395 nm; in contrast, the peak position of Ag nanoshells with the same outer diameter as the solid NPs was red-shifted to 506 nm [107]. Fendler found that the LSPR peak of Ag solid nanocubes was located in the range of 320-550 nm, whereas that of Ag nanocages was red-shifted to ~530 nm

[108]. Also, as the particle size went up, not only did the light absorption edge have a red shift, the absorption band became broader as well, resulting in an improved photocatalytic activity [109]. As reported by Pawinrat and co-workers, the reaction rate of MB degradation on Au-loaded ZnO increased from 0.89 to 1.14 h^{-1} when the particle size of Au was rose from 4.1 to 6.3 nm [110]. Nevertheless, sometimes metal NPs with a relatively small size do not manifest LSPR performance. For instance, the LSPR effect of neither Au nor Pt NPs was observed when they were loaded on Cu_2ZnSnS_4 separately due to their relatively low concentration and very small size [111].

Table 4 Specific surface area of the pure and noble metal loaded BiOCl. Adapted with permission from [99]. Copyright (2013) Elsevier.

Sample	$\mathbf{S/(m^2g^{-1})}$
BiOCl	10.1
Pd(0.5%)/BiOCl	8.3
Pd(1%)/BiOCl	8.8
Pd(2%)/BiOCl	6.1
Pd(4%)/BiOCl	9.6
Rh(0.5%)/BiOCl	9.8
Rh(1%)/BiOCl	9.6
Rh(2%)/BiOCl	8.5
Pt(0.5%)/BiOCl	7.8
Pt(1%)/BiOCl	7.0
Pt(2%)/BiOCl	6.4
Pt(4%)/BiOCl	6.3

On the other hand, increasing particle size may also decrease both the specific surface area and active sites. The dielectric constant of both the loaded metal NPs and the semiconductor matrix have an impact on the intensity of the LSPR effect as well. Same as doping, there is an optimal concentration in loading, above which the photocatalytic processes may be impaired. Excessive metal NPs would cover a part of the semiconductor surface, especially active sites exposed to the

irradiation as well as pores, hampering light penetration and thus photon absorption [91,92,100]. Also, excessive loading content may weaken the anchoring factors, leading to a poor attachment among different particles [112]. Furthermore, excessive metal NPs may cause agglomeration and thus restrain photocatalysis due to the decreased specific surface area. On the Au-loaded ZnO composites, the average diameters of Au particle/cluster increased from 3 nm to 7 nm as the loading amount was rose from 1 wt% to 3 wt%. The photocatalytic activity was higher on 1 wt% Au-loaded ZnO than that when the Au content was 3 wt%, attributed to the lower LSPR intensity of Au NPs when the particle size went up as a result of the increasing content. [110] Finally, the excessive metal NPs may also act as recombination centers [75,101]. The research on depositing Pd, Rh, and Pt onto BiOCl is clearly illustrated in Table 4 [99].

2.3.4 Semiconductors Coupling

2.3.4.1 Introduction

It is inevitable that doped metal ions would dissolve in the solution and may be more toxic than the original substrates, or act as recombination centers [58]. As for metal nanoparticles loading, except for metal leaching and formed recombination centers, light-responsive area on deposited semiconductor may be shielded, negatively impacting on light absorption [91,92]. In addition, it is obvious that whether doping or loading, only one semiconductor is involved, so the enhancement in photocatalytic performance is limited. Also, although semiconductors with narrower band gaps have wider light absorption spectra, the energy resistance for recombination is low as well. Semiconductors coupling, on the other hand, is carried out between two or more semiconductors with distinctive band gaps, and effectively separates electrons and holes into different semiconductors. Depending on the relative bandgaps and electronic affinity, semiconductors coupling can be classified into three cases: type-I, type-II, and type-III band alignments as shown in Figure 12 [113].

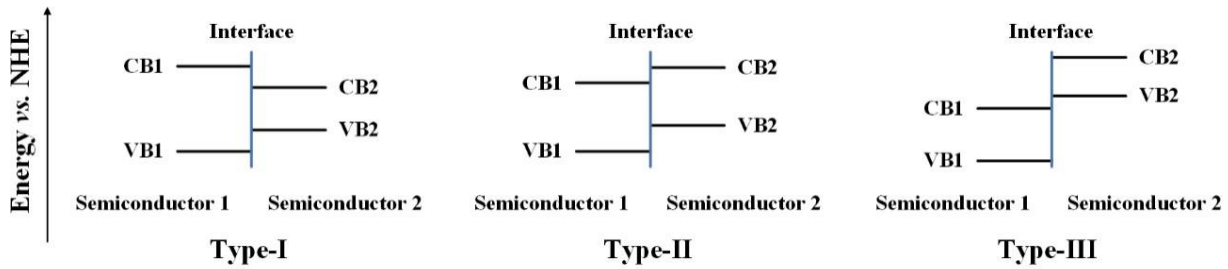

Figure 12 Schematic energy band diagram of three types of semiconductor heterojunctions.

For type-I heterojunctions, electrons and holes generated in both semiconductors accumulate in the same semiconductor with a narrower band gap and thus no enhancement in charge separation can be expected. For type-II heterojunctions, the staggered energy band arrangement makes the flow of charge carriers possible at the interface of the two semiconductors, thus facilitating electron/hole separation. For type-III heterojunctions, the energy differences between the corresponding band gaps are too high for charge carriers to overcome.

For the above reasons, type-II band alignment is most preferred. The following discussions will focus on the type-II heterojunctions unless particularly stated. As shown in Figure 12, in a type-II heterojunction, the band energies follow a staggered structure. Depending on the movement of charge carriers as well as energy bands, there are three mechanisms: conventional heterojunction, p-n heterojunction, and Z-scheme heterojunction.

2.3.4.2 Conventional Heterojunction

Conventional heterojunction usually happens between semiconductors with the same type [7]. In a conventional heterojunction, electrons produced at the more negative CB transfer to the less negative one, while holes generated at the more positive VB move to the less positive one, as indicated in Figure 13. Whether both (Figure 13(a)) or one (Figure 13(b)-(c)) of the semiconductors respond to the irradiation, electrons and holes will be effectively separated in different semiconductors, leading to better photocatalytic performance.

separated in different semiconductors, leading to better photocatalytic performance.

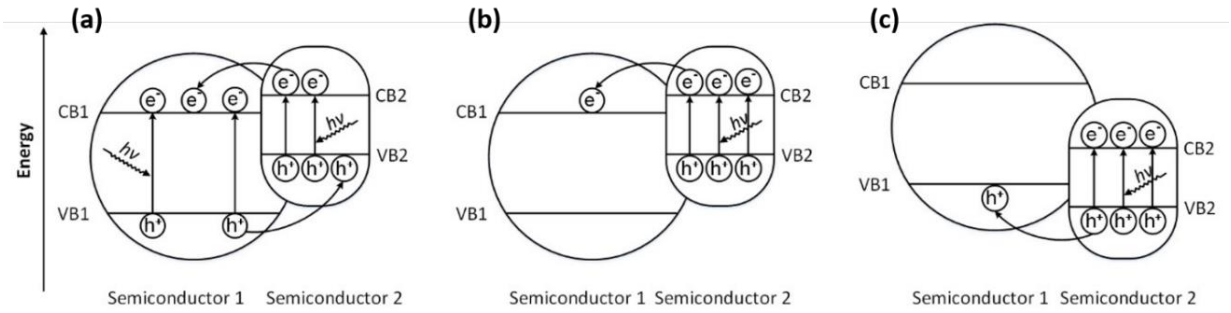

Figure 13 Transfer of photogenerated carriers in n- and n-type semiconductors coupling when: (a) both are excited by irradiation, and (b) only one is excited.

Yan et al. fabricated a $CdS/MnWO_4$ heterojunction via multi-step hydrothermal method, where $MnWO_4$ and CdS correspond to SC1 and SC2 in Figure 13(a), respectively. UV–vis DRS showed a gradually red shifted absorption range of $CdS/MnWO_4$ composites when increasing the amount of CdS. EIS Nyquist plots revealed a better electron/hole separation. The specific surface area of $MnWO_4$ was also increased after CdS particles grew. Under visible light irradiation (λ>420 nm), 91% of MB was degraded after 90 min on the $CdS/MnWO_4$ composite, which was only 50% and 7% of pure CdS and $MnWO_4$, respectively. The degradation efficiency of MV within 60 min was also promoted. [114]

A novel $SnO_2/ZnO/TiO_2$ ternary composite photocatalyst was successfully synthesized using sol-gel and solid-state methods by Yang's group and has been utilized for MO degradation. Results obtained from both UV and visible light irradiation showed an enhancement in the photocatalytic performance compared to each of the semiconductors working alone or any two of them coupled, which was mainly benefitted from the formed staggered type-II heterojunction as shown in Figure 14. Meanwhile, combining TiO_2 with SnO_2 and ZnO could promote the TiO_2 phase transition from less-active anatase to more-active rutile. The increased specific surface area was also responsible for the enhanced catalytic efficiency. [115] Zhang et al. prepared SnS_2/SnO_2 composites via an in situ hydrothermal oxidation of SnS_2 nanoparticles in H_2O_2 aqueous solutions. Under visible light irradiation, SnS_2 was activated while SnO_2 was not. Electrons produced on the SnS_2 CB migrated to of SnO_2, while the holes remained in SnS_2, which matched the configuration of Figure 13(b). The reaction rate constant of the composite for MO was promoted to 1.6 times that of pure SnS_2. However, when the SnO_2 content exceeded 18.1 wt%, not only did the light-sensitive and reactive sites on SnS_2 were shielded, the attachment between

the two semiconductors also became slack due to the aggregation of SnO_2 particles, suggesting a weakened interaction and thus an inferior electron transfer at the interface. [116]

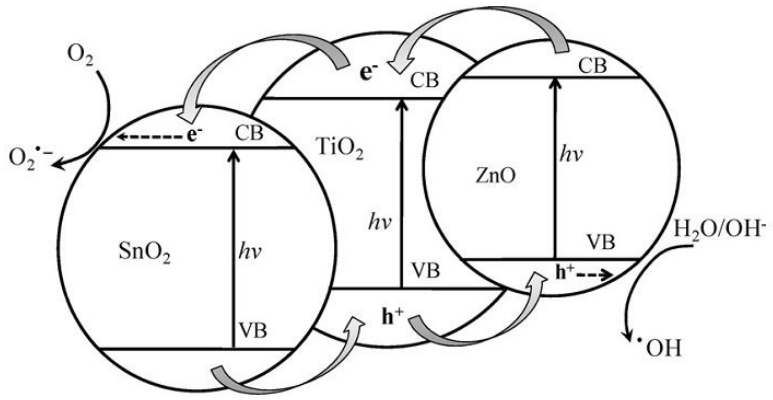

Figure 14 Schematic energy band structure and electron–hole pair separation process of $SnO_2/ZnO/TiO_2$ composite semiconductor system. Reprinted with permission from [115]. Copyright (2012) Elsevier.

A one-dimensional BiOBr nanosheets/TiO_2 nanofibers composite was obtained by solvothermal treatment. The movement of photogenerated electrons and holes under visible light followed the configuration of Figure 13(c), where BiOBr was excited while TiO_2 was not. The enhancement in photocatalytic degradation of 4-NP was attributed to the extended absorption in the visible light region from the narrow band-gap of BiOBr and the more effective photogenerated electron-hole separation via the $BiOBr/TiO_2$ heterojunction. [117]

Core-shell configuration is a special scenario of type-II heterojunction. In a core-shell heterojunction, a narrower-band-gap semiconductor (SN) caps the entire surface of a wide-band-gap semiconductor (SW) by forming an outer shell. SN works as not only a separation center for photogenerated electrons and holes, but also a sensitizer especially when SW is not responsive to the irradiation. Yang et al. observed a 90% degradation ratio for methyl blue in the presence of $ZnIn_2S_4$-capped TiO_2, which was 0% and 71% on pure TiO_2 and $ZnIn_2S_4$, respectively. They proposed that electrons which moved to the TiO_2 core were capable of capturing O_2 to produce $O_2^{\bullet-}$, as expected in general coupling because of the non-compact deposition of $ZnIn_2S_4$. Since $ZnIn_2S_4$ nanosheets were uniformly grown on the surface of TiO_2, excessive aggregation of $ZnIn_2S_4$ was avoided, which further increased active sites and improved substrate adsorption as well. [118] However, when the shell semiconductor compactly disperses on the core surface, only one carrier, either electrons or holes, is accessible on the composite surface while the other one

gathers in the core, which renders a strong carrier transport barrier and thus inhibits the degradation process [119]. This deduction has been proven in a study by Huang's group, where the ZnS shell layer reduced the photocatalytic efficiency of ZnO in the methyl orange degradation [120].

2.3.4.3 p-n Heterojunction

In conventional heterojunctions, although photogenerated electrons and holes accumulate in different semiconductors, recombination is still serious. Moreover, migration of electrons from CB2 to the electron-rich CB1 and the corresponding migration of holes from VB1 to the hole-rich VB2 are physically unfavorable because of the electrostatic repulsion among same charge carriers.

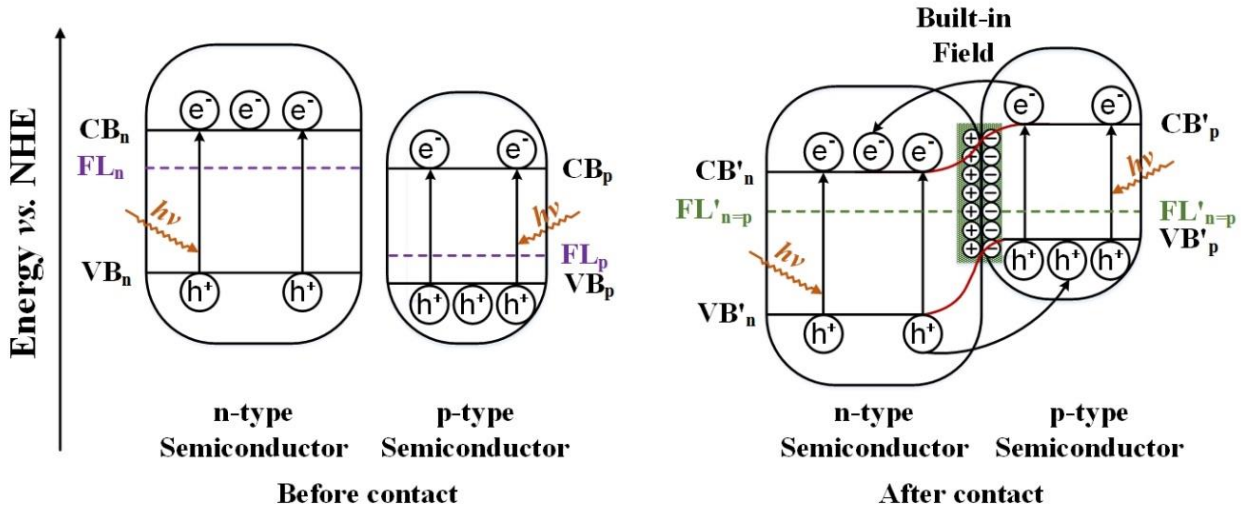

Figure 15 Band bending and built-in field in p- and n-type semiconductors coupling (a) before and (b) after contact.

When a heterojunction is composed of an n-type and a p-type semiconductor, which are both excited, however, the difference between their Fermi levels drives energy bands to realign until a Fermi-level-equilibrium is reached. During this process, electrons flow from the n-type semiconductor to the p-type one, and holes move in the opposite direction simultaneously. Thus, electrons would accumulate on the p-type semiconductor side while holes on the other side at the interface, bringing about a band-bending, which is similar to Schottky barrier. As a result, a built-in spatial charge layer is formed, driving electrons and holes to further separate to the n-type and p-type semiconductor, respectively, due to electrostatic attraction. The separated charge carriers would participate in the subsequent reactions, resulting in a better photocatalytic performance. It is worth to mention that although the aligned energy bands of the coupled semiconductors follow

the type-II heterojunction, they do not need to be a type-II configuration before alignment. Also, as the Fermi levels change to an equilibrium state, the levels of CBs and VBs of both semiconductors would also change to maintain the same bandgaps.

By employing $BiOI/CeO_2$ p-n heterojunction photocatalysts fabricated using a facile in situ chemical bath method, Wen et. Realized an improved decomposition efficiency with regard to both MO and BPA, compared to that when the two semiconductors worked separately. Photocurrent experiment and EIS measurements confirmed the enhanced electron/hole separation. The dominant species were indicated to be h^+ and $O_2^{\bullet-}$ radicals. The high stability and superior reusability of the $BiOI/CeO_2$ composite was proven by recycling for four runs. [28] Upon the $BiOBr/m\text{-}LaVO_4$ p-n heterocomposite synthesized by a two-step hydrothermal process, Ma et al. promoted the photodegradation rate of RhB under visible light irradiation within 60 min to 83%, up from 12% and 55% on pure $m\text{-}LaVO_4$ and pure BiOBr, respectively. This enhancement was mainly ascribed to the facilitated charge separation at the composite interface carried out by the formed p-n heterostructure. The reduced of BiOBr particle size induced by the deposition of $m\text{-}LaVO_4$ might be another reason for the improved photocatalytic activity. [121]

Peng et al. fabricated a one-dimensional $BiOI/Bi_2O_2CO_3/Bi_4O_5I_2$ ternary p-n-p heterojunction photocatalyst by a low-temperature solution method using Bi_2O_3 nanorods as sacrificial templates. The schematic diagram for energy bands and the formation of the p-n-p junction is illustrated by Figure 16. After the energy bands and Fermi levels rearranged, all of the three components were excited. $Bi_2O_2CO_3$ worked as the electron reservoir while holes generated there migrated to the VBs of the other two semiconductors. Its superior photocatalytic activity under visible light irradiation was verified by degrading RhB. This enhanced photocatalytic performance was ascribed to the high separation rate of photo-generated carriers in the internal electric field due to the formation of p–n–p junctions and a relatively large BET surface area. More importantly, a 1D heterostructure was beneficial for the transport of photo-generated electron–hole pairs which further improves the rate of photocatalytic reaction. [122]

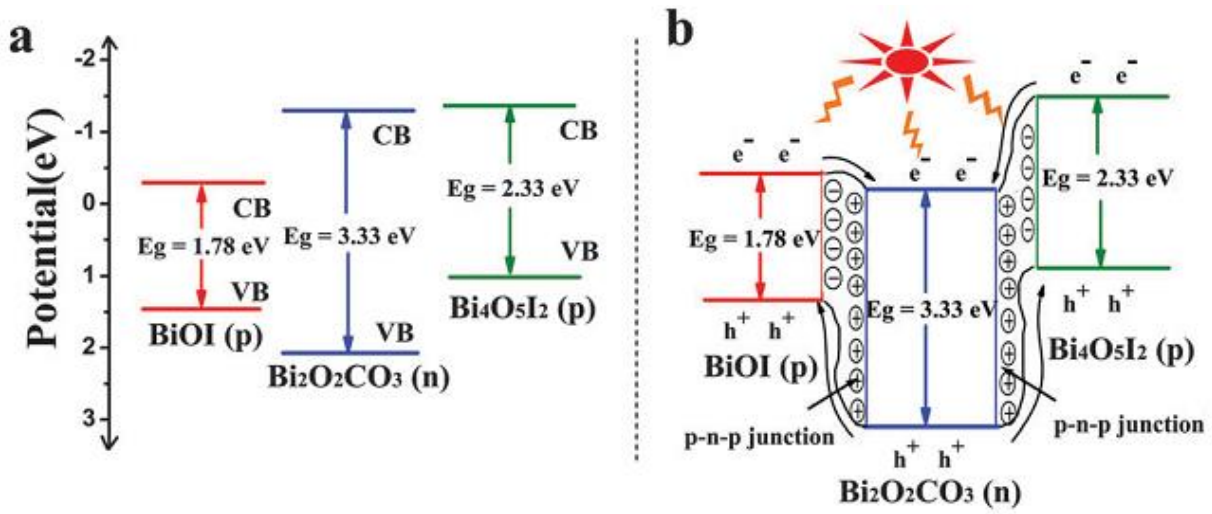

Figure 16 Schematic diagram for (a) energy band of BiOI, $Bi_4O_5I_2$ and $Bi_2O_2CO_3$ and (b) the formation of the p–n-p junction and the possible charge separation. Reprinted with permission from [122]. Copyright (2015) Royal Society of Chemistry.

2.3.4.4 Z-Scheme Heterojunction

Although conventional separation and p-n heterojunction models are capable of extending the spectral range of light absorption and facilitating electron/hole separation, redoxidation power of energy bands will be inevitably undermined [123]. Therefore, it is desirable to enhance the charge separation of composites while maintaining the strongest oxidation and reduction potentials. Z-scheme heterojunction is carried out by the recombination between electrons and holes from different semiconductors whilst leaving the corresponding holes and electrons at their original locations. This process is thermodynamically and physically more favorable due to electrostatic attraction between electrons and holes [123,124]. As shown in Figure 17, there are two types of Z-scheme heterojunction: one is the direct Z-scheme heterojunction without the assistance of mediators (Figure 17(a)), and the other is the indirect Z-scheme heterojunction which is realized in the presence of mediators (Figure 17(b)).

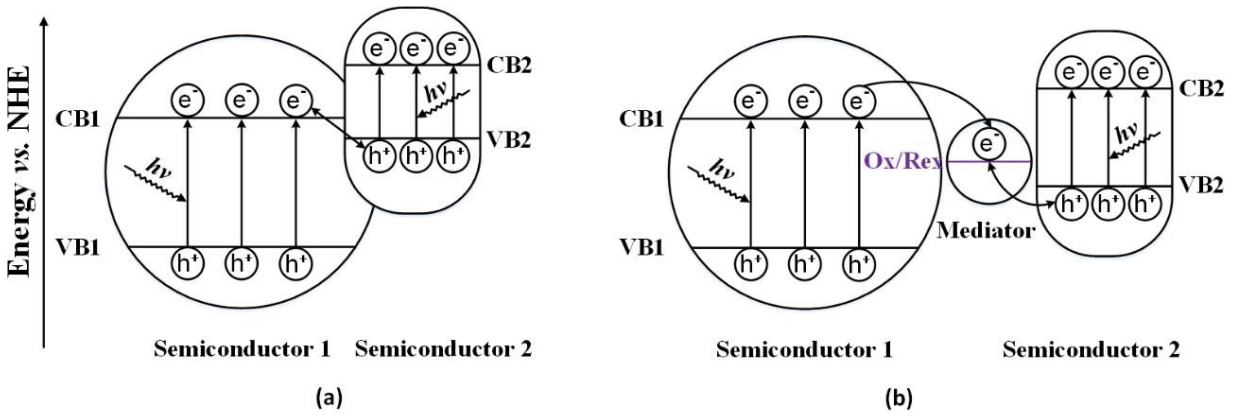

Figure 17 Electron transfer following the p-n type photochemical diode model: (a) without mediator, and (b) with mediators.

A novel Z-scheme $SnS_2/BiOBr$ heterojunction photocatalysts were constructed via a facile in situ growth strategy. Under visible light irradiation, $SnS_2/BiOBr$ composite exhibited superior photocatalytic activity towards the RhB degradation, which was 75 and 2.2 times of that on bare SnS_2 and BiOBr, respectively. Through radical quenching experiments, $O_2^{\bullet-}$ was found to be the predominant active species. However, since the reduction potential of the BiOBr CB is lower than the redox potential of $O_2/O_2^{\bullet-}$, $O_2^{\bullet-}$ could not be produced by electrons on the CB of BiOBr. Therefore, the composition prefers a direct Z-scheme mechanism, where electrons on the BiOBr CB and holes on the SnS_2 VB recombined, while electrons and holes with higher redox potentials produced on the BiOBr CB and SnS_2 VB were maintained and took part in the subsequent reactions. Also, the excellent photostability was reflected by the negligible efficiency decrease after four runs. [125] By means of employing CuS/WO_3 composites synthesized by a facile solution method at low temperature, the degradation rate constant of RhB under visible light was promoted to 9.2 and 4.4 times higher than that on the bare CuS and WO_3, respectively. Band structure analysis showed that the CB of WO_3 was only ~0.01eV higher than the VB of CuS, and the dominant reactive species were h^+ and $O_2^{\bullet-}$ as indicated by quenching experiments. PL spectra revealed an intensely hindered recombination in WO_3. This suggested that the electrons produced on the WO_3 CB recombined with holes generated from the VB of CuS, resulting in a Z-scheme heterojunction. [126] Yu et al. reported a controlled preparation of $Bi_2S_3/SnS_2/Bi_2O_3$ double Z-scheme ternary heterojunction photocatalyst by a simple one-pot solvothermal route. The experimental results with regard to RhB degradation showed a significantly enhanced catalytic activity of the as-fabricated heterojunctions compared to pure Bi_2S_3. By further investigating the

charge separation and migration behaviors with EIS and photocurrent response analysis, studying the band structure, as well as conducting the active species trapping experiments, a possible double Z-scheme photocatalytic mechanism was proposed, which highlighted the efficient e^-/h^+ separation while maintaining the strongest oxidation and reduction potential of VB holes generated in Bi_2O_3 and the CB electrons produced in Bi_2S_3, respectively, as shown in Figure 18. [127]

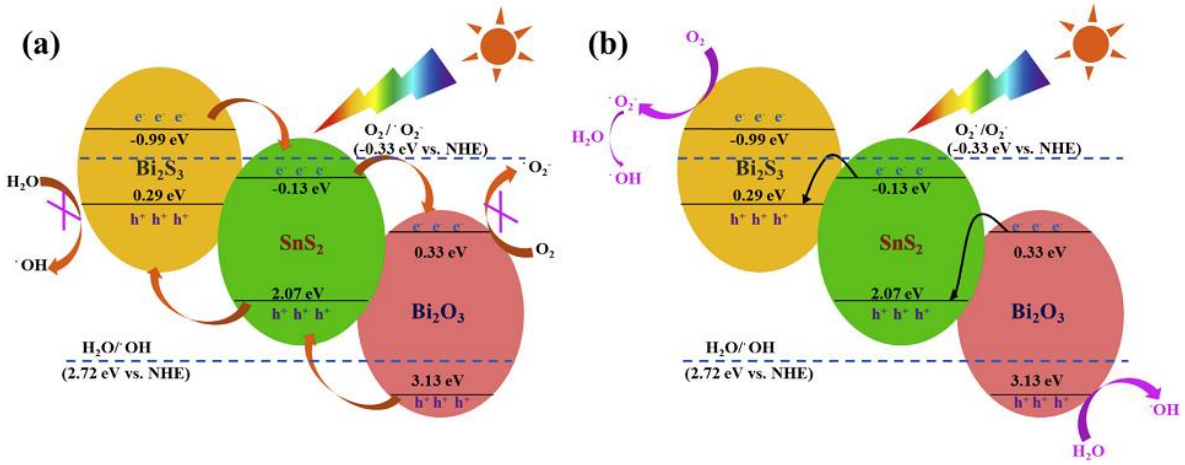

Figure 18 Proposed mechanism for charge transfer path over $Bi_2S_3/SnS_2/Bi_2O_3$ photocatalyst under sunlight irradiation: (a) traditional path and (b) double Z-scheme model. Reprinted with permission from [127]. Copyright (2017) Elsevier.

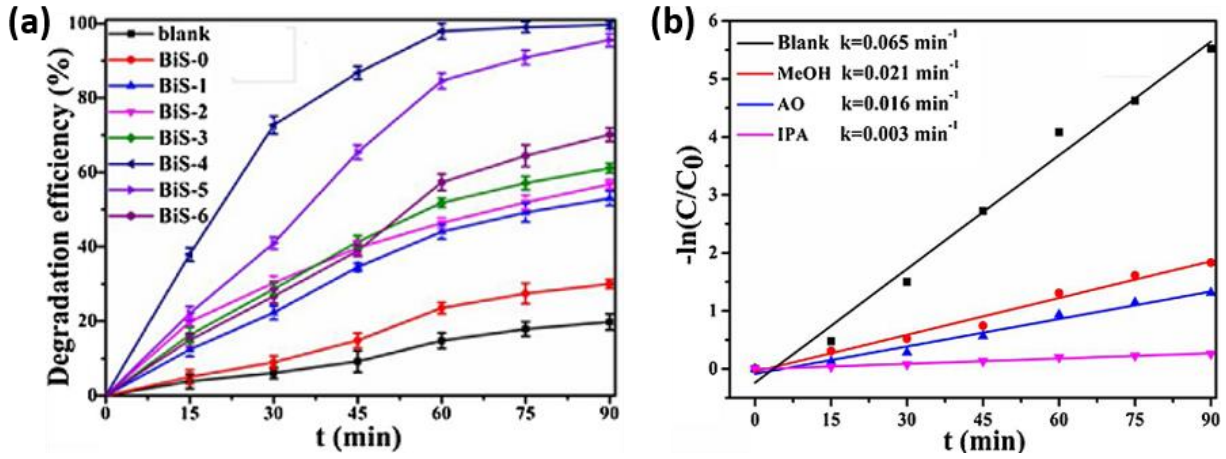

Figure 19 (a) Comparison of degradation efficiencies of the RhB-contained wastewater under simulated sunlight irradiation in the presence of samples fabricated with various amount of $SnCl_4 \bullet 5H_2O$, which was 0, 0.03, 0.05, 0.1, 0.15, 0.2 and 0.25 mmol for BiS-0, BiS-1, BiS-2, BiS-3, BiS-4, BiS-5, BiS-6, respectively; (b) photocatalytic degradation kinetics of RhB solution over BiS-4 with methyl alcohol (MeOH), ammonium oxalate (AO), and isopropanol (IPA) working as scavengers of $O_2^{\bullet-}$, $\bullet OH$, and h^+, respectively. Reprinted with permission from [127]. Copyright (2017) Elsevier.

However, sometimes the difference in energy potential between the CB electrons and the VB holes from different semiconductors is too high to overcome, or the movability of the charges are too weak. Mediators with a redox potential in between the two energy levels will therefore be helpful. Mediators may work as either the electron-hole recombination center or the electron transportation system [128]. In the Z-scheme system consisting of $BiVO_4$ and $Ru/SrTiO_3$: Rh photocatalysts, the Rh^{4+}/Rh^{3+} redox couple acted as the combination center capturing electrons from the VB of $BiVO_4$ and holes from the VB of the $Ru/SrTiO_3$: Rh [129]. Solid mediators, which are metal nanoparticles with high electron-conductivity in most cases, are more favorable in terms of catalyst recovery [130]. Li et al. constructed a Z-scheme photocatalyst $BiOCl/Au/CdS$ by a stepwise deposition of Au and CuS. The degradation of four different organic pollutants all exhibited evidently higher sunlight-driven photocatalytic activity of $BiOCl/Au/CdS$ compared to the case of $BiOCl$, $BiOCl/Au$, and $BiOCl/CdS$. The radical trapping experiments indicated that $O_2^{\bullet-}$ was the main reactive species responsible for the degradation of the oganic substrates. Based on examinations on photoelectrochemical properties, it was concluded that the Z-scheme structure was formed between $BiOCl$ and CdS with the assistantce of Au nanoparticles functioning as the recombination center by capturing electrons from the CB of $BiOCl$ and holes from the VB of CdS. [131] In fact, the metal NPs-assisted indirect Z-scheme heterojunctions usually takes advantage of the synergistic effect of metal NP loading and semiconductor coupling, which will be discussed in detail in Section 2.3.6.

The primary differences of conventional, p-n, and Z-scheme heterojunctions are summarized in Table 5.

Table 5 Comparison of conventional, p-n, and z-scheme heterojunctions

Type of heterojunction	**Energy band and Fermi level rearrangement**	**Enhancement mechanism**
Conventional Heterojunction	No	Transfer and accumulate e^- and h^+ into different semiconductors
p-n Heterojunction	Yes	
Z-Scheme Heterojunction	No	Recombine e^- and h^+ from different semiconductors, while remain the rest h^+ and e^- in each semiconductor, respectively.

2.3.4.5 Coupling with Functional Organics

Coupling inorganic semiconductors with light-responsive organics is another coupling strategy, which happens on graphitic carbon nitride (g-C_3N_4) and polyaniline (PANI) in most cases.

Graphitic carbon nitride (g-C_3N_4) is the most stable allotrope of carbon nitrides and has an optical bandgap of 2.7 eV, possessing an intrinsic semiconductor-like absorption in the visible light spectrum [132], and therefore has been introduced as a non-toxic metal-free organic photocatalyst for solar-driven applications [133,134]. Additionally, due to its high nitrogen content and facile synthesis procedure, g-C_3N_4 may provide more active reaction sites than other N-carbon materials [135]. Furthermore, compared to bulk g-C_3N_4, g-C_3N_4 nanosheets exhibit a better performance due to their large surface area and fast charge transport [136]. Dispersing the non-visible-light responsive species $KTaO_3$ on g-C_3N_4 with a typical layered platelet-like morphology not only sensitized $KTaO_3$ with injected electrons from the excited g-C_3N_4, but also enlarged the specific surface area and thus facilitated substrate adsorption. The degradation efficiency towards RhB was promoted up to 1.5 times higher than that on pure g-C_3N_4 [137].

Polyaniline (PANI) is an extensively investigated conductive polymer mainly due to its high absorption coefficients in the visible range and high mobility of charge carriers [138]. PANI is responsive to both UV and visible light. Electrons and holes will be generated on its LUMO (equivalent to CB in inorganic semiconductors) and HOMO (equivalent to VB in inorganic semiconductors), respectively [138,139]. Furthermore, it is a good electron acceptor as well as an efficient hole provider when coupling with inorganic semiconductors. Therefore, PANI is usually loaded on semiconductors surface with broad bandgaps. The alignment structure is similar to a conventional type-II heterojunction so that the carrier separation is facilitated. The degradation rate of RhB on $BiVO_4$ was 62% within 120 min under visible light; while with PANI coupling, a complete degradation was realized in 60 min, which was attributed to the synergetic effect between PANI and$BiVO_4$, promoting the migration efficiency of photogenerated charge carriers. [140] Zhang et al. found that dispersing PANI onto a ZnO surface not only increased the MB degradation rate up to 98% and maintained both the surface area and phase structure of the pristine ZnO, strong inhibition of photocorrosion on bare ZnO was also realized under UV irradiation. This is because when illuminated by UV irradiation, PANI was excited while ZnO was not. Holes generated on

the VB of ZnO, which was indicated as the main oxidant and the dominant reason for photocorrosion of ZnO, transfered to the HOMO of PANI and took part in the subsequent reactions. [141]. Xiong et al. found that the surface of PANI dispersed in aqueous solution was usually positively charged, which guarantees a strong adsorption of anionic and neutral dyes, and thus enhanced their degradation [142].

Polyrrole (Ppy) is another photosensitive polymer that has been used in photocatalysis. With a narrow band gap of 2.2~2.5 eV, electrons at the LUMO of Ppy can be excited to the HOMO under visible light, leaving a hole at the LUMO (π^*-orbital), just like the electron migration in semiconductors [143]. The energy band alignments of semiconductor/Ppy composites usually match the type-II heterojunction, where Ppy works as the electron donor and hole acceptor in most cases, leading to an effective electron/hole separation. By preparing $Ppy/ZnIn_2S_4$ composites via facile hydrothermal method in the presence of Ppy powder, the time required for a complete removal of CAP was reduced to 60 min from 120 min on pure $ZnIn_2S_4$. 48.5% TOC removal was achieved by $Ppy/ZnIn_2S_4$ after 3 h photocatalytic degradation, which was two times higher than that on $ZnIn_2S_4$. This enhancement was attributed to the synergetic effect of the improved light absorption efficiency carried out by Ppy and the promoted e^-/h^+ separation at the $Ppy/ZnIn_2S_4$ interface. [144] Xu et al. reported a bifunctional role of Ppy in the Ppy/BiOI composites. Ppy functioned not only as the hole acceptor, facilitating photogenerated charge separation, but also increased the specific surface area which benefitted adsorption and generation of more active sites. Results showed more than 50% of the substrate RhB was adsorbed within 30 min in dark, and nearly 90% was degraded after 5 h under visible light; while the adsorption and degradation ratio of BiOI were only 1% and 15%, respectively. [145] Harraz et al. also found the amount of Ppy was responsible for the decreased particle size of Fe_2O_3, which was enhanced light absorption and also improved the specific surface area [146].

On the other hand, while some other C-group materials are not able to employ light as the energy source, their satisfactory electron conductivity and large surface area are in favor of e^-/h^+ pair separation and adsorbing substrates as well as providing active sites for photocatalytic reactions. These organics usually work as supporting materials on which photocatalyst particles deposit. [147–149] The most common organic supporting materials are graphene and its derivatives.

Graphene, a single layer of carbon atoms densely packed into a two-dimensional benzene-ring structure, possesses high conductivity, superior electron mobility and extremely high specific surface area [10,150]. Gao et al. found the photocatalytic activity of Bi_2WO_6 towards degrading RhB under visible light was greatly enhanced when it was supported on graphene. This was attributed to the negative shift of the Fermi level and elevation of the Bi_2WO_6 CB, which was caused by the electronic interaction and charge equilibration between graphene and Bi_2WO_6, as well as the inhibited photogenerated charge recombination. [151] Arshad et al. reported an improved solar-light-triggered catalytic performance with regard to MB decomposition in the presence of $CuO/GNPs$ (graphene nanoplatelets) composites. A 99.44% photodegradation of MB was achieved after being irradiated for 80 min, which was much better than using pure CuO, for which the degradation was only 75%. This improvement was proposed as the subsequence of the combined effect of increased adsorption of dye molecules and delayed recombination of charge carriers due to the attachment of graphene nanoplatelets on the CuO nanosheets in an optimized ratio. [152]

As a derivative of graphene, graphene oxide (GO) also possesses superior electron mobility and high conductivity, while its strong adsorption not only comes from the large specific surface area as graphene does, but the abundant surface oxygen-containing functional groups such as hydroxyl, carbonyl, carboxyl and epoxy groups as well. [153] Dispersing CdS nanoparticles on GO sheets not only prohibited electron/hole recombination due to the strong electron conductivity of GO sheets, the uniform deposition of CdS on GO sheets eliminated aggregation of CdS nanoparticles as well. More importantly, the strong interaction between GO and CdS inhibited the photocorrosion of CdS as well as the leaching of Cd^{2+} considering its toxicity: only 3.5 wt% Cd^{2+} of $GO\text{-}CdS$ was leached out while 38.6 wt% Cd^{2+} of CdS was lost after the reaction. [154]

Reduced graphene oxide (rGO) has been used as a support of photocatalysts as well. For instance, under visible light, electrons were produced at the $BiVO_4$ CB and then flowed to rGO and reduced O_2 there to give $O_2^{\bullet-}$, while holes stayed in $BiVO_4$and took part in the RhB degradation by either giving out $\bullet OH$ from OH^-/H_2O or directly, thus that the effective electron/hole separation was realized. Meanwhile, RhB molecules adsorbed on the rGO surface made it easier to degrade. As a result, $BiVO_4/rGO$ composites exhibited an approximately 3 times higher degradation rate towards RhB compared with that on the pristine $BiVO_4$. [155]

Carbon nanotubes (CNTs), taking advantage of high conductivity, large surface area, high chemical stability, nontoxicity and low price, have been recognized as an excellent electron-acceptor/transport matrix in photocatalysis for retarding electron/hole recombination as well as enhancing light absorption efficiency [156,157]. Yang et al. synthesized a novel Cu_2O/CNTs hierarchical chrysanthemum-like nanocomposites by a facile wet chemical method. Its excellent photocatalytic activity was attributed to the unique chrysanthemum-like structure of the composite, as well as the tight connection between Cu_2O NPs and the highly conductive CNTs. The former improved both the range and the intensity of light absorption, while the latter facilitated electron flowing from the visible-light-excited Cu_2O to the CNTs. [158] Jiang et al. obtained a g-C_3N_4/CNTs/Bi_2WO_6 ternary Z-scheme heterojunction with CNTs as the efficient electron mediator. Photocatalytic degradation towards TC under visible light indicated the highest activity in the presence of the g-C_3N_4/CNTs/Bi_2WO_6 ternary composite compared to any single or binary composite of them in the system. [159] Li and co-workers reported a novel heterostructure of multiwalled carbon nanotubes (NWCNTs) coated with BiOI nanosheets prepared via a simple solvothermal method. The remarkably enhanced photocatalytic activity for the degradation of RhB, MO, and 4-CP under visible light compared with pure BiOI was predominantly due to the significantly promoted electron/hole separation carried out by the strong coupling interface of the two components. [156]

Other carbon group materials have also been employed in photocatalysis. The degradation efficiency of MO on Ag/AgCl composites was increased from 15.1% to 97.9% after being loaded on AC, taking advantage of strong adsorption of porous AC towards MO molecules, hot electrons produced by LSPR effect of Ag NPs, as well as the oxidation of Br^- to Br^o which was also deemed as a reactive species of MO degradation [160]. Fu's group dispersed C_{60} molecules with a monomolecular layer state on the surface of ZnO and formed the hybridized interaction betweenthem. The as-prepared C_{60}-hybridized ZnO showed enhanced photocatalytic activity for the degradation of MB, and the photocorrosion of ZnO was successfully inhibited in the presence of C_{60} molecules. The former was due to the excellent electron movability at the interface of C_{60} and ZnO, which was produced by the interaction of C_{60} and ZnO with a conjugative π-system. The latter could be attributed to the reduced activation of surface oxygen atom. The enhancement degree of photocatalytic activity was strongly depended on the coverage of C_{60} molecules on the

surface of ZnO nanoparticles, and the optimum hybridization effect was found at a weight ratio of 1.5% (C_{60}/ZnO), above which C_{60} tended to aggregate on the surface of ZnO, resulting in the slower transformation of the photoinduced electrons. [161]

2.3.5 Synergetic Effects between Doping and Semiconductors Coupling

Considering that doping and semiconductors coupling are both capable of improving the efficiencies of light absorption and electron/hole separation, the coexistence of them may further promote the photocatalytic efficiency.

Shi et al. synthesized a series of Cr-doped $Bi_4Ti_3O_{12}/Bi_2Ti_2O_7$ (BTO) heterojunction fibers, where Cr was doped in both semiconductors. The band gaps of $Bi_4Ti_3O_{12}$ and $Bi_2Ti_2O_7$ were narrowed down due to the lower CB level brought about by Cr doping, resulting in a significant improvement of spectral absorption in the visible region. A conventional type-II heterojunction was formed between the two doped semiconductors, leading to an efficient e^-/h^+ separation, which exhibited a remarkably enhanced current intensity in the transient photocurrent response (Figure 20). A complete MO degradation was realized within 90 min on Cr-doped BTO, while the non-doped BTO was not visible-light-responsive. [162] Yang et al. obtained a magnetic N-doped $FeVO_4/Fe_2O_3$ composite with a rod-like structure. XPS spectra showed a successful doping of N^{3-} into the $FeVO_4$ lattice, leading to the formation of an impurity level above i VB to capture electrons, which narrowed the bandgap of $FeVO_4$ and thus expanded its light absorption spectra. After coupling with Fe_2O_3 and being excited by UV irradiation, photogenerated electrons flowed from $FeVO_4$ to Fe_2O_3 while the holes moved in the opposite direction. The improved RhB degradation efficiency was attributed to the enhanced light absorption as well as the facilitated charge separation. [163] Li and co-workers found that doping might be induced by the interaction between two coupled semiconductors. In the N-doped P25 TiO_2/amorphous Al_2O_3 composites system, not only did the VB level of TiO_2 get elevated by exotic N^{4-} dopants, its CB level was also debased by domestic Al^{3+} dopants generated from the dissolved Al_2O_3 molecules, such that the TiO_2 bandgap was intensely narrowed down and thus light absorption was expanded to the visible region. Under visible light, the doped TiO_2 was excited while amorphous Al_2O_3 was not.

However, the defect levels in amorphous Al_2O_3 lattice were lower than the CB of TiO_2, which provided electron trapping levels and thus facilitated carrier separation. The amorphous structure of Al_2O_3 also brought about a high specific surface area. As a result, the degradation rate of methyl orange under visible light was improved by up to 43.6 times that on pure TiO_2. [33]

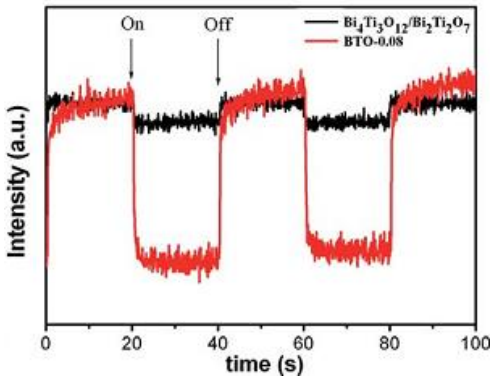

Figure 20 Transient photocurrent response of $Bi_4Ti_3O_{12}/Bi_2Ti_2O_7$ and $BTO-0.08$ (amount of $Cr(NO_3)_3 \bullet 9H_2O$ in the precursor was 0.08g) in 0.5 M Na_2SO_4 aqueous solutions under visible-light irradiation at 0 V vs. Hg/Hg_2Cl_2. Reprinted with permission from [162]. Copyright (2015) Royal Society of Chemistry.

Recently, a novel V^{4+} and Ce^{3+} self-doped $BiVO_4/CeO_2$ p-n heteojunction nanocomposite with a large surface area was synthesized by Chen's group. The V^{4+}/V^{5+} pairs, coming from the doped V^{4+} and the pristine V^{5+} in the p-type $BiVO_4$, could form defect energy states, acting as electron/hole trap centers and thus prohibiting recombination. Additionally, the Ce^{4+}/Ce^{3+} pairs in the n-type CeO_2 not only efficiently separated e^-/h^+ pairs, but also produced more $O_2^{\bullet-}$ radicals. Moreover, a p-n heterojunction was formed at the interface between the V^{4+}-self doped $BiVO_4$ and the Ce^{3+} self doped-CeO_2, which further facilitated charge separation. The remarkably enhanced photocatalytic activity towards degrading RhB under visible light could be mainly attributed to the formed p-n heterojunction nanostructures, the presence of defect states induced by oxygen vacancies, and self-doped V^{4+} and Ce^{3+} centers, as well as the large surface area. [164]

2.3.6 Synergetic Effects between Metal Nanoparticles Loading and Semiconductor Coupling

As aforementioned, metal NPs deposited on semiconductor surfaces are capable of helping electron/hole separation by forming the Schottky barrier at the interface of metal/semiconductor

and/or enhancing light absorption by LSPR effect. Considering the enhanced charge separation in semiconductor heterojunctions, attempts at combining coupling and metal NPs loading have been made to further optimize the photocatalytic performance.

Lu et al. fabricated a new $Bi_2WO_6/TiO_2/Pt$ composite, where the Pt NPs were loaded on the TiO_2 surface and then coupled with Bi_2WO_6 to form a conventional heterojunction. UV-Vis DRS and photocurrent measurements displayed that the $Bi_2WO_6/TiO_2/Pt$ composite exhibited enlarged photoresponse range and enhanced charge transfer. Degradation of RhB and BPA under simulated sunlight irradiation on the $Bi_2WO_6/TiO_2/Pt$ composite was the fastest compared to the photocatalysts containing one- component (TiO_2, Bi_2WO_6) or two components (TiO_2/Pt, Bi_2WO_6/Pt). The enhanced photocatalysis benefited from the increased light harvesting due to the excitation of both TiO_2 and Bi_2WO_6 and the high quantum efficiency due to the heterojunction between Bi_2WO_6 and TiO_2, as well as the Schottky barrier between TiO_2 and Pt where the conduction electrons flowed from TiO_2 to Pt because of the lower Fermi level of Pt NPs [165] Wen's group reported a Ag-decorated Ag_2O/CeO_2 p-n heterojunction, which exhibited enhanced photocatalytic activity for the photodegradation of EFA under visible light irradiation, which was 3.5 and 122 times that with bare Ag_2O and CeO_2, respectively. The inverted "V-shape" Mott-Schottky curve indicated the existence of a p-n junction. The improved photocatalytic activity was related to the inner electric field at the Ag_2O/CeO_2 interface facilitating electron/hole separation, as well as the LSPR effect of Ag NPs producing hot electrons which flowed to the CB of the p-type Ag_2O and eventually reached that of the n-type CeO_2 to participate in photocatalytic degradation by producing $O_2^{\bullet-}$ from adsorbed O_2 molecules. The stability of the Ag_2O/CeO_2 heterojunction photocatalyst was also improved due to the efficient transfer of electrons from Ag_2O. [166]

The synergistic effects of semiconductor coupling and metal NPs loading are more common in Z-scheme heterojunctions, where the metal NPs may work as the mediator for the formation of Z-scheme heterojunctions and/or present the LSPR effect providing hot electrons to sensitizing non-excited semiconductors. For example, a Z-scheme photocatalyst between Cu_2O and $BiPO_4$ was realized with the assistantce of Au NPs, which not only worked as a mediator providing recombination centers for electrons on the $BiPO_4$ CB and holes from the Cu_2O VB , but also presented the LSPR effect. [167] For a ternary flower-like photocatalyst $Ag@AgCl/Bi_2WO_6$

synthesized by hydrothermal treatment and in situ oxidation reaction, a special Z-scheme heterojunction was formed at the interface of Bi_2WO_6 and Ag NPs, where recombination happened between the electrons in the photoexcited Bi_2WO_6 and holes in Ag NPs generated from the LSPR effect under visible light. On the other hand, the hot electrons produced in Ag NPs migrated to the CB of the non-responsive AgCl. Thus, holes and electrons were separated and accumulated in Bi_2WO_6 and AgCl, respectively. Moreover, holes dissolving in the substrate solution coming from Bi_2WO_6 could not only oxidize the pollutant molecules either directly or indirectly, but could also oxidize Cl^- from AgCl to Cl^0 which was responsible for the enhanced degradation of BPA. [168]

2.3.7 Dye-sensitization

Some organic dyes, such as RhB [169], MO [170], MB [171], rose Bengal [172], and RR120 dyes [173] are responsive to irradiation, exciting electrons in the HOMO to the LUMO, and the dyes themselves are excited to their excited states as the result [112]. When they are adsorbed on the semiconductor with a less negative CB compared to their LUMOs, electrons generated on excited dye molecules (also called dye-sensitizers) can be injected to the semiconductor and take part in the subsequent photocatalytic reactions. By this means, semiconductors without visible-light-responsivity can be sensitized and the light absorption spectrum of the semiconductor/dye-sensitizer system will be extended to the visible region. When the semiconductor responds to the irradiation as well, visible light absorbance would be enhanced in the presence of both the conventional excitation occurring on the semiconductor and the sensitization effect carried out by the dye-sensitizer. However, holes produced at the semiconductor VB would not migrate into the dye sensitizers in most cases. [8,40]

Depending on the destiny of the excited dye molecules, dye-sensitization used for water decontamination is classified into two groups. One is the degradation of the dye-sensitizers itself as shown in Figure 21(a); the other is used to decompose foreign contaminates and the dye-sensitizers can be regenerated by accepting electrons from electron donors, as shown in Figure 21(b).

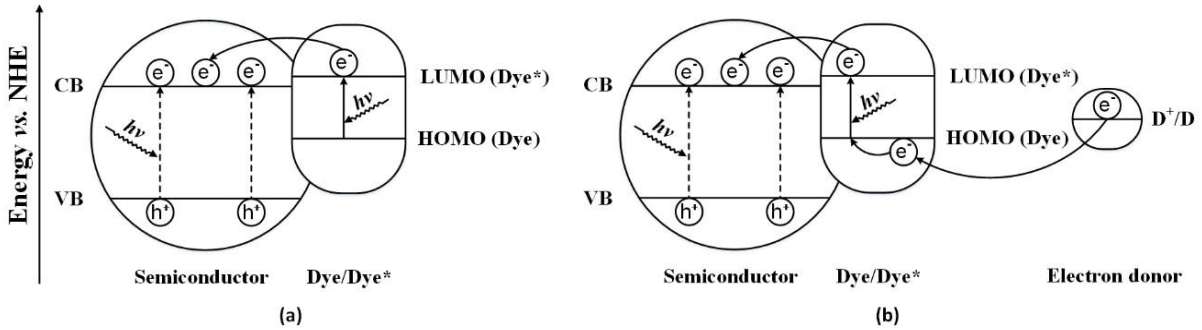

Figure 21 Electron transfer between the photocatalyst and the dye molecule when the dye acts as: (a) both the sensitizer and the substrate, and (b) only sensitizer in the presence of foreign electron donors.

In the process of self-degraded sensitization, dye molecules on their ground and excited state can both be degraded [174]. Moreover, the excited dyes may be much easier to be decomposed and further mineralized than those on their ground state due to their higher energy level. Park et al. proved the contribution of the self-dye-sensitized mechanism during the degradation of MO, MB, and RhB in the presence of Ag- and Ti- loaded BiOI under visible light irradiation [170]. Another study also indicated an obvious degradation of MB when the photocatalyst, $CaIn_2O_4$, poorly absorbed light irradiation. This was attributed to the dye-sensitization effect of MB, providing electrons for $CaIn_2O_4$ and bringing itself to an excited state which was much easier to decompose compared to its ground state. [175] Similarly, the degradation of MG carried out on $SrTiO_3$ was proposed to be primarily attributed to dye sensitization because $SrTiO_3$ on its own is almost inactive in the visible region [52]. The better performance of Zr/Ag-coloaded ZnO towards oxidizing reactive red 120 (RR120) under visible light over UV irradiation further revealed the contribution of dye-sensitization considering the worse light absorption efficiency in the visible region. [176]

Photoexcited dyes are also able to sensitize the semiconductors hosts to help with the degradation of other contaminations in the system. Muszkat et al. reported a significantly accelerated photocatalytic oxidation of bromacil on TiO_2 in terms of the half-living time, $t_{1/2}$, in the presence of sensitization effect brought about by methyl blue. [177] However, dye-sensitizers may be consumed severely. Ross et al. observed an only 15-min lifetime of the dye-sensitizer, rose bengal, in sensitizing TiO_2 to decomposite terbutylazine under visible light [178]. This was because after transferring electrons to the semiconductor, the dye itself was converted to its cationic radical, which was easier to degrade compared with its ground state as mentioned above. Therefore, the

introduction of electron donors would be helpful for sensitizer regeneration [179]. An electron donor can be a molecule or a mediating redox couple in a regenerative cell, which produces electrons to reduce the excited dyes back to their ground state and thus hinders their decomposition. [180] Chowdhury and co-workers used TEOA as the sacrificial electron donor to prevent the corrosion of the dye-sensitizer, EY, in the system of decomposing phenol with TiO_2 under visible solar light. It is well-known that TiO_2 is not capable of responding to visible light. However, through the excitation of EY from its ground state (EY) to the excited state (EY^*), electrons were produced on EY and then transferred to the CB of TiO_2 to participate in the following photooxidation of phenol. Subsequently, EY^* could interact with phenol, water, or the electron donor TEOA to return back to its ground state. As a result, the substrate phenol was completely degraded within 2h with the assistance of TEOA, which was less than 60% without TEOA. No significant loss of EY was observed. [179]

2.3.8 Quantum Dots

2.3.8.1 Inorganic Semiconductor Quantum Dots

Inorganic semiconductor quantum dots (QDs) are defined as zero-dimensional particles with the size smaller than that of the exciton (photogenerated electron) Bohr radius, which is the characteristic distance between the exciton and its hole of a given semiconductor [181]. The small size confines the produced electrons and holes inside a semiconductor QD, and the energy structure of the QD budges as its particle size changes in accordance to what is called the quantum size effect [181]. Quantum size effect is an important property controlling the performance of inorganic QDs. As the size of a QD gets smaller, its E_g becomes higher leading to stronger redox potentials of energy bands, while a blue shift in light absorption spectrum would be caused as well. A comparison of MB degradation was carried out on ZnO QDs with different sizes under UV irradiation. Results exhibited a much better performance on small QDs (5-8 nm) than on large QDs (15-20 nm) due to the higher crystallinity of the former which provided more active sites for the oxidation reactions. [182] Additionally, the interface between the QDs and the bulk semiconductor they deposited on would be increased, which facilitates photogenerated charge carriers flow between the two components and thus inhibits recombination. Yu's group also found an increased

BET specific surface area when bulk CdS was fabricated to their QDs. When the size of CdS QDs increased from 4.5 to 7.2 nm, S_{BET} decreased from 27.4 to 22.4 m^2g^{-1}, and E_g reduced from 2.36 to 2.25 eV. As the size further rose to the bulk size (15.9 nm), S_{BET} continuously decreased, while E_g did not reduce anymore after reaching the minimum value (2.14 eV). [183] As the size of QDs decreases (typically smaller than 10 nm), the quantum confinement effect would become increasingly dominant [184]. Therefore, semiconductor QDs exhibit highly size-dependent exceptional optical and electrical behaviors that are not found in their bulk counterparts, which would greatly increase the energy conversion efficiency [185,186]. One of the most striking ones is the multiple-exciton-generation (MEG) property as the result of absorbing one single photon with high energy [186]. CdS QDs were found to be more effective when degrading MB and RhB under visible light irradiation compared to the bulk CdSdue to the specific MEG property of QDs. [187]

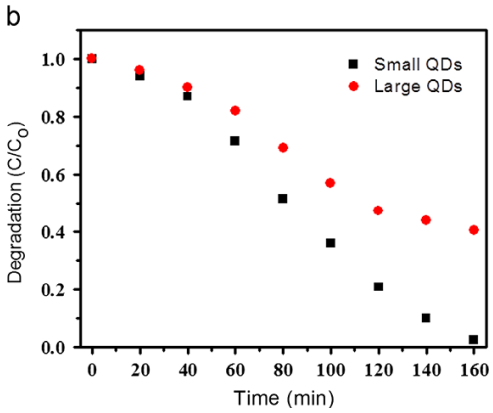

Figure 22 Comparison of MO degradation and small and large ZnO QDs. Reprinted with permission from [182]. Copyright (2014) Elsevier.

QDs are easy to aggregate due to their relatively small sizes and fairly high surface energy, which makes stabilizing (passivation) agents necessary to cover the QDs surface in order to prevent the agglomeration and oxidization of the QDs [188]. For example, 2-mercaptoethanol, L-arginine, and poly vinylpyrrolidone (PVP) were used as the stabilizing agents for systems involving ZnS [181], CdS [187] and ZnO [182] QDs, respectively. Chitosan (a biopolymer) was also used as the passivation agent for ZnS QDs to reduce the number of dangling bonds on the particles surface and thus the recombination between electrons and holes [185]. However, these agents may have a negative impact on the superficial contact between the contaminant molecules and the QDs [189].

To solve this problem, some researchers attempted to anchor QDs on a supporting matrix with a large surface area, which might be either organic or inorganic. Reduced graphene oxide (rGO) can function as not only a good stabilizer but also a good electron mediator, transporting electrons from the semiconductor particles to oxygen molecules. Sun et al. proved that rRO possessed such functions when acting as the support for Bi_2WO_6 QDs. Results revealed an 8-fold higher electron lifetime, as well as a higher degradation efficiency of both RhB and MB compared to the case of pure Bi_2WO_6 QDs working alone. [189] Inactive inorganics have also been used as the matrix for loading semiconductor QDs. ZnO-QDs/SiO_2 composite exhibited not only a higher degradation efficiency of RhB under UV irradiation, but also a better photostability which was attributed to the strong Zn-O-Si bonds. The large surface area as well as excellent electron conductivity of SiO_2 guaranteed excellent substrate adsorption and satisfactory productivity of $O_2^{\bullet-}$, respectively. [190]

Instead of working alone, semiconductor QDs are more often applied by being deposited onto the surface of other semiconductor particles as sensitizers or separation centers. In addition to the MEG property, QDs may also induce a greatly promoted specific surface area due to their relatively small sizes, as shown in the Cu_2O-QDs/BiOBr composite, where a 2 times higher specific surface area was obtained with a 3wt% loading rate of the Cu_2O QDs. On the other hand, the overloaded Cu_2O QDs tended to agglomerate to some extent which could decrease the specific surface area instead and reduce the active sites on BiOBr. Furthermore, the interfacial charge transfer might also be suppressed due to the unsuitable ratio between Cu_2O QDs and BiOBr. [191] Rajabi and co-workers doped Fe^{3+} into ZnS QDs, the mechanism of the enhanced performance was declared to be the same as doped bulk ZnS particles [181].

Most semiconductor QDs/bulk semiconductor systems follow the classical separation model as in bulk semiconductor coupling such as CdSe-QDs/ZnO [120], CdSe-QDs/Bi_2WO_6 [192], CdS-QDs/ Bi_2WO_6 [186], CdS -QDs/ BiOBr [193], Cu_2O -QDs/ BiOBr [191] and Bi_2O_3 -QDs/N-Bi_3NbO_7 [194]. Some of them are able to form a p-n heterojunction structure, such as Ag_3PO_4-QDs/$BiPO_4$ [195], CuO-QDs/In_2O_3 [196], and AgBr-QDs/Bi_2WO_6 [197]. Wang et al. enhanced the degradation efficiency of MB under visible light upon mesoporous Bi_2WO_6 by depositing AgBr QDs. AgBr QDs in the AgBr-QDs/Bi_2WO_6 heterojunction structure not only responded to the irradiation and provided reactive sites, but also increased collisions between the fluid and the pore walls and thereby reduced the mean free path. [197] Meng et al. successfully

synthesized a p-n heterogeneous MoS_2 QDs-interspersed Bi_2WO_6 via a simple bath sonication method. The MoS_2 QDs were obtained during the ultrasonic treatment of MoS_2 nanoflowers. The narrow bandgap and the relatively high specific surface area of MoS_2 QDs brought about superior capacity of absorbing visible light and adsorbing substrate, respectively. The formed p-n heterostructure effectively separated the photogenerated electrons and holes to the CB of the n-type Bi_2WO_6 and the VB of the p-type MoS_2, respectively. Photocatalytic degradation of RhB exhibited a 3 times higher reaction rate constant to that in the presence of bare Bi_2WO_6. The reduction rate of TOC was promoted to 42% within 90 min compared to 6% and 1% in the presence of pure Bi_2WO_6 and MoS_2, respectively. [198]

Upconverted luminescence (UCL) is another exceptional property exhibited on semiconductor QDs. It refers to the process of a QD emitting low-wavelength (high-frequency) light by means of absorbing and converting long-wavelength (low-frequency) light. Three mechanisms for UCL have been reported: carriers can gain extra energy by phonon-assisted processes, multi-photon absorption, or Auger processes [199]. Meanwhile, the emission PL wavelength is proportional to the size of the QD; the larger the QD, the redder its color. [184] A study on CdSe QDs observed a size-dependent emission wavelength, in which the emission light shifted from red to blue when the diameter of the CdSe QDs reduced from 6 to 2 nm [200].

Several other semiconductor QDs have been found to possess this upconversion property, such as CdS [201], InAs [199], PbSe [202], CdTe [203], and ZnCdS [201]. However, applications of the UCL property for photocatalytic water decontamination is extremely scarce. This is because inorganic semiconductors taking advantage of the PL property are usually used for biological probes, and peaks of both the absorption and emission spectra are located in the long-wavelength visible region, which is meaningless for photocatalysis since semiconductors that can be excited by such a long-wavelength light is rare. Furthermore, inorganic semiconductor QDs luminesce only in specific surroundings. For example, the mostly researched CdSe QDs can only exhibit the desirable PL property in organic solutions. When the solution was mixed with water, luminescence was strongly inhibited. [204] Thus, the UCL property of inorganic semiconductor QDs may be infeasible for photocatalytic water decontamination. On the other hand, this property plays a vital role in carbon-containing QDs.

2.3.8.2 Carbon-containing Quantum Dots

Different from inorganic semiconductor quantum dots, carbon-containing quantum dots (CCQDs) refer to those zero-dimensional carbon-containing nanoparticles with the size of generally 3-20 nanometers [205]. In addition to the general functions inorganic carbon-containing materials provide, such as accepting electrons, facilitating charge separation, increasing surface area, and providing active sites [205–207], the most significant application of CCQDs is to sensitize semiconductors on which they deposit with their extraordinary upconverted luminescence property. Specifically, after absorbing one photon from NIR or IR light, multiple electrons can be generated in CCQDs and their recombination with holes emits visible light or UV, which can be absorbed by the host semiconductor [208–210]. Besides, the upconversion property of QDs is strongly size-dependent: as size becomes larger, E_g decreases, and the emissionn spectrum has a blue shift. This makes the CCQDs/semiconductor composites capable of effectively using the full spectrum of sunlight and thus extensively promotes the light absorption efficiency [209]. The most heavily researched CCQDs so far is carbon quantum dots (CQDs) and graphene quantum dots (GQDs).

With the assistance of PL and electron capture carried out by CQDs, 90% of the initial MO was degraded under NIR in the presence of the CQDs/Cu_2O composite. In comparison, pure Cu_2O was not responsive to NIR directly. PL spectra examination showed that the incident NIR with the wavelength of larger than 700 nm was converted to the useful area (390-564 nm), which could be employed for exciting Cu_2O. [206] Zhang et al. proposed an interesting mechanism when CQDs-deposited Ag_3PO_4 was used for decomposing MO under visible light. By uniformly and compactly dispersing CQDs on the Ag_3PO_4 surface, the insoluble CQDs layer could effectively protect Ag_3PO_4 from dissolution in aqueous solution. During the photocatalytic process, CQDs acted as not only electron reservoirs by accepting redundant electrons from Ag_3PO_4 but converted incident with the wavelength longer than 530nm to shorter-wavelength photons that can triger Ag_3PO_4 as well, which benefited from its upconversion property. Hence, both the photogenerated charge separation efficiency and light absorption ability was promoted, resulting in a much better photocatalytic performance, where the target MO was completely decomposed within 10 min in the presence of CQDs/ Ag_3PO_4 composite, while within 80 min on bare Ag_3PO_4 . [209] Furthermore, the conjugated structure of CQDs enables them to form a π-π interaction with

benzene structures, which is contributive to the degradation of pollutants containing benzene, such as MB [206]. Yu and Kwak deposited CQDs on mesoporous α- Fe_2O_3 and intensely promoted the degradation efficiency of MB to up to 87.7%, which was attributed to the synergistic effects of the mesoporous structure of α- Fe_2O_3 and the strongly conjugated network structure of CQDs [211]. Li et al. investigated the influence of the amount of CDQ layers, and found the heterostructure of CQDs/ZnO with four layers of CQDs exhibited the highest photocatalytic activity, which was 3 times as that of the bare ZnO [212].

Graphene quantum dots (GQDs) is another type of zero-dimensional material with a typical size range from 3 to 20 nm. The crystalline nature of GQDs has been demonstrated as similar to that of bulk graphene. [213] Similar to CQDs, GQDs possess the upconversion property as well. As shown in the research by Zhuo's group, the excitation wavelength was converted from 500-700 nm to an emission wavelength with the peak of approximately 407 nm, which could be used by rutile TiO_2, so that the photocatalytic efficiency of degrading MB over CQDs/TiO_2 reached 97% within 60 min under visible light. [214] Similarly, the upconversion property of g- C_3N_4 quantum dots (CNQDs) have also been reported with regard to photocatalytic water decontamination. Wang et al. observed emissions in the range of 350-600 nm after being irradiated with 705-862 nm light on CNQDs. This indicated that CNQDs have the potential to be harnessed as a universal energy transfer component in photocatalysis. [215]

2.4 Summaries

Tables summarizing semiconductor modification strategies are provided in Appendix B.

2.5 Conclusions, Challenges, and Perspectives

With the rapid industrialization and urbanization occurring around the world, water pollution becomes an urgent problem that needs to be properly addressed. Heterogeneous photocatalysis has emerged as an environmental benign strategy for organic decontamination in water as it harnesses inexhaustible solar light as the energy source and takes advantage of easy catalyst recycling and reusing. On the other hand, suffering from narrow light absorption area and severe electron/hole recombination, traditional semiconductors need to be modified in order to realize a high quantum

efficiency. In this review, fundamental aspects and principles of heterogeneous photocatalysis was discussed in detail. Attempts made in the last decade on the modification of photocatalysts and their background mechanisms were illustrated. Investigations on operating parameters influencing photocatalyst performance was also explained, along with corresponding examples, explanations and conclusions stated. Strategies coupling heterogeneous photocatalysis with other treatments were mentioned and analyzed as well.

Although numerous novel photocatalysts have been devised in the recent years, deep investigations on the preparation and function mechanisms of novel photocatalysts are still at the primary stage and not comprehensive. Also, research with respect to kinetics are not clear either. Most of the studies declare that the photocatalytic degradation of pollutant substrates follows the pseudo-first-order model, but the presented data often shows a nonnegligible discrepancy. This is because the concentration of a substrate is usually indicated by the absorbance of its characteristic peak, and multiple intermediates would be produced during the reaction, whose characteristic peaks are different from that of the pristine substrate. As the reaction processing, the substrate solution becomes a mixture of the pristine substrate, the produced intermediates, and final productions, which makes the degradation process is with respect to not only the substrate, but some of the intermediates as well, so that the position and intensity of the cauterization peak of the mixture would be difficult to predict. Additionally, since it is the characteristic peak of the original substrate that is monitered during degradation, its intensity decreasing may not reflect the real concentration change of the substrate accurately.

As the energy derivation of photocatalysis, light source controls the amount of generated electron/hole pairs and thus dominates the photocatalytic efficiency. However, the light source used by most of the present studies are artificial lamps, which have a great difference from the natural solar irradiation. On the other hand, endeavors extending the light absorption spectra of photocatalysts are usually focused on the visible region, while those regarding the near infrared area covering ca. 50% of the total irradiation energy are scarce.

Most achievements made in heterogeneous photocatalysis are still at the laboratory stage and is far from industrial applications, which is primarily due to the operating difficulty and complexity as well as economic issues. For example, substrates used in the current studies are usually aqueous

solutions containing a single contaminant at a low concentration, which is quite different from real wastewater that contains multiple contaminants with much higher concentrations. Therefore, dilution is necessary in industrial applications since excessive substrate particles would cover active sites on the catalyst surface or screening the irradiation if they are colored. Also, real industrial wastewater normally contains multiple contaminants and may be corrosive, which necessitate high stability and reusability of the catalysts, especially for heterostructures containing multiple semiconductors where a tight interaction between the different components is required. Moreover, catalyst dosage in laboratory studies is pretty high (e.g., 1 g/L), while the daily processing amount of a medium-scale sewage plant is $10^7 - 10^8$ liters, meaning that the total amount of catalyst would be tremendous. Although the reusability of photocatalysts has been reported by many works, the reported reuse times are 3-5 in most cases, which is still deficient for industrial applications. Also, industrial wastewater may be corrosive which would strongly undermine the stability of the catalysts. Additionally, the reported post-use treatments are realized by either filtering or centrifuging. The former may cause huge catalyst lost, while the latter requires specific equipment, resulting in a significant source of power consumption.

Finally, the comparison of photocatalytic performance among the plentiful novel photocatalysts is difficult due to the complexity of photocatalysis, as the reaction conditions are different and hard to be converted to a uniform standard. To this end, quantum efficiencies of different photocatalytic systems are expected to be given out.

References:

[1] M.A. Gondal, M.N. Sayeed, Z.H. Yamani, A.R. Al-Arfaj, Efficient removal of phenol from water using Fe2O3 semiconductor catalyst under UV laser irradiation, J. Environ. Sci. Heal. Part a-Toxic/Hazardous Subst. Environ. Eng. 44 (2009) 515–521. doi:10.1080/10934520902720033.

[2] R. Daghrir, P. Drogui, D. Robert, Modified TiO2 For Environmental Photocatalytic Applications: A Review, Ind. Eng. Chem. Res. 52 (2013) 3581–3599. doi:10.1021/ie303468t.

[3] S.M. Gupta, M. Tripathi, A review of TiO2 nanoparticles, Chinese Sci. Bull. 56 (2011) 1639–1657. doi:10.1007/s11434-011-4476-1.

[4] K. Kabra, R. Chaudhary, R.L. Sawhney, R. Kabra, Kavita. Chaudhary, Rubina. Sawhney, K. Kabra, R. Chaudhary, R.L. Sawhney, Treatment of Hazardous Organic and Inorganic Compounds through Aqueous-Phase Photocatalysis: A Review, Ind. Eng. Chem. Res. 43 (2004) 7683–7696. doi:10.1021/ie0498551.

[5] S.G. Kumar, L.G. Devi, Review on Modified TiO2 Photocatalysis under UV/ Visible Light: Selected Results and Related Mechanisms on Interfacial Charge Carrier Transfer Dynamics, Phys. Chem. A. 115 (2011) 13211–13241. doi:10.1021/jp204364a.

[6] V.C. Padmanaban, M.S. Giri Nandagopal, G. Madhangi Priyadharshini, N. Maheswari, G. Janani Sree, N. Selvaraju, Advanced approach for degradation of recalcitrant by nanophotocatalysis using nanocomposites and their future perspectives, Int. J. Environ. Sci. Technol. 13 (2016) 1591–1606. doi:10.1007/s13762-016-1000-9.

[7] Z. Wang, Y. Liu, B. Huang, Y. Dai, Z. Lou, G. Wang, X. Zhang, X. Qin, Progress on extending the light absorption spectra of photocatalysts, Phys. Chem. Chem. Phys. 16 (2014) 2758. doi:10.1039/c3cp53817f.

[8] P.A.K.V.L. Reddy, P.A.K.V.L. Reddy, E. Kwon, K. Kim, T. Akter, S. Kalagara, P.A. Kumar, P.V. Laxma, E. Kwon, K. Kim, T. Akter, S. Kalagara, Recent advances in photocatalytic treatment of pollutants in aqueous media, Environ. Int. 91 (2016) 94–103. doi:10.1016/j.envint.2016.02.012.

[9] Y. Qu, X. Duan, Progress, challenge and perspective of heterogeneous photocatalysts, Chem. Soc. Rev. 42 (2013) 2568–2580. doi:10.1039/C2CS35355E.

[10] H. Wang, L. Zhang, Z. Chen, J. Hu, S. Li, Z. Wang, J. Liu, X. Wang, Semiconductor heterojunction photocatalysts: design, construction, and photocatalytic performances, Chem. Soc. Rev. 43 (2014) 5234. doi:10.1039/C4CS00126E.

[11] J. Low, J. Yu, M. Jaroniec, S. Wageh, A.A. Al-Ghamdi, Heterojunction Photocatalysts, Adv. Mater. 29 (2017) 1601694. doi:10.1002/adma.201601694.

[12] S. Dong, J. Feng, M. Fan, Y. Pi, L. Hu, X. Han, RSC Advances Recent developments in heterogeneous photocatalytic water treatment using visible light- responsive photocatalysts : a review, RSC Adv. 5 (2015) 14610–14630. doi:10.1039/C4RA13734E.

[13] Y. Wang, Q. Wang, X. Zhan, F. Wang, M. Safdar, J. He, Visible light driven type II heterostructures and their enhanced photocatalysis properties: a review, Nanoscale. 5 (2013) 8326–39. doi:10.1039/c3nr01577g.

[14] C. Yu, W. Zhou, H. Liu, Y. Liu, D.D. Dionysiou, Design and fabrication of microsphere photocatalysts for environmental purification and energy conversion, Chem. Eng. J. 287 (2016) 117–129. doi:10.1016/j.cej.2015.10.112.

[15] D. Kandi, S. Martha, K.M. Parida, Quantum dots as enhancer in photocatalytic hydrogen evolution: A review, Int. J. Hydrogen Energy. 42 (2017) 9467–9481. doi:10.1016/j.ijhydene.2017.02.166.

[16] K. Wenderich, G. Mul, Methods, Mechanism, and Applications of Photodeposition in Photocatalysis: A Review, Chem. Rev. 116 (2016) 14587–14619. doi:10.1021/acs.chemrev.6b00327.

[17] U.I. Gaya, Heterogeneous Photocatalysis Using Inorganic Semiconductor Solids, Springer Netherlands, Dordrecht, 2014. doi:10.1007/978-94-007-7775-0.

[18] H.J. Snaith, Estimating the maximum attainable efficiency in Dye-sensitized solar cells, Adv. Funct. Mater. 20 (2010) 13–19. doi:10.1002/adfm.200901476.

[19] J. Tauc, Optical properties and electronic structure of amorphous Ge and Si, Mater. Res. Bull. 3 (1968) 37–46. doi:10.1016/0025-5408(68)90023-8.

[20] Y. Xiang, P. Ju, Y. Wang, Y. Sun, D. Zhang, J. Yu, Chemical etching preparation of the Bi2WO6/BiOI p-n heterojunction with enhanced photocatalytic antifouling activity under visible light irradiation, Chem. Eng. J. 288 (2016) 264–275. doi:10.1016/j.cej.2015.11.103.

[21] W.L. Miller, M.A. Moran, W.M. Sheldon, R.G. Zepp, S. Opsahl, Determination of apparent quantum yield spectra for the formation of biologically labile photoproducts, Limnol. Oceanogr. 47 (2002) 343–352. doi:10.4319/lo.2002.47.2.0343.

[22] A. Kudo, Y. Miseki, Heterogeneous photocatalyst materials for water splitting., Chem. Soc. Rev. 38 (2009) 253–278. doi:10.1039/b800489g.

[23] W.L. Miller, Effects of UV Radiation on Aquatic Humus: Photochemical Principles and Experimental Considerations, in: D.O. Hessen, L.J. Tranvik (Eds.), Aquat. Humic Subst. Ecol. Biogeochem., Springer Berlin Heidelberg, Berlin, Heidelberg, 1998: pp. 125–143. doi:10.1007/978-3-662-03736-2_7.

[24] M. Grazel, Heterogeneous Photochemical Electron Transfer, Boca Raton, FL, 1989.

doi:10.1017/CBO9781107415324.004.

[25] R.A. Palominos, M.A. Mondaca, A. Giraldo, G. Penuela, M. Perez-Moya, H.D. Mansilla, Photocatalytic oxidation of the antibiotic tetracycline on TiO2 and ZnO suspensions, Catal. Today. 144 (2009) 100–105. doi:10.1016/j.cattod.2008.12.031.

[26] M.A. Rauf, S.S. Ashraf, Fundamental principles and application of heterogeneous photocatalytic degradation of dyes in solution, Chem. Eng. J. 151 (2009) 10–18. doi:10.1016/j.cej.2009.02.026.

[27] K. Jing, J. Xiong, N. Qin, Y. Song, L. Li, Y. Yu, S. Liang, L. Wu, Development and photocatalytic mechanism of monolayer Bi2MoO 6 nanosheets for the selective oxidation of benzylic alcohols, Chem. Commun. 53 (2017) 8604–8607. doi:10.1039/C7CC04052K.

[28] X.-J. Wen, C.-G. Niu, L. Zhang, G.-M. Zeng, Novel p–n heterojunction BiOI/CeO2 photocatalyst for wider spectrum visible-light photocatalytic degradation of refractory pollutants, Dalt. Trans. 46 (2017) 4982–4993. doi:10.1039/C7DT00106A.

[29] L. Zhang, W. Tian, Y. Chen, J. Chen, H. Teng, J. Zhou, J. Shi, Y. Sun, Light-driven removal of rhodamine B over SrTiO3 modified Bi2WO6 composites, RSC Adv. 6 (2016) 83471–83481. doi:10.1039/C6RA13022D.

[30] Y. Huang, S. Kang, Y. Yang, H. Qin, Z. Ni, S. Yang, X. Li, Facile synthesis of Bi/Bi2WO6 nanocomposite with enhanced photocatalytic activity under visible light, Appl. Catal. B. 196 (2016) 89–99. doi:10.1016/j.apcatb.2016.05.022.

[31] G. Dukovic, M.G. Merkle, J.H. Nelson, S.M. Hughes, A.P. Alivisatos, Photodeposition of Pt on colloidal CdS and CdSe/CdS semiconductor nanostructures, Adv. Mater. 20 (2008) 4306–4311. doi:10.1002/adma.200800384.

[32] X. Chen, L. Li, W. Zhang, Y. Li, Q. Song, J. Zhang, D. Liu, Multi-pathway photoelectron migration in globular flower-like In2O3/AgBr/Bi2WO6 synthesized by microwave-assisted method with enhanced photocatalytic activity, J. Mol. Catal. A Chem. 414 (2016) 27–36. doi:10.1016/j.molcata.2015.12.023.

[33] F.T. Li, Y. Zhao, Y.J. Hao, X.J. Wang, R.H. Liu, D.S. Zhao, D.M. Chen, N-doped P25 TiO2-amorphous Al2O3 composites: One-step solution combustion preparation and enhanced visible-light photocatalytic activity, J. Hazard. Mater. 239–240 (2012) 118–127. doi:10.1016/j.jhazmat.2012.08.016.

[34] J. Jiang, H. Li, L. Zhang, New insight into daylight photocatalysis of AgBr@Ag: Synergistic effect between semiconductor photocatalysis and plasmonic photocatalysis, Chem. - A Eur. J. 18 (2012) 6360–6369. doi:10.1002/chem.201102606.

[35] H. Hou, X. Wang, C. Chen, D.M. Johnson, Y. Fang, Y. Huang, Mechanism of photocatalytic oxidation of guanine by BiOBr under UV irradiation, Catal. Commun. 48 (2014) 65–68. doi:10.1016/j.catcom.2014.01.023.

[36] M.A. Lazar, S. Varghese, S.S. Nair, Photocatalytic Water Treatment by Titanium Dioxide: Recent Updates, Catalysts. 2 (2012) 572–601. doi:10.3390/catal2040572.

[37] Y. Chan, S. Pung, S. Sreekantan, F. Yeoh, Photocatalytic activity of β-MnO2 nanotubes grown on PET fibre under visible light irradiation, J. Exp. Nanosci. 11 (2016) 603–618. doi:10.1080/17458080.2015.1102342.

[38] C. Wu, L. Shen, Y.C. Zhang, Q. Huang, Solvothermal synthesis of Cr-doped ZnO nanowires with visible light-driven photocatalytic activity, Mater. Lett. 65 (2011) 1794–1796. doi:10.1016/j.matlet.2011.03.070.

[39] C. Feng, S. Wang, B. Geng, Ti(iv) doped WO3 nanocuboids: fabrication and enhanced visible-light-driven photocatalytic performance, Nanoscale. 3 (2011) 3695–3699. doi:10.1039/c1nr10460h.

[40] S. Malato, P. Fernández-Ibáñez, M.I. Maldonado, J. Blanco, W. Gernjak, Decontamination and disinfection of water by solar photocatalysis: Recent overview and trends, Catal. Today. 147 (2009) 1–59. doi:10.1016/j.cattod.2009.06.018.

[41] J.B. Zhong, J.Z. Li, Y. Lu, X.Y. He, J. Zeng, W. Hu, Y.C. Shen, Fabrication of Bi3+-doped ZnO with enhanced photocatalytic performance, Appl. Surf. Sci. 258 (2012) 4929–4933. doi:10.1016/j.apsusc.2012.01.121.

[42] M. Faisal, A.A. Ibrahim, H. Bouzid, S.A. Al-Sayari, M.S. Al-Assiri, A.A. Ismail, Hydrothermal synthesis of Sr-doped α-Bi2O3 nanosheets as highly efficient photocatalysts under visible light, J. Mol. Catal. A Chem. 387 (2014) 69–75. doi:10.1016/j.molcata.2014.02.018.

[43] R. Mohan, K. Krishnamoorthy, S.-J. Kim, Enhanced photocatalytic activity of Cu-doped ZnO nanorods, Solid State Commun. 152 (2012) 375–380. doi:10.1016/j.ssc.2011.12.008.

[44] H.F. Moafi, M.A. Zanjanchi, A.F. Shojaie, Tungsten-doped ZnO nanocomposite: Synthesis, characterization, and highly active photocatalyst toward dye photodegradation, Mater. Chem. Phys. 139 (2013) 856–864. doi:10.1016/j.matchemphys.2013.02.044.

[45] K. Jayanthi, S. Chawla, A.G. Joshi, Z.H. Khan, R.K. Kotnala, Fabrication of luminescent, magnetic hollow core nanospheres and nanotubes of Cr-doped ZnO by inclusive coprecipitation method, J. Phys. Chem. C. 114 (2010) 18429–18434. doi:10.1021/jp107086h.

[46] A. Gholami, M. Maddahfar, Synthesis and characterization of novel samarium-doped CuAl2O4 and its photocatalytic performance through the modified sol–gel method, J. Mater. Sci. Mater. Electron. 27 (2016) 3341–3346. doi:10.1007/s10854-015-4163-0.

[47] R. Niishiro, H. Kato, A. Kudo, Nickel and either tantalum or niobium-codoped TiO2 and SrTiO3 photocatalysts with visible-light response for H2 or O2 evolution from aqueous solutions, Phys. Chem. Chem. Phys. 7 (2005) 2241. doi:10.1039/b502147b.

[48] J.C. Fan, K.M. Sreekanth, Z. Xie, S.L. Chang, K. V. Rao, P-Type ZnO materials: Theory, growth, properties and devices, Prog. Mater. Sci. 58 (2013) 874–985. doi:10.1016/j.pmatsci.2013.03.002.

[49] D. Li, J.F. Huang, L.Y. Cao, J.Y. Li, H.B. Ouyang, C.Y. Yao, Microwave hydrothermal synthesis of K+ doped ZnO nanoparticles with enhanced photocatalytic properties under visible-light, Mater. Lett. 118 (2014) 17–20. doi:10.1016/j.ceramint.2013.10.061.

[50] Y. Hu, H.J. Chen, Origin of green luminescence of ZnO powders reacted with carbon black, J. Appl. Phys. 101 (2007) 2005–2008. doi:10.1063/1.2745301.

[51] C. Wu, L. Shen, H. Yu, Q. Huang, Y.C. Zhang, Synthesis of Sn-doped ZnO nanorods and their photocatalytic properties, Mater. Res. Bull. 46 (2011) 1107–1112. doi:10.1016/j.materresbull.2011.02.043.

[52] A. Jia, X. Liang, Z. Su, T. Zhu, S. Liu, Synthesis and the effect of calcination temperature on the physical-chemical properties and photocatalytic activities of Ni,La codoped SrTiO3, J. Hazard. Mater. 178 (2010) 233–242. doi:10.1016/j.jhazmat.2010.01.068.

[53] A.T. Tizro, M. Kamali, Synthesis of Ag-doped PbTiO3 nanoparticles: feasibility study of its decolorization of simulated methyl orange dye wastewater, J. Mater. Sci. Mater. Electron. 27 (2016) 8613–8618. doi:10.1007/s10854-016-4880-z.

[54] R. Wang, G. Jiang, X. Wang, R. Hu, X. Xi, S. Bao, Y. Zhou, T. Tong, S. Wang, T. Wang, W. Chen, Efficient visible-light-induced photocatalytic activity over the novel Ti-doped BiOBr microspheres, Powder Technol. 228 (2012) 258–263. doi:10.1016/j.powtec.2012.05.028.

[55] G. Voicu, O. Oprea, B.S. Vasile, E. Andronescu, Photoluminescence and Photocatalytic Activity of Mn-doped ZnO Nanoparticles, Dig. J. Nanomater. Biostructures. 8 (2013) 667–675.

[56] A. Zhang, J. Zhang, Effects of europium doping on the photocatalytic behavior of BiVO4, J. Hazard. Mater. 173 (2010) 265–272. doi:10.1016/j.jhazmat.2009.08.079.

[57] Y. Huang, Y. Wei, S. Cheng, L. Fan, Y. Li, J. Lin, J. Wu, Photocatalytic property of nitrogen-doped layered perovskite K2La2Ti3O10, Sol. Energy Mater. Sol. Cells. 94 (2010) 761–766. doi:10.1016/j.solmat.2009.12.020.

[58] M. Wang, H. Zheng, Q. Liu, C. Niu, Y. Che, M. Dang, High performance B doped BiVO4 photocatalyst with visible light response by citric acid complex method, Spectrochim. Acta - Part A Mol. Biomol. Spectrosc. 114 (2013) 74–79. doi:10.1016/j.saa.2013.05.032.

[59] G. Tan, L. Zhang, H. Ren, J. Huang, W. Yang, A. Xia, Microwave hydrothermal synthesis of N-doped BiVO4 nanoplates with exposed (040) facets and enhanced visible-light photocatalytic properties, Ceram.

Int. 40 (2014) 9541–9547. doi:10.1016/j.ceramint.2014.02.028.

[60] B. Hu, Y. Liu, Nitrogen-doped Nb2O5 nanobelt quasi-arrays for visible light photocatalysis, J. Alloys Compd. 635 (2015) 1–4. doi:10.1016/j.jallcom.2015.02.109.

[61] N. Arunkumar, R. Vijayaraghavan, Enhanced photocatalytic activity of nanocrystalline N-doped ZnSb2O6: role of N doping, cation ordering, particle size and crystallinity, RSC Adv. 4 (2014) 65223–65231. doi:10.1039/C4RA12612B.

[62] F. Meng, Z. Hong, J. Arndt, M. Li, M. Zhi, F. Yang, N. Wu, Visible light photocatalytic activity of nitrogen-doped La2Ti2O7 nanosheets originating from band gap narrowing, Nano Res. 5 (2012) 213–221. doi:10.1007/s12274-012-0201-x.

[63] S. Chen, W. Zhao, S. Zhang, W. Liu, Preparation, characterization and photocatalytic activity of N-containing ZnO powder, Chem. Eng. J. 148 (2009) 263–269. doi:10.1016/j.cej.2008.08.039.

[64] L. Ma, L. Xu, X. Xu, X. Zhou, L. Zhang, One-Pot Hydrothermal Synthesis of Sulfur-Doped SnO2 Nanoparticles and their Enhanced Photocatalytic Properties, Nanobr. Reports Rev. 11 (2016) 1650035. doi:10.1142/S1793292016500351.

[65] J. Yu, B. Wei, L. Zhu, H. Gao, W. Sun, L. Xu, Flowerlike C-doped BiOCl nanostructures: Facile wet chemical fabrication and enhanced UV photocatalytic properties, Appl. Surf. Sci. 284 (2013) 497–502. doi:10.1016/j.apsusc.2013.07.124.

[66] A.M. Al-Hamdi, M. Sillanpaa, J. Dutta, M. Sillanpää, J. Dutta, Photocatalytic degradation of phenol by iodine doped tin oxide nanoparticles under UV and sunlight irradiation, J. Alloys Compd. 618 (2015) 366–371. doi:10.1016/j.jallcom.2014.08.120.

[67] H. Lin, X. Li, J. Cao, S. Chen, Y. Chen, Novel I--doped BiOBr composites: Modulated valence bands and largely enhanced visible light phtotocatalytic activities, Catal. Commun. 49 (2014) 87–91. doi:10.1016/j.catcom.2014.02.010.

[68] S. Lázaro-Navas, S. Prashar, M. Fajardo, S. Gómez-Ruiz, Visible light-driven photocatalytic degradation of the organic pollutant methylene blue with hybrid palladium–fluorine-doped titanium oxide nanoparticles, J. Nanoparticle Res. 17 (2015) 1–14. doi:10.1007/s11051-015-2902-z.

[69] M. Wang, Q. Liu, Y. Che, L. Zhang, D. Zhang, Characterization and photocatalytic properties of N-doped BiVO4 synthesized via a sol–gel method, J. Alloys Compd. 548 (2013) 70–76. doi:10.1016/j.jallcom.2012.08.140.

[70] C. Wang, Z. Zhao, B. Luo, M. Fu, F. Dong, Tuning the Morphological Structure and Photocatalytic Activity of Nitrogen-Doped (BiO)2CO3 by the Hydrothermal Temperature, J. Nanomater. 2014 (2014).

[71] G. Muruganandam, N. Mala, S. Pandiarajan, N. Srinivasan, R. Ramya, E. Sindhuja, K. Ravichandran, Synergistic effects of Mg and F doping on the photocatalytic efficiency of ZnO nanoparticles towards MB and MG dye degradation, J. Mater. Sci. Mater. Electron. 28 (2017) 18228–18235. doi:10.1007/s10854-017-7771-z.

[72] X. Ding, K. Zhao, L. Zhang, Enhanced photocatalytic removal of sodium pentachlorophenate with self-doped Bi2WO6 under visible light by generating more superoxide ions, Environ. Sci. Technol. 48 (2014) 5823–5831. doi:10.1021/es405714q.

[73] Y. Ding, F. Yang, L. Zhu, N. Wang, H. Tang, Bi3+ self doped NaBiO3 nanosheets: Facile controlled synthesis and enhanced visible light photocatalytic activity, Appl. Catal. B Environ. 164 (2015) 151–158. doi:10.1016/j.apcatb.2014.09.019.

[74] X. Zhang, L. Zhang, Electronic and band structure tuning of ternary semiconductor photocatalysts by self doping: The case of BiOI, J. Phys. Chem. C. 114 (2010) 18198–18206. doi:10.1021/jp105118m.

[75] M.R. Khan, T.W. Chuan, A. Yousuf, M.N.K. Chowdhury, C.K. Cheng, Schottky barrier and surface plasmonic resonance phenomena towards the photocatalytic reaction: study of their mechanisms to enhance photocatalytic activity, Catal. Sci. Technol. 5 (2015) 2522–2531. doi:10.1039/C4CY01545B.

[76] D.B. Ingram, P. Christopher, J.L. Bauer, S. Linic, Predictive model for the design of plasmonic

metal/semiconductor composite photocatalysts, ACS Catal. 1 (2011) 1441–1447. doi:10.1021/cs200320h.

[77] S. Sarina, E.R. Waclawik, H. Zhu, Photocatalysis on supported gold and silver nanoparticles under ultraviolet and visible light irradiation, Green Chem. 15 (2013) 1814. doi:10.1039/c3gc40450a.

[78] E.L. Runnerstrom, A. Llordés, S.D. Lounis, D.J. Milliron, Nanostructured electrochromic smart windows: traditional materials and NIR-selective plasmonic nanocrystals, Chem. Commun. (Camb). 50 (2014) 10555–10572. doi:10.1039/c4cc03109a.

[79] M.K. Kumar, S. Krishnamoorthy, L.K. Tan, S.Y. Chiam, S. Tripathy, H. Gao, Field effects in plasmonic photocatalyst by precise SiO2 thickness control using atomic layer deposition, ACS Catal. 1 (2011) 300–308. doi:10.1021/cs100117v.

[80] R. Jiang, B. Li, C. Fang, J. Wang, Metal/semiconductor hybrid nanostructures for plasmon-enhanced applications, Adv. Mater. 26 (2014) 5274–5309. doi:10.1002/adma.201400203.

[81] S. Sun, W. Wang, L. Zhang, M. Shang, L. Wang, Ag@C core/shell nanocomposite as a highly efficient plasmonic photocatalyst, Catal. Commun. 11 (2009) 290–293. doi:10.1016/j.catcom.2009.09.026.

[82] X. Zhang, Y.L. Chen, R.-S. Liu, D.P. Tsai, Plasmonic photocatalysis, Reports Prog. Phys. 76 (2013) 046401. doi:10.1088/0034-4885/76/4/046401.

[83] P.K. Jain, W. Huang, M.A. El-Sayed, On the Universal Scaling Behavior of the Distance Decay of Plasmon Coupling in Metal Nanoparticle Pairs: A Plasmon Ruler Equation, Nano Lett. 7 (2007) 2080–2088. doi:10.1021/nl071008a.

[84] P. Christopher, H. Xin, S. Linic, Visible-light-enhanced catalytic oxidation reactions on plasmonic silver nanostructures, Nat. Chem. 3 (2011). doi:10.1038/nchem.1032.

[85] X. Lin, F. Rong, D. Fu, C. Yuan, Enhanced photocatalytic activity of fluorine doped TiO2 by loaded with Ag for degradation of organic pollutants, Powder Technol. 219 (2012) 173–178. doi:10.1016/j.powtec.2011.12.037.

[86] D. Tsukamoto, Y. Shiraishi, Y. Sugano, S. Ichikawa, S. Tanaka, T. Hirai, Gold nanoparticles located at the interface of anatase/rutile TiO 2 particles as active plasmonic photocatalysts for aerobic oxidation, J. Am. Chem. Soc. 134 (2012) 6309–6315. doi:10.1021/ja2120647.

[87] J.J. Mock, D.R. Smith, S. Schultz, Local Refractive Index Dependence of Plasmon Resonance Spectra from Individual Nanoparticles, Nano Lett. 3 (2003) 485–491. doi:10.1021/nl0340475.

[88] G. Mie, Beitrage zur Optik truber Medien, speziell kolloidaler Metallosungen, Ann. Phys. 330 (1908) 377–445. doi:10.1002/andp.19083300302.

[89] A. Tcherniak, J.W. Ha, S. Dominguez-Medina, L.S. Slaughter, S. Link, Probing a century old prediction one plasmonic particle at a time, Nano Lett. 10 (2010) 1398–1404. doi:10.1021/nl100199h.

[90] P. Christopher, D.B. Ingram, S. Linic, Enhancing photochemical activity of semiconductor nanoparticles with optically active Ag nanostructures: Photochemistry mediated by Ag surface plasmons, J. Phys. Chem. C. 114 (2010) 9173–9177. doi:10.1021/jp101633u.

[91] Y. Liang, H. Wang, L. Liu, P. Wu, W. Cui, J.G. McEvoy, Z. Zhang, Microwave-assisted synthesis of a superfine Ag/AgI photocatalyst with high activity and excellent durability, J. Mater. Sci. 50 (2015) 6935–6946. doi:10.1007/s10853-015-9245-0.

[92] M.J. Sampaio, M.J. Lima, D.L. Baptista, A.M.T. Silva, C.G. Silva, J.L. Faria, Ag-loaded ZnO materials for photocatalytic water treatment, Chem. Eng. J. (2016). doi:10.1016/j.cej.2016.05.105.

[93] H. Daupor, S. Wongnawa, Urchinlike Ag/AgCl photocatalyst: Synthesis, characterization, and activity, Appl. Catal. A Gen. 473 (2014) 59–69. doi:10.1016/j.apcata.2013.12.036.

[94] H.-Y. Jiang, K. Cheng, J. Lin, Crystalline metallic Au nanoparticle-loaded α-Bi2O3 microrods for improved photocatalysis, Phys. Chem. Chem. Phys. 14 (2012) 12114. doi:10.1039/c2cp42165h.

[95] N. Pugazhenthiran, P. Sathishkumar, S. Murugesan, S. Anandan, Effective degradation of acid orange 10 by catalytic ozonation in the presence of Au-Bi2O3 nanoparticles, Chem. Eng. J. 168 (2011) 1227–1233.

doi:10.1016/j.cej.2011.02.020.

[96] G. Xi, J. Ye, Q. Ma, N. Su, H. Bai, C. Wang, In situ growth of metal particles on 3D urchin-like WO3 nanostructures, J. Am. Chem. Soc. 134 (2012) 6508–6511. doi:10.1021/ja211638e.

[97] S. Anandan, N. Pugazhenthiran, G.J. Lee, J.J. Wu, Photocatalytic degradation of ceftiofur sodium using Au loaded Bi2CuO4 nanoparticles, J. Mol. Catal. A Chem. 379 (2013) 112–116. doi:10.1016/j.molcata.2013.08.002.

[98] R. Abe, H. Takami, N. Murakami, B. Ohtani, Pristine Simple Oxides as Visible Light Driven Photocatalysts: Highly Efficient Decomposition of Organic Compounds over Platinum-Loaded Tungsten Oxide, J. Am. Chem. Soc. 130 (2008) 7780–7781. doi:10.1021/ja800835q.

[99] C. Yu, F. Cao, G. Li, R. Wei, J.C. Yu, R. Jin, Q. Fan, C. Wang, Novel noble metal (Rh, Pd, Pt)/BiOX(Cl, Br, I) composite photocatalysts with enhanced photocatalytic performance in dye degradation, Sep. Purif. Technol. 120 (2013) 110–122. doi:10.1016/j.seppur.2013.09.036.

[100] H. Xu, H. Li, C. Wu, J. Chu, Y. Yan, H. Shu, Z. Gu, Preparation, characterization and photocatalytic properties of Cu-loaded BiVO4, J. Hazard. Mater. 153 (2008) 877–884. doi:10.1016/j.jhazmat.2007.09.039.

[101] A. Márquez-Herrera, V.M. Ovando-Medina, B.E. Castillo-Reyes, M. Zapata-Torres, M. Meléndez-Lira, J. González-Castañeda, Facile synthesis of SrCO3-Sr(OH)2/PPy nanocomposite with enhanced photocatalytic activity under visible light, Materials (Basel). 9 (2016) 89–99. doi:10.3390/ma9010030.

[102] H. Yu, G. Cao, F. Chen, X. Wang, J. Yu, M. Lei, Enhanced photocatalytic performance of Ag3PO4 by simutaneous loading of Ag nanoparticles and Fe(III) cocatalyst, Appl. Catal. B Environ. 160–161 (2014) 658–665. doi:10.1016/j.apcatb.2014.06.015.

[103] G. Jiang, R. Wang, X. Wang, X. Xi, R. Hu, Y. Zhou, S. Wang, T. Wang, W. Chen, Novel highly active visible-light-induced photocatalysts based on BiOBr with Ti doping and Ag decorating, ACS Appl. Mater. Interfaces. 4 (2012) 4440–4444. doi:10.1021/am301177k.

[104] S. Eustis, M. a El-Sayed, Why gold nanoparticles are more precious than pretty gold: Noble metal surface plasmon resonance and its enhancement of the radiative and nonradiative properties of nanocrystals of different shapes, Chem. Soc. Rev. 35 (2006) 209–217. doi:10.1039/B514191E.

[105] M. Rycenga, C.M. Cobley, J. Zeng, W. Li, C.H. Moran, Controlling the Synthesis and Assembly of Silver Nanostructures for Plasmonic Applications, Chem Rev. 111 (2012) 3669–3712. doi:10.1021/cr100275d.Controlling.

[106] J. Zeng, S. Roberts, Y. Xia, Nanocrystal-based time-temperature indicators, Chem. - A Eur. J. 16 (2010) 12559–12563. doi:10.1002/chem.201002665.

[107] S.F. Wang, F. Gu, M.K. Lü, Sonochemical synthesis of hollow PbS nanospheres, Langmuir. 22 (2006) 398–401. doi:10.1021/la0518647.

[108] J.H. Fendler, Surfactant vesicles as membrane mimetic agents: characterization and utilization, Acc. Chem. Res. 13 (1980) 7–13. doi:10.1021/ar50145a002.

[109] M.M. Alvarez, J.T. Khoury, T.G. Schaaff, M. Shafigullin, I. Vezmar, R.L. Whetten, Critical sizes in the growth of Au clusters, Chem. Phys. Lett. 266 (1997) 91–98. doi:10.1016/S0009-2614(96)01535-7.

[110] P. Pawinrat, O. Mekasuwandumrong, J. Panpranot, Synthesis of Au-ZnO and Pt-ZnO nanocomposites by one-step flame spray pyrolysis and its application for photocatalytic degradation of dyes, Catal. Commun. 10 (2009) 1380–1385. doi:10.1016/j.catcom.2009.03.002.

[111] X. Yu, A. Shavel, X. An, Z. Luo, M. Ibáñez, A. Cabot, Cu2ZnSnS4-Pt and Cu2ZnSnS4-Au Heterostructured Nanoparticles for Photocatalytic Water Splitting and Pollutant Degradation, J. Am. Chem. Soc. 136 (2014) 9236–9239. doi:10.1021/ja502076b.

[112] X. Meng, Z. Zhang, Ag/AgCl Loaded Bi2WO6 Composite: A Plasmonic Z-Scheme Visible Light-Responsive Photocatalyst, Int. J. Photoenergy. 2016 (2016) 1–11. doi:10.1155/2016/4054351.

[113] Y. Wang, Q. Wang, X. Zhan, F. Wang, M. Safdar, Visible light driven type II heterostructures and their

enhanced photocatalysis properties : a review, (2013) 8326–8339. doi:10.1039/c3nr01577g.

[114] X. Yan, K. Liu, W. Shi, Facile synthesis of CdS/MnWO4 heterojunction with enhanced visible-light-driven photocatalytic activity and mechanism investigation, Colloids Surfaces A Physicochem. Eng. Asp. 520 (2017) 138–145. doi:10.1016/j.colsurfa.2017.01.065.

[115] G. Yang, Z. Yan, T. Xiao, Preparation and characterization of SnO2/ZnO/TiO2 composite semiconductor with enhanced photocatalytic activity, Appl. Surf. Sci. 258 (2012) 8704–8712. doi:10.1016/j.apsusc.2012.05.078.

[116] Y.C. Zhang, Z.N. Du, K.W. Li, M. Zhang, D.D. Dionysiou, High-Performance Visible-Light-Driven SnS2/SnO2 Nanocomposite Photocatalyst Prepared via In situ Hydrothermal Oxidation of SnS2 Nanoparticles, ACS Appl. Mater. Interfaces. 3 (2011) 1528–1537.

[117] Y. Wang, J. Sunarso, B. Zhao, C. Ge, G. Chen, One-dimensional BiOBr nanosheets/TiO2 nanofibers composite: Controllable synthesis and enhanced visible photocatalytic activity, Ceram. Int. 43 (2017) 15769–15776. doi:10.1016/j.ceramint.2017.08.140.

[118] S. Yang, L. Li, W. Yuan, Z. Xia, Enhanced visible light photocatalytic activity of ZnIn2S4 modified by semiconductors, Dalt. Trans. 44 (2015) 6374–6383. doi:10.1039/C5DT00147A.

[119] R. Kennedy, I. Martini, G. Hartland, P. V Kamat, Capped semiconductor colloids: Synthesis and photochemistry of CdS capped SnO2 nanocrystallites, J. Chem. Sci. 109 (1997) 497–507. doi:10.1007/BF02869209.

[120] J. Huang, S. Liu, L. Kuang, Y. Zhao, T. Jiang, S. Liu, X. Xu, Enhanced photocatalytic activity of quantum-dot-sensitized one-dimensionally-ordered ZnO nanorod photocatalyst, J. Environ. Sci. (China). 25 (2013) 2487–2491. doi:10.1016/S1001-0742(12)60330-1.

[121] J. Ma, S. Liu, G. Qi, Synthesis of m-LaVO4 /BiOBr composite photocatalysts and their photocatalytic performance under visible light, Mater. Res. Bull. 95 (2017) 146–151. doi:10.1016/j.materresbull.2017.07.032.

[122] Y. Peng, P.-P. Yu, H.-Y. Zhou, A.-W. Xu, Synthesis of BiOI/Bi4O5I2/Bi2O2CO3 p–n–p heterojunctions with superior photocatalytic activities, New J. Chem. 39 (2015) 8321–8328. doi:10.1039/C5NJ01662B.

[123] M. Miyauchi, T. Hanayama, D. Atarashi, E. Sakai, Photoenergy Conversion in p-Type Cu2ZnSnS4 Nanorods and n-Type Metal Oxide Composites, J. Phys. Chem. C. 116 (2012) 23945–23950. doi:10.1021/jp307949n.

[124] Y. Min, G. He, Q. Xu, Y. Chen, Self-assembled encapsulation of graphene oxide/Ag@AgCl as a Z-scheme photocatalytic system for pollutant removal, J. Mater. Chem. A. 2 (2014) 1294–1301. doi:10.1039/C3TA13687F.

[125] F. Qiu, W. Li, F. Wang, H. Li, X. Liu, J. Sun, In-situ synthesis of novel Z-scheme SnS2/BiOBr photocatalysts with superior photocatalytic efficiency under visible light, J. Colloid Interface Sci. 493 (2017) 1–9. doi:10.1016/j.jcis.2016.12.066.

[126] C. Song, X. Wang, J. Zhang, X. Chen, C. Li, Enhanced performance of direct Z-scheme CuS-WO3 system towards photocatalytic decomposition of organic pollutants under visible light, Appl. Surf. Sci. 425 (2017) 788–795. doi:10.1016/j.apsusc.2017.07.082.

[127] C. Yu, K. Wang, P. Yang, S. Yang, C. Lu, Y. Song, S. Dong, J. Sun, J. Sun, One-pot facile synthesis of Bi2S3/SnS2/Bi2O3 ternary heterojunction as advanced double Z-scheme photocatalytic system for efficient dye removal under sunlight irradiation, Appl. Surf. Sci. 420 (2017) 233–242. doi:10.1016/j.apsusc.2017.05.147.

[128] D. Zheng, C. Pang, X. Wang, The function-led design of Z-scheme photocatalytic systems based on hollow carbon nitride semiconductors, Chem. Commun. 51 (2015) 17467–17470. doi:10.1039/C5CC07867A.

[129] A. Kudo, Z-scheme photocatalyst systems for water splitting under visible light irradiation, MRS Bull. 36 (2011) 32–38. doi:10.1557/mrs.2010.3.

[130] A. Iwase, Y.H. Ng, Y. Ishiguro, A. Kudo, R. Amal, Reduced Graphene Oxide as a Solid-state Electron

Mediator in Z-scheme Photocatalytic Water Splitting under Visible light Reduced Graphene Oxide as a Solid-state Electron Mediator in Z- scheme Photocatalytic Water Splitting under Visible light, Am. Chem. Soc. (2011) 11054–11057.

[131] Q. Li, Z. Guan, D. Wu, X. Zhao, S. Bao, B. Tian, J. Zhang, Z-Scheme BiOCl-Au-CdS Heterostructure with Enhanced Sunlight-Driven Photocatalytic Activity in Degrading Water Dyes and Antibiotics, ACS Sustain. Chem. Eng. 5 (2017) 6958–6968. doi:10.1021/acssuschemeng.7b01157.

[132] X. Wang, K. Maeda, A. Thomas, K. Takanabe, G. Xin, J.M. Carlsson, K. Domen, M. Antonietti, A metal-free polymeric photocatalyst for hydrogen production from water under visible light, Nat. Mater. 8 (2009) 76–80. doi:10.1038/nmat2317.

[133] S. Wang, D. Li, C. Sun, S. Yang, Y. Guan, H. He, Synthesis and characterization of g-C3N4/Ag3VO4 composites with significantly enhanced visible-light photocatalytic activity for triphenylmethane dye degradation, Appl. Catal. B Environ. 144 (2014) 885–892. doi:10.1016/j.apcatb.2013.08.008.

[134] J. Fu, B. Chang, Y. Tian, F. Xi, X. Dong, Novel C3N4–CdS composite photocatalysts with organic–inorganic heterojunctions: in situ synthesis, exceptional activity, high stability and photocatalytic mechanism, J. Mater. Chem. A. 1 (2013) 3083. doi:10.1039/c2ta00672c.

[135] L. Ye, J. Liu, Z. Jiang, T. Peng, L. Zan, Facets coupling of BiOBr-g-C3N4 composite photocatalyst for enhanced visible-light-driven photocatalytic activity, Appl. Catal. B Environ. 142–143 (2013) 1–7. doi:10.1016/j.apcatb.2013.04.058.

[136] P. Niu, L. Zhang, G. Liu, H.M. Cheng, Graphene-like carbon nitride nanosheets for improved photocatalytic activities, Adv. Funct. Mater. 22 (2012) 4763–4770. doi:10.1002/adfm.201200922.

[137] Z. Yong, J. Ren, H. Hu, P. Li, S. Ouyang, H. Xu, D. Wang, Synthesis , Characterization , and Photocatalytic Activity of g-C3N4/KTaO3 Composites under Visible Light Irradiation, J. Nanomater. 2015 (2015) 1–7. doi:10.1155/2015/821986.

[138] Y. Lin, D. Li, J. Hu, G. Xiao, J. Wang, W. Li, X. Fu, Highly Efficient Photocatalytic Degradation of Organic Pollutants by PANI-Modified TiO2 Composite, J. Phys. Chem. C. 116 (2012) 5764–5772. doi:10.1021/jp211222w.

[139] H. Gülce, V. Eskizeybek, B. Haspulat, F. Sarı, A. Gülce, A. Avcı, Preparation of a New Polyaniline/CdO Nanocomposite and Investigation of Its Photocatalytic Activity: Comparative Study under UV Light and Natural Sunlight Irradiation, Ind. Eng. Chem. Res. 52 (2013) 10924–10934. doi:10.1021/ie401389e.

[140] M. Shang, W. Wang, S. Sun, J. Ren, L. Zhou, L. Zhang, Efficient Visible Light-Induced Photocatalytic Degradation of Contaminant by Spindle-like PANI/BiVO4, J. Phys. Chem. C. 113 (2009) 20228–20233. doi:10.1021/jp9067729.

[141] H. Zhang, R. Zong, Y. Zhu, Photocorrosion Inhibition and Photoactivity Enhancement for Zinc Oxide via Hybridization with Monolayer Polyaniline, J. Phys. Chem. C. 113 (2009) 4605–4611. doi:10.1021/jp810748u.

[142] P. Xiong, Q. Chen, M. He, X. Sun, X. Wang, Cobalt ferrite-polyaniline heteroarchitecture: a magnetically recyclable photocatalyst with highly enhanced performances, J. Mater. Chem. 22 (2012) 17485–17493. doi:10.1039/c2jm31522j.

[143] F. Duan, Q. Zhang, D. Shi, M. Chen, Enhanced visible light photocatalytic activity of Bi2WO6 via modification with polypyrrole, Appl. Surf. Sci. 268 (2013) 129–135. doi:10.1016/j.apsusc.2012.12.031.

[144] B. Gao, W. Chen, S. Dong, J. Liu, T. Liu, L. Wang, M. Sillanpää, Polypyrrole/ZnIn2S4 composite photocatalyst for enhanced mineralization of chloramphenicol under visible light, J. Photochem. Photobiol. A Chem. 349 (2017) 115–123. doi:10.1016/j.jphotochem.2017.09.018.

[145] J. Xu, Y. Hu, C. Zeng, Y. Zhang, H. Huang, Polypyrrole decorated BiOI nanosheets: Efficient photocatalytic activity for treating diverse contaminants and the critical role of bifunctional polypyrrole, J. Colloid Interface Sci. 505 (2017) 719–727. doi:10.1016/j.jcis.2017.06.054.

[146] F.A. Harraz, A.A. Ismail, S.A. Al-Sayari, A. Al-Hajry, Novel α-Fe2O3/polypyrrole nanocomposite with enhanced photocatalytic performance, J. Photochem. Photobiol. A Chem. 299 (2015) 18–24.

doi:10.1016/j.jphotochem.2014.11.001.

[147] Q. Xiang, J. Yu, M. Jaroniec, Graphene-based semiconductor photocatalysts, Chem. Soc. Rev. 41 (2012) 782. doi:10.1039/c1cs15172j.

[148] S. Chowdhury, R. Balasubramanian, Graphene/semiconductor nanocomposites (GSNs) for heterogeneous photocatalytic decolorization of wastewaters contaminated with synthetic dyes: A review, Appl. Catal. B Environ. 160–161 (2014) 307–324. doi:10.1016/j.apcatb.2014.05.035.

[149] J. Gamage McEvoy, W. Cui, Z. Zhang, Synthesis and characterization of Ag/AgCl–activated carbon composites for enhanced visible light photocatalysis, Appl. Catal. B Environ. 144 (2014) 702–712. doi:10.1016/j.apcatb.2013.07.062.

[150] K.S. Novoselov, Electric Field Effect in Atomically Thin Carbon Films, Science (80-.). 306 (2004) 666–669. doi:10.1126/science.1102896.

[151] E. Gao, W. Wang, M. Shang, J. Xu, Synthesis and enhanced photocatalytic performance of graphene-Bi2WO6 composite, Phys. Chem. Chem. Phys. PCCP. 13 (2011) 2887–2893. doi:10.1039/c0cp01749c.

[152] A. Arshad, J. Iqbal, M. Siddiq, M.U. Ali, A. Ali, H. Shabbir, U. Bin Nazeer, M.S. Saleem, Solar light triggered catalytic performance of graphene-CuO nanocomposite for waste water treatment, Ceram. Int. 43 (2017) 10654–10660. doi:10.1016/j.ceramint.2017.03.165.

[153] R. Sitko, B. Zawisza, E. Malicka, Graphene as a new sorbent in analytical chemistry, TrAC - Trends Anal. Chem. 51 (2013) 33–43. doi:10.1016/j.trac.2013.05.011.

[154] P. Gao, J. Liu, D.D. Sun, W. Ng, Graphene oxide-CdS composite with high photocatalytic degradation and disinfection activities under visible light irradiation, J. Hazard. Mater. 250–251 (2013) 412–420. doi:10.1016/j.jhazmat.2013.02.003.

[155] S.Y. Dong, Y.R. Cui, Y.F. Wang, Y.K. Li, L.M. Hu, J.Y. Sun, J.H. Sun, Designing three-dimensional acicular sheaf shaped BiVO4/reduced graphene oxide composites for efficient sunlight-driven photocatalytic degradation of dye wastewater, Chem. Eng. J. 249 (2014) 102–110. doi:DOI 10.1016/j.cej.2014.03.071.

[156] S. Li, S. Hu, K. Xu, W. Jiang, J. Liu, Z. Wang, A Novel Heterostructure of BiOI Nanosheets Anchored onto MWCNTs with Excellent Visible-Light Photocatalytic Activity, Nanomaterials. 7 (2017) 22. doi:10.3390/nano7010022.

[157] G. Zhao, D. Zhang, J. Yu, Y. Xie, W. Hu, F. Jiao, Multi-walled carbon nanotubes modified Bi2S3 microspheres for enhanced photocatalytic decomposition efficiency, Ceram. Int. 43 (2017) 15080–15088. doi:10.1016/j.ceramint.2017.08.036.

[158] L. Yang, D. Chu, L. Wang, X. Wu, J. Luo, Synthesis and photocatalytic activity of chrysanthemum-like Cu2O/Carbon Nanotubes nanocomposites, Ceram. Int. 42 (2016) 2502–2509. doi:10.1016/j.ceramint.2015.10.051.

[159] D. Jiang, W. Ma, P. Xiao, L. Shao, D. Li, M. Chen, Enhanced photocatalytic activity of graphitic carbon nitride/carbon nanotube/Bi2WO6 ternary Z-scheme heterojunction with carbon nanotube as efficient electron mediator, J. Colloid Interface Sci. 512 (2018) 693–700. doi:10.1016/j.jcis.2017.10.074.

[160] J. Gamage McEvoy, Z. Zhang, Synthesis and characterization of Ag/AgBr-activated carbon composites for visible light induced photocatalytic detoxification and disinfection, J. Photochem. Photobiol. A Chem. 321 (2016) 161–170. doi:10.1016/j.jphotochem.2016.02.004.

[161] H. Fu, T. Xu, S. Zhu, Y. Zhu, Photocorrosion Inhibition and Enhancement of Photocatalytic Activity for ZnO via Hybridization with C Photocorrosion Inhibition and Enhancement of Photocatalytic Activity for ZnO via Hybridization with C60, 42 (2008) 8064–8069. doi:10.1021/es801484x.

[162] H. Shi, H. Tan, W. Zhu, Z. Sun, Y. Ma, E. Wang, Electrospun Cr-doped Bi4Ti3O12/Bi2Ti2O7 heterostructure fibers with enhanced visible-light photocatalytic properties, J. Mater. Chem. A. 3 (2015) 6586–6591. doi:10.1039/C4TA06736C.

[163] W. Yang, G. Tan, J. Huang, H. Ren, A. Xia, C. Zhao, Enhanced magnetic property and photocatalytic activity of UV-light responsive N-doped Fe2O3/FeVO4 heterojunction, Ceram. Int. 41 (2015) 1495–1503.

doi:10.1016/j.ceramint.2014.09.084.

[164] L. Chen, D. Meng, X. Wu, A. Wang, J. Wang, Y. Wang, M. Yu, In Situ Synthesis of V4+ and Ce3+ Self-Doped BiVO4/CeO2 Heterostructured Nanocomposites with High Surface Areas and Enhanced Visible-Light Photocatalytic Activity, J. Phys. Chem. C. 120 (2016) 184548–18559. doi:10.1021/acs.jpcc.6b04131.

[165] Y. Lu, K. Zhao, Y. Zhao, S. Zhu, X. Yuan, M. Huo, Y. Zhang, Y. Qiu, Bi2WO6/TiO2/Pt nanojunction system: A UV-vis light responsive photocatalyst with high photocatalytic performance, Colloids Surfaces A Physicochem. Eng. Asp. 481 (2015) 252–260. doi:10.1016/j.colsurfa.2015.05.037.

[166] X.J. Wen, C.G. Niu, L. Zhang, C. Liang, G.M. Zeng, A novel Ag2O/CeO2 heterojunction photocatalysts for photocatalytic degradation of enrofloxacin: possible degradation pathways, mineralization activity and an in depth mechanism insight, Appl. Catal. B Environ. 221 (2018) 701–714. doi:10.1016/j.apcatb.2017.09.060.

[167] J. Li, H. Yuan, Z. Zhu, Fabrication of Cu2O/Au/BiPO4 Z-scheme photocatalyst to improve the photocatalytic activity under solar light, J. Mol. Catal. A Chem. 410 (2015) 133–139. doi:10.1016/j.molcata.2015.09.013.

[168] J. Zhu, S. Liu, Q. Yang, P. Xu, J. Ge, X. Guo, Fabrication of flower-like Ag@AgCl/Bi2WO6 photocatalyst and its mechanism of photocatalytic degradation, Colloids Surfaces A Physicochem. Eng. Asp. 489 (2016) 275–281. doi:10.1016/j.colsurfa.2015.11.009.

[169] X. Meng, L. Jiang, W. Wang, Z. Zhang, Enhanced Photocatalytic Activity of BiOBr/ZnO Heterojunction Semiconductors Prepared by Facile Hydrothermal Method, Int. J. Photoenergy. 2015 (2015) 1–9. doi:10.1155/2015/747024.

[170] Y. Park, Y. Na, D. Pradhan, B.-K. Min, Y. Sohn, Adsorption and UV/Visible photocatalytic performance of BiOI for methyl orange, Rhodamine B and methylene blue: Ag and Ti-loading effects, CrystEngComm. 16 (2014) 3155. doi:10.1039/c3ce42654h.

[171] Y. Zhou, Y. Zhang, M. Lin, J. Long, Z. Zhang, H. Lin, J.C.S. Wu, X. Wang, Monolayered Bi2WO6 nanosheets mimicking heterojunction interface with open surfaces for photocatalysis, Nat. Commun. 6 (2015) 1–8. doi:10.1038/ncomms9340.

[172] Z. Li, Y. Wu, G. Lu, Highly efficient hydrogen evolution over Co(OH)2 nanoparticles modified g-C3N4 co-sensitized by Eosin Y and Rose Bengal under Visible Light Irradiation, Appl. Catal. B Environ. 188 (2016) 56–64. doi:10.1016/j.apcatb.2016.01.057.

[173] B. Subash, B. Krishnakumar, M. Swaminathan, M. Shanthi, β-Ag2S-ZnO as a novel sunshine photocatalyst for the effective degradation of RR 120 dye, Powder Technol. 241 (2013) 49–59. doi:10.1016/j.powtec.2013.03.002.

[174] L. Shi, L. Liang, J. Ma, F. Wang, J. Sun, Enhanced photocatalytic activity over the Ag2O–g-C3N4 composite under visible light, Catal. Sci. Technol. 4 (2014) 758. doi:10.1039/c3cy00871a.

[175] J. Tang, Z. Zou, J. Yin, J. Ye, Photocatalytic degradation of methylene blue on CaIn2O4 under visible light irradiation, Chem. Phys. Lett. 382 (2003) 175–179. doi:10.1016/j.cplett.2003.10.062.

[176] B. Subash, B. Krishnakumar, M. Swaminathan, M. Shanthi, Highly Efficient, Solar Active, and Reusable Photocatalyst: Zr-Loaded Ag–ZnO for Reactive Red 120 Dye Degradation with Synergistic Effect and Dye-Sensitized Mechanism, Langmuir. 29 (2013) 939–949. doi:10.1021/la303842c.

[177] L. Muszkat, L. Feigelson, L. Bir, K.A. Muszkat, Photocatalytic degradation of pesticides and bio-molecules in water, Pest Manag. Sci. 58 (2002) 1143–1148. doi:10.1002/ps.578.

[178] H. Ross, J. Bendig, S. Hecht, Sensitized photocatalytical oxidation of terbutylazine, Sol. Energy Mater. Sol. Cells. 33 (1994) 475–481. doi:10.1016/0927-0248(94)90007-8.

[179] P. Chowdhury, J. Moreira, H. Gomaa, A.K. Ray, Visible-solar-light-driven photocatalytic degradation of phenol with dye-sensitized TiO2: Parametric and kinetic study, Ind. Eng. Chem. Res. 51 (2012) 4523–4532. doi:10.1021/ie2025213.

[180] P. Chowdhury, H. Gomaa, A.K. Ray, Dye-sensitized photocatalyst: A breakthrough in green energy and environmental detoxification, ACS Symp. Ser. 1124 (2013) 231–266. doi:10.1021/bk-2013-1124.ch013.

[181] H.R. Rajabi, O. Khani, M. Shamsipur, V. Vatanpour, High-performance pure and Fe3+-ion doped ZnS quantum dots as green nanophotocatalysts for the removal of malachite green under UV-light irradiation, J. Hazard. Mater. 250–251 (2013) 370–378. doi:10.1016/j.jhazmat.2013.02.007.

[182] R. Khan, M.S. Hassan, H.-S. Cho, A.Y. Polyakov, M.-S. Khil, I.-H. Lee, Facile low-temperature synthesis of ZnO nanopyramid and its application to photocatalytic degradation of methyl orange dye under UV irradiation, Mater. Lett. 133 (2014) 224–227. doi:10.1016/j.matlet.2014.07.006.

[183] J. Yu, J. Zhang, M. Jaroniec, Preparation and enhanced visible-light photocatalytic H2-production activity of CdS quantum dots-sensitized Zn1−xCdxS solid solution, Green Chem. 12 (2010) 1611. doi:10.1039/c0gc00236d.

[184] T.R. Pisanic II, Y. Zhang, T.H. Wang, Quantum dots in diagnostics and detection: principles and paradigms, Analyst. 139 (2014) 2968. doi:10.1039/c4an00294f.

[185] A.A.P. Mansur, H.S. Mansur, F.P. Ramanery, L.C. Oliveira, P.P. Souza, "Green" colloidal ZnS quantum dots/chitosan nano-photocatalysts for advanced oxidation processes: Study of the photodegradation of organic dye pollutants, Appl. Catal. B Environ. 158–159 (2014) 269–279. doi:10.1016/j.apcatb.2014.04.026.

[186] L. Ge, J. Liu, Efficient visible light-induced photocatalytic degradation of methyl orange by QDs sensitized CdS-Bi2WO6, Appl. Catal. B Environ. 105 (2011) 289–297. doi:10.1016/j.apcatb.2011.04.016.

[187] Y. Guo, L. Wang, L. Yang, J. Zhang, L. Jiang, X. Ma, Optical and photocatalytic properties of arginine-stabilized cadmium sulfide quantum dots, Mater. Lett. 65 (2011) 486–489. doi:10.1016/j.matlet.2010.10.057.

[188] M.R. Hoffmann, S.T. Martin, W.Y. Choi, D.W. Bahnemannt, D.W. Bahnemann, Environmental Applications of Semiconductor Photocatalysis, Chem. Rev. 95 (1995) 69–96. doi:10.1021/cr00033a004.

[189] S. Sun, W. Wang, L. Zhang, Bi2WO6 Quantum Dots Decorated Reduced Graphene Oxide: Improved Charge Separation and Enhanced Photoconversion Efficiency, J. Phys. Chem. C. 117 (2013) 9113–9120. doi:10.1021/jp4004592.

[190] X. Zhang, C. Shao, Z. Zhang, J. Li, P. Zhang, M. Zhang, J. Mu, Z. Guo, P. Liang, Y. Liu, In situ Generation of Well-Dispersed ZnO Quantum Dots on Electrospun Silica Nanotubes with High Photocatalytic Activity, ACS Appl. Mater. Interfaces. 4 (2012) 785–790. doi:10.1021/am201420b.

[191] W. Cui, W. An, L. Liu, J. Hu, Y. Liang, Novel Cu2O quantum dots coupled flower-like BiOBr for enhanced photocatalytic degradation of organic contaminant, J. Hazard. Mater. 280 (2014) 417–427. doi:10.1016/j.jhazmat.2014.08.032.

[192] X. Liu, M. Zhou, G. Yao, W. Shi, C. Ma, P. Lv, Y. Tang, Y. Yan, Hydrothermal synthesis and enhanced visible-light photocatalytic activity of octahedral Bi2WO6 modified with CdSe quantum dots, RSC Adv. 4 (2014) 18264–18269. doi:10.1039/c3ra46590j.

[193] Z. Liu, B. Wu, Y. Zhu, F. Wang, L. Wang, Cadmium sulphide quantum dots sensitized hierarchical bismuth oxybromide microsphere with highly efficient photocatalytic activity, J. Colloid Interface Sci. 392 (2013) 337–342. doi:10.1016/j.jcis.2012.09.062.

[194] J. Hou, Z. Wang, S. Jiao, H. Zhu, Bi2O3 quantum-dot decorated nitrogen-doped Bi3NbO7 nanosheets: in situ synthesis and enhanced visible-light photocatalytic activity, CrystEngComm. 14 (2012) 5923. doi:10.1039/c2ce25504a.

[195] H. Lin, H. Ye, B. Xu, J. Cao, S. Chen, Ag3PO4 quantum dot sensitized BiPO4: A novel p-n junction Ag3PO4/BiPO4 with enhanced visible-light photocatalytic activity, Catal. Commun. 37 (2013) 55–59. doi:10.1016/j.catcom.2013.03.026.

[196] L. Yu, Y. Huang, G. Xiao, D. Li, Application of long wavelength visible light ($\lambda > 650$ nm) in photocatalysis with a p-CuO-n-In2O3 quantum dot heterojunction photocatalyst, J. Mater. Chem. A. 1 (2013) 9637–9640. doi:10.1039/C3TA12207G.

[197] D. Wang, L. Guo, Y. Zhen, L. Yue, G. Xue, F. Fu, AgBr quantum dots decorated mesoporous Bi2WO6 architectures with enhanced photocatalytic activities for methylene blue, J. Mater. Chem. A. 2 (2014) 11716. doi:10.1039/C4TA01444H.

[198] X. Meng, Z. Li, H. Zeng, J. Chen, Z. Zhang, MoS2 quantum dots-interspersed Bi2WO6 heterostructure for visible light-induced detoxification and disinfection, Appl. Catal. B. 210 (2017) 160–172. doi:10.1016/j.apcatb.2017.02.083.

[199] A. Baumgartner, A. Chaggar, A. Patanè, L. Eaves, M. Henini, Upconversion electroluminescence in InAs quantum dot light-emitting diodes, Appl. Phys. Lett. 92 (2008). doi:10.1063/1.2885074.

[200] I.L. Medintz, H.T. Uyeda, E.R. Goldman, H. Mattoussi, Quantum dot bioconjugates for imaging, labelling and sensing, Nat. Mater. 4 (2005) 435–446. doi:10.1038/nmat1390.

[201] W.C. Jianying Ouyang, Upconversion Luminescence of collidal CdS and ZnCdS semiconductor quantum dots, Jounal Phys. Chem. C. 111 (2007) 16261–16266.

[202] C. Bonati, A. Cannizzo, D. Tonti, A. Tortschanoff, F. Van Mourik, M. Chergui, Subpicosecond near-infrared fluorescence upconversion study of relaxation processes in PbSe quantum dots, Phys. Rev. B - Condens. Matter Mater. Phys. 76 (2007) 1–4. doi:10.1103/PhysRevB.76.033304.

[203] X. Wang, W. Yu, J. Zhang, J. Aldana, X. Peng, M. Xiao, Photoluminescence upconversion in colloidal CdTe quantum dots, Phys. Rev. B. 68 (2003) 1–6. doi:10.1103/PhysRevB.68.125318.

[204] K. Yu, B. Zaman, S. Singh, D. Wang, J.A. Ripmeester, The effect of dispersion media on photoluminescence of colloidal CdSe nanocrystals synthesized from TOP, Chem. Mater. 17 (2005) 2552–2561. doi:10.1021/cm048457l.

[205] J. Di, J. Xia, Y. Ge, H.H.H. Li, H. Ji, H. Xu, Q. Zhang, H.H.H. Li, M. Li, Novel visible-light-driven CQDs/Bi2WO6 hybrid materials with enhanced photocatalytic activity toward organic pollutants degradation and mechanism insight, Appl. Catal. B. 168–169 (2015) 51–61. doi:10.1016/j.apcatb.2014.11.057.

[206] H. Li, R. Liu, Y. Liu, H. Huang, H. Yu, H. Ming, S. Lian, S.-T. Lee, Z. Kang, Carbon quantum dots/Cu2O composites with protruding nanostructures and their highly efficient (near) infrared photocatalytic behavior, J. Mater. Chem. 22 (2012) 17470. doi:10.1039/c2jm32827e.

[207] J. Di, J. Xia, M. Ji, H.H. Li, H. Xu, H.H. Li, R. Chen, The synergistic role of carbon quantum dots for the improved photocatalytic performance of Bi2MoO6, Nanoscale. 7 (2015) 11433–11443. doi:10.1039/C5NR01350J.

[208] H. Yu, H. Zhang, H. Huang, Y. Liu, H. Li, H. Ming, Z. Kang, ZnO/carbon quantum dots nanocomposites: one-step fabrication and superior photocatalytic ability for toxic gas degradation under visible light at room temperature, New J. Chem. 36 (2012) 1031. doi:10.1039/c2nj20959d.

[209] H. Zhang, H. Huang, H. Ming, H. Li, L. Zhang, Y. Liu, Z. Kang, Carbon quantum dots/Ag3PO4 complex photocatalysts with enhanced photocatalytic activity and stability under visible light, J. Mater. Chem. 22 (2012) 10501. doi:10.1039/c2jm30703k.

[210] J. Shen, Y. Zhu, C. Chen, X. Yang, C. Li, Facile preparation and upconversion luminescence of graphene quantum dots, Chem. Commun. 47 (2011) 2580–2582. doi:10.1039/C0CC04812G.

[211] B.Y. Yu, S.-Y. Kwak, Carbon quantum dots embedded with mesoporous hematite nanospheres as efficient visible light-active photocatalysts, J. Mater. Chem. 22 (2012) 8345. doi:10.1039/c2jm16931b.

[212] Y. Li, B.P. Zhang, J.X. Zhao, Z.H. Ge, X.K. Zhao, L. Zou, ZnO/carbon quantum dots heterostructure with enhanced photocatalytic properties, Appl. Surf. Sci. 279 (2013) 367–373. doi:10.1016/j.apsusc.2013.04.114.

[213] H. Sun, L. Wu, W. Wei, X. Qu, Recent advances in graphene quantum dots for sensing, Mater. Today. 16 (2013) 433–442. doi:10.1016/j.mattod.2013.10.020.

[214] S. Zhuo, M. Shao, S.-T. Lee, Upconversion and dowconversion fluorescent graphene quantum dots: ultrasonic preparation and photocatalysis, ACS Nano. (2012) 1059–1064.

[215] W. Wang, J.C. Yu, Z. Shen, D.K. Chan, T. Gu, g-C3N4 quantum dots: direct synthesis, upconversion properties and photocatalytic application, Chem Commun. 50 (2014) 10148–10150. doi:10.1039/c4cc02543a.

Chapter III

Facile Synthesis of $NaNbO_3/Bi_2WO_6$ Heterostructure with Enhanced Visible-Light-Driven Photocatalytic Performance towards RhB Degradation and A New Insight into Photocatalytic Mechanism of Bi_2WO_6-based Type-II Heterostructures

Abstract

In this study, a series novel $NaNbO_3/Bi_2WO_6$ heterojunction composites with a type-II alignment were fabricated *via* a facile wet impregnation method. The as-prepared photocatalysts were characterized by powder X-ray diffraction (XRD), scanning electron microscopy (SEM), high-resolution transmission electron microscopy (HRTEM), X-ray photoelectron spectroscopy (XPS), diffuse reflectance UV-Vis spectroscopy (DRS), photocurrent (PC) and electrochemical impedance spectroscopy (EIS) analyses. The 30 wt% $NaNbO_3/Bi_2WO_6$ composite exhibited the best performance in the case of degrading rhodamine B (RhB) aqueous solution under visible light

irradiation (λ > 410 nm), which was ~2.5 times and ~40 times that of pure Bi_2WO_6 and $NaNbO_3$, respectively. The improved photocatalytic performance may be attributed to the enhanced electron-hole separation efficiency in Bi_2WO_6 with the assistance of $NaNbO_3$, as well as the dye-sensitization effect of RhB dye itself. Intermediates produced during the reaction and RhB degradation pathway were investigated as well. Radical quenching experiments revealed h^+ played the predominant role; $O_2^{\bullet-}$ functioned as well to some degree. Based on experimental results, the potential functioning mechanism was proposed, which is different from previously reported type-II heterostructure systems when Bi_2WO_6 works as the electron reservoir and $O_2^{\bullet-}$ is one of the dominant active species. The as-prepared photocatalyst composite exhibited excellent stability after repetitively running five times. Effects of several operating parameters on the catalyst performance including initial RhB concentration, catalyst dosage, reaction temperature and initial pH were also discussed. This study provides solid evidence for $NaNbO_3$ to be a promising candidate for photocatalysis and gives out a novel photocatalytic mechanism of Bi_2WO_6-based type-II heterostructures.

Highlights

- Prepared novel $NaNbO_3/Bi_2WO_6$ type-II heterostructures via a facile wet impregnation method.
- The 30wt% $NaNbO_3$ composite exhibited the best performance for RhB photocatalytic degradation.
- Pointed out the hydrothermal infeasibility of previously reported mechanism of Bi_2WO_6-based type-II heterostructures.
- Proposed a novel mechanism interpreting the enhanced photocatalytic performance.
- Investigated several functioning factors influencing photocatalytic activity.

Keywords:

Photocatalysis; $NaNbO_3/Bi_2WO_6$ heterostructure; photocatalytic mechanism.

3.1 Introduction

Water contamination, as a significant part in environmental crisis, is threatening not only the development of industries, but all kinds of life activities on Earth. Organic pollutants, especially chromatic dyes, have been widely applied in industries such as food, textile, cosmetics, dyeing and leather [1]. Rhodamine B is one of the most commonly used water-soluble xanthene dyes and is well-known for its toxicity, good stability and non-biodegradability [2,3]. Conventional strategies removing RhB from water are generally based on physical adsorption without chemical decomposition or degradation.

Recently, advanced oxidation processes (AOPs), utilizing powerful oxidizing agents generated *in situ* for water decontamination, has drawn a lot of attention [3–7]. As a member of AOPs, semiconductor-based heterogeneous photocatalysis harnesses inexhaustible solar light as the source of energy in the presence of solid semiconductors, and thus is considered as environmentally benign.

Perovskite sodium niobate ($NaNbO_3$) has emerged as a wide-bandgap semiconductor due to its physical and chemical stability, high crystallinity, low-environmental impact, and low-cost [8]. Its photocatalytic performance has been proven in water splitting [9], water decontamination [10], and CO_2 reduction [11] under UV irradiation. Although $NaNbO_3$ does not respond to visible light due to its wide bandgap, it may work as the electron/hole separation center when coupled with a narrow-bandgap-semiconductor, such as Ag_2S [12], BiOI [13], and Cu_2O [14]. Bismuth tungstate (Bi_2WO_6), the simplest Aurivillius oxide with the general formula of $Bi_2A_{n-1}B_nO_{3n+3}$ ($A = Ca, Sr, Ba, Pb, Bi, Na$ and K, $B = Ti, Nb, Ta, Mo, W$ and Fe) that exhibits a layered structure constituted by alternating $[WO_4]^{2-}$ and $[Bi_2O_2]^{2+}$ sheets with shared corner-oxygen atoms, has been a promising candidate for photocatalyst in the recent decades [15,16]. Its conduction band consists of W 5d orbitals and its valence band is composed of hybridized O 2p and Bi 6s orbitals, which make Bi_2WO_6 possesses a narrow bandgap of ca. 2.7 eV, and thus a visible-light responsivity [17]. However, rapid recombination between photogenerated electrons and holes limits its further use. Therefore, strategies fabricating type-II heterojunction composites of Bi_2WO_6 with other semiconductors such as $SrTiO_3$ [18], Ag_2O [19], BiOI [20], MoS_2 [17], Ag_3VO_4 [21], g–C_3N_4 [22], *etc.*, taking advantage of the facilitated charge carrier transfer at the

interface, have been made to realize effective electron/hole separation. Yet, although numerous photocatalytic systems performed on bare Bi_2WO_6 or Bi_2WO_6-based type-II heterojunction composites have been reported, their mechanisms when Bi_2WO_6 worked as the electron reservoir and $O_2^{\bullet-}$ functioned as one of major active species were explained as that $O_2^{\bullet-}$ generated from the reduction of O_2 by electrons on the Bi_2WO_6 CB [23–32] . However, the less negative reduction potential of the Bi_2WO_6 CB compared to that of the $O_2/O_2^{\bullet-}$ makes this process thermodynamically impossible. This work provides a more thermodynamically favorable and exhaustive explanation on the mechanism for this kind of systems with the assistance of dye-sensitization.

Herein, a series of $NaNbO_3/Bi_2WO_6$ heterojunction composites with a type-II alignment were successfully fabricated for the first time *via* a facile wet-impregnation method. The physical, chemical, and electrochemical properties of the samples were characterized by multiple techniques. The photocatalytic activities were estimated in the case of RhB degradation under visible light irradiation ($\lambda > 410$ nm), followed by intermediates produced during the reaction and possible degradation pathway identified and speculated. The reusability and stability were also verified. The thermodynamic impossibility of preciously reported photocatalytic mechanism of type-II heterostructures when Bi_2WO_6 works as the electron reservoir and $O_2^{\bullet-}$ is one of the dominant reactive species is pointed out. A more plausible mechanism was proposed and discussed in detail to interpret the enhanced photocatalytic performance in the above-mentioned systems. Finally, operating parameters that may have influence on the photocatalytic performance were investigated as well.

3.2 Experimental

3.2.1 Materials

Bismuth nitrate pentahydrate ($Bi(NO_3)_2 \bullet 5H_2O$), sodium tungstate dihydrate ($Na_2WO_4 \bullet 2H_2O$), acetic acid (CH_3COOH), anhydrous ethanol (C_2H_5OH), rhodamine B (RhB), and nitric acid (HNO_3) were purchased from Fisher Scientific. Sodium hydroxide ($NaOH$), niobium oxide (Nb_2O_5), ammonium oxalate (AO), p-benzoquinone (BQ), tert-Butyl alcohol (TBA), and Sodium sulfate

(Na_2SO_4) were provided by Sigma-Aldrich. All chemicals were of analytical purity and used as received without further purification. Deionized water (DDW) was obtained by using a Milli-Q water purification system by Millipore and was used throughout the entire experiment.

3.2.2 Preparation of Photocatalysts

Hydrothermal Synthesis of $NaNbO_3$ Microcubes. At first, 14g NaOH tablets were dissolved in 30 ml DDW in a 100 ml beaker. After stirring for 30 min, 2g Nb_2O_5 was dispersed in the above concentrated NaOH solution. After magnetically stirring for 2h, the precursor was poured into a 45 ml Teflon-lined stainless-steel autoclave and heated to 200 ^{0}C. After reacting for 12 h, the autoclave was taken out of the oven and cooled down naturally to room temperature. The white precipitates were filtered and washed with DDW and ethanol for 3 times, respectively, and then dried at 60 ^{0}C overnight.

Hydrothermal Synthesis of Bi_2WO_6 Microflowers. At first, 33 mL of acetic acid was mixed with 100 ml DDW in a 250 ml Erlenmeyer flask. After stirring for 10 min, 4.37g of $Bi(NO_3)_2 \bullet 5H_2O$ was dissolved in the above mixture and stirred for 30 min (Solution A). At the same time, 1.56 g $Na_2WO_4 \bullet 2H_2O$ was dissolved in 67 ml DDW in a 150 ml beaker and stirred for 30 min (Solution B). Then, Solution B was dropwisely added into Solution A slowly. After magnetically stirring for another 1h, the precursor was separated into two 125 ml Teflon-lined autoclaves and heated up to 180 ^{0}C. After reacting for 12h, the autoclaves were taken out of the oven and cooled down naturally to room temperature. The pale-yellow precipitates were filtered and washed with DDW and ethanol for 3 times, respectively, and then dried at 60 ^{0}C overnight.

Facile Preparation of $NaNbO_3/Bi_2WO_6$ heterojunction composites. The $NaNbO_3/Bi_2WO_6$ heterojunction composites with different $NaNbO_3$ contents were fabricated via a facile wet-impregnation method. Specifically, 20 mL EtOH was mixed with 10 mL of DDW in a 50 ml beaker. After magnetically stirring for 10 min, a specific amount of as-prepared $NaNbO_3$ powders were added and ultrasonically treated in ice bath for 8h. After that, a designate amount of as-prepared Bi_2WO_6 particles were dispersed into the above solution. After continuously stirring with naturally evaporating for 12 h, the slurry was heated up to 60 ^{0}C under magnetic stirring until evaporation finished. The total weight of $NaNbO_3$ and Bi_2WO_6 remained as 0.5g. Composites

with $NaNbO_3$ content of 10, 20, 30, 40 and 50 wt% were prepared, and expressed as xwt% NBO (x represents the weight percentage of $NaNbO_3$). The 0wt% NBO sample was prepared without the addition of Bi_2WO_6.

3.2.3 Characterization

X-ray diffraction (XRD) analysis was realized using a Rigaku Ultima IV Diffractometer with a Cu K(α) source (λ=0.15418 nm) operating at 40 kV and 44 mA. Morphologies of the as-prepared samples were investigated using a scanning electron microscope (SEM, JEOL JSM-7500F) technique accelerated at 2.0 kV and equipped with an energy dispersive X-ray spectroscope (EDS), and a high-resolution transmission electron microscopy (HR-TEM) technique. X-ray photoelectron spectroscopy (XPS) was carried out on a Kratos Analytical Axis Ultra DLD instrument operating at 140 W with mono-chromated Al X-rays, and the peaks were deconvoluted and analyzed *via* XPSPEAKK4.1 software. The Ultraviolet-visible (UV-vis) diffuse reflectance spectra (DRS) of the prepared catalyst samples were recorded on a Thermo Evolution 300 UV/Vis spectrophotometer equipped with a Praying Mantis diffuse reflectance accessory, and the spectra were scanned in the range of 200-700nm at a scan rate of 240 nm min^{-1}.

3.2.4 Photocatalytic Experiment

3.2.4.1 Photoreactor

Photocatalytic performance was quantified by the degradation of RhB aqueous solution as a model organic pollutant under visible light irradiation. The entire reaction system was kept in a constructed reflective housing to prevent irradiation exchange with the outside. The reactor was composed of a 250-ml beaker (Pyrex), a magnetic stirrer, and an external water-bath jacket to keep a constant operating temperature. Illumination was provided by a 300-W halogen tungsten projector lamp (Ushio, USA) with the main wavelength located in the range of 310-800 nm. The intensity was measured to be ~4.7×10^{-3} Einstein m^{-2} s^{-2} using a quantum meter (Biospherical QSL-2100; 400 nm < λ < 700 nm). A cut-off filter (Kenko Zeta, transmittance > 90%) was used to filter out the irradiation with a wavelength below 410 nm. The distance between the filter and the beaker was fixed at 10 cm, and the stirring rate was set up to 300 rpm.

3.2.4.2 RhB Photocatalytic Degradation

For the photocatalysis tests, a specific amount of the as-prepared catalyst was dispersed into 100 ml of RhB aqueous solution with a designated concentration kept at a constant temperature. The reaction suspension was allowed to equilibrate in the dark under magnetic stirring for 30 min in order to reach the adsorption-desorption equilibrium prior to each experiment. After light was turned on, 1 ml of samples were drawn periodically and centrifuged at 13,800 rpm in an accuSpin Micro 17 (Fisher Scientific) for 5 min to remove the suspended catalyst particles. The supernatant was then analyzed using a Biochrom Ultraspec 60 UV/Vis spectrophotometer with the wavelength fixed at 554 nm, which is the characteristic peak of RhB. A calibration curve was used to determine the RhB concentration from absorbance (Figure S1), which follows the Beer-Lambert law.

The photocatalytic degradation efficiency was calculated by the following equation:

$$E\% = \frac{C_0 - C}{C_0}$$

where $E\%$ is the degradation efficiency, C_0 is the initial concentration of RhB (ppm) at the beginning of photocatalytic process after an adsorption-desorption equilibrium is reached in the absence of irradiation, and C is the concentration of RhB (ppm) at anytime (min) during the degradation process.

Total organic carbon (TOC) removal measurement was realized on an Apollo 9000 TOC analyzer equipped with a Non-Dispersive Infra-Red (NDIR) detector. TOC removal efficiency was calculated by the above equation as well, where C represents TOC concentration in the reaction system.

3.2.5 Electrochemical Measurement

Electrochemical properties of the samples were measured on a three-electrode CHI 604E electrochemical analyzer with the electrolyte of 0.5M Na_2SO_4 solution. The working electrode was an indium tin oxide conductive glass (ITO, 75 X 25 X 1.1 mm, 15-25 Ω) with the as-prepared catalyst particles deposited on it. A platinum wire was used as the counter electrode, and a calomel

reference electrode was applied as well. The source of irradiation was the same as that in photocatalytic experiment, as well as the filter.

3.3 Results and Discussion

3.3.1 Characterization

3.3.1.1 Crystal Structure

The phase composition and crystal structure of the as-prepared samples were confirmed by XRD analysis, as shown in Figure 23. The strong and sharp diffraction peaks indicate high crystallinity of the prepared samples. The typical diffraction peaks of both pristine $NaNbO_3$ and Bi_2WO_6 exhibited orthorhombic phases, which could be indexed to JCPDS No. 01-079-7432 [33] and JCPDS No. 01-073-1126 [34], respectively. Peaks attributed to $NaNbO_3$ and Bi_2WO_6 were both found in the composite spectra without new peaks appeared, and as the $NaNbO_3$ content increased, the intensity of peaks corresponding to $NaNbO_3$ became stronger while those identified as Bi_2WO_6 were weakened, which validated the coexistence of the two components in the composites as well as the negligible impurity production during preparation. Additionally, no significant shift of 2θ was observed in the spectra of the composites, suggesting that the lattice structure of the two components retained after coupling.

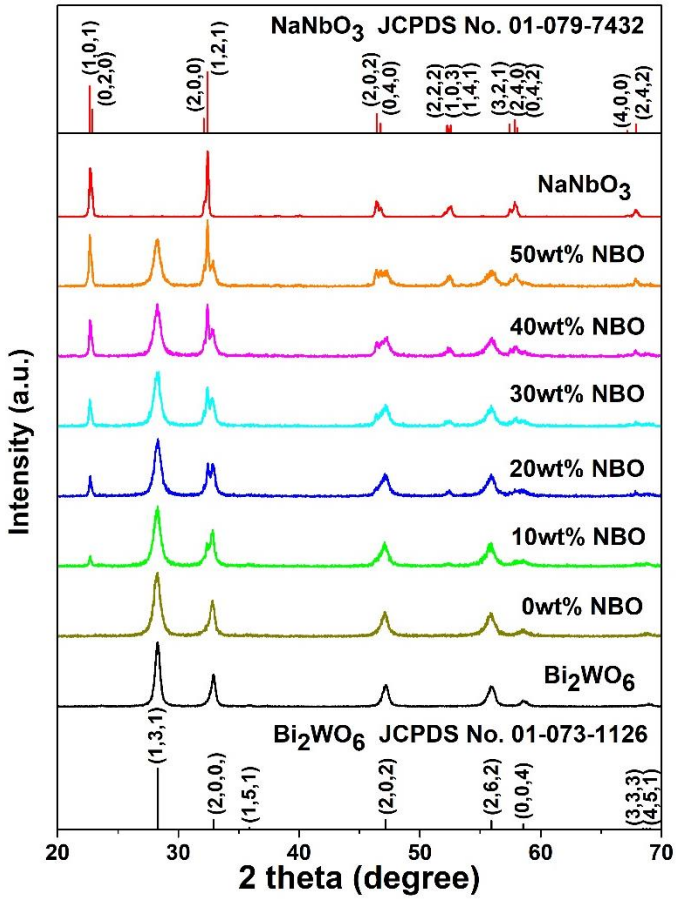

Figure 23 XRD patterns of pristine Bi_2WO_6, pristine $NaNbO_3$, and NBO composites with different $NaNbO_3$ contents.

3.3.1.2 Morphology and Composition

The micromorphology and microstructure of the as-prepared samples were investigated by SEM technique, as displayed in Figure 24. Figure A-2a shows that the as-prepared $NaNbO_3$ particles agglomerated severely and became much smaller after being ultrasonically treated (Figure A-2b). Figure 24(a) exhibits the typical structure of ultrasonicated $NaNbO_3$, which was a microcube with the side length of ca. 2 μm. As can be seen from Figure 24(b), the as-prepared pristine Bi_2WO_6 exhibited a hierarchical flower-like microstructure composed of intercrossed nanoflakes, with the diameter of 3-4 μm. As clearly presented in Figure 24(c), the original morphologies of $NaNbO_3$ and Bi_2WO_6 remained after combination. The tight interaction and intimate interface between $NaNbO_3$ microcubes and Bi_2WO_6 microflowers were obvious. The tiny fragments might be parts of the $NaNbO_3$ and Bi_2WO_6 particles caused by long-time ultrasonication or magnetic stirring during preparation. EDS spectrum Figure 24(d) was provided to verify the element composition at

the $NaNbO_3/Bi_2WO_6$ interface in the composites. Results demonstrate that the composite is composed of Na, Nb, Bi, W and O elements, and the C peak came from the graphite background. To further confirm the interaction between $NaNbO_3$ and Bi_2WO_6, TEM analysis was carried out. Figure A-3 verifies the nanoflake structure consisting of Bi_2WO_6 microflowers. HRTEM image of the 30wt% NBO composite in Figure 25 displays a clear fringe spacing of 0.389 nm and 0.273 nm, which corresponded to the (1 0 1) and (2 0 0) lattice plane of $NaNbO_3$ (JCPDS No. 01-079-7432) and Bi_2WO_6 (JCPDS No. 01-073-1126), respectively [35,36]. SEM, HRTEM, and EDS analyses proves the successful and tight combination of $NaNbO_3$ and Bi_2WO_6, which may favor the electron/hole transfer at the interface.

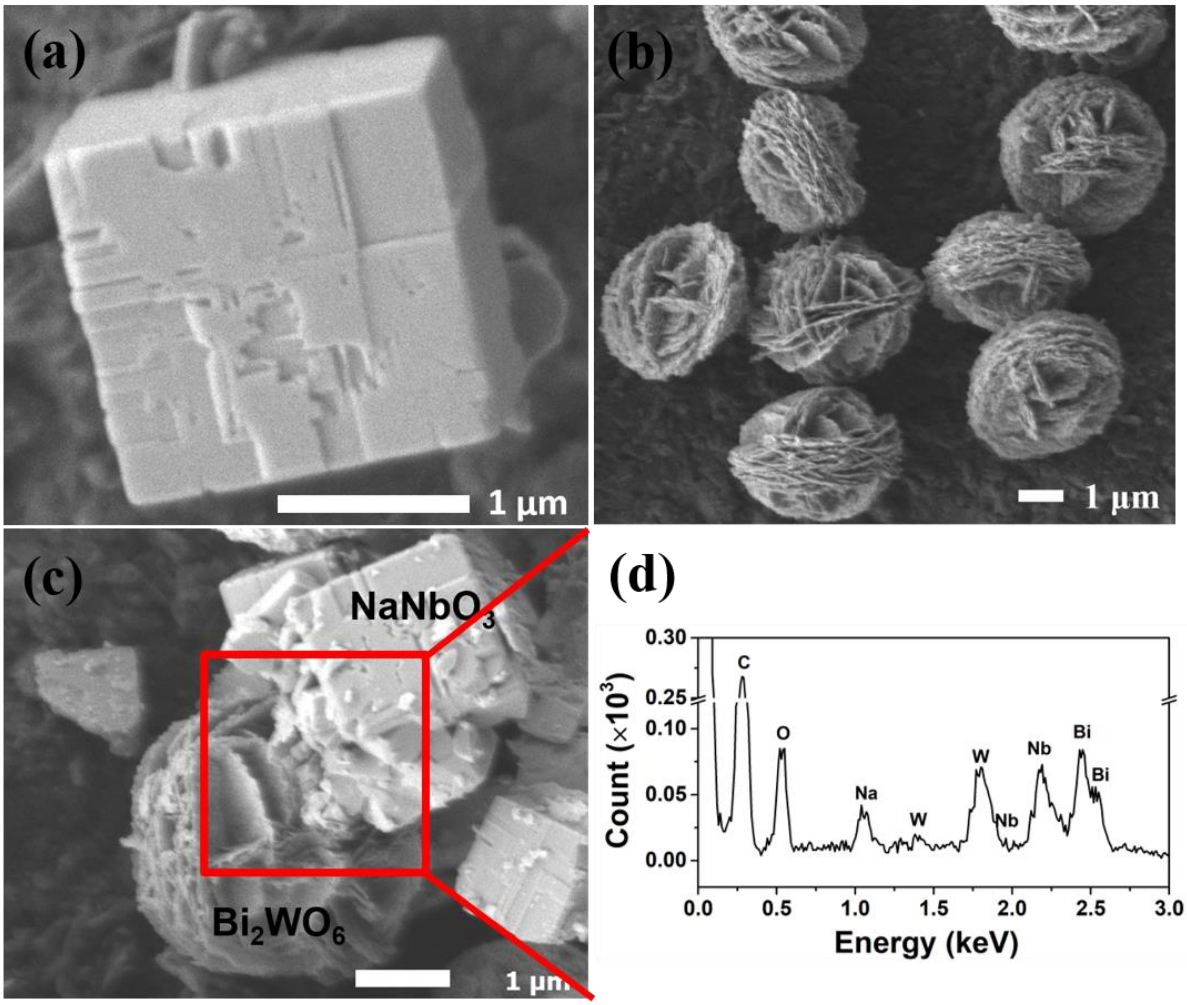

Figure 24 (a) SEM images of pristine $NaNbO_3$ microcube, (b) pristine Bi_2WO_6 microflowers, (c) and 30wt% NBO composite, and (d) the corresponding EDS spectra.

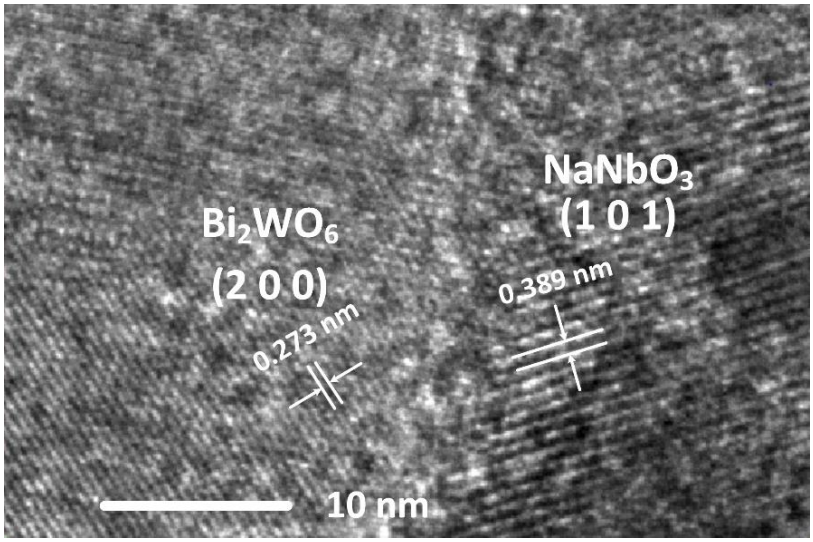

Figure 25 HRTEM image of the 30wt% NBO composite.

C 1s peak at 284.6 eV. In the XPS survey spectra of the 30wt% NBO composite (Figure 26(a)), signals assigned to Na, Nb, Bi, W, and O was detected, indicating the purity of the sample, which is in accordance with XRD and EDS results. High-resolution spectra of each element in the composite had lower intensities compared to those of the pristine semiconductors (Figure 26(b)-(f)), which was attributed to the decreased surface concentration, implying the coexistence of $NaNbO_3$ and Bi_2WO_6 in the composite. For 30wt% NBO, the single peak located at 1071.10 eV was assigned to Na 1s (Figure 26(b)), which agrees well with the previous report [37]. In Figure 26(c), the spectrum of Nb 3d in the composite was deconvoluted into two peaks at 209.55 eV and 206.80 eV, which are identified as Nb $3d_{3/2}$ and Nb $3d_{5/2}$, respectively, revealing the Nb^{5+} oxidation state [38]. The peaks of Bi 4f Figure 26(d)) in the composite appeared at 164.45 eV and 159.20 eV, corresponding to Bi $4f_{5/2}$ and Bi $4f_{7/2}$, respectively, which was assigned to Bi^{3+} [39]. The two peaks at 37.35 eV and 35.20 eV ascribed to the W $4f_{5/2}$ and W $4f_{7/2}$ orbitals demonstrated W element was at its oxidation state of +6 (Figure 26(e)) [40]. As for the O 1s spectrum, the three main peaks located at 529.44 eV, 530.50 eV, and 533.89 eV in $NaNbO_3$ originated from $Nb-O$, $C-O$, and surface adsorbed H_2O, respectively (Figure 26(f)) [32,41]. Those for Bi_2WO_6, appear at 529.80 eV, 530.67 eV, and 532.11 eV were indexed to $Bi-O$, $W-O$, and surface adsorbed O_2, respectively [42]. O 1s spectrum of the composite could be separated into three parts. The peak at 529.68 eV might result from $Nb-O$ and $Bi-O$, which were too close to be convoluted. Similarly, the peak located at 530.62 eV between $C-O$ and $W-O$ might

come from the combination of these two peaks. The weak one at 532.11 eV was associated with surface adsorbed O_2. Additionally, the slightly positive shift of Na 1s and Nb 3d peaks and the negatively budged Bi 4f and W 4f peaks in 30wt% NBO compared to those of the pristine $NaNbO_3$ and Bi_2WO_6, respectively, as well as the combined O 1s peaks, suggest that the composite was a heterojunction containing two components, $NaNbO_3$ and Bi_2WO_6, with a strong electronic interaction between them, instead of a physical mixture.

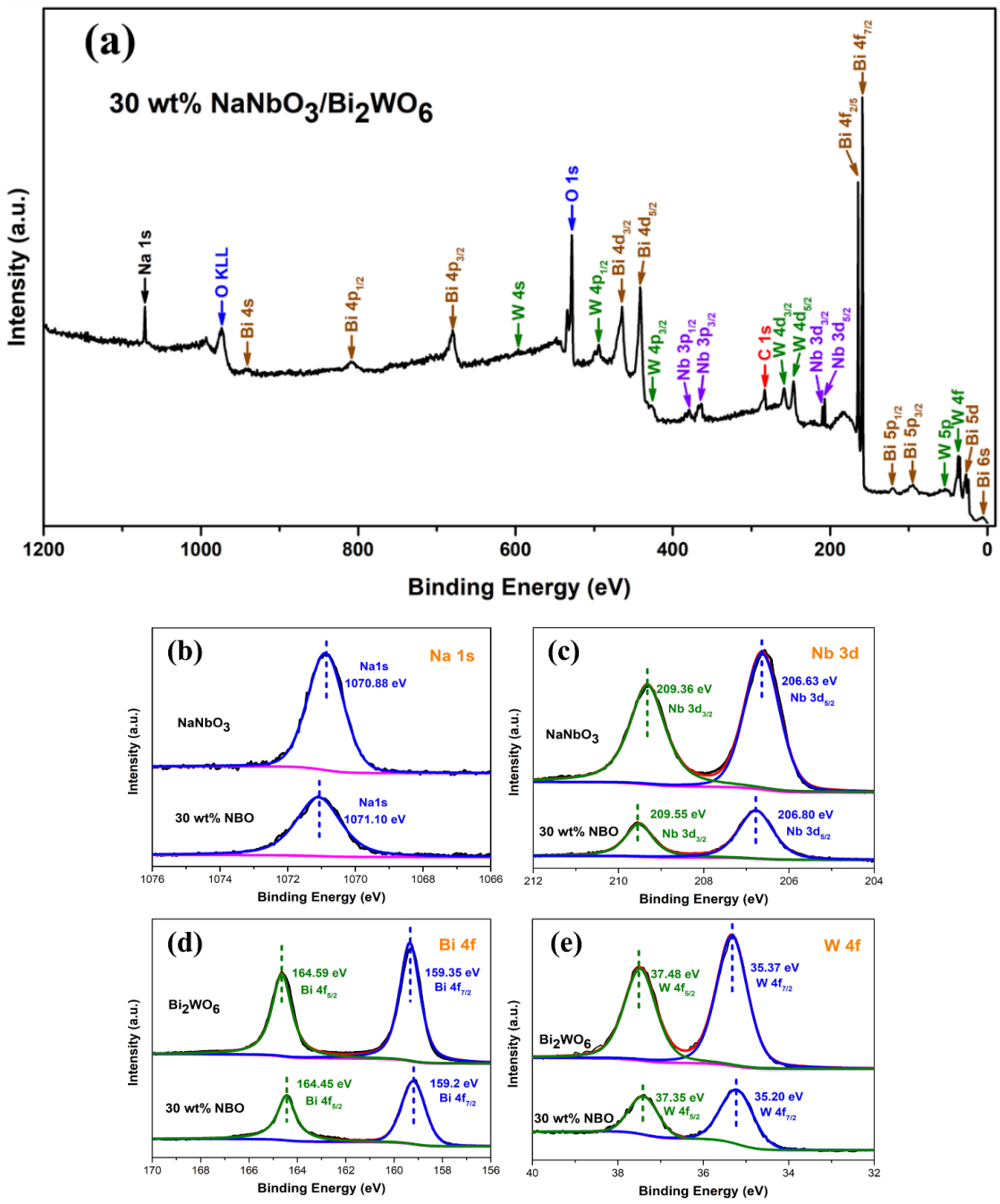

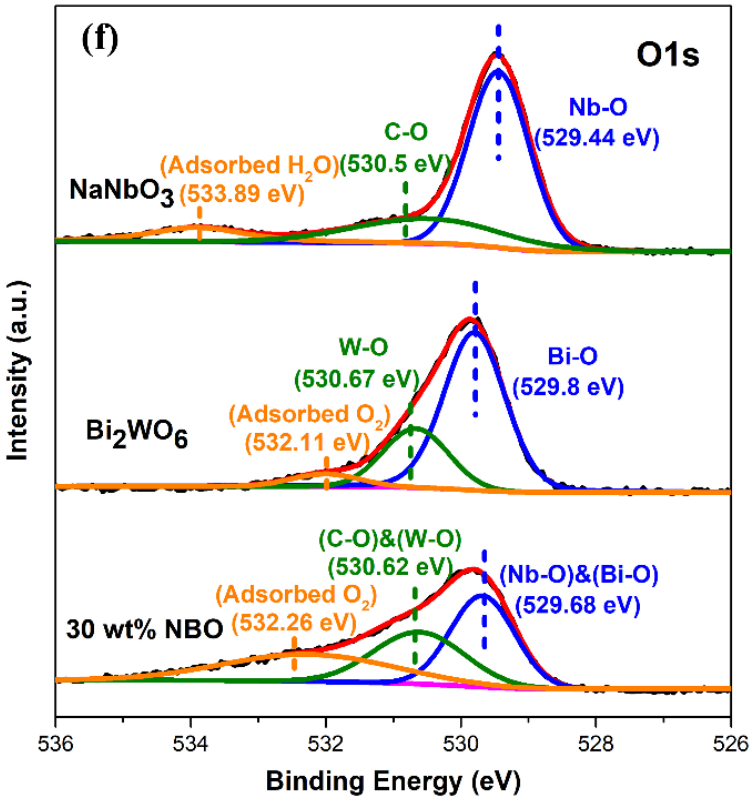

Figure 26 XPS (a) survey spectrum of 30wt% NBO; high-resolution spectra of (b) Na 1s, (c) Nb 3d, (d) Bi 4f, (e) W 4f, and (f) O 1s.

3.3.1.3 Optical Absorption Properties

The optical absorption properties of the prepared samples were characterized by UV-Vis diffuse reflectance spectroscopy (DRS) in the range of 200-700 nm as shown in Figure 27. The absorption edge of pure $NaNbO_3$ was ca. 385 nm, which is in the UV range; while the pristine Bi_2WO_6 had absorbance until $\lambda > 460$ nm, which validates its visible-light-responsivity. Absorption spectra of all the composites exhibited a red shift in terms of $NaNbO_3$ and a blue shift compared to Bi_2WO_6, demonstrating the possible interaction between them. The slight difference in spectra of the 0wt% NBO sample and the pristine Bi_2WO_6 might be attributed to the produced Bi_2WO_6 fragments during long-time stirring during preparation, which increased the exposed light-absorption site on Bi_2WO_6 surface. The bandgaps of pure $NaNbO_3$ and pure Bi_2WO_6 can be calculated by the classical Tauc approach:

$$\alpha h\nu = A(h\nu - E_g)^{n/2}$$

where α is the absorption coefficient, h is the Plank constant, ν is the light frequency, A is a constant, E_g is the band gap of the semiconductor, and n is determined by the type of optical transition in a semiconductor (n=1 for direct transition, and for indirect transition n=4) [43]. Bandgaps of $NaNbO_3$ (n=1 [44]) and Bi_2WO_6 (n=4 [45]) were determined to be 3.48 eV and 2.70 eV, respectively (insert of Figure 27).

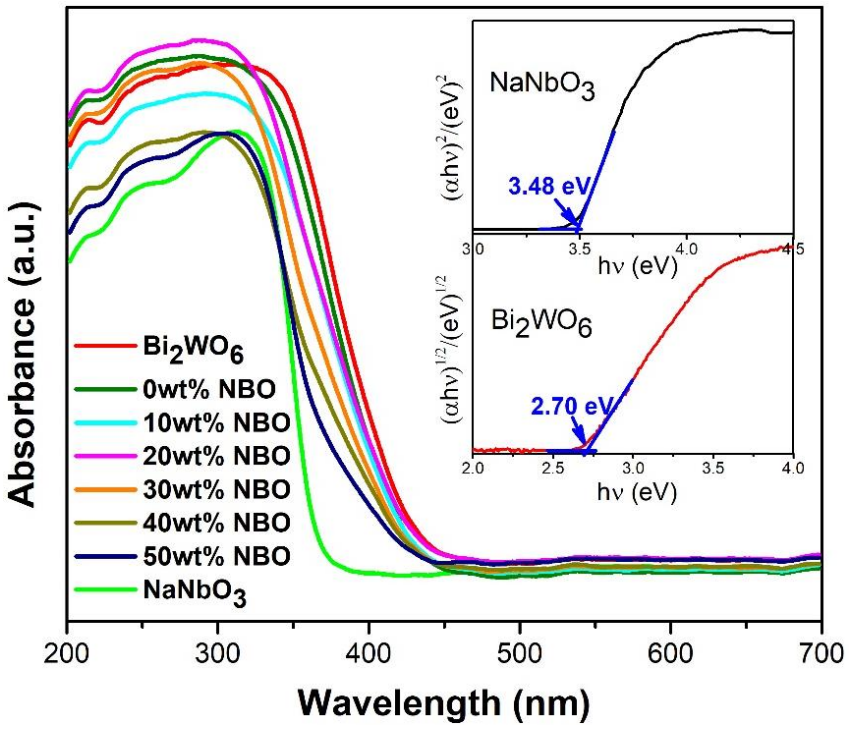

Figure 27 UV-Vis absorption spectra of the prepared samples (insert: bandgap estimation based on Tauc approach).

Energy potential of energy bands in a semiconductor can be estimated according to the following empirical equations:

$$E_{CB} = \chi - E^e - 0.5\, E_g$$

$$E_{VB} = E_g + E_{CB}$$

where E_{CB} and E_{VB} are the edge potential of the conduction and valence band, respectively, χ is the electronegativity of the semiconductor (χ = 5.44 for $NaNbO_3$ [44] and 6.36 for Bi_2WO_6 [46]) and E^e is the energy of free electrons on the hydrogen scale (~4.5 eV vs. NHE) [20]. The calculated values are listed below:

Table 6 Calculated energy band potentials of pure NNO and BWO

Component	E_{CB}/eV	E_{VB}/eV	E_g/eV
$NaNbO_3$	-0.8	2.68	3.48
Bi_2WO_6	0.51	3.21	2.70

3.3.2 Photocatalytic Activity

Photocatalytic activities of the samples were evaluated by the degradation of an RhB aqueous solution under visible light irradiation ($\lambda > 410$ nm). As exhibited in Figure 28(a), the photocatalytic activity was promoted as $NaNbO_3$ content increased from 10 to 30wt% and decreased afterwards. Additionally, before $NaNbO_3$ content reached 50wt%, the performance of all composites was better than that of the bare Bi_2WO_6. This is because $NaNbO_3$ does not respond to visible light while Bi_2WO_6 does; the excessive $NaNbO_3$ particles would cover the light-responsive sites on Bi_2WO_6 surface and thus inhibit light absorption. Photolysis of RhB showed almost no concentration decrease, suggesting the negligible dye-sensitivity of RhB dye itself in the absence of photocatalysts. However, with the addition of $NaNbO_3$, which does not respond to visible light irradiation, ca. 10% of RhB was degraded. This is possibly due to the enhanced dye-sensitization of RhB with the assistance of $NaNbO_3$, which will be discussed in detail in Section 3.4. The activity of 0wt% NBO slightly increased compared to the pristine Bi_2WO_6. This is due to the fact that after long-time stirring during preparation, a few Bi_2WO_6 particles would be broken into fragments that exposes more light-responsive and reactive sites which used to be inside the microflowers, as demonstrated by the SEM (Figure 24(c)) and TEM (Figure 25) images. For the mechanical mixture, 0.03g $NaNbO_3$ and 0.07g Bi_2WO_6 were added to the reaction system simultaneously without prior blending. The slightly improved activity compared to the pure Bi_2WO_6 might be caused by the synergistic effect among photocatalysis carried out by Bi_2WO_6, dye-sensitization of RhB itself, as well as the contact and probably minute amount of produced heterojunction between $NaNbO_3$ and Bi_2WO_6 during stirring in the reaction system. Therefore, the enhanced photocatalytic performance of the composites is mainly attributed to the interaction between $NaNbO_3$ and Bi_2WO_6, which was favorable for electron/hole separation.

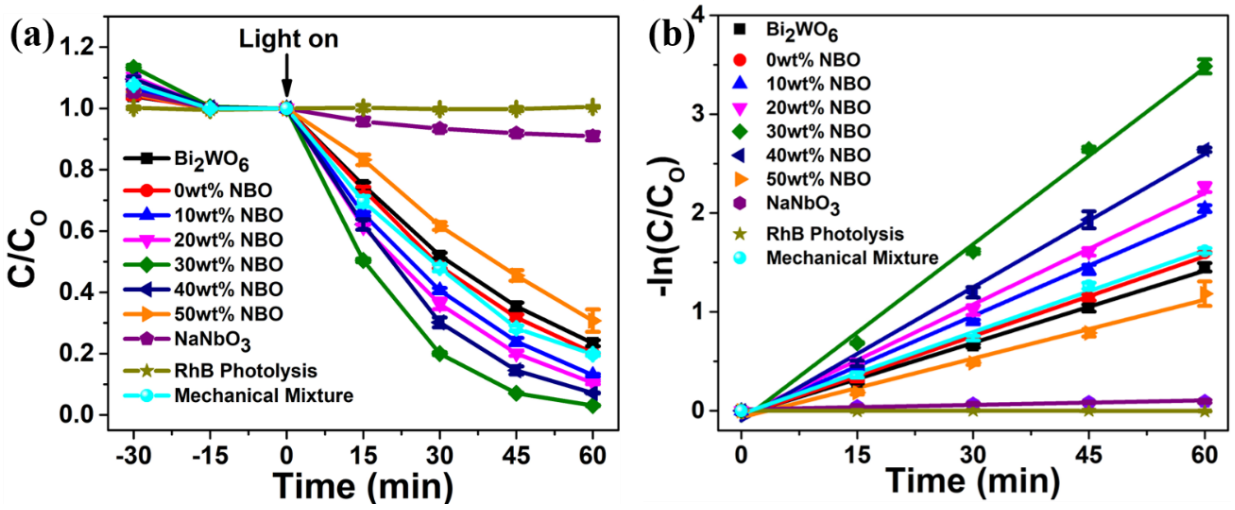

Figure 28 (a) Photocatalytic performance and (b) kinetic linear simulation curves of RhB degradation (10 ppm) in the presence of prepared catalyst samples (1.0 g/L) with different NNO contents under visible light irradiation (λ>410 nm) at 20 ^{0}C.

For the kinetics study of photocatalysis involved with degradation of organic substrates in aqueous solution, the pseudo-first-order model is most commonly used, as expressed by the following equation:

$$-\ln(C/C_0) = K_{app}t$$

where C, C_0, K_{app}, and t represents the RhB concentration at arbitrary time, the initial RhB concentration when photocatalytic degradation begins, the apparent reaction rate constant, and the reaction time, respectively. The apparent reaction rate constant K_{app} can be obtained by linearly fitting $-\ln(C/C_0)$ as a function of t, as shown in Figure 28(b). The fitted values of K_{app} and coefficients of determination are listed in Table 7. The reaction rate constant of 30wt% NBO is ca. 40 and 2.5 times that of the pure $NaNbO_3$ and Bi_2WO_6, respectively. The results substantiate that the formation of heterojunction and the interaction between $NaNbO_3$ and Bi_2WO_6 were responsible for the enhanced photocatalytic performance.

Table 7 Kinetic linear simulation data of RhB degradation (10 ppm) in the presence of prepared catalyst samples (1.0 g/L) with different $NaNbO_3$ contents under visible light irradiation (λ>410 nm) at 20 ^{0}C.

Samplest	K_{app}/min^{-1}	R^2
Bi_2WO_6	0.0244	0.9960
0 wt% NBO	0.0269	0.9957
10 wt% NBO	0.0340	0.9948
20 wt% NBO	0.0376	0.9967
30 wt% NBO	0.0595	0.9960
40 wt% NBO	0.0449	0.9947
50 wt% NBO	0.0198	0.9847
$NaNbO_3$	0.0015	0.9979
RhB Photolysis	-	-
Mechanical Mixture	0.0276	0.9953

3.3.3 RhB Degradation Pathway

To investigate the RhB photocatalytic degradation pathway over 30wt% NBO under visible light, UV-Vis spectra of samples taken at each time interval was performed. As can be seen from Figure 29, the spectra intensity decreased as time prolonged, indicating a reduction in concentration of light-absorbing substances in the solution. The characteristic maximum absorbance peak (λ_{max}) blue-shifted from 554 nm to 499 nm gradually with a broaden area, and then almost unchanged. Considering previously reported RhB degradation pathway [47,48], it can be speculated that RhB suffered from three processes, N-deethylation, chromophore cleavage and mineralization. N-deethylation was responsible for the blue-shifted and broadened absorption area while chromophore cleavage and mineralization were the reasons for the decreased absorbance intensity. At the durst stage of degradation (0-75 min), N-deethylation dominated. RhB ($\lambda_{max} = 554$ nm) was decomposed to rhodamine ($\lambda_{max} = 498$ nm) through N, N, N'-triethyl rhodamine ($\lambda_{max} = 539$ nm), N, N'-diethyl rhodamine ($\lambda_{max} = 522$ nm), and N-ethyl rhodamine ($\lambda_{max} = 510$ nm) step-by-step [31]. The unchanged characteristic peak after 75 min indicated the end of N-deethylation. Chromophore cleavage and the subsequent opening ring and mineralization of rhodamine into CO_2, H_2O, and other simple inorganic molecules dominated afterwards [49–51].

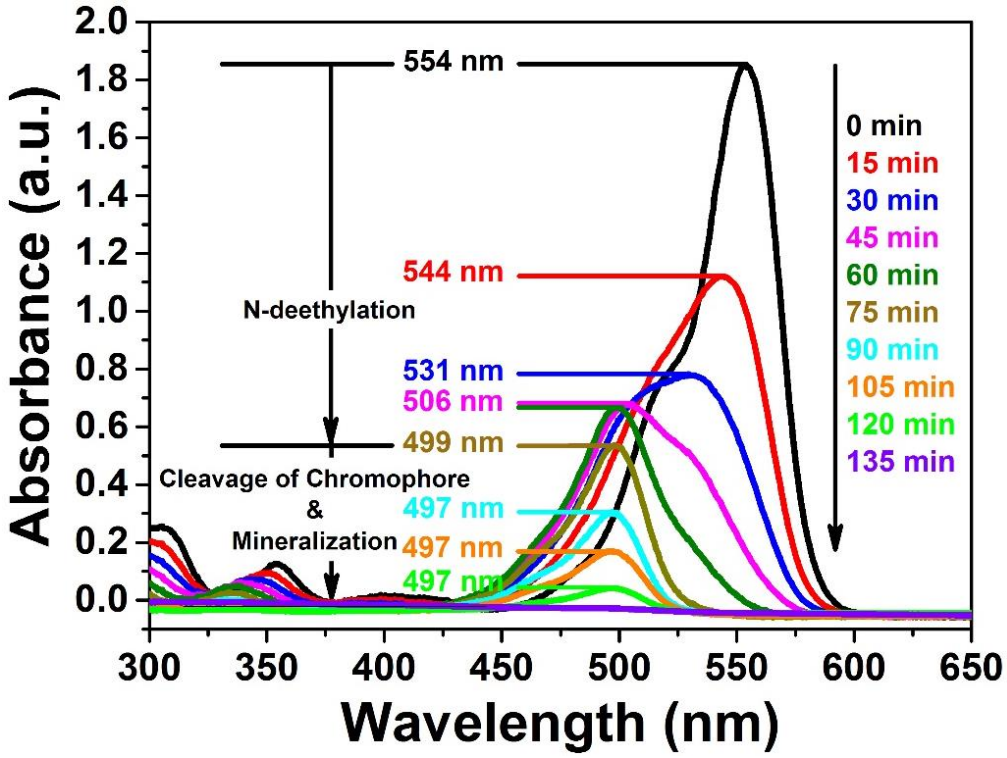

Figure 29 (a) Temporal evolution of UV-Vis absorption spectra and (b) TOC removal efficiency of RhB solution (10 ppm) in the presence of 30wt% NBO composite (1.0 g/L) under visible light irradiation (λ>410 nm) at 20 ^{0}C.

3.3.4 Electrochemical Measurement

In order to compare the electrochemical properties of the pristine Bi_2WO_6 and the 30wt% NBO composite more perspicuously, photocurrent measurements were performed. From Figure 30(a), the photocurrent intensity at steady state produced by 30wt% NBO was ca. 7 times that of Bi_2WO_6, which elucidates the facilitated electron/hole transfer at the $NaNbO_3/Bi_2WO_6$ interface. This conclusion was further proven by EIS Nyquist plot, as exhibited in Figure 30(b). The much smaller radius of 30wt% NBO revealed the improved electron/hole separation efficiency. The equivalent circuit is given in the insert, where R_s, R_{ct}, and CPE represent the electrode resistance, the interfacial charge transfer resistance between the photocatalyst and electrolyte, and the constant phase element for the semiconductor/electrolyte interface, respectively [52,53]. The fitted parameters are summarized in Table 8. The evidently reduced R_{ct} of 30w% NBO, which was ca. 1/10 of that of the pristine Bi_2WO_6, suggests the strongly enhanced interfacial charge transfer.

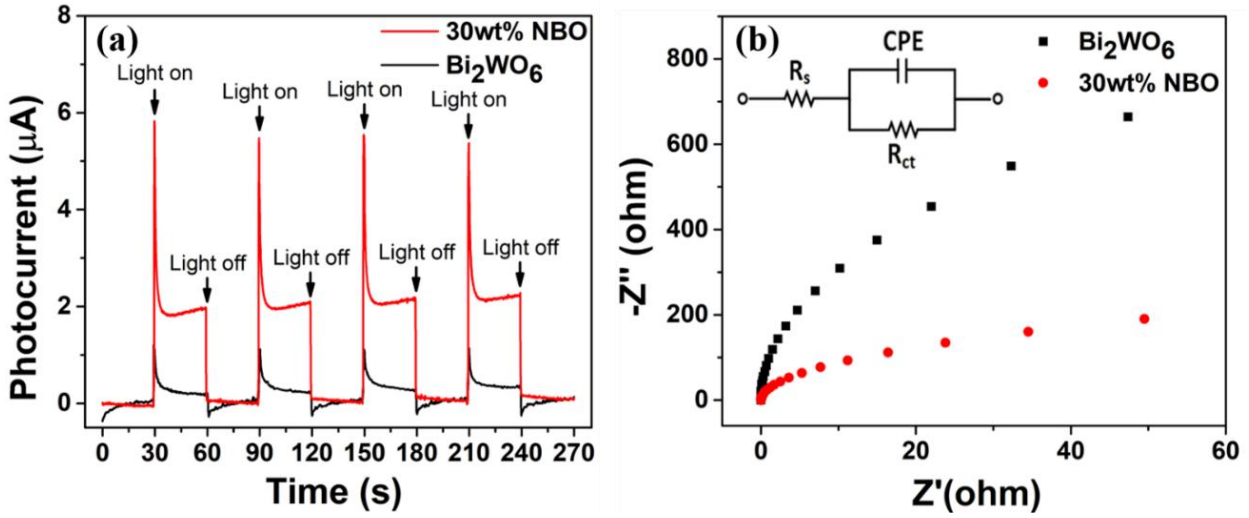

Figure 30 (a) Transient photocurrent response and (b) EIS Nyquist plot of Bi_2WO_6 (black) and 30wt% NBO composite (red) in a solution of 0.5 M Na_2SO_4 under visible light irradiation (λ>410 nm) at 20 ^{0}C.

Table 8 Fitted electrochemical parameters of the prepared pristine Bi_2WO_6 and 30wt% NBO composite

Photocatalyst	**Electrochemical Parameter**		
	R_s (Ω)	**R_{ct} (kΩ)**	**CPE (μF)**
Bi_2WO_6	46.38	9348	196.8
30wt% NBO	45.32	783.6	532.7

3.3.5 Proposed Photocatalytic Mechanism

Since it is the reactive species produced in the reaction system that are responsible for substrate degradation, the predominant reactive species need to be determined in order to investigate the possible mechanism of the improved photocatalytic performance. Quenching experiments were carried out in the presence of 30wt% NBO composite with 1 mM ammonia acetate (AO) as the hole (h^+) scavenger, 1 mM p-benzoquinone (BQ) as the superoxide radical ($O_2^{\bullet-}$) scavenger, and 1 mM tert-Butyl alcohol (TBA) as the hydroxyl radical (• OH) scavenger. Results (Figure 31) reveal that the photocatalytic degradation was greatly suppressed with the addition of AO but negligibly influenced by TBA and the effect of BQ was in between, which indicates h^+ played the major role and $O_2^{\bullet-}$ functioned to some degree as well.

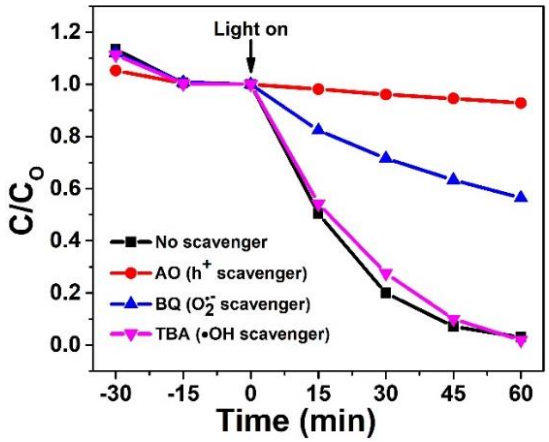

Figure 31 Effect of reactive species scavengers on the photocatalytic degradation of RhB in the presence of the 30wt% NBO composite (1.0 g/L) under visible light irradiation (λ>410 nm) at 20 ^{0}C.

In previous studies, the mechanism of type-II photocatalyst composites in which the CB of Bi_2WO_6 was the most negative among the coupled semiconductors and thus worked as the electron reservoir and $O_2^{\bullet-}$ was one of the dominant reactive species was explained that $O_2^{\bullet-}$ were produced from the reduction of adsorbed O_2 by photogenerated electrons accumulated on Bi_2WO_6 CB. Unfortunately, this is thermodynamically infeasible due to the weaker reduction potential of the Bi_2WO_6 CB (ca. 0.25-0.5 eV) compared to that of the $O_2/O_2^{\bullet-}$ redox pair (-0.33eV).

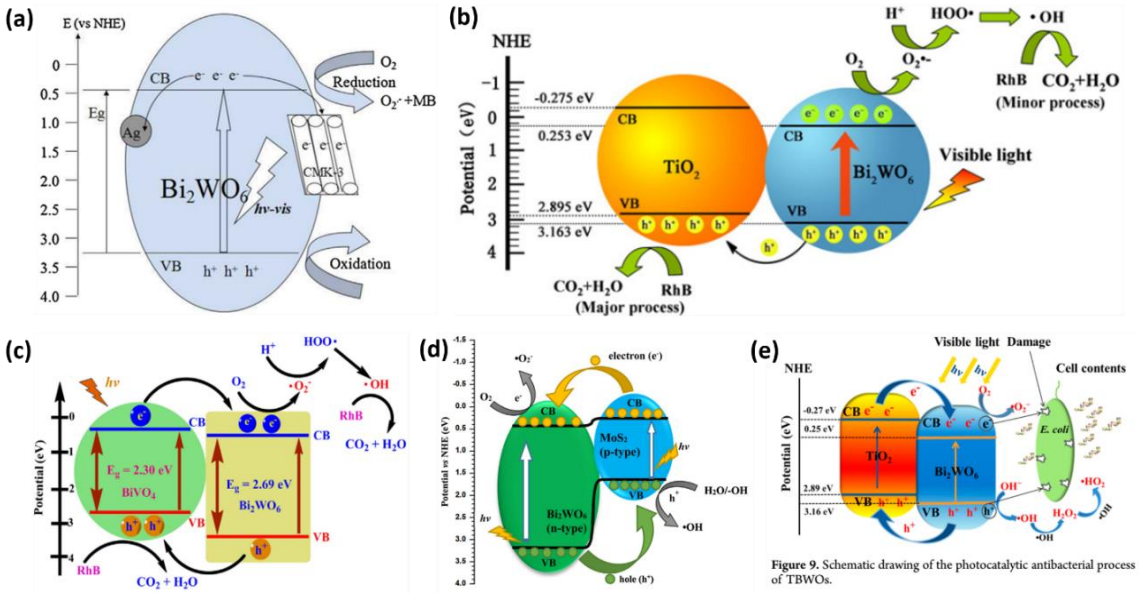

Figure 32 Previously reported Bi_2WO_6-based photocatalyst composites when Bi_2WO_6 worked as the electron reservoir and $O_2^{\bullet-}$ was one of the dominant reactive species. (a) is reprinted from permission from [51]. Copyright (2012) Elsevier. (b) is reprinted from permission from [52]. Copyright (2015) Elsevier. (c) is reprinted from permission

from [23]. Copyright (2013) Elsevier. (d) is reprinted from permission from [31]. Copyright (2017) Elsevier. (e) is reprinted with permission from [32]. Copyright (2016) American Chemical Society.

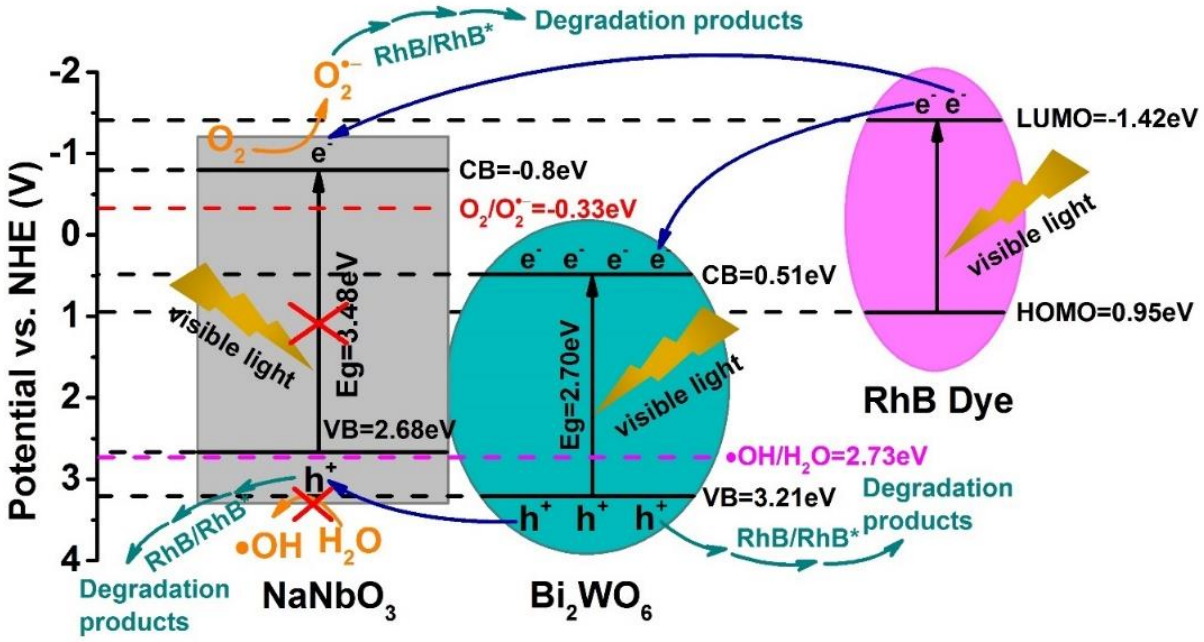

Scheme 1 Proposed mechanism of RhB photocatalytic degradation over NBO composite under visible light irradiation (λ>410 nm).

Based on experiment results as well as redox potential of the energy bands and involved redox pairs, a more thermodynamically favored mechanism was proposed, as shown in Scheme 1. Under visible light irradiation, Bi_2WO_6 was triggered and produced electrons and holes on the conduction and valence band, respectively; while $NaNbO_3$ could not be excited. Due to the more positive VB of Bi_2WO_6 (3.21 eV) compared to that of $NaNbO_3$ (2.68 eV), most of the holes generated on Bi_2WO_6 VB would flow to $NaNbO_3$ and the rest of them would react with the substrate RhB molecules directly. Holes reached $NaNbO_3$ VB could not produce $\bullet OH$ by oxidizing adsorbed H_2O molecules due to its lower oxidation potential compared to that of the $\bullet OH/H_2O$ redoxidation pair (2.73 eV), and therefore would react with the substrates directly as well. On the other hand, RhB molecules could produce a few electrons by absorbing photons from visible light owing to its dye-sensitization effect and transform from the ground state RhB to its excited state RhB*, which was easier to degrade. The produced electrons would flow to the CBs of $NaNbO_3$ and Bi_2WO_6, driven by the difference in reduction potential. Electrons arrive at $NaNbO_3$ CB would react with adsorbed O_2, yielding $O_2^{\bullet-}$ for RhB degradation. This also explains

the weak degradation efficiency of RhB exhibited over the non-excited $NaNbO_3$ under visible light in Figure 28(a). Electrons accumulated on Bi_2WO_6 CB would further migrate to the solution be consumed by positive species in the solution such as H^+ (the natural pH of RhB solution was acidic) and dispersed h^+, or recombine with holes on the Bi_2WO_6 CB, as well as other intermediate cations produced during degradation. As a result, photogenerated electrons and holes would separate and accumulate in Bi_2WO_6 and $NaNbO_3$, respectively. The enhanced photocatalytic activity was realized by the synergistic effect of the enhanced interfacial charge carrier flow at the $NaNbO_3/Bi_2WO_6$ interface and the production of $O_2^{\bullet-}$ carried out by the improved dye-sensitization effect of RhB in the presence of $NaNbO_3$.

3.3.6 Reusability and Stability

To evaluate the reusability and stability of the 30wt% NBO sample, five repetitive runs were carried out in terms of the photocatalytic degradation of RhB under visible light irradiation. The catalytic particles after each run were separated out by centrifugation and used in the next run without further regeneration. From Figure 33(a), no obvious decrease in catalytic activity or efficiency was observed after five runs. The slight change might be attributed to the weight loss during centrifugation separation. Furthermore, the XRD pattern (Figure 33(b)) of the recycled composite had no distinct discrepancy compared to the fresh one, which elucidates the superior reusability and stability of the as-prepared composite.

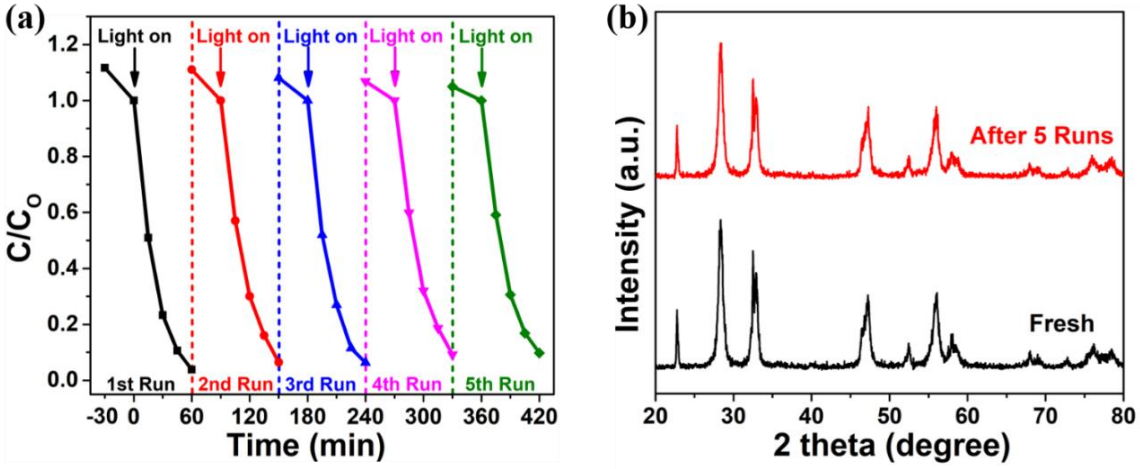

Figure 33 (a) Cycling runs for the photocatalytic degradation of RhB (10 ppm) in the presence of the 30wt% NBO composite (1.0 g/L) under visible light irradiation (λ>410 nm) at 20 ^{0}C; (b) XRD patterns of fresh (black) and five-runs-cycled (red) 30wt% NBO catalyst particles.

3.3.7 Effect of Operating Parameters

To investigate the influence of different operating parameters, the RhB photodegradation was carried out under various reaction environments.

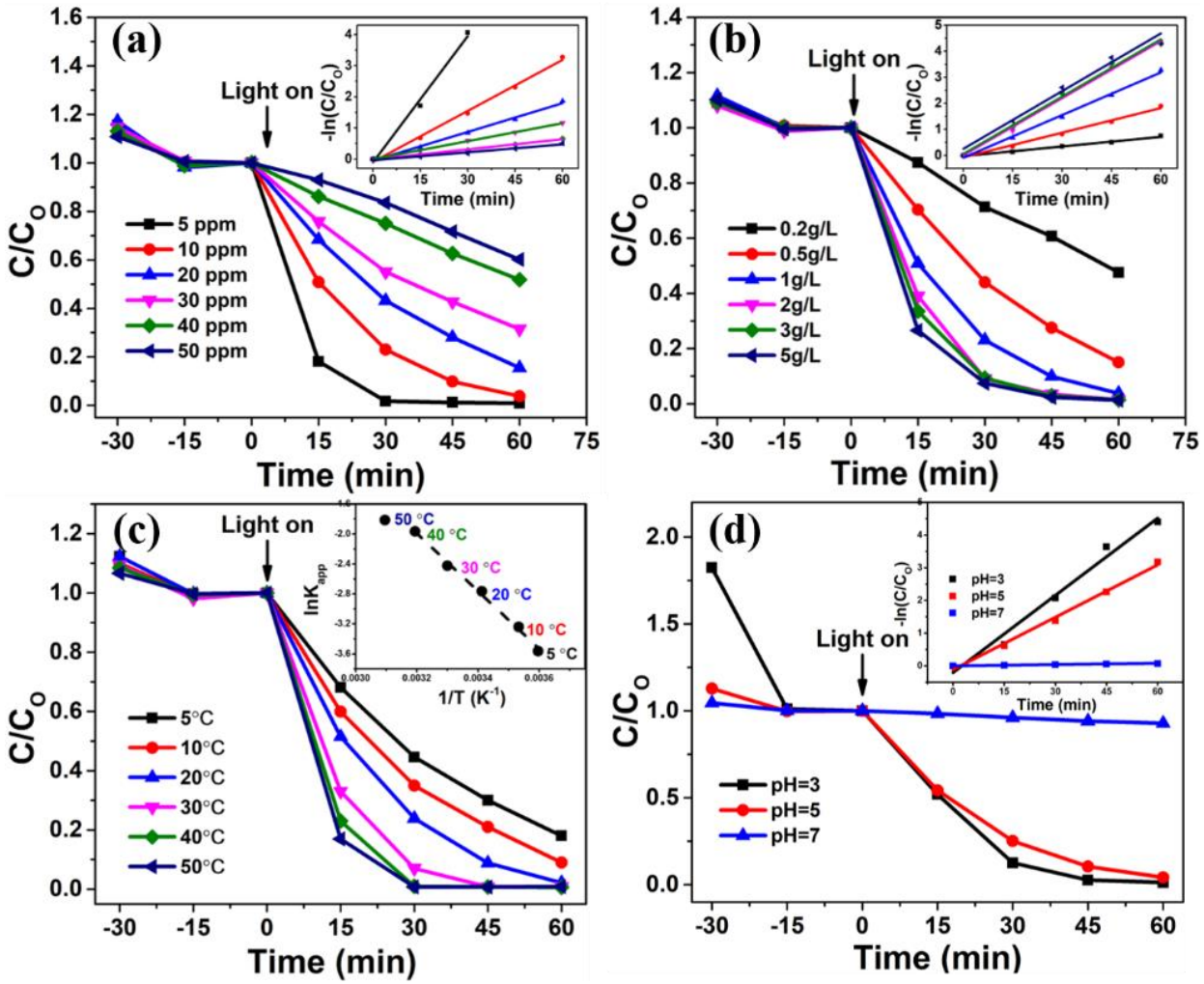

Figure 34 Effect of (a) initial RhB concentration (catalyst dosage: 1.0 g/L, reaction temperature: 20 ^{0}C, natural pH: ca. 5), (b) catalyst dosage (initial RhB concentration: 10 ppm, reaction temperature: 20 ^{0}C, natural pH: ca. 5), (c) reaction temperature (insert: Arrhenius plot) (initial RhB concentration: 10 ppm, catalyst dosage: 1.0 g/L, natural pH: ca. 5), and (d) initial pH (RhB concentration: 10 ppm, catalyst dosage: 1.0 g/L, reaction temperature: 20 ^{0}C) on the photocatalytic degradation of RhB solution in the presence of 30 wt% NBO composite under visible light irradiation (λ>410 nm).

3.3.7.1 Initial RhB Concentration

The influence of initial RhB concentration was performed over the concentration range of 5-50 ppm, and the results are presented in Figure 34(a), where the inset exhibits the change of reaction rate. It can be seen that the degradation activity decreased as the initial RhB concentration increased. This is because at lower RhB concentration, more irradiation-responsive and reactive sites on the catalyst surface were available. The former was responsible for photon absorption and thus the production of electron/hole pairs; while the latter provided space for RhB adsorption and the subsequent degradation process to take place. As the RhB concentration increased, part of these functional sites would be covered by the adsorbed RhB molecules. Additionally, since RhB is a chromatic organic, high concentration would reduce the transmittance of the reaction suspension as well as scatter the irradiation, intercepting photons before they reach the catalyst surface, and thus jeopardize photocatalysis.

3.3.7.2 Catalyst Dosage

Catalyst dosage plays a significant role mainly due to its relationship with the cost. From Figure 34(b), the activity was evidently enhanced when catalyst dosage rose from 0.2 g/L to 2 g/L, and almost remained the same after that. This phenomenon can be explained by the increased irradiation-responsive and active sites as the catalyst dosage rose up at a lower level. However, the excessive catalyst particles would increase the opacity of the suspension system, leading to a shorter penetration pathway of the photon, blocking and scattering them from reaching catalyst surface, and thus inhibit light absorption.

3.3.7.3 Reaction Temperature

The impact of temperature was studied in the range of 5-50 ^{0}C, as shown in Figure 34(c). The linear relation between the reaction rate constant and temperature exhibited in the inset followed Arrhenius equation in the range of 5-40 ^{0}C, which explains the accelerated reaction rate as temperature increases. On the other hand, high temperature may induce to a strong desorption of both the substrates and reactive species onto the catalyst surface and thus is unfavorable to the degradation process, which interprets the slightly retarded reaction rate above 40 ^{0}C.

$$\ln K_{app} = \ln A - \frac{E_a}{R} * \frac{1}{T}$$

where, A is the pre-exponential factor, which is independent with temperature, and E_a is the activation energy, which can be regarded as a constant in a wide temperature range.

3.3.7.4 Initial pH

Since the natural pH of 10 ppm RhB solution is around 4.7, the influence of pH was investigated under three circumstances: pH=3, 5, and 7 (Figure 34(d)). The severely prohibited adsorption with increasing pH might be attributed to the large amount of OH^- in the solution, which would strongly combine with the cationic RhB molecules due to Coulomb forces, inhibiting them from adsorbing onto the catalyst surface and thus subsequent degradation. Moreover, it has been reported that the massive OH^- ions in the reaction system could facilitate the production of •OH carried out by h^+; while for acidic solutions, the degradation of substrates would be realized predominately by h^+ [56]. Considering that h^+ was the predominant reactive species in the presence of 30wt% NBO while •OH barely functioned, as substantiated in the quenching experiment, it interprets the similar degradation efficiencies at pH= 3 and 5, as well as the obviously restrained activity at pH=7.

3.4 Conclusion

In summary, a series of novel $NaNbO_3/Bi_2WO_6$ heterojunction composites with a type-II alignment were successfully fabricated *via* a facile wet impregnation method. The 30wt% NBO sample exhibited the best photocatalytic performance towards RhB degradation under visible light, which was 40 and 2.5 times that of the pristine $NaNbO_3$ and Bi_2WO_6, respectively. Based on the calculated energy band positions and quenching experiment results, the mechanism of the enhanced photocatalytic activity was proposed and discussed in detail. This novel mechanism mainly took advantage of the facilitated electron/hole separation and promoted $O_2^{\bullet-}$ production by dye-sensitization effect of RhB in the presence of $NaNbO_3$. The as-prepared composite also showed excellent photostability after five runs. This study provides evidence for $NaNbO_3$ to be a promising cocatalyst in photocatalysis and proposed a new perspective when Bi_2WO_6 works as

the electron reservoir in type-II photocatalyst heterostructures and $O_2^{\bullet-}$ is one of the dominant reactive species.

3.5 Supplementary Information

See Appendix A.

Acknowledgments

This work was financially supported by the Natural Sciences and Engineering Research Council of Canada (NSERC). The authors would like to acknowledge Dr. Yun Liu and Dr. Alexander Mommers at the Center for Catalysis Research and Innovation (University of Ottawa, CCRI), as well as Mr. Xiangchao Meng for their help with material characterization.

Conflicts of Interest

The authors declare no conflict of interest.

References

[1] J. Anandkumar, B. Mandal, Adsorption of chromium(VI) and Rhodamine B by surface modified tannery waste: Kinetic, mechanistic and thermodynamic studies, J. Hazard. Mater. 186 (2011) 1088–1096. doi:10.1016/j.jhazmat.2010.11.104.

[2] M. Soylak, Y.E. Unsal, E. Yilmaz, M. Tuzen, Determination of rhodamine B in soft drink, waste water and lipstick samples after solid phase extraction, Food Chem. Toxicol. 49 (2011) 1796–1799. doi:10.1016/j.fct.2011.04.030.

[3] L. Ma, G. Wang, C. Jiang, H. Bao, Q. Xu, Synthesis of core-shell TiO2@g-C3N4 hollow microspheres for efficient photocatalytic degradation of rhodamine B under visible light, Appl. Surf. Sci. 430 (2018) 263–272. doi:10.1016/j.apsusc.2017.07.282.

[4] M. Samanta, M. Mukherjee, U.K. Ghorai, S. Sarkar, C. Bose, K.K. Chattopadhyay, Ultrasound assisted catalytic degradation of textile dye under the presence of reduced Graphene Oxide enveloped Copper Phthalocyanine nanotube, Appl. Surf. Sci. 449 (2018) 113–121. doi:10.1016/j.apsusc.2018.01.118.

[5] L. Zhang, X. Yang, E. Han, L. Zhao, J. Lian, Applied Surface Science Reduced graphene oxide wrapped Fe 3 O 4 – Co 3 O 4 yolk – shell nanostructures for advanced catalytic oxidation based on sulfate radicals, Appl. Surf. Sci. 396 (2017) 945–954. doi:10.1016/j.apsusc.2016.11.066.

[6] Y. Wang, J. Wang, B. Du, Y. Wang, Y. Xiong, Y. Yang, X. Zhang, Applied Surface Science Synthesis of hierarchically porous perovskite-carbon aerogel composite catalysts for the rapid degradation of fuchsin basic under microwave irradiation and an insight into probable catalytic mechanism, Appl. Surf. Sci. 439 (2018) 475–487. doi:10.1016/j.apsusc.2017.12.196.

[7] W. Li, X. Wu, S. Li, W. Tang, Y. Chen, Applied Surface Science Magnetic porous Fe 3 O 4 / carbon octahedra derived from iron-based metal-organic framework as heterogeneous Fenton-like catalyst, Appl. Surf. Sci. 436 (2018) 252–262. doi:10.1016/j.apsusc.2017.11.151.

[8] S. Kumar, S. Khanchandani, M. Thirumal, A.K. Ganguli, Achieving enhanced visible-light-driven photocatalysis using type-II NaNbO3/CdS core/shell heterostructures, ACS Appl. Mater. Interfaces. 6 (2014) 13221–13233. doi:10.1021/am503055n.

[9] D. Zhang, J. Cheng, F. Shi, Z. Cheng, X. Yang, M. Cao, Low-temperature synthesis of ribbon-like orthorhombic NaNbO3 fibers and their photocatalytic activities for H2 evolution., RSC Adv. 5 (2015) 33001–33007. doi:10.1039/C5RA02155C.

[10] L. Wang, H. Gu, J. He, T. Zhao, X.X. Zhang, C. Xiao, H. Liu, X.X. Zhang, Y. Li, Scale synthesized cubic NaNbO3 nanoparticles with recoverable adsorption and photodegradation for prompt removal of methylene blue, J. Alloys Compd. 695 (2017) 599–606. doi:10.1016/j.jallcom.2016.10.327.

[11] F. Fresno, P. Jana, P. Reñones, J.M. Coronado, D.P. Serrano, V.A. de la Peña O'Shea, CO2 reduction over NaNbO3 and NaTaO3 perovskite photocatalysts, Photochem. Photobiol. Sci. 16 (2017) 17–23. doi:10.1039/C6PP00235H.

[12] S. Kumar, A.P. Singh, C. Bera, M. Thirumal, B.R. Mehta, A.K. Ganguli, Visible-Light-Driven Photoelectrochemical and Photocatalytic Performance of NaNbO3/Ag2S Core-Shell Heterostructures, ChemSusChem. 9 (2016) 1850–1858. doi:10.1002/cssc.201600397.

[13] M. Sun, Q. Yan, Y. Shao, C. Wang, T. Yan, P. Ji, B. Du, Facile fabrication of BiOI decorated NaNbO3 cubes: A p–n junction photocatalyst with improved visible-light activity, Appl. Surf. Sci. 416 (2017) 288–295. doi:10.1016/j.apsusc.2017.04.136.

[14] M. Fan, B. Hu, X. Yan, C. Song, T. Chen, Y. Feng, W. Shi, Excellent visible-light-driven photocatalytic performance of Cu2O sensitized NaNbO3 heterostructures, New J. Chem. 39 (2015) 6171–6177. doi:10.1039/C5NJ00751H.

[15] Z. Jiang, X. Liang, H. Zheng, Y. Liu, Z. Wang, P. Wang, X. Zhang, X. Qin, Y. Dai, M.H. Whangbo, B. Huang, Photocatalytic reduction of CO2 to methanol by three-dimensional hollow structures of Bi2WO6 quantum dots, Appl. Catal. B. 219 (2017) 209–215. doi:10.1016/j.apcatb.2017.07.023.

[16] H. Huang, R. Cao, S. Yu, K. Xu, W. Hao, Y. Wang, F. Dong, T. Zhang, Y. Zhang, Single-unit-cell layer established Bi2WO6 3D hierarchical architectures: Efficient adsorption, photocatalysis and dye-sensitized photoelectrochemical performance, Appl. Catal. B. 219 (2017) 526–537. doi:10.1016/j.apcatb.2017.07.084.

[17] W. Dai, J. Yu, Y. Deng, X. Hu, T. Wang, X. Luo, Facile synthesis of MoS2/Bi2WO6 nanocomposites for enhanced CO2 photoreduction activity under visible light irradiation, Appl. Surf. Sci. 403 (2017) 230–239. doi:10.1016/j.apsusc.2017.01.171.

[18] L. Zhang, W. Tian, Y. Chen, J. Chen, H. Teng, J. Zhou, J. Shi, Y. Sun, Light-driven removal of rhodamine B over SrTiO3 modified Bi2WO6 composites, RSC Adv. 6 (2016) 83471–83481. doi:10.1039/C6RA13022D.

[19] H. Yu, R. Liu, X. Wang, P. Wang, J. Yu, Enhanced visible-light photocatalytic activity of Bi2WO6 nanoparticles by Ag2O cocatalyst, Appl. Catal. B. 111–112 (2012) 326–333. doi:10.1016/j.apcatb.2011.10.015.

[20] Y. Xiang, P. Ju, Y. Wang, Y. Sun, D. Zhang, J. Yu, Chemical etching preparation of the Bi2WO6/BiOI p-n heterojunction with enhanced photocatalytic antifouling activity under visible light irradiation, Chem. Eng. J. 288 (2016) 264–275. doi:10.1016/j.cej.2015.11.103.

[21] S. Li, S. Hu, W. Jiang, Y. Liu, J. Liu, Z. Wang, Facile synthesis of flower-like Ag3VO4/Bi2WO6heterojunction with enhanced visible-light photocatalytic activity, J. Colloid Interface Sci. 501 (2017) 156–163. doi:10.1016/j.jcis.2017.04.057.

[22] G. Long, J. Ding, L. Xie, R. Sun, M. Chen, Y. Zhou, X. Huang, G. Han, Y. Li, W. Zhao, Fabrication of mediator-free g-C3N4/Bi2WO6 Z-scheme with enhanced photocatalytic reduction dechlorination performance of 2,4-DCP, Appl. Surf. Sci. 455 (2018) 1010–1018. doi:10.1016/j.apsusc.2018.06.072.

[23] P. Ju, P. Wang, B. Li, H. Fan, S. Ai, D. Zhang, Y. Wang, A novel calcined Bi2WO6/BiVO4 heterojunction photocatalyst with highly enhanced photocatalytic activity, Chem. Eng. J. 236 (2014) 430–437. doi:10.1016/j.cej.2013.10.001.

[24] X. Zhang, S. Yu, Y. Liu, Q. Zhang, Y. Zhou, Photoreduction of non-noble metal Bi on the surface of Bi2WO6for enhanced visible light photocatalysis, Appl. Surf. Sci. 396 (2017) 652–658. doi:10.1016/j.apsusc.2016.11.002.

[25] S. Yu, Y. Zhang, M. Li, X. Du, H. Huang, Non-noble metal Bi deposition by utilizing Bi2WO6 as the self-sacrificing template for enhancing visible light photocatalytic activity, Appl. Surf. Sci. 391 (2017) 491–498. doi:10.1016/j.apsusc.2016.07.028.

[26] X. Zhang, L. Zhang, J.-S. Hu, C.-L. Pan, C.-M. Hou, Facile hydrothermal synthesis of novel Bi12TiO20-Bi2WO6 heterostructure photocatalyst with enhanced photocatalytic activity, Appl. Surf. Sci. 346 (2015) 33–40. doi:10.1016/j.apsusc.2015.03.104.

[27] Q. Zhao, M. Gong, W. Liu, Y. Mao, S. Le, S. Ju, F. Long, X. Liu, K. Liu, T. Jiang, Enhancement of visible-light photocatalytic activity of silver and mesoporous carbon co-modified Bi2WO6, Appl. Surf. Sci. 332 (2015) 138–146. doi:10.1016/j.apsusc.2015.01.122.

[28] L. Yan, Y. Wang, H. Shen, Y. Zhang, J. Li, D. Wang, Photocatalytic activity of Bi2WO6/Bi2S3heterojunctions: the facilitation of exposed facets of Bi2WO6substrate, Appl. Surf. Sci. 393 (2017) 496–503. doi:10.1016/j.apsusc.2016.10.039.

[29] Y. Tian, B. Chang, J. Lu, J. Fu, F. Xi, X. Dong, Hydrothermal Synthesis of Graphitic Carbon Nitride–Bi2WO6 Heterojunctions with Enhanced Visible Light Photocatalytic Activities, ACS Appl. Mater. Interfaces. 5 (2013) 7079–7085. doi:10.1021/am4013819.

[30] Y. Huang, S. Kang, Y. Yang, H. Qin, Z. Ni, S. Yang, X. Li, Facile synthesis of Bi/Bi2WO6 nanocomposite with enhanced photocatalytic activity under visible light, Appl. Catal. B. 196 (2016) 89–99. doi:10.1016/j.apcatb.2016.05.022.

[31] X. Meng, Z. Li, H. Zeng, J. Chen, Z. Zhang, MoS2 quantum dots-interspersed Bi2WO6 heterostructure for visible light-induced detoxification and disinfection, Appl. Catal. B. 210 (2017) 160–172. doi:10.1016/j.apcatb.2017.02.083.

[32] Y. Jia, S. Zhan, S. Ma, Q. Zhou, Fabrication of TiO2–Bi2WO6 Binanosheet for Enhanced Solar Photocatalytic Disinfection of E.coli : Insights on the Mechanism, ACS Appl. Mater. Interfaces. 8 (2016) 6841–6851. doi:10.1021/acsami.6b00004.

[33] K.E. Johnston, C.C. Tang, J.E. Parker, K.S. Knight, P. Lightfoot, S.E. Ashbrook, The polar phase of NaNbO3: A combined study by powder diffraction, solid-state NMR, and first-principles calculations, J. Am. Chem. Soc. 132 (2010) 8732–8746. doi:10.1021/ja101860r.

[34] W.-K. Jo, J.Y. Lee, T.S. Natarajan, Fabrication of hierarchically structured novel redox-mediator-free ZnIn2S4 marigold flower/Bi2WO6 flower-like direct Z-scheme nanocomposite photocatalysts with superior visible light photocatalytic efficiency, Phys. Chem. Chem. Phys. 18 (2016) 1000–1016. doi:10.1039/C5CP06176H.

[35] X. Li, Q. Li, L. Wang, The effects of NaNbO3 particle size on the photocatalytic activity for 2-propanol photodegradation, Phys. Chem. Chem. Phys. 15 (2013) 14282–9. doi:10.1039/c3cp51790j.

[36] Z.-P. Nie, D.-K. Ma, G.-Y. Fang, W. Chen, S.-M. Huang, Concave Bi2WO6 nanoplates with oxygen vacancies achieving enhanced electrocatalytic oxygen evolution in near-neutral water, J. Mater. Chem. A. 4 (2016) 2438–2444. doi:10.1039/C5TA09536K.

[37] G. Li, N. Yang, W. Wang, W.F. Zhang, Synthesis, photophysical and photocatalytic properties of N-doped sodium niobate sensitized by carbon nitride, J. Phys. Chem. C. 113 (2009) 14829–14833. doi:10.1021/jp905559m.

[38] Q. Liu, Y. Chai, L. Zhang, J. Ren, W.-L. Dai, Highly efficient Pt/NaNbO3 nanowire photocatalyst: Its morphology effect and application in water purification and H2 production, Appl. Catal. B. 205 (2017) 505–513. doi:10.1016/j.apcatb.2016.12.065.

[39] J. Di, J. Xia, Y. Ge, H.H.H. Li, H. Ji, H. Xu, Q. Zhang, H.H.H. Li, M. Li, Novel visible-light-driven CQDs/Bi2WO6 hybrid materials with enhanced photocatalytic activity toward organic pollutants degradation and mechanism insight, Appl. Catal. B. 168–169 (2015) 51–61. doi:10.1016/j.apcatb.2014.11.057.

[40] J. Wang, L. Tang, G. Zeng, Y. Liu, Y. Zhou, Y. Deng, J. Wang, B. Peng, Plasmonic Bi Metal Deposition and g-C3N4 Coating on Bi2WO6 Microspheres for Efficient Visible-Light Photocatalysis, ACS Sustain. Chem. Eng. 5 (2017) 1062–1072. doi:10.1021/acssuschemeng.6b02351.

[41] Q. Gu, Q. Sun, K. Zhu, J. Liu, J. Qiu, Low-temperature sintering and enhanced dielectric properties of alkali niobate ceramics prepared from solvothermally synthesized nanopowders, Ceram. Int. 43 (2017) 1135–1144. doi:10.1016/j.ceramint.2016.10.054.

[42] X. Qian, D. Yue, Z. Tian, M. Reng, Y. Zhu, M. Kan, T. Zhang, Y. Zhao, Carbon quantum dots decorated Bi2WO6 nanocomposite with enhanced photocatalytic oxidation activity for VOCs, Appl. Catal. B. 193 (2016) 16–21. doi:10.1016/j.apcatb.2016.04.009.

[43] S. Chen, H. Nan, X. Zhang, Y. Yan, Z. Zhou, Y. Zhang, K. Wang, One-step hydrothermal treatment to fabricate Bi2WO6-reduced graphene oxide nanocomposites for enhanced visible light photoelectrochemical performance, J. Mater. Chem. B. 5 (2017) 3718–3727. doi:10.1039/C6TB02493A.

[44] C. Shifu, J. Lei, T. Wenming, F. Xianliang, Fabrication, characterization and mechanism of a novel Z-scheme photocatalyst NaNbO3/WO3 with enhanced photocatalytic activity, Dalt. Trans. 42 (2013) 10759. doi:10.1039/c3dt50699a.

[45] J. Zhao, Y. Yang, X. Dong, Q. Ma, W. Yu, J. Wang, G. Liu, Electrospinning construction of Bi2WO6/RGO composite nanofibers with significantly enhanced photocatalytic water splitting activity, RSC Adv. 6 (2016) 64741–64748. doi:10.1039/C6RA09720K.

[46] L. Chen, H. Hua, Q. Yang, C. Hu, Visible-light photocatalytic activity of Ag2O coated Bi2WO6hierarchical microspheres assembled by nanosheets, Appl. Surf. Sci. 327 (2015) 62–67. doi:10.1016/j.apsusc.2014.11.117.

[47] L. Hu, G. Deng, W. Lu, S. Pang, X. Hu, Deposition of CdS nanoparticles on MIL-53(Fe) metal-organic framework with enhanced photocatalytic degradation of RhB under visible light irradiation, Appl. Surf. Sci. 410 (2017) 401–413. doi:10.1016/j.apsusc.2017.03.140.

[48] J.F. Guo, B. Ma, A. Yin, K. Fan, W.L. Dai, Photodegradation of rhodamine B and 4-chlorophenol using plasmonic photocatalyst of Ag-AgI/Fe3O4@SiO2 magnetic nanoparticle under visible light irradiation, Appl. Catal. B. 101 (2011) 580–586. doi:10.1016/j.apcatb.2010.10.032.

[49] S. Murcia López, M.C. Hidalgo, J.A. Navío, G. Colón, Novel Bi2WO6-TiO2heterostructures for Rhodamine B degradation under sunlike irradiation, J. Hazard. Mater. 185 (2011) 1425–1434. doi:10.1016/j.jhazmat.2010.10.065.

[50] T.S. Natarajan, M. Thomas, K. Natarajan, H.C. Bajaj, R.J. Tayade, Study on UV-LED/TiO2process for degradation of Rhodamine B dye, Chem. Eng. J. 169 (2011) 126–134. doi:10.1016/j.cej.2011.02.066.

[51] L. Hu, G. Deng, W. Lu, S. Pang, X. Hu, Deposition of CdS nanoparticles on MIL-53(Fe) metal-organic framework with enhanced photocatalytic degradation of RhB under visible light irradiation, Appl. Surf. Sci. 410 (2017) 401–413. doi:10.1016/j.apsusc.2017.03.140.

[52] J. Ran, T.Y. Ma, G. Gao, X.-W. Du, S.Z. Qiao, Porous P-doped graphitic carbon nitride nanosheets for synergistically enhanced visible-light photocatalytic H2 production, Energy Environ. Sci. 8 (2015) 3708–3717. doi:10.1039/C5EE02650D.

[53] J. Li, J. Zhou, H. Hao, W. Li, G. Liu, Exposed specific (040) and (110) facets of BiVO4 modified with Bi2WO6 nanoparticles for enhanced photocatalytic performance, New J. Chem. 41 (2017) 6922–6927. doi:10.1039/C7NJ01278K.

[54] F. Duan, Q. Zhang, D. Shi, M. Chen, Enhanced visible light photocatalytic activity of Bi2WO6 via modification with polypyrrole, Appl. Surf. Sci. 268 (2013) 129–135. doi:10.1016/j.apsusc.2012.12.031.

[55] Y. Liu, H. Tang, H. Lv, P. Zhang, Z. Ding, S. Li, J. Guang, Facile hydrothermal synthesis of TiO2/Bi2WO6

hollow microsphere with enhanced visible-light photoactivity, Powder Technol. 283 (2015) 246–253. doi:10.1016/j.powtec.2015.05.032.

[56] J. Gamage McEvoy, W. Cui, Z. Zhang, Synthesis and characterization of Ag/AgCl–activated carbon composites for enhanced visible light photocatalysis, Appl. Catal. B Environ. 144 (2014) 702–712. doi:10.1016/j.apcatb.2013.07.062.

Chapter IV

Conclusions and Future Work

4.1 Project Conclusions

In this project, a series of novel $NaNbO_3/Bi_2WO_6$ heterojunction composites with a type-II alignment were successfully fabricated via a facile wet impregnation method. Based on experimental results, the following conclusions can be summarized:

- A heterojunction instead of a physical mixture was generated between the prepared $NaNbO_3$ microcube and Bi_2WO_6 microflowers, as confirmed by XRD, SEM, HRTEM, XPS, DRS, PC, and EIS analyses.

- The bandgap of $NaNbO_3$ and Bi_2WO_6 were evaluated to be ca. 3.48 eV and 2.70 eV, respectively.

- The composite sample with the $NaNbO_3$ content of 30wt% exhibited the highest photocatalytic activity towards RhB degradation under visible light irradiation, which was 40 and 2.5 times that with the pure $NaNbO_3$ and Bi_2WO_6, respectively.

- Kinetics of the as-prepared samples followed the pseudo-first-order reaction model.

- The RhB molecules suffered from N-demethylation, de-ethylation and mineralization synchronously. The decomposition of rhodamine B into rhodamine molecules played the

most important role at the first stage, and the mineralization of rhodamine dominated afterwards.

- By means of the quenching experiment, the photogenerated holes were found to be the predominant reactive species and superoxide radicals functioned as well to some degree, while hydroxyl radical barely functioned.

- The thermodynamic infeasibility of previously reported photocatalytic mechanism of Bi_2WO_6-based type-II heterostructures when Bi_2WO_6 worked as the reservoir and $O_2^{\bullet-}$ was one of the dominant species was pointed out.

- Based on calculated energy band potentials and the quenching experiment, a plausible mechanism of the enhanced photocatalytic performance on NBO composites was proposed, which was mainly attributed to the facilitated electron/hole separation at the $NaNbO_3/Bi_2WO_6$ interface, with the assistance of the dye-sensitization effect of RhB itself.

- Effects of several operation parameters on the catalytic performance were investigated:

  - Initial RhB concentration

    The photocatalytic activity decreased with the increase in initial RhB concentration, which was associated with the reduced irradiation-responsivity and reactive sites on the catalyst surface, as well as the transmittance of the reaction suspension.

  - Catalyst dosage

    An optimized catalyst dosage at 2 g/L was obtained, after which the catalyst performance almost unchanged owing to the blocking effect of catalyst particles as well as the scattered photons.

  - Reaction temperature

    The reaction rate followed the Arrhenius equation before the reaction temperature reached 40 ^{0}C. The slowly increased reaction rate afterwards was caused by the inhibited adsorption of both the substrates and reactive species on the catalyst surface.

- Initial pH

  RhB degradation in the presence of 30 wt% NBO under visible light irradiation was slightly promoted in an acidic environment while strongly prohibited in a basic surrounding, which was determined by the dominantly functioning reactive species.

4.2 Recommendation of Future Work

- Preparation conditions and methods were found to drastically affect the catalyst performance. Thus, further investigations in terms of the synthesis process may be required. For example, the total amount of $NaNbO_3$ and Bi_2WO_6, the composition of the dispersion media, the reaction time and temperature, as well as the mixing approach during the facile wet-impregnation fabrication may be modified in the future.

- Considering the experimental results of this project and the recent achievements in photocatalysis, recommendation of future work should be more focused on industrial applications.

  - As the source of energy in photocatalysis, irradiation controls the amount of generated electron/hole pairs and thus dominates photocatalytic performance. Illumination in this work was provided by an artificial lamp and only the visible region covering less than 50% of the total solar irradiation was employed. Additionally, since photocatalysis is a surface process, the surrounding environmental parameters, such as temperature, humidity, brightness, etc., may have a great impact on the catalyst performance as well. Therefore, future works should utilize simulated or natural solar irradiation, as well as take the potential influence of the surrounding environment into consideration.

  - The substrate used in this study was RhB aqueous solution at low concentrations, which is quite different from real wastewater containing multiple contaminants with high concentrations and may also be corrosive. As exhibited by the TOC removal result, 60% of the initial TOC still remained after reacting for 135 min. Hence, more strategies would be expected to improve the photocatalytic mineralization efficiency as well as the stability of photocatalysts.

- The optimal catalyst dosage for NBO composites to work was found to be 2 g/L, which is pretty high for industrial utilization. Even though it showed excellent reusability and stability, the post-use treatment realized by centrifugation requires great power consumption.

Appendices

Appendix A. Supporting Information of Chapter III

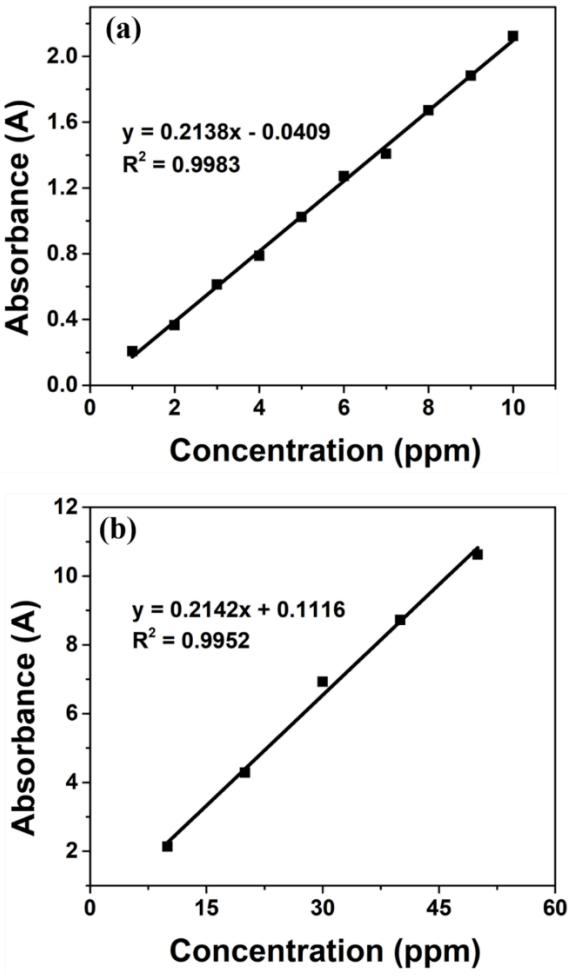

Figure A- 1 Calibration curve correlating the concentration and absorbance (at λ=554 nm) of RhB solution: (a) RhB concentration in the range of 1-10 ppm, and (b) RhB concentration in the range of 10-50 ppm.

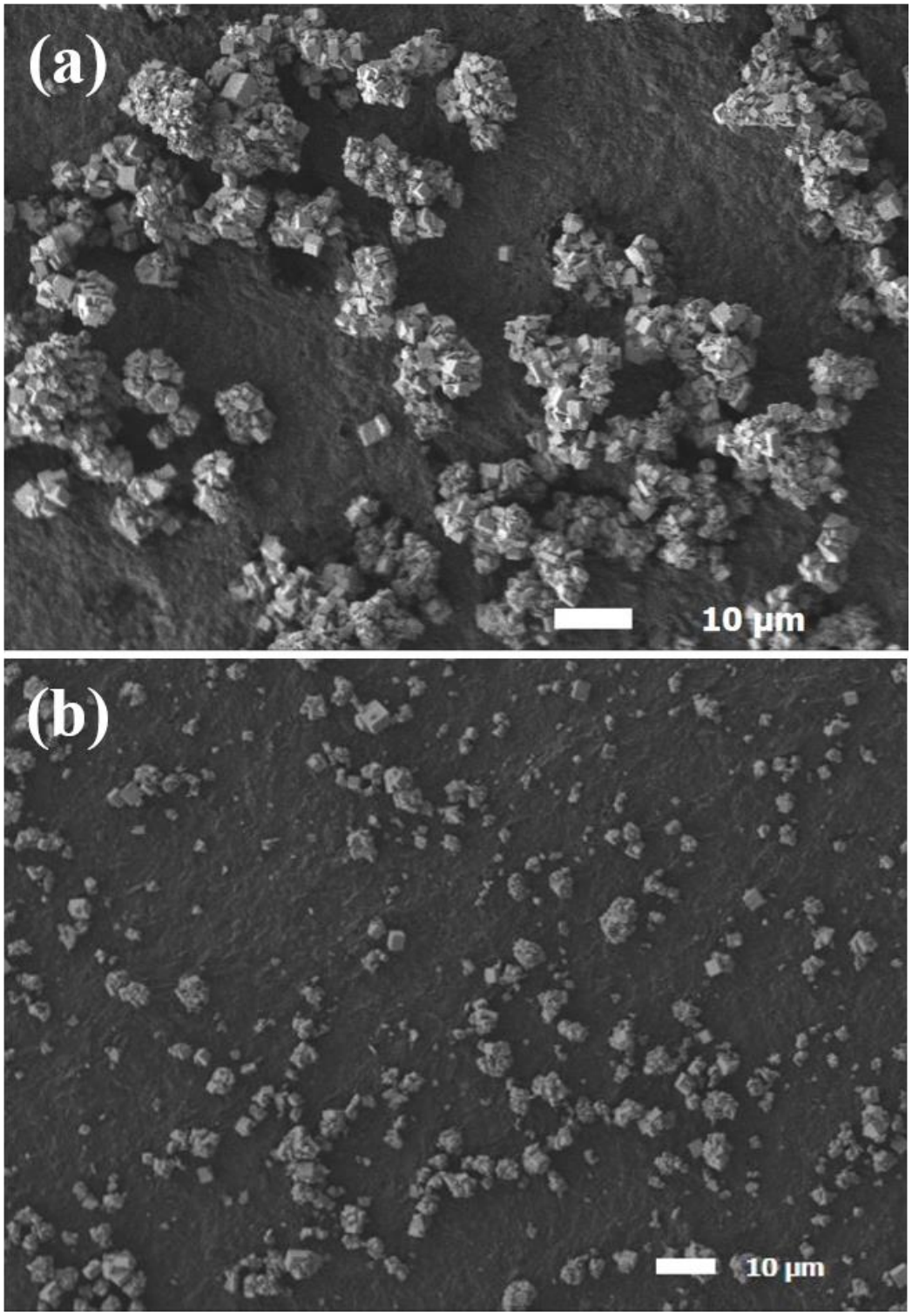

Figure A- 2 SEM images of the as-prepared pristine $NaNbO_3$ particles (a) before and (b) after ultrasonication.

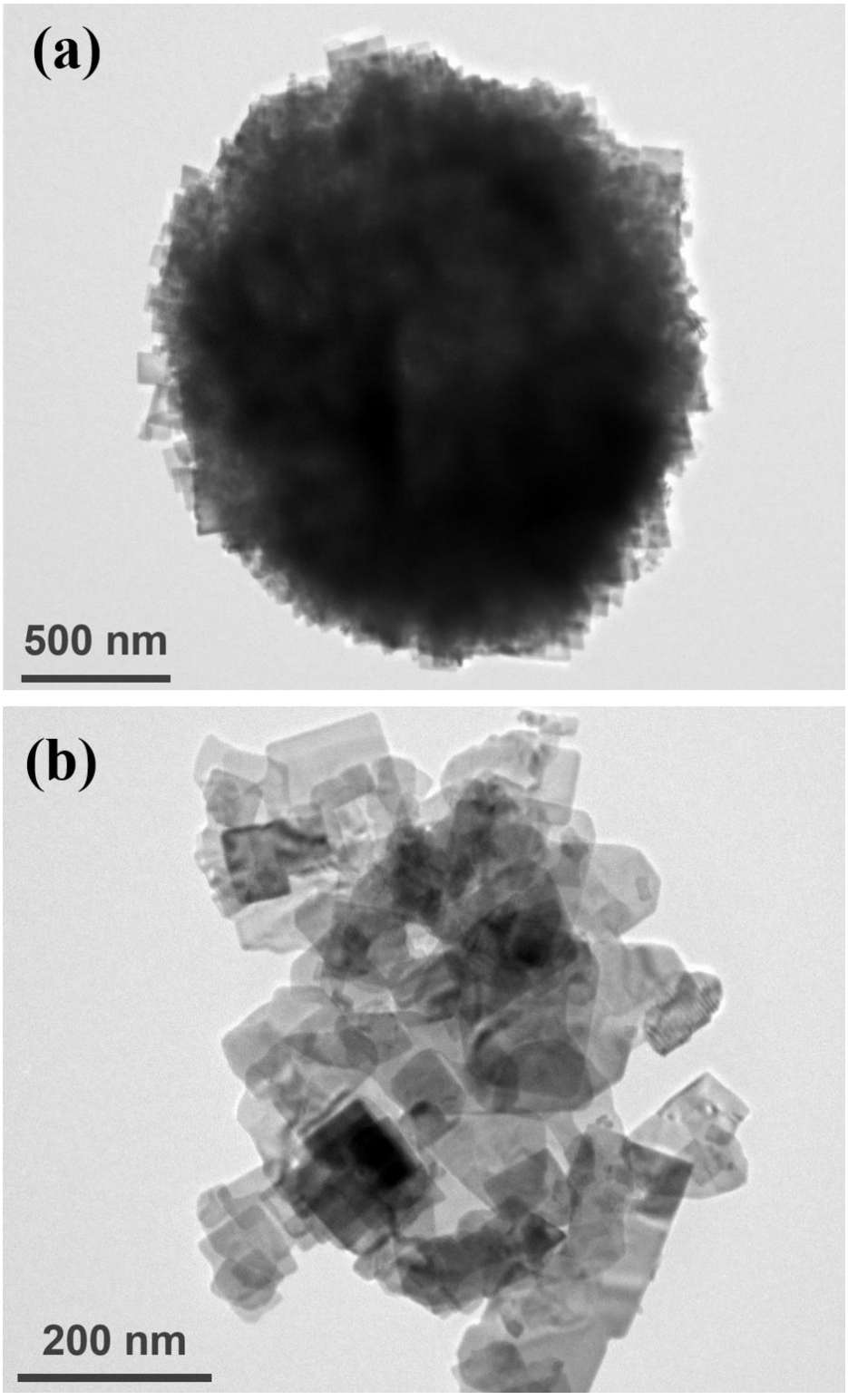

Figure A- 3 HRTEM image of the as-prepared pristine Bi_2WO_6 particle: (a) microflower and (b) fragments.

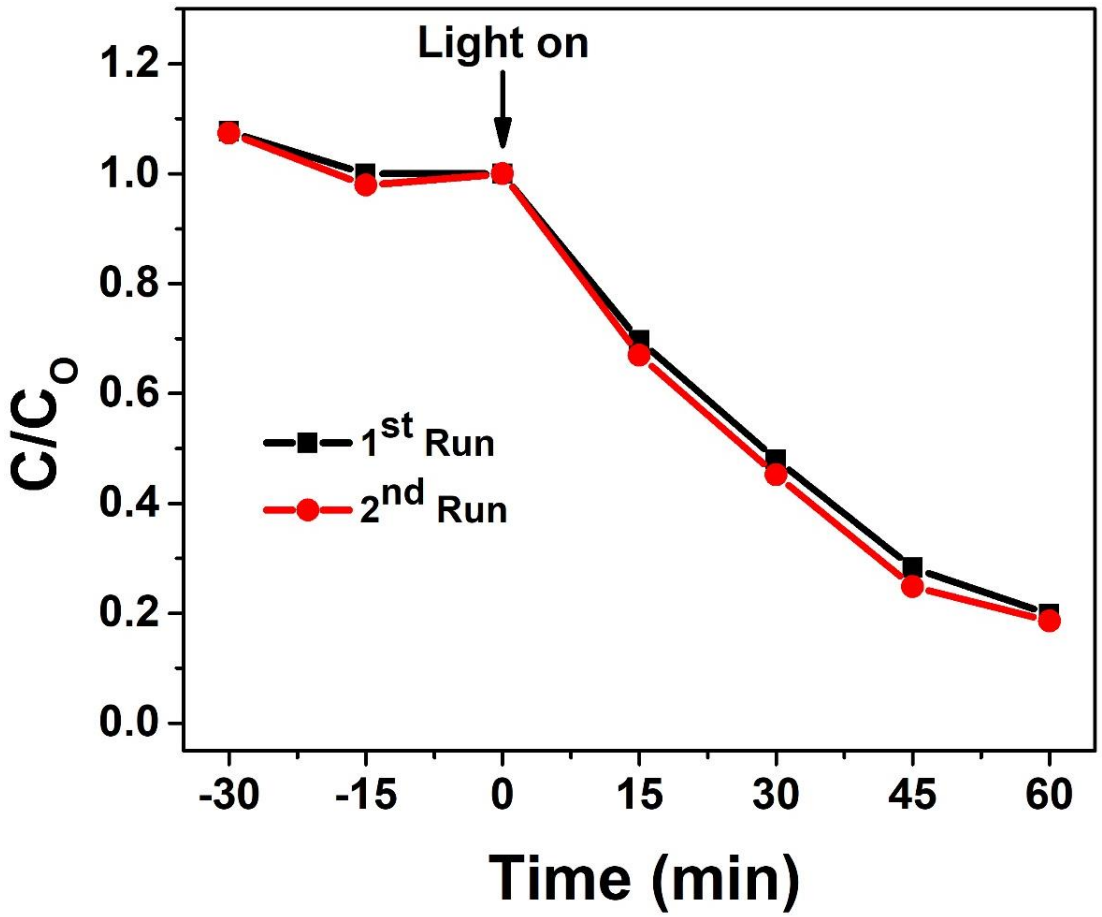

Figure A- 4 Two runs of mechanical mixture towards photocatalytic degradation of RhB under visible light irradiation (λ>410 nm) at 20 ^{0}C.

As shown in Figure A-4, the photocatalytic efficiency of the mechanical mixture had a minute enhancement in the second run of reaction compared to the first one, suggesting that the interaction between the pristine $NaNbO_3$ and Bi_2WO_6 particles may increase as the reaction time prolonged. However, it was still not comparative to the enhancement realized by the produced 30 wt% NBO heterojunction composite.

Appendix B. Summary of Semiconductor Modification Strategies

Table B- 1 Abbreviations

Abbreviation	Full Name	Abbreviation	Full Name
2,4-DCP	2,4-Dichlorophenol	ER	Erionyl Red
4-CP	4-Chlorophenol	EFA	Enrofloxacin
4-ABA	4-Aminobenzoic Acid	MB	Methyl Blue
AA	Acetaldehyde	MG	Malachite Green
AB	Acid Black	MO	Methyl Orange
AF	Acid Fuchsin	MR	Methyl Red
AO	Acid Orange	NY	Neutral Dark Yellow
AY	Acid Light Yellow	RhB	Rhodamine B
BF	Basic Fuchsin	RR	Reactive Red
BL-G	Active Black	RY	Reactive Yellow
BPA	Bisphenol A	RZ	Resazurin
BR	Bromacil	SPC	Sodium Pentachlorophenate
CFS	Ceftiofur Sodium	ST dye	Dafranine T dye
CR	Congo Red	SD	Antibiotic Sulfadiazine
CV	Crystal Violet	TC	Tetracycline Hydrochloride
CY	Cibacron Yellows		

Table B- 2 Performance of photocatalysts doped with ions for organic pollutant treatment in aqueous media

Photocatalyst	Substrate	Degradation Efficiency	Effect(s) of Dopant(s)	Dopant source	Preparation Method	Light Source	Optimal Dopant Content	Ref.
K-doped ZnO	RhB	95% in 80 min	(i) Formed superficial defects, leading to more active sites; (ii) increased the specific surface area; (iii) narrowed down the bandgap, and therefore extended the photon absorption region to the visible region.	KNO_3	Microwave hydrothermal method	Vis	0.3 mol%	[1]
Cr-doped ZnO	MO	58.7% in 140 min	(i) The s-d and p-d exchange interactions between the conduction band electrons of ZnO and the localized d electrons of the Cr^{3+} ions which the substituted Zn^{2+} ions led to a negative and a positive correction to the CB and the VB edges, respectively, resulting in a strong visible-light absorption; (ii) increased the specific surface area.	$Cr(NO_3)_3 \bullet 9H_2O$	Solvothermal method	Vis	2.97 at.%	[2]
Cu-doped ZnO	RZ	~90% in 25 min	(i) Introduced an impurity energy level trapping holes; (ii) increased the amount of surface oxygen vacancies; (iii) increased the specific surface area.	$CuCl_2$	Vapor transport method	UV	15 mol%	[3]
Ga-doped ZnO	MO	~90% in 60 min	(i) Increased the specific surface area; (ii) changed the morphology of ZnO; (iii) improved the photogenerated carrier separate rate.	$Ga(NO_3)_3$	Parallel flow coprecipitation method	Vis	1 mol%	[4]
Sn-doped ZnO	MO	100% in 120 min	Introduced an impurity energy level in the presence of singly ionized oxygen vacancy defects which trapped holes, decreasing the bandgap and thus broadened the light absorption range to visible region.	$SnCl_4$	Hydrothermal method	Vis	5 mol%	[5]
W-doped ZnO	MB	87% in 60 min	(i) Narrowed down the bandgap; (ii) facilitated separation of photogenerated carriers; (iii) reduced particle size, and thus increased specific surface area.	Na_2WO_4	Sol-gel method	UV	4 mol%	[6]

La-doped $NaTaO_3$	ST dye	~90% in 120 min	The substitution of La^{3+} ions for Na^{+} ions might increase the n-type property of $NaTaO_3$, resulting an increased electric conductivity and therefore a narrower bandgap.	$La(NO_3)_3$	Hydrothermal method	UV	2 mol%	[7]
Eu-doped $BiVO_4$	MO	93.6% in 90 min	(i) Enhanced light absorbance in visible region with the formation of a new absorption band; (ii) suppressed recombination between photogenerated electrons and holes; (iv) improved the adsorption ability of dye molecules over the catalyst surfaces.	$Eu(NO_3)_3$	Hydrothermal method	Vis	1.46 wt%	[8]
Sr-doped α-Bi_2O_3	MB	90% in 120 min	Formed a sheets-like structure, which induced charge carrier transfer and high crystallinity of the α-Bi_2O_3 phase.	$SrCl_3 \bullet 6H_2O$	Hydrothermal method	Vis	7.5 mol%	[9]
B-doped $BiVO_4$	MB	~98% in 20 min	(i) Formed a monoclinic $BiVO_4$ structure; (ii) increased the amount of V^{4+} and oxygen vacancies; (iii) enhanced the light responsivity in visible region.	H_3BO_3	Citric acid complex method	Vis	0.04 mol%	[10]
N-doped $BiVO_4$	RhB	97% in 180 min	(i) Decreased particle size; (ii) narrowed down the bandgap; (iii) introduced multi-atomic BiV_4 centers and surface oxygen vacancies.	NaN_3	Facile microwave hydrothermal method	Vis	-	[11]
C-doped BiOCl	MO Phenol	~100% in 30 min ~70% in 180 min	(i) Introduced an impurity energy level; (ii) enhanced photon absorption in visible region.	Polyacrylamide (PAM)	Low temperature Wet-chemical method	UV	0.4g PAM	[12]
S-doped SnO_2	RhB	93% in 120 min	(i) Narrowed down the bandgap; (ii) facilitated separation of photogenerated carriers.	$SnCl_4$	One-pot hydrothermal method	Vis	15.01 at%	[13]
I-doped BiOBr	MO	100% in 6 hr	Introduced an impurity energy level, and thus narrowed down the bandgap.	KI	Chemical precipitation method	Vis	10.0 mol%	[14]
I-doped SnO_2	Phenol	93.4% in 150 min 60% in 90 min	(i) Introduced an impurity energy level; (ii) increased the amount of oxygen vacancies; (iii) decreased the crystal size.	I_2	Sol-gel method	UV Vis	1 mol%	[15]
I^{-}- self doped BiOI	MO	79% in 4 h	(i) Narrowed down the bandgap; (ii) increased the specific surface area.	KI	Solvothermal method	Vis	$n_{I/Bi} = 1:1.5$	[16]

Bi^{3+}- self doped Bi_2WO_6	SPC	90% in 60 min	Facilitated the mobility and separation of photogenerated carriers without changing their redox power.	$Bi(NO_3)_3 \bullet 5H_2O$	Hydrothermal method	Vis	$n_{Bi/w} = 2.1$	[17]
Bi^{3+}- self doped $NaBiO_3$	RhB	100% in 25 min	(i) Enhanced photon absorption in visible region; (ii) facilitated separation of photogenerated carriers.	$NaBiO_3 \bullet 2H_2O$	Hydrolysis of $NaBiO_3 \bullet 2H_2O$	Vis	$\frac{c(HNO_3}{c(NaBiO_3)} = 0.2$	[18]
	BPA	100% in 40 min						
F/Mg-codoped ZnO	MB	88% in 45min	(i) F dopant generated excess reactive oxygen species; (ii) Mg dopant decreased the the crystallite size and thus increased the specific surface area, more defect states and more singly ionized oxygen vacancies which produced more $O_2^{\bullet-}$.	NH_4F $MgCl_2 \bullet 6H_2O$	Sol-gel method	Vis	12 at.% (Mg)	[19]
	MG	97% in 30 min						

Table B- 3 Performance of photocatalysts loaded with metal nanoparticles for organic pollutant treatment in aqueous media

Photocatalyst	Substrate	Degradation Efficiency	Effects of the Loaded Mental Nanoparticles	Predominant Active Species	Light Source	Optimal Loading Content	Ref.
Ag-loaded BiOCl	RhB	> Bulk BiOCl	LSPR effect caused an enhancement in photon absorption in visible region, formed a Schottky barrier and facilitated e^- transferring from Ag to BiOCl, leading to more production of $O_2^{\bullet-}$.	-	UV/ Vis	0.46 at%	[20]
Pt-loaded BiOCl		< Bulk BiOCl	The loaded metal nanoparticles trapped h^+ generated on the VB of BiOCl due to their lower work function (higher Fermi level), deteriorating the oxidative ability of the VB of BiOCl.		UV	0.18 at%	
Pd-loaded BiOCl		< Bulk BiOCl				0.56 at%	
Rh-loaded BiOCl		< Bulk BiOCl				0.49 at%	
Ag-loaded ZnO-t	Phenol	58% in 60 min (mineralizaion)	(i) LSPR effect generated hot electrons, which could reduce O_2 to produce $O_2^{\bullet-}$. (ii) captured e^- from the CB of ZnO-t, facilitating the separation of photogenerated carriers.	h^+	Vis	0.25 at%	[21]
Au-loaded Bi_2CuO_4	CFS	56% in 60 min	(i) LSPR effect caused an enhancement in photon absorption in visible region; (ii) Hot electrons produced at Au NPs due to LSPR effect transferred to the CB of Bi_2CuO_4, promoting the generation of reactive species.	•OH	Vis	-	[22]
Au-loaded α-Bi_2O_3	RhB	80% in 180 min	(i) LSPR effect caused an enhancement in photon absorption in visible region; (ii) captured e^- from the CB of α-Bi_2O_3, facilitating the separation of photogenerated carriers.	•OH	Vis	1.0 wt%	[23]
	2,4-DCP	65% TOC removal: 53% (in 12 h)					
Au-loaded $KNbO_3$	RhB	47% in 160 min	(i) LSPR effect caused an enhancement in photon absorption in both the UV and the visible region; (ii) captured e^- from the CB of $KNbO_3$, facilitating the separation of photogenerated carriers.	•OH, h^+	UV	8.0 wt%	[24]
		82% in 110 min			Vis		

Nobel Metal (Rh, Pd, Pt)-loaded BiOX (Cl, Br, I)	AO II	$Pt > Pd > Rh$	(i) LSPR effect caused an enhancement in photon absorption in visible region; (ii) captured e^- from the CB of BiOX, facilitating the separation of photogenerated carriers. (iii) enhanced the adsorption of pollutant substrates.	•OH	UV	$\frac{Pd}{BiOBr} = 0.5wt\%$ $\frac{Pt}{BiOCl} = 1wt\%$ $\frac{Pd}{BiOCl} = 2wt\%$ $\frac{Pd}{BiOBr} = 4wt\%$	[25]
		$Rh > Pt > Pd$			Vis	$\frac{Pd}{BiOI} = 0.5wt\%$ $\frac{Rh}{BiOCl} = 1wt\%$	
Bi-loaded Bi_2WO_6	RhB	>90% in 25 min	(i) LSPR effect caused an enhancement in photon absorption in visible region; (ii) captured e^- from the CB of Bi_2WO_6, facilitating the separation of photogenerated carriers.	h^+, $O_2^{\bullet-}$	Vis	5.0 wt%	[26]
Ag-loaded & Fe(III)- doped Ag_3PO_4	MO	55.6% in 15 min	(i) LSPR effect of the loaded Ag NPs caused the enhancement of photon absorption in visible region; (ii) Hot electrons generated on Ag clusters due to LSPR effect could transfer to the CB of Ag_3PO_4, facilitating the production of reactive species. (iii) h^+ generated on the VB of Ag_3PO_4 was captured by the doped Fe^{3+} ions, facilitating the separation of photogenerated carriers.	-	Vis	Ag: 20.3 at% Fe(III): 2.6 at%	[27]
Ag-loaded on Ti(IV)- doped BiOBr	RhB	100% in 1 h	(i) LSPR effect of the loaded Ag NPs and the doped Ag^+ ions (dissolved from Ag nanoparticles) caused the enhancement of photon absorption in visible region; (ii) enhanced the adsorption of pollutant substrates.	-	Vis	3 mol% (Ag)	[28]

Table B- 4 Performance of photocatalysts coupled with other compounds for organic pollutant treatment in aqueous media

Photocatalyst	Type of Heterojunction	Substrate	Degradation Efficiency	Degradation Rate Constant**	Predominant Active Species	Light Source	Optimal Content*	Ref.
SnS_2/SnO_2	Conventional heterojunction	MO	100% in 80 min	$1.56 * K_{SnS_2}$	-	Vis	18.1 wt%	[29]
$MoS_2/BiOBr$	Conventional heterojunction	RhB	95% in 50 min	$2.5 * K_{BiOBr}$	h^+	Vis	3 wt%	[30]
$SnO_2/ZnO/TiO_2$	Ternary conventional heterojunction	MO	85% in 40 min	-	•OH	UV	Molar ratio: 5%/5%/90%	[31]
			27% in 3 h	-		Vis	Mass ratio: 6%/6%/88%	
$BiOI/Bi_2O_2CO_3/Bi_4O_5I_2$	Ternary p-n-p heterojunction	RhB	100% in 3 h	$20 * K_{BiOI}$ $12 * K_{Bi_2O_2CO_3}$ $2.5 * K_{Bi_4O_5I_2}$	h^+	Vis	$n_{Bi_2O_2:I^-:Bi^{3+}} = 7.5:2:2$ (in precursor)	[32]
			100% in 45 min	$40 * K_{BiOI}$ $25 * K_{Bi_2O_2CO_3}$ $10 * K_{Bi_4O_5I_2}$		Solar light		
$Ag_2O/Ag_3VO_4/Ag_4V_2O_7$	LSPR-assisted conventional heterojunction	RhB	99% in 120 min	-	h^+	Vis	$n_{Ag:V} = 6:1.5$	[33]
$ZnInS_4/TiO_2$	Core-shell heterojunction $ZnInS_4$: core; TiO_2: shell	MB	90% in 3 h	-	h^+, •OH	Vis	-	[34]
$CuO/ZnInS_4$	Conventional heterojunction		97% in 3 h	-			10 mol%	
N-doped TiO_2/Al_2O_3	Doping-assisted conventional heterojunction	MO	75% in 30 min	-	h^+, $O_2^{\bullet-}$	Vis	60 mol%	[35]
		MB	47.5%	$3.2 * K_{N/TiO_2}$	•OH			
Ag/AgCl-loaded Bi_2WO_6	LSPR-assisted conventional heterojunction	RhB	~100% in 45 min	$5.4 * K_{Bi_2WO_6}$	h^+	Vis	10 wt% (Ag/AgCl)	[36]
BiOBr/ZnO	p-n heterojunction BiOBr: p-type; ZnO: n-type	RhB	97% in 60min	$1.3 * K_{BiOBr}$ $10.6 * K_{ZnO}$	•OH	Vis	50 wt%	[37]
$CuBi_2O_4/SrO$	p-n heterojunction $CuBi_2O_4$: p-type; SrO: n-type	CR	97.22% in 220 min	$26.5 * K_{CuBi_2O_4}$	$O_2^{\bullet-}$, •OH, •OOH	UV	20 wt%	[38]

$BiOI/CeO_2$	p-n heterojunction BiOI: p-type; CeO_2: n-type	MO	97.35% in 50 min	$3.5 * K_{BiOI}$ $21.7 * K_{CeO_2}$	h^+, $O_2^{\bullet-}$	Vis	$n_{Bi:Ce} = 1:1$	[39]
		BPA	92.02% in 90 min	$3 * K_{BiOI}$ $7 * K_{CeO_2}$				
$BiOI/Bi_2O_2CO_3/Bi_4O_5I_2$	Ternary p-n-p heterojunction	RhB	100% in 3 h	$20 * K_{BiOI}$ $12 * K_{Bi_2O_2CO_3}$ $2.5 * K_{Bi_4O_5I_2}$	h^+	Vis	$n_{Bi_2O_2:I^-:Bi^{3+}} = 7.5:2:2$ (in precursor)	[32]
			100% in 45 min	$40 * K_{BiOI}$ $25 * K_{Bi_2O_2CO_3}$ $10 * K_{Bi_4O_5I_2}$		Solar light		
$Ag\text{-}Ag_2O/CeO_2$	LSPR-assisted p-n heterojunction Ag_2O: p-type; CeO_2: n-type	EFA	88% in 120 min	$3.5 * K_{Ag_2O}$ $122 * K_{CeO_2}$	h^+, $O_2^{\bullet-}$	Vis	25.82 wt% (Ag_2O)	[40]
$SnS_2/BiOBr$	Direct Z-scheme heterojunction	RhB	100% in 30 min	$75 * K_{SnS_2}$ $2.2 * K_{BiOBr}$	$O_2^{\bullet-}$	Vis	20 mol%	[41]
CuS/WO_3	Direct Z-scheme heterojunction	RhB	100% in 150 min	$9.2 * K_{CuS}$ $4.4 * K_{WO_3}$	h^+, $O_2^{\bullet-}$	Vis	1 wt%	[42]
$Bi_2S_3/SnS_2/Bi_2O_3$	Ternary direct double Z-scheme heterojunction	RhB	100% in 90 min	-	•OH	Vis	$n_{Sn:Bi} = 0.15:1$	[43]
$BiOCl/Au/CdS$	Metal NPs-mediated Z-scheme heterojunction	MO	100% in 180 min	-	$O_2^{\bullet-}$	Vis	-	[44]
		RhB	100% in 30 min					
		Phenol	100% in 100 min					
		SD	100% in 4 h					

*: The optimal content refers to the weight (wt%) or molar (mol%) content of semiconductor 1 (before the slash) in the composite unless specifically stated.
**: The model of degradation rate is pseudo-first-order model unless specifically stated.

Table B- 5 Performance of photocatalysts coupled with functional organics for organic pollutant treatment in aqueous media

Photocatalyst	Organic Metarial	Substrate	Degradation Efficiency	Predominant Active Species	Effect the of the Functional Organic Material	Light Source	Ref.
ZnO	gC_3N_4	MB	90 % in 60 min	h^+	(i) Accepted h^+ from the excited ZnO, facilitating the separation of photogenerated carriers and protected ZnO from photocorrosion as well; (ii) π-π stacking between MB and gC_3N_4 enhanced the adsorption of MB on the catalyst composite surface.	UV	[45]
			72.3 % in 5 h		(i) Responded to the irradiation and produced electrons and holes on its LUMO and HOMO, respectively. The electrons then flowed to the CB of the unexcited ZnO to participate in the subsequent photocatalytic reactions; (ii) π-π stacking between MB and gC_3N_4 enhanced the adsorption of MB on the catalyst composite surface.	Vis	
AgI	gC_3N_4	MB	96% in 120 min	-	(i) Responded to the irradiation and produced electrons and holes on its LUMO and HOMO, respectively; (ii) formed a core-shell type-II heterostructure by coating onto the surface of AgI, which facilitated the separation of photogenerated carriers by providing electrons to the CB of AgI while accepting holes from the VB of AgI, as well as inhibited the dissolution of AgI in aqueous solution.	Vis	[46]
N-doped ZnO	gC_3N_4	RhB	100% in 60 min	•OH	(i) Responded to the irradiation and produced electrons and holes on its LUMO and HOMO, respectively; (ii) formed a Z-scheme heterostructure by coating onto the surface of N-doped ZnO (NZO), which facilitated the separation of photogenerated carriers by providing electrons to the CB of NZO while accepting holes from the VB of NZO; (ii) π-π stacking between RhB and gC_3N_4 enhanced the adsorption of RhB on the catalyst composite surface.	Vis	[47]
TiO_2	Polyaniline (PANI)	MO	TOC removal: 82% in 125 min	h^+, $O_2^{\bullet-}$	(i) Responded to the irradiation and produced electrons and holes on its LUMO and HOMO, respectively; (ii) formed a type-II heterostructure with TiO_2, which facilitated the separation of photogenerated carriers by providing electrons to the CB of TiO_2 while accepting holes from the VB of TiO_2; (ii) π-π stacking between MO and gC_3N_4 enhanced the adsorption of MO on the catalyst composite surface.	UV	[48]
			96% TOC removal: 21% in 6 h			Vis	

$ZnIn_2S_4$	Polyrrole (Ppy)	Chloram-phenicol	100% in 60 min TOC removal: 48.5% in 5 h	$O_2^{\bullet-}$	(i) Responded to the irradiation and produced electrons and holes on its LUMO and HOMO, respectively; (ii) formed a type-II heterostructure with $ZnIn_2S_4$, which facilitated the separation of photogenerated carriers by providing electrons to the CB of $ZnIn_2S_4$ while accepting holes from the VB of $ZnIn_2S_4$.	Vis	[49]
BiOI	Polyrrole (Ppy)	RhB	90% in 5 h	h^+, $O_2^{\bullet-}$	(i) Accepted holes from the VB of BiOI, facilitating the separation of photogenerated carriers; (ii) Increased the specific surface area of the composite, which was in favor of the adsorption of the substrates, as well as generating more active sites.	Vis	[50]
MoO_3 and ZrO_2	Carbon clusters	MB	77% in 180 min	-	Formed a Z-scheme heterostructure between MoO_3 and ZrO_2 by accepting photogenerated e^- from the CB of MoO_3 and transporting it to recombine with the h^+ on the VB of ZrO_2.	Vis	[51]
ZnO	C_{60}	MB	95% in 75 min	-	Facilitated the separation of the photogenerated carriers and inhibited the photocorrosion of ZnO due to the high conductivity towards electrons of C_{60} as well as the form conjugative π-system at the C_{60}/ZnO interface.	UV	[52]
Cu_2O	Carbon Nanotubes (CNTs)	Phenol	85% in 60 min	-	(i) Formed a hierarchical chrysanthemum-like morphology composite by being deposited on the Cu_2O surface, which improved both the range and te intensity of light absoption; (ii) the tight connection between Cu_2O NPs and the highly conductive CNTs facilitated electrons flowing from the visible-light-excited Cu_2O to the CNTs and thus the separation of photogenerated carriers.	Vis	[53]
Bi_2WO_6	Carbon Nanotubes (CNTs) and gC_3N_4	TC	87.65% in 90 min	$O_2^{\bullet-}$	Mediated to form a Z-scheme heterostructure between gC_3N_4 and Bi_2WO_6 by functioning as the recombination center for holes from the VB of gC_3N_4 and electrons from the CB of Bi_2WO_6, facilitating the separation of photogenerated carriers.	Vis	[54]
BiOI	Multiwalled CNTs	4-CP	80% in 180 min	h^+, $O_2^{\bullet-}$	Facilitated the separation of photogenerated carriers by accepting electrons from the CB of BiOI.	Vis	[55]
$BiVO_4$	Graphene	MO MB RhB BL-G	99% in 300 min	h^+	Transported photogenerated e^- from the CB of $BiVO_4$ to adsorbed O_2, producing reactive species $O_2^{\bullet-}$.	Vis	[56]
CdS	Graphene Oxide	AO7 dye	100% in 30 min	•OH	(i) Transferred photogenerated e^- from the CB of CdS to adsorbed O_2, producing reactive species $O_2^{\bullet-}$; (ii) made the after-use recovery of the composite easier; (iii) prevented CdS from leaching out with a strong adhesion.	Vis	[57]

Ag_2O/Ag_3VO_4 /$Ag_4V_2O_7$	Graphene Oxide	RhB	99.2% in 45 min	•OH	(i) Helped with the separation of photogenerated electrons and holes produced on all the three semiconductors; (ii) enhanced the adsorption of the substrates; (iii) inhibited photocorrosion of the silver species in aqueous solution by accepting photogenerated e^-.	Vis	[58]
		MO	92% in 45 min				
$BiVO_4$	Reduced Graphene Oxide	RhB	98.5% in 10 h	h^+	(i) Increased the specific surface area and thus enhanced the adsorption of dye molecules; (ii) transported e^- generated on the CB of $BiVO_4$ to produce $O_2^{\bullet-}$ through reducing the adsorbed O_2.	Vis	[59]
Ag-loaded AgCl	Reduced Graphene Oxide	MB	100% in 60 min	$O_2^{\bullet-}$, Cl^o	Did not respond to the irradiation, but formed a Z-scheme heterojunction with AgCl by accepting photogenerated holes from the VB of the excited AgCl with the mediation of Ag NPs on the AgCl surface, which facilitates the separation of photogenerated carriers.	Vis	[60]

Table B- 6 Performance of photocatalysts with the assistance of dye-sensitization for organic pollutant treatment in aqueous media

Photocatalyst	Dye-Sensitizer	Substrate	Degradation Efficiency	Predominant Active Species	Light Source	Effect(s) of Dye-Sensitizer	Ref.
ZnO	RR 120	RR 120	64% in 60 min	$O_2^{\bullet-}$	UV	Dye-sensitization effect did not exhibit.	[61]
			77% in 60 min		Solar light	Self-sensitizer with dual effects: (i) responded to the visible light irradiation, producing electrons and injected them to the CB of the unexcited ZnO and then participated in the subsequent photocatalytic reactions, which realized the sensitization of ZnO in the visible region; (ii) RR 120 molecules that responded to the irradiation lost electrons and transformed to their excited state, which was easier to be degraded compared to those on their ground state.	
$Bi_2S_3/BiOCl$	RhB	RhB	98% in 12 min	$O_2^{\bullet-}$, h^+	Vis	Self-sensitizer with dual effects: (i) responded to the visible light irradiation, producing electrons and injected them to the CB of the unexcited BiOCl and then participated in the subsequent photocatalytic reactions, which improved the light absorption efficiency of the $Bi_2S_3/BiOCl$ composites; (ii) RhB molecules that responded to the irradiation lost electrons and transformed to their excited state, which was easier to be degraded compared to those on their ground state.	[62]
$SrTiO_3$	MG	MG	100% in 60 min	-	Vis	Self-sensitizer with dual effects: (i) responded to the visible light irradiation, producing electrons and injected them to the CB of the unexcited $SrTiO_3$ and then participated in the subsequent photocatalytic reactions, which improved the light absorption efficiency of $SrTiO_3$; (ii) MG molecules that responded to the irradiation lost electrons and transformed to their excited state, which was easier to be degraded compared to those on their ground state.	[63]

Table B- 7 Performance of photocatalysts employing quantum dots (QDs) for organic pollutant treatment in aqueous media

QDs	Support Matrix	Size of QDs (nm)*	Substrate	Degradation Efficiency	Light Source	Functions of QDs	Ref.
ZnO	-	5-8	MO	97% in 160 min	UV	(i) Possessed more active sites with higher crystallinity; (ii) responded to the UV irradiation as bulk ZnO does.	[64]
		15-20		59% in 160 min			
CdS	-	7.44	MB	91.6% (Bulk: 43) in 90 min	Vis	(i) Broadened the light absorption band from 200 to 500 nm; (ii) responded to the visible light irradiation as bulk CdS does.	[65]
			RhB	44% (Bulk: 10) in 90 min			
ZnO	SiO_2	3-5	RhB	100% in 50 min	UV	Responded to the UV irradiation as bulk ZnO does.	[66]
CdSe	Bi_2WO_6	< 10	TC	65.38% in 60 min	Vis	(i) Responded to the visible light irradiation as bulk CdSe does; (ii) increased the visible light response, producing more electron/hole pairs due to the quantum size effect; (iii) increased the specific surface area, facilitating the adsorption of substrates; (iii) accelerated electron transition between CdSe and Bi_2WO_6, facilitating the separation of photogenerated carriers.	[67]
Cu_2O	BiOBr	10	Phenol	86.2% in 5 h	Vis	(i) Responded to the visible light irradiation as bulk Cu_2O does; (ii) formed a type-II band alignment with BiOBr, donating e^- and accepting h^+, and thus facilitated the separation of photogenerated carriers; (iii) improved visible light absorption and increased photon conversion efficiencies due to the quantum effects; (ii) increased the specific surface area, which was beneficial for the adsorption of substrates.	[68]
			MB	95% in 60 min			

Bi_2O_3	N-Bi_3NbO_7	2-8	MB	98.5% in 40 min	Vis	(i) Responded to the visible light irradiation as bulk Bi_2O_3 does; (ii) formed a type-II band alignment with N-Bi_3NbO_7, facilitating the separation of photogenerated carriers by accepting e^- from the CB of N-Bi_3NbO_7 while donating h^+ to the VB of N-Bi_3NbO_7; (iii) enhanced the light absorbance due to the multiple reflections in the heterostructure; (iv) increased the specific surface area, which was beneficial for the adsorption of substrates.	[69]
Ag_3PO_4	$BiPO_4$	5	MO	97% in 30 min	Vis	(i) Responded to the visible light irradiation as bulk Ag_3PO_4 does; (ii)enhanced visible light absorption due to the quantum size effect; (iii) formed a p-n heterojunction with the non-visible-light-responsive $BiPO_4$, sensitizing it by injecting e^- to its CB, which was also advantageous for the separation of photogenerated carriers.	[70]
CdS	Bi_2WO_6	2-5	MO	97.1% in 3 h	Vis	(i) Responded to the visible light irradiation as bulk Cu_2O does; (ii) strongly absorbed visible light due to multiple excitations from the absorption of a single photon, and thus improved the energy conversion efficiency of the system; (iii) formed a type-II band alignment with BiOBr, donating e^- and accepting h^+, which facilitated the separation of photogenerated carriers.	[71]
			Phenol	97% in 3 h			
AgBr	Mesoporous Bi_2WO_6	10	MB	100% in 60 min	Vis	(i) Responded to the visible light irradiation as bulk AgBr does; (ii) formed a p-n heterojunction with the mesoporous Bi_2WO_6, donating e^- and accepting h^+, which facilitated the separation of photogenerated carriers.	[72]
CdS	Functionalized-multi-walled carbon nanotubes	1.3	MO	100% in 80 min	UV	Responded to the UV irradiation as bulk CdS and Ag_2S do.	[73]
Ag_2S		8.4		100% in 110 min			
Bi_2WO_6	Reduced graphene oxide	3-5	RhB	95% in 15 min	Vis	Responded to the visible light irradiation as bulk Bi_2WO_6 does.	[74]
			MB	88% in 25 min			
ZnS	Chitosan	3.8	MB	87% in 120 min	UV	Significantly increased the absorption of UV irradiation compared to bulk ZnS due to the size confinement caused by the small dimension of the QDs, producing a higher redox potential in the system.	[75]

Carbon	Cu_2O	-	MB	90% in 240 min	NIR	(i) Upconverted the incident light with the wavelength of longer than 700 nm to the range of 390-564 nm that could be absorbed by Cu_2O, which improved the energy conversion efficiency of the photocatalytic system; (ii) accepted e^- from the CB of Cu_2O, facilitating the separation of photogenerated carriers; (iii) increased the specific surface area; (iv) formed a π-π interaction between the conjugated structure of CQDs and the benzene ring of MB, which facilitated the adsorption of MB.	[76]
Carbon	BiOBr	5	RhB	100% in 50 min	Vis	(i) Upconverted long-wavelength incident to shorter-wavelength emission that could be absorbed by BiOBr or BiOCl, which improved the energy conversion efficiency of the photocatalytic system; (ii) accepted e^- from the VB of BiOBr or BiOCl, facilitating the separation of photogenerated carriers.	[77]
			CIP	68% in 4 h			
			BPA	55% in 3 h			
	BiOCl		RhB	100% in 50 min			
			CIP	69% in 4 min			
Carbon	Mesoporous α-Fe_2O_3	3	MB	87.7% in 90 min	Vis	(i) Facilitated e^- transfer due to its conjugated network structure, which enhanced the separation of photogenerated carriers and produced more reactive species as well; (ii) increased the specific surface area, which was in favor of substrate adsorption.	[78]
Graphene	TiO_2	9.6	MB	97	Vis	Upconverted the incident light with the wavelength in the range of 500-700 nm to the useful area of ~407 nm that could be absorbed by rutile TiO_2, which improved the energy conversion efficiency of the photocatalytic system.	[79]

*: This is the average diameter of the produced quantum dots.
**: Pseudo-second-order reaction was sued as the models unless stated.
Note: all degradation efficiency and rate constant are obtained under the optimal reaction conditions in each research.

References:

[1] D. Li, J.F. Huang, L.Y. Cao, J.Y. Li, H.B. Ouyang, C.Y. Yao, Microwave hydrothermal synthesis of K+ doped ZnO nanoparticles with enhanced photocatalytic properties under visible-light, Mater. Lett. 118 (2014) 17–20. doi:10.1016/j.ceramint.2013.10.061.

[2] C. Wu, L. Shen, Y.C. Zhang, Q. Huang, Solvothermal synthesis of Cr-doped ZnO nanowires with visible light-driven photocatalytic activity, Mater. Lett. 65 (2011) 1794–1796. doi:10.1016/j.matlet.2011.03.070.

[3] R. Mohan, K. Krishnamoorthy, S.-J. Kim, Enhanced photocatalytic activity of Cu-doped ZnO nanorods, Solid State Commun. 152 (2012) 375–380. doi:10.1016/j.ssc.2011.12.008.

[4] J.B. Zhong, J.Z. Li, J. Zeng, X.Y. He, W. Hu, Y.C. Shen, Enhanced photocatalytic performance of Ga3+-doped ZnO, Mater. Res. Bull. 47 (2012) 3893–3896. doi:10.1016/j.materresbull.2012.08.031.

[5] C. Wu, L. Shen, H. Yu, Q. Huang, Y.C. Zhang, Synthesis of Sn-doped ZnO nanorods and their photocatalytic properties, Mater. Res. Bull. 46 (2011) 1107–1112. doi:10.1016/j.materresbull.2011.02.043.

[6] H.F. Moafi, M.A. Zanjanchi, A.F. Shojaie, Tungsten-doped ZnO nanocomposite: Synthesis, characterization, and highly active photocatalyst toward dye photodegradation, Mater. Chem. Phys. 139 (2013) 856–864. doi:10.1016/j.matchemphys.2013.02.044.

[7] X. Li, J. Zang, Hydrothermal synthesis and characterization of Lanthanum-doped $NaTaO_3$ with high photocatalytic activity, Catal. Commun. 12 (2011) 1380–1383. doi:10.1016/j.catcom.2011.05.004.

[8] A. Zhang, J. Zhang, Effects of europium doping on the photocatalytic behavior of BiVO4, J. Hazard. Mater. 173 (2010) 265–272. doi:10.1016/j.jhazmat.2009.08.079.

[9] M. Faisal, A.A. Ibrahim, H. Bouzid, S.A. Al-Sayari, M.S. Al-Assiri, A.A. Ismail, Hydrothermal synthesis of Sr-doped α-Bi2O3 nanosheets as highly efficient photocatalysts under visible light, J. Mol. Catal. A Chem. 387 (2014) 69–75. doi:10.1016/j.molcata.2014.02.018.

[10] M. Wang, H. Zheng, Q. Liu, C. Niu, Y. Che, M. Dang, High performance B doped BiVO4 photocatalyst with visible light response by citric acid complex method, Spectrochim. Acta - Part A Mol. Biomol. Spectrosc. 114 (2013) 74–79. doi:10.1016/j.saa.2013.05.032.

[11] G. Tan, L. Zhang, H. Ren, J. Huang, W. Yang, A. Xia, Microwave hydrothermal synthesis of N-doped BiVO4 nanoplates with exposed (040) facets and enhanced visible-light photocatalytic properties, Ceram. Int. 40 (2014) 9541–9547. doi:10.1016/j.ceramint.2014.02.028.

[12] J. Yu, B. Wei, L. Zhu, H. Gao, W. Sun, L. Xu, Flowerlike C-doped BiOCl nanostructures: Facile wet chemical fabrication and enhanced UV photocatalytic properties, Appl. Surf. Sci. 284 (2013) 497–502. doi:10.1016/j.apsusc.2013.07.124.

[13] L. Ma, L. Xu, X. Xu, X. Zhou, L. Zhang, One-Pot Hydrothermal Synthesis of Sulfur-Doped SnO2 Nanoparticles and their Enhanced Photocatalytic Properties, Nanobr. Reports Rev. 11 (2016) 1650035. doi:10.1142/S1793292016500351.

[14] H. Lin, X. Li, J. Cao, S. Chen, Y. Chen, Novel I--doped BiOBr composites: Modulated valence bands and largely enhanced visible light phtotocatalytic activities, Catal. Commun. 49 (2014) 87–91. doi:10.1016/j.catcom.2014.02.010.

[15] A.M. Al-Hamdi, M. Sillanpaa, J. Dutta, M. Sillanpää, J. Dutta, Photocatalytic degradation of phenol by iodine doped tin oxide nanoparticles under UV and sunlight irradiation, J. Alloys Compd. 618 (2015) 366–371. doi:10.1016/j.jallcom.2014.08.120.

[16] X. Zhang, L. Zhang, Electronic and band structure tuning of ternary semiconductor photocatalysts by self doping: The case of BiOI, J. Phys. Chem. C. 114 (2010) 18198–18206. doi:10.1021/jp105118m.

[17] X. Ding, K. Zhao, L. Zhang, Enhanced photocatalytic removal of sodium pentachlorophenate with self-doped Bi2WO6 under visible light by generating more superoxide ions, Environ. Sci. Technol. 48 (2014) 5823–5831. doi:10.1021/es405714q.

[18] Y. Ding, F. Yang, L. Zhu, N. Wang, H. Tang, Bi3+ self doped NaBiO3 nanosheets: Facile controlled

synthesis and enhanced visible light photocatalytic activity, Appl. Catal. B Environ. 164 (2015) 151–158. doi:10.1016/j.apcatb.2014.09.019.

[19] G. Muruganandam, N. Mala, S. Pandiarajan, N. Srinivasan, R. Ramya, E. Sindhuja, K. Ravichandran, Synergistic effects of Mg and F doping on the photocatalytic efficiency of ZnO nanoparticles towards MB and MG dye degradation, J. Mater. Sci. Mater. Electron. 28 (2017) 18228–18235. doi:10.1007/s10854-017-7771-z.

[20] L. Kong, Z. Jiang, H.H.C. Lai, T. Xiao, P.P. Edwards, Does noble metal modification improve the photocatalytic activity of BiOCl?, Prog. Nat. Sci. Mater. Int. 23 (2013) 286–293. doi:10.1016/j.pnsc.2013.05.002.

[21] M.J. Sampaio, M.J. Lima, D.L. Baptista, A.M.T. Silva, C.G. Silva, J.L. Faria, Ag-loaded ZnO materials for photocatalytic water treatment, Chem. Eng. J. (2016). doi:10.1016/j.cej.2016.05.105.

[22] S. Anandan, N. Pugazhenthiran, G.J. Lee, J.J. Wu, Photocatalytic degradation of ceftiofur sodium using Au loaded Bi2CuO4 nanoparticles, J. Mol. Catal. A Chem. 379 (2013) 112–116. doi:10.1016/j.molcata.2013.08.002.

[23] H.-Y. Jiang, K. Cheng, J. Lin, Crystalline metallic Au nanoparticle-loaded α-Bi2O3 microrods for improved photocatalysis, Phys. Chem. Chem. Phys. 14 (2012) 12114. doi:10.1039/c2cp42165h.

[24] J. Lan, X. Zhou, G. Liu, J. Yu, J. Zhang, L. Zhi, G. Nie, Enhancing photocatalytic activity of one-dimensional KNbO3 nanowires by Au nanoparticles under ultraviolet and visible-light, Nanoscale. 3 (2011) 5161. doi:10.1039/c1nr10953g.

[25] C. Yu, F. Cao, G. Li, R. Wei, J.C. Yu, R. Jin, Q. Fan, C. Wang, Novel noble metal (Rh, Pd, Pt)/BiOX(Cl, Br, I) composite photocatalysts with enhanced photocatalytic performance in dye degradation, Sep. Purif. Technol. 120 (2013) 110–122. doi:10.1016/j.seppur.2013.09.036.

[26] Y. Huang, S. Kang, Y. Yang, H. Qin, Z. Ni, S. Yang, X. Li, Facile synthesis of Bi/Bi2WO6 nanocomposite with enhanced photocatalytic activity under visible light, Appl. Catal. B. 196 (2016) 89–99. doi:10.1016/j.apcatb.2016.05.022.

[27] H. Yu, G. Cao, F. Chen, X. Wang, J. Yu, M. Lei, Enhanced photocatalytic performance of Ag3PO4 by simutaneous loading of Ag nanoparticles and Fe(III) cocatalyst, Appl. Catal. B Environ. 160–161 (2014) 658–665. doi:10.1016/j.apcatb.2014.06.015.

[28] G. Jiang, R. Wang, X. Wang, X. Xi, R. Hu, Y. Zhou, S. Wang, T. Wang, W. Chen, Novel highly active visible-light-induced photocatalysts based on BiOBr with Ti doping and Ag decorating, ACS Appl. Mater. Interfaces. 4 (2012) 4440–4444. doi:10.1021/am301177k.

[29] Y.C. Zhang, Z.N. Du, K.W. Li, M. Zhang, D.D. Dionysiou, High-Performance Visible-Light-Driven SnS2/SnO2 Nanocomposite Photocatalyst Prepared via In situ Hydrothermal Oxidation of SnS2 Nanoparticles, ACS Appl. Mater. Interfaces. 3 (2011) 1528–1537.

[30] J. Di, J. Xia, Y. Ge, L. Xu, H. Xu, J. Chen, M. He, H. Li, Facile fabrication and enhanced visible light photocatalytic activity of few-layer MoS2 coupled BiOBr microspheres, Dalt. Trans. 43 (2014) 15429–15438. doi:10.1039/c4dt01652a.

[31] G. Yang, Z. Yan, T. Xiao, Preparation and characterization of SnO2/ZnO/TiO2 composite semiconductor with enhanced photocatalytic activity, Appl. Surf. Sci. 258 (2012) 8704–8712. doi:10.1016/j.apsusc.2012.05.078.

[32] Y. Peng, P.-P. Yu, H.-Y. Zhou, A.-W. Xu, Synthesis of BiOI/Bi4O5I2/Bi2O2CO3 p–n–p heterojunctions with superior photocatalytic activities, New J. Chem. 39 (2015) 8321–8328. doi:10.1039/C5NJ01662B.

[33] R. Ran, J.G. McEvoy, Z. Zhang, Ag2O/Ag3VO4/Ag4V2O7 heterogeneous photocatalyst prepared by a facile hydrothermal synthesis with enhanced photocatalytic performance under visible light irradiation, Mater. Res. Bull. 74 (2016) 140–150. doi:10.1016/j.materresbull.2015.08.028.

[34] S. Yang, L. Li, W. Yuan, Z. Xia, Enhanced visible light photocatalytic activity of ZnIn2S4 modified by semiconductors, Dalt. Trans. 44 (2015) 6374–6383. doi:10.1039/C5DT00147A.

[35] F.T. Li, Y. Zhao, Y.J. Hao, X.J. Wang, R.H. Liu, D.S. Zhao, D.M. Chen, N-doped P25 TiO2-amorphous Al2O3 composites: One-step solution combustion preparation and enhanced visible-light photocatalytic activity, J. Hazard. Mater. 239–240 (2012) 118–127. doi:10.1016/j.jhazmat.2012.08.016.

[36] X. Meng, Z. Zhang, Ag/AgCl Loaded Bi2WO6 Composite: A Plasmonic Z-Scheme Visible Light-Responsive Photocatalyst, Int. J. Photoenergy. 2016 (2016) 1–11. doi:10.1155/2016/4054351.

[37] X. Meng, L. Jiang, W. Wang, Z. Zhang, Enhanced Photocatalytic Activity of BiOBr/ZnO Heterojunction Semiconductors Prepared by Facile Hydrothermal Method, Int. J. Photoenergy. 2015 (2015) 1–9. doi:10.1155/2015/747024.

[38] E. Abdelkader, L. Nadjia, B. Ahmed, Synthesis, characterization and UV-A light photocatalytic activity of 20wt%SrO–CuBi2O4 composite, Appl. Surf. Sci. 258 (2012) 5010–5024. doi:10.1016/j.apsusc.2012.01.044.

[39] X.-J. Wen, C.-G. Niu, L. Zhang, G.-M. Zeng, Novel p–n heterojunction BiOI/CeO2 photocatalyst for wider spectrum visible-light photocatalytic degradation of refractory pollutants, Dalt. Trans. 46 (2017) 4982–4993. doi:10.1039/C7DT00106A.

[40] X.J. Wen, C.G. Niu, L. Zhang, C. Liang, G.M. Zeng, A novel Ag2O/CeO2 heterojunction photocatalysts for photocatalytic degradation of enrofloxacin: possible degradation pathways, mineralization activity and an in depth mechanism insight, Appl. Catal. B Environ. 221 (2018) 701–714. doi:10.1016/j.apcatb.2017.09.060.

[41] F. Qiu, W. Li, F. Wang, H. Li, X. Liu, J. Sun, In-situ synthesis of novel Z-scheme SnS2/BiOBr photocatalysts with superior photocatalytic efficiency under visible light, J. Colloid Interface Sci. 493 (2017) 1–9. doi:10.1016/j.jcis.2016.12.066.

[42] C. Song, X. Wang, J. Zhang, X. Chen, C. Li, Enhanced performance of direct Z-scheme CuS-WO3 system towards photocatalytic decomposition of organic pollutants under visible light, Appl. Surf. Sci. 425 (2017) 788–795. doi:10.1016/j.apsusc.2017.07.082.

[43] C. Yu, K. Wang, P. Yang, S. Yang, C. Lu, Y. Song, S. Dong, J. Sun, J. Sun, One-pot facile synthesis of Bi2S3/SnS2/Bi2O3 ternary heterojunction as advanced double Z-scheme photocatalytic system for efficient dye removal under sunlight irradiation, Appl. Surf. Sci. 420 (2017) 233–242. doi:10.1016/j.apsusc.2017.05.147.

[44] Q. Li, Z. Guan, D. Wu, X. Zhao, S. Bao, B. Tian, J. Zhang, Z-Scheme BiOCl-Au-CdS Heterostructure with Enhanced Sunlight-Driven Photocatalytic Activity in Degrading Water Dyes and Antibiotics, ACS Sustain. Chem. Eng. 5 (2017) 6958–6968. doi:10.1021/acssuschemeng.7b01157.

[45] Y. Wang, R. Shi, J. Lin, Y. Zhu, Enhancement of photocurrent and photocatalytic activity of ZnO hybridized with graphite-like C3N4, Energy Environ. Sci. 4 (2011) 2922–2929. doi:10.1039/c0ee00825g.

[46] L. Liu, Y. Qi, J. Yang, W. Cui, X. Li, Z. Zhang, An AgI@g-C3N4 hybrid core@shell structure: Stable and enhanced photocatalytic degradation, Appl. Surf. Sci. 358 (2015) 319–327. doi:10.1016/j.apsusc.2015.07.212.

[47] S. Kumar, A. Baruah, S. Tonda, B. Kumar, V. Shanker, B. Sreedhar, Cost-effective and eco-friendly synthesis of novel and stable N-doped ZnO/g-C3N4 core-shell nanoplates with excellent visible-light responsive photocatalysis, Nanoscale. 6 (2014) 4830–42. doi:10.1039/c3nr05271k.

[48] Y. Lin, D. Li, J. Hu, G. Xiao, J. Wang, W. Li, X. Fu, Highly Efficient Photocatalytic Degradation of Organic Pollutants by PANI-Modified TiO2 Composite, J. Phys. Chem. C. 116 (2012) 5764–5772. doi:10.1021/jp211222w.

[49] B. Gao, W. Chen, S. Dong, J. Liu, T. Liu, L. Wang, M. Sillanpää, Polypyrrole/ZnIn2S4 composite photocatalyst for enhanced mineralization of chloramphenicol under visible light, J. Photochem. Photobiol. A Chem. 349 (2017) 115–123. doi:10.1016/j.jphotochem.2017.09.018.

[50] J. Xu, Y. Hu, C. Zeng, Y. Zhang, H. Huang, Polypyrrole decorated BiOI nanosheets: Efficient photocatalytic activity for treating diverse contaminants and the critical role of bifunctional polypyrrole, J. Colloid Interface Sci. 505 (2017) 719–727. doi:10.1016/j.jcis.2017.06.054.

[51] H. Matsui, A. Ishiko, S. Karuppuchamy, M. Yoshihara, Synthesis and characterization of MoO3/carbon clusters/ZrO2 composite materials, J. Alloys Compd. 473 (2009) 33–38. doi:10.1016/j.jallcom.2008.06.039.

[52] H. Fu, T. Xu, S. Zhu, Y. Zhu, Photocorrosion Inhibition and Enhancement of Photocatalytic Activity for ZnO via Hybridization with C Photocorrosion Inhibition and Enhancement of Photocatalytic Activity for ZnO via Hybridization with C60, 42 (2008) 8064–8069. doi:10.1021/es801484x.

[53] L. Yang, D. Chu, L. Wang, X. Wu, J. Luo, Synthesis and photocatalytic activity of chrysanthemum-like Cu2O/Carbon Nanotubes nanocomposites, Ceram. Int. 42 (2016) 2502–2509. doi:10.1016/j.ceramint.2015.10.051.

[54] D. Jiang, W. Ma, P. Xiao, L. Shao, D. Li, M. Chen, Enhanced photocatalytic activity of graphitic carbon nitride/carbon nanotube/Bi2WO6 ternary Z-scheme heterojunction with carbon nanotube as efficient electron mediator, J. Colloid Interface Sci. 512 (2018) 693–700. doi:10.1016/j.jcis.2017.10.074.

[55] S. Li, S. Hu, K. Xu, W. Jiang, J. Liu, Z. Wang, A Novel Heterostructure of BiOI Nanosheets Anchored onto MWCNTs with Excellent Visible-Light Photocatalytic Activity, Nanomaterials. 7 (2017) 22. doi:10.3390/nano7010022.

[56] Y. Fu, X. Sun, X. Wang, BiVO4–graphene catalyst and its high photocatalytic performance under visible light irradiation, Mater. Chem. Phys. 131 (2011) 325–330. doi:10.1016/j.matchemphys.2011.09.049.

[57] P. Gao, J. Liu, D.D. Sun, W. Ng, Graphene oxide-CdS composite with high photocatalytic degradation and disinfection activities under visible light irradiation, J. Hazard. Mater. 250–251 (2013) 412–420. doi:10.1016/j.jhazmat.2013.02.003.

[58] R. Ran, X. Meng, Z. Zhang, Facile preparation of novel graphene oxide-modified Ag2O/Ag3VO4/AgVO3 composites with high photocatalytic activities under visible light irradiation, Appl. Catal. B Environ. 196 (2016) 1–15. doi:10.1016/j.apcatb.2016.05.012.

[59] S.Y. Dong, Y.R. Cui, Y.F. Wang, Y.K. Li, L.M. Hu, J.Y. Sun, J.H. Sun, Designing three-dimensional acicular sheaf shaped BiVO4/reduced graphene oxide composites for efficient sunlight-driven photocatalytic degradation of dye wastewater, Chem. Eng. J. 249 (2014) 102–110. doi:DOI 10.1016/j.cej.2014.03.071.

[60] Y. Min, G. He, Q. Xu, Y. Chen, Self-assembled encapsulation of graphene oxide/Ag@AgCl as a Z-scheme photocatalytic system for pollutant removal, J. Mater. Chem. A. 2 (2014) 1294–1301. doi:10.1039/C3TA13687F.

[61] R. Velmurugan, M. Swaminathan, An efficient nanostructured ZnO for dye sensitized degradation of Reactive Red 120 dye under solar light, Sol. Energy Mater. Sol. Cells. 95 (2011) 942–950. doi:10.1016/j.solmat.2010.11.029.

[62] Y. Mi, H. Li, Y. Zhang, R. Zhang, W. Hou, One-pot synthesis of belt-like Bi2S3/BiOCl hierarchical composites with enhanced visible light photocatalytic activity, Appl. Surf. Sci. 423 (2017) 1062–1071. doi:10.1016/j.apsusc.2017.06.324.

[63] A. Jia, X. Liang, Z. Su, T. Zhu, S. Liu, Synthesis and the effect of calcination temperature on the physical-chemical properties and photocatalytic activities of Ni,La codoped SrTiO3, J. Hazard. Mater. 178 (2010) 233–242. doi:10.1016/j.jhazmat.2010.01.068.

[64] R. Khan, M.S. Hassan, H.S. Cho, A.Y. Polyakov, M.S. Khil, I.H. Lee, Facile low-temperature synthesis of ZnO nanopyramid and its application to photocatalytic degradation of methyl orange dye under UV irradiation, Mater. Lett. 133 (2014) 224–227. doi:10.1016/j.matlet.2014.07.006.

[65] Y. Guo, L. Wang, L. Yang, J. Zhang, L. Jiang, X. Ma, Optical and photocatalytic properties of arginine-stabilized cadmium sulfide quantum dots, Mater. Lett. 65 (2011) 486–489. doi:10.1016/j.matlet.2010.10.057.

[66] X. Zhang, C. Shao, Z. Zhang, J. Li, P. Zhang, M. Zhang, J. Mu, Z. Guo, P. Liang, Y. Liu, In situ Generation of Well-Dispersed ZnO Quantum Dots on Electrospun Silica Nanotubes with High Photocatalytic Activity, ACS Appl. Mater. Interfaces. 4 (2012) 785–790. doi:10.1021/am201420b.

[67] X. Liu, M. Zhou, G. Yao, W. Shi, C. Ma, P. Lv, Y. Tang, Y. Yan, Hydrothermal synthesis and enhanced visible-light photocatalytic activity of octahedral Bi2WO6 modified with CdSe quantum dots, RSC Adv. 4 (2014) 18264–18269. doi:10.1039/c3ra46590j.

[68] W. Cui, W. An, L. Liu, J. Hu, Y. Liang, Novel Cu2O quantum dots coupled flower-like BiOBr for enhanced

photocatalytic degradation of organic contaminant, J. Hazard. Mater. 280 (2014) 417–427. doi:10.1016/j.jhazmat.2014.08.032.

[69] J. Hou, Z. Wang, S. Jiao, H. Zhu, Bi2O3 quantum-dot decorated nitrogen-doped Bi3NbO7 nanosheets: in situ synthesis and enhanced visible-light photocatalytic activity, CrystEngComm. 14 (2012) 5923. doi:10.1039/c2ce25504a.

[70] H. Lin, H. Ye, B. Xu, J. Cao, S. Chen, Ag3PO4 quantum dot sensitized BiPO4: A novel p-n junction Ag3PO4/BiPO4 with enhanced visible-light photocatalytic activity, Catal. Commun. 37 (2013) 55–59. doi:10.1016/j.catcom.2013.03.026.

[71] L. Ge, J. Liu, Efficient visible light-induced photocatalytic degradation of methyl orange by QDs sensitized CdS-Bi2WO6, Appl. Catal. B Environ. 105 (2011) 289–297. doi:10.1016/j.apcatb.2011.04.016.

[72] D. Wang, L. Guo, Y. Zhen, L. Yue, G. Xue, F. Fu, AgBr quantum dots decorated mesoporous Bi2WO6 architectures with enhanced photocatalytic activities for methylene blue, J. Mater. Chem. A. 2 (2014) 11716. doi:10.1039/C4TA01444H.

[73] G.M. Neelgund, A. Oki, Photocatalytic activity of CdS and Ag2S quantum dots deposited on poly(amidoamine) functionalized carbon nanotubes, Appl. Catal. B Environ. 110 (2011) 99–107. doi:10.1016/j.apcatb.2011.08.031.

[74] S. Sun, W. Wang, L. Zhang, Bi2WO6 Quantum Dots Decorated Reduced Graphene Oxide: Improved Charge Separation and Enhanced Photoconversion Efficiency, J. Phys. Chem. C. 117 (2013) 9113–9120. doi:10.1021/jp4004592.

[75] A.A.P. Mansur, H.S. Mansur, F.P. Ramanery, L.C. Oliveira, P.P. Souza, "Green" colloidal ZnS quantum dots/chitosan nano-photocatalysts for advanced oxidation processes: Study of the photodegradation of organic dye pollutants, Appl. Catal. B Environ. 158–159 (2014) 269–279. doi:10.1016/j.apcatb.2014.04.026.

[76] H. Li, R. Liu, Y. Liu, H. Huang, H. Yu, H. Ming, S. Lian, S.-T. Lee, Z. Kang, Carbon quantum dots/Cu2O composites with protruding nanostructures and their highly efficient (near) infrared photocatalytic behavior, J. Mater. Chem. 22 (2012) 17470. doi:10.1039/c2jm32827e.

[77] J. Xia, J. Di, H.H. Li, H. Xu, H.H. Li, S. Guo, Ionic liquid-induced strategy for carbon quantum dots/BiOX (X=Br, Cl) hybrid nanosheets with superior visible light-driven photocatalysis, Appl. Catal. B Environ. 181 (2016) 260–269. doi:10.1016/j.apcatb.2015.07.035.

[78] B.Y. Yu, S.-Y. Kwak, Carbon quantum dots embedded with mesoporous hematite nanospheres as efficient visible light-active photocatalysts, J. Mater. Chem. 22 (2012) 8345. doi:10.1039/c2jm16931b.

[79] S. Zhuo, M. Shao, S.-T. Lee, Upconversion and dowconversion fluorescent graphene quantum dots: ultrasonic preparation and photocatalysis, ACS Nano. (2012) 1059–1064.

Appendix C. Effects of Operation Parameters on Heterogeneous Photocatalysis: A Brief Review

C-1 Introduction

Heterogeneous photocatalysis processing in liquid media in the presence of solid semiconductor particles is influenced by the surrounding reaction environment. Irradiation, as the source of energy, influences photon absorption and thus the production of electron/hole pairs. Initial pH and temperature of the reaction suspension impact on the adsorption of substrates, reactive radicals, and other species in the system. Initial substrate concentration and catalyst dosage not only affect the interaction between the substrate and catalyst particles but may influence light absorption effect by changing the transmittance of the slurry reaction system as well. The presence of additional oxidants determines the amount of produced reactive species, and even the functioning mechanism in a specific system. The existence of other ions may also influence the production of reactive species by reacting with photogenerated charge carriers or the initially produced reactive species.

C-2 Irradiation Source

Light irradiation, as the source of energy, plays a significant role in photocatalytic water decontamination. The energy an emitted photon is related to its wavelength following Equation (1), while the total amount of photons input in a system depends on the intensity of the irradiation. Therefore, both the wavelength and intensity of the irradiation need to be considered.

C-2.1 Light Wavelength

Since only incident photons with the energy greater than or equal to the bandgap energy of the employed semiconductors can be absorbed and used for the subsequent surface reaction, and considering the inverse proportionality between energy and wavelength, there is a maximal wavelength of light that can trigger a specific semiconductor. Solar radiation reaching the earth

can be divided into three groups depending on the wavelength: UV (λ < 390nm), visible (390nm < λ < 700nm), and infrared irradiation (λ > 700nm).

As the origin and most comprehensively studied catalyst of photocatalytic water decontamination, TiO_2 makes use of UV irradiation, based on its bandgap energy (~3.2 eV), which makes UV irradiation the most common energy source. Conventional UV source in photocatalysis includes mercury vapor lamps [1–4], xenon arc Lamps (300-800W) [5,6], halogen lamps [7,8], tungsten-halogen lamps [9,10], , etc.. The electromagnetic spectrum of UV irradiation can be classified as UV-A (315-400 nm, 3.10-3.94 eV), UV-B (280-315nm, 3.94-4.43 eV), and UV-C (100-280nm, 4.43-12.4 eV) according to the emitting wavelength and energy.

However, considering the disadvantages of traditional UV lamps, such as short lifetime, instability of the output power and the hazardous materials from the emitted wastes and harmful light to humans, novel UV sources have been proposed. Optical fibers were explored to be a novel light source by Ollis and Marinangeli as they realized the remote delivery of photon energy to the reactive sites on the photocatalyst [11], and have been applied in numbers of novel photoreactors [12–15] as the main development in improving the quantum efficiency. Yet, the most significant drawback of using optical fibers is that the light intensity decays exponentially along the axial direction of the coated fibers [16]. In 2005, Chen et al. used a novel UV LED as the radiation source for photocatalysis for the first time, which facilitated perchloroethylene degradation on Degussa P-255. UV LEDs take advantages of long-lasting, robust, small size and high efficiency, as well as narrow light-emission spectra and adjustable wavelength that can be designed to reach desirable positions. Plus, they do not contain mercury vapor as fluorescent lamps do. [17] Hence, they are regarded as a promising light source for photocatalysis. Shie et al. compared the effects of three light sources, UV-A, UV-C, and UV LEDs on the photocatalytic decomposition of formaldehyde using Ag-loaded TiO_2. It can be seen from C-1 that with the similar decomposition efficiency, the energy effectiveness using 40 UV LEDs was 99 and 131 times to that using UVA and UVC as the light source, respectively. [18]

Table C- 1 Decomposition efficiency (η_D) and energy effectiveness (E_e) for the photocatalytic decomposition of formaldehyde using Ag/TiO_2 in UV light reaction system. Adapted with permission from [18]. Copyright (2007) Elsevier.

Light Source	η_D (%)	Reaction time (h)	E_e ($mg\ kW^{-1}\ h^{-1}$)
UV-A	96	7	0.0070
UV-C	97	7	0.0053
40 UV LEDs	95	7	0.6942

In terms of visible light, the most applied radiation source is 300-500 W Xe lamp accompanied by a cut-off filter placed underneath to exclude the wavelength lower than 400 or 420 nm. The filter can be made by glass [19] or methyl methacrylate (PMMA) materials [20]. Sometimes high-pressure Xe lamps and Xe-arc lamps with suitable filters are also employed, such as the research on RhB degradation on the $BiOBr/g\text{-}C_3N_4$ composite [21] and $CQDs/Bi_2WO_6$ [22], respectively. Halogen and halogen-tungsten lamps with filters are also widely used as visible light sources [8,9]. Wang et al. investigated the photocatalytic activity of AgBr-QDs/Bi_2WO_6 composites using a Xe-arc lamp with a 420 nm cut-off filter as the visible light source, and realized a complete degradation of methylene blue within 1 h [23]. Some other lamps being capable of providing visible light, such as regular daylight lamps [24], halide lamps [25], metal halide lamps [26], and Hg lamps [27], are also harnessed with filters eliminating the ultraviolet part.

Same as UV LED irradiation, the energy saving effect was also found on 450 nm visible light LED illumination, as indicated by Dai et al. [28]. Furthermore, Wang et al. investigated visible-light photocatalytic degradation of Penicillin G using Ag-AgBr/TiO_2/rGO under different colors of LED irradiation, LED-W (white light, emissino wavelength λ=450 nm), LED-B (blue light, 465 nm), LED-G (green light, 523 nm), and LED-Y (yellow light, 589 nm). Results manifested that the degradation efficiencies were 99%, 88%, 50% and 28 % after 2h irradiated by LED-W, B, G and Y irradiations, respectively, as shown in Figure C-1. It was indicated that Ag-AgBr/TiO_2/rGO could be photoexcited when the wavelength reached as high as 600 nm, while AgBr possessed a band gap of 2.6 eV and thus could be responsive to irradiation with the wavelength at less than 477 nm. Therefore, it was implied that Ag NPs were responsible for light absorption in the region of 477 to 600 nm, which was attributed to its LSPR effect. [29]

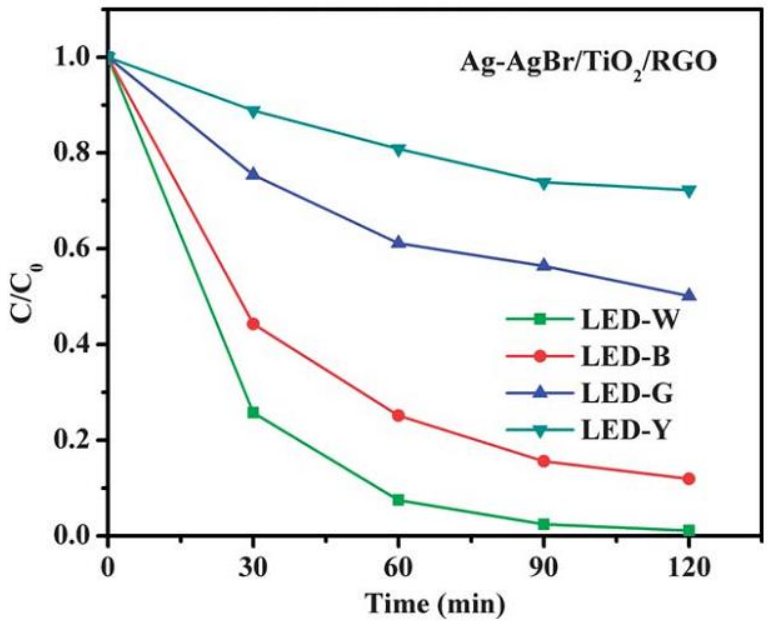

Figure C- 1 Photocatalytic degradation of PG using Ag-AgBr/TiO_2/rGO under different colors of LED irradiation. Reprinted with permission from [29]. Copyright (2013) Royal Society of Chemistry.

In a dual Z-scheme $BiVO_4/Ag/Cu_2O$ system using 300 W Xe lamp as the light source where Ag NPs acted as the mediator for photogenerated charge transfer, the effect of light wavelength was investigated by using and removing a UV cutoff filter (λ>420 nm). Towards TC decomposition, photocatalytic performance of the catalyst composite was better when the UV filter was removed. This was because without the filter, the photocatalysts could utilize the full spectrum of the Xe lamp, including the photons with the wavelength less than 420 nm, which possess higher energy than those with longer wavelength. [30] Similarly, in the photocatalytic degradation of MO with Bi_4NbO_8Cl, Bi_3O_4Cl, and anatase TiO_2 working separately, the photocatalytic performances followed the order of $Bi_4NbO_8Cl > Bi_3O_4Cl >$ anatase TiO_2 with the full arc of 600 W Xe lamp, while it was $Bi_3O_4Cl >$ anatase $TiO_2 > Bi_4NbO_8Cl$ with a cutoff filter at the wavelength of 405 nm [31] .

Additionally, some distinction effects in photocatalysis, such as the SPR effect of metal NPs, dye-sensitization, and the upconversion property of QDs, may only exhibit in the presence of visible light, so that the photocatalytic performance may be better compared to in the case of UV irradiation. For example, Melorose et al. investigated the effect of N^{4-}/Ag^{+}-codoped ZnO with respect to the decomposition of MR under UV and visible light irradiation. Results showed that both the reaction rate and the degradation efficiency were higher when the system was illuminated

by visible light. This was explained by the SPR effect of Ag^{o} NPs generated from Ag^{+} accepting e^{-} during the reaction under visible light irradiation. [32]

C-2.2 Light Intensity

Light intensity determines the amount of emitted photons at a given wavelength; the higher the light intensity is, the more photons emitted [33]. Furthermore, considering that energy needed for producing e^{-}/h^{+} pairs is provided by absorbed photons, more carriers are expected to be produced with higher light intensity. Yet, since the produced carriers are involved not only in surface reactions, but also in recombination, there are no absolute relations between the light intensity and reaction rates, rather, the correlation differs as the intensity changes. The effects of light intensity on photocatalytic kinetics has been summarized as the follows: (i) at low light intensities, reaction rate increases linearly with the increasing light intensity; (ii) at medium light intensities, reaction rate depends on the square root of the light intensity and; (iii) at high light intensities, reaction rate is independent of light intensity This can be explained as the following correspondingly: (i) at low light intensity, the formation of e^{-}/h^{+} pairs predominates, and recombination is negligible due to the small amount of photogenerated carriers; (ii) as the light intensity increasing to a medium level, more carriers are induced, and recombination becomes a rival of carrier transfer, thereby the facilitation of photocatalysis carried out by the latter gets lower; (iii) when the light intensity raises so high that an absorption saturation is reached, reaction rate will not be affected anymore. [34,35]

In a TiO_2/UV system, investigations carried out at different light intensities indicated that the rate of EDTA degradation was proportional to the square root of the light intensity at moderate values and became independent from the light intensity at higher values [36]. Gupta et al. reported a linear relationship between the pseudo-first order rate constant and the light intensity at a low intensity level during the degradation of an azo dye Amaranth in the TiO_2/UV process. The same conclusion was also manifested in the degradation of phenol and chloroform in a ZnO/UV system. Table C-2 shows the comparison of efficiencies of different light intensities on the degradation rate of AB 14 carried out on ZnO and TiO_2. [37] However, Peill and Hoffmann proposed that the light intensity was inversely proportional to the quantum efficiency in photocatalysis [38], attributed to easy recombination of charge carriers at a relatively high intensity [39]. Therefore, the selection of light sources needs to be deliberate.

Table C- 2 Effect of light intensity on degradation rate of acid brown 14. Adapted with permission from [37]. Copyright (2002) Elsevier.

Light intensity ($\times 10^5$lx)	ZnO		TiO_2	
	K_{App}	R	K_{App}	R
0.28-0.39	3.08	3.08	0.33	0.33
0.50-0.80	3.35	3.35	0.48	0.48
0.85-0.90	3.58	3.58	0.83	0.83
0.88-0.92	3.75	3.75	1.27	1.27
0.92-1.21	4.17	4.17	1.40	1.40
1.21-1.31	4.27	4.27	2.45	2.45
1.24-1.32	5.27	5.27	2.70	2.70
1.31-1.35	5.48	5.48	3.00	3.00
1.32-1.37	7.48	7.48	3.08	3.08

Where, K_{App} is the pseudo first-order rate constant ($\times 10^{-4}, s^{-1}$), R is the initial reaction rate ($\times 10^{-8}$, mol L^{-1} s^{-1}), concentration of acid brown 14 is 5×10^{-4} mol L^{-1}, catalyst amount is 2.5 g L^{-1}, pH is 9.41.

It was also found that the illumination mode may also have an impact on the photocatalytic activity. For example, UV LEDs were reported to possess the genetic character of high-frequency periodic lighting capacity, which was 7-10 times higher than for those with continuous illumination [40]. Buechler et al. compared the photonic efficiency of two systems under the periodic and continuous UV light irradiation, respectively, and found the efficiency of the former was 4 times higher than that of the latter [41]. A similar result was reported by Wang and Ku, who investigated the effect of periodic illumination on the photocatalytic decomposition rate of RR 22, and found the overall photo efficiency ($18.9 - 24.3 \times 10^{-3}$) was much higher than that (about 2.5×10^{-3}) conducted with continuous illumination [40]. Xu et al. applied two UV radiation sources, a continuous-wave UV lamp and an excimer laser, for the photocatalytic oxidation of 2-propanol and acetone on TiO_2 powders by in situ FTIR. Results indicated that the excimer laser source accelerated the degradation of 2-propanol while decelerated that of acetone as compared to the continuous-wave source. The reason was speculated that the laser source changed the reaction mechanism by introducing an abrupt temperature increase, and hence impacted on the thermal decomposition. [42]

Light intensity may closely relate with the employed photoreactors as well. During the MB decomposition in the TiO_2/UV system, identical high-pressure mercury lamps were used for two different reactors: one had a cylindrical shape with a bottom optical window through which the suspension was irradiated, and the other was equipped with a plunging tube containing the lamp. With other reaction conditions remaining the same, the UV intensity reaching the reactor of the former was ~1.16 times that of the latter, which was attributed to the different reactor structures. [43]

C-3 Initial pH

Since the produced reactive radicals, intermediates and products during the reaction would influence the pH of a system, the effects of pH is usually with regard to the initial pH value before photocatalysis begins.

pH plays multiple roles in photocatalysis due to its effects on surface charge properties [44], energy bands [45] of the catalysts, and production distribution [46], etc.. Furthermore, industrial wastewater is usually not neutral, but rather, very acidic or basic. Thus, the effects of pH are necessary to be taken into consideration.

The most important effect of pH is its influence on the surface charge property of semiconductors [47,48]. For each catalyst, there is a particular pH value called the point of zero charge (pH_{PZC}), at which its net surface charge is zero. There are three situations of the comparison between the its pH_{PZC} and the initial pH and:

i) When the initial pH$>$ pH_{PZC}, the semiconductor surface will be negatively charged by adsorbed hydroxyl ions in the reaction media. Therefore, the adsorption of cationic pollutants on the semiconductor surface will be enhanced, and the production of •OH will be facilitated as well because of the large amount of adsorbed OH^-, which is deemed as the source of •OH following Equation (C.1), resulting in a better photocatalytic performance. On the contrary, the adsorption of anionic substrate adsorption would be hindered, and so would its degradation.

$$h_{VB}{}^{+} + OH^- \rightarrow \bullet OH \qquad (C.1)$$

ii) At pH_{PZC}, the interaction among particles present in the system is minimal due to the absence of electrostatic force, and hence hard to be separated by interactional rejection. As a result, aggregation of substrates and sedimentation of catalysts will occur and uniform distribution cannot be guaranteed, which is in favored to photocatalysis. On the other hand, this property may be useful for catalyst recovery and reuse. It was reported that with such a neutralization strategy, almost 97% of the catalysts (TiO_2) were successfully recovered [35].

iii) When the initial pH< pH_{PZC}, the semiconductor surface will be positively charged with H^+ ions in the reaction media, leading to a strong adsorption of anionic compounds while weak towards cationic substrates. Since the adsorbed H^+ covers a large part of the catalyst surface, which would attract photogenerated electrons and hinder the adsorption of OH^-, producing less •OH. Thus, h^+ would be the primary reactive species in this case [44,46].

From the investigation of the effect of pH on the photocatalytic degradation of BPA over C-doped ZnO, pH_{PZC} of the photocatalyst was 7.5 measured by the pH drift method, while the pKa of BPA was approximately 9.6. Therefore, at acidic pH less than 7.5 both C-doped ZnO and BPA were positively charged, so that the poor interaction between them led to an inferior degradation. At pH between 7.5 and 9.6, C-doped ZnO was negatively charge while BPA was positively charged. At pH greater than 9.6, the catalyst and BPA were both negatively charged. As a result, the TOC conversion of the BPA photocatalytic degradation was ~22% and 31% at the pH of 3 and 11, respectively, while 50%~70% at pH between 7.3 (natural pH of 5 ppm BPA aqueous solution) and 9. [49] During the photocatalytic decomposition of 2-NP on Bi_2WO_6/TiO_2 nanotube array composite under visible light irradiation, pH influenced not only the adsorption of 2-NP on the catalyst, but the amount of • OH as well. At pH 6.0, both the adsorption of 2-NP on Bi_2WO_6/TiO_2 composites and the density of produced hydroxyl radicals reached the optimal condition and thus exhibited the highest photodegradation efficiency. [50]

Except for the adsorption amount, adsorption mode may also be influenced by pH. For the as-prepared Bi_2WO_6/SnS heterostructured composites, the attaching modes of RhB on the catalyst surface changed from via the carboxylic group to the amino group as pH increased, which favors the photosensitization of RhB under visible light irradiation because the benzene ring that links to the carboxylic group is twisted against the chromophoric group, making the electron injection

through the carboxylic group impossible. The $pH_{PZC}$was found to be 3.7 by zeta potential test. Thus, the influence of pH in this case depended on the synergistic effect of adsorption and photosensitization. Specifically, in the pH region from 2 to 6, photosensitization predominated, resulting in an increased photocatalytic efficiency although the adsorption amount of RhB decreased as pH rose in this range. While in the pH region from 6 to 9, adsorption decreased sharply and photosensitization was greatly inhibited as well, leading to a drastic decrease in photocatalytic efficiency. [51]

The stability of catalysts and substrates under extreme pH is another factor influencing the photocatalytic performance. Liu et al. found the prepared Bi_2WO_6 was unstable in acidic solution and completely transformed into H_2WO_4 and Bi_2O_3, and thus the decomposition of MB was severely deteriorated [52]. Yue et al. observed a dramatically increased photolysis of TC at pH 11, where more than 80% of the origin TC decomposed due to photolysis, so that the photocatalytic performance of the catalyst, a novel MWNTs-Bi_2WO_6, was hard to be determined [53].

Also, it was found that the band levels of semiconductors usually shift with a change in pH (0.059V/pH) for oxide materials, which was attributed to the adsorption-desorption equilibrium of H^+ or OH^- between the semiconductor surface and the solution [45,54].

Moreover, since surface charge properties is responsible for the product distribution given that redox reactions are very sensitive to modifications on semiconductor surface, the distribution of different products may also be influenced by pH [55]. McEvoy et al. prepared a novel Ag/AgCl-activated carbon composite photocatalyst and applied it to degrade MO. From the obtained data, the reaction rate was greatly rose with a decreasing pH. This was attributed to the different states of MO, an anionic dye, which was anionic in aqueous solutions at pH 7 and above due to the sodium ion dissolution, while amphoteric in acidic conditions because hydrogen became attached to nitrogen in the azo bond associated with the ring structure (See Figure C-2) [56]. Since the surface of both the Ag/AgCl and MO in alkaline solution were negatively charged, Coulombic repulsion on the surface hindered the adsorption. This effect was not present in acidic media, where MO took on an amphoteric structure. [46]

Figure C- 2 Methyl Orange structure in (a) acidic media, and (b) basic media. Adapted with permission from [46]. Copyright (2013) Elsevier.

C-4 Reaction Temperature

Studies discussing the effects of operation temperature on photocatalysis have found that the relation between the apparent first order rate constant (K_{app}) and temperature T follows the Arrhenius equation (Equation (C.2)), which shows a positive correlation between K_{app} and 1/T (Equation (C.3)). [47]

$$K_{app} = A * \exp(-\frac{E_a}{RT}) \quad (C.2)$$

It can also be expressed as:

$$\ln K_{app} = \ln A - \frac{E_a}{R} * \frac{1}{T} \quad (C.3)$$

where, A is the pre-exponential factor, which is independent with temperature, and E_a is the activation energy, which can be regarded as a constant in a wide temperature range.

For photocatalytic processes, activation energy (E_a) is normally small due to being driven by the rapid carrier transfer [57] and slightly rises as temperature goes up in the optimizing range. For example, E_a of RhB degradation over Ag/AgI under visible light was calculated to be 20.05 kJ/mol in the temperature range of 0-25 ^{0}C. The small activation energy indicated a weak effect of reaction temperature [26]. A similar conclusion was obtained in the ZnO/UV system decomposing C.I. Acid Yellow 23, where E_a was 12.39 kJ/mol [11].

Theoretically, as temperature increases, activities of microscopic particles are promoted thermodynamically, leading to a strong product desorption from the surface of reactants and catalyst particles. On the other hand, a high temperature also retards the adsorption of substrates onto the semiconductor surface, and recombination would be facilitated as well, which is

unfavorable to the degradation process. [47] Therefore, the impact of temperature needs to be considered deliberately, and an optimized temperature region is usually indispensable. For most photocatalytic experiments carried out under the temperature lying in the optimizing range, both reaction rate and degradation efficiency will be promoted as the temperature goes up [58–60]. When ZnO was used to degrade C.I. Acid Yellow 23 under UV irradiation, Behnajady et al. found an increasing temperature helped the reaction to compete more effectively with e^-/h^+ recombination and resulted in a better reaction efficiency [11]. Alkaim et al. observed an enhanced photocatalytic activity of EDTA degradation in the presence of TiO_2 at elevated temperature [36]. Chithambararaj et al. investigated the photocatalytic performance of a novel h-MoO_3 towards MB degradation under various temperatures under visible light, and found it was highly temperature-sensitive, reasonably attributed to the endothermic process in the suspension, which kinetically enhanced the interaction between h-MoO_3 and MB, enhanced the radical ($\bullet$ OH) generation, and prohibited recombination as well [58].

However, when temperature gets too high, E_a increases greatly, which may make the substrate thermocatalysis dominates instead, such that the over-high temperature would be detrimental to photocatalysis, and the substrate adsorption would become the rate limiting step in this case [57]. As indicated by Liang et al., the degradation efficiency of RhB on Ag/AgI catalyst decreased with the reaction temperature increased from 25 to 40 ^{0}C, mainly attributed to the reduced reactant desorption rate on the catalyst surface [26]. When temperature is lower than the minimum boundary of the optimizing spectrum, on the other hand, the apparent activation energy increases, and desorption of final products would be so restrained that become the rate-limiting step and turns to the heat of adsorption product adsorption. Meanwhile, recombination would compete more effectively with the photocatalytic reactions. [61]

C-5 Initial Substrate Concentration

Initial substrates concentration is another significant parameter controlling the photocatalysts performance. There is usually a low concentration range, in which both the photocatalytic activity and efficiency increase with the initial substrate concentration goes up due to the insufficient substrate supply. While when the concentration rose continuously, too much substrate molecules would be adsorbed on the catalyst surface, covering the effective photon-sensitive and reactive

sites. The former would reduce the number of absorbed photons and thus produce less e^-/h^+ pairs; while the latter would carry out less places for the photocatalytic processes to take place. Meanwhile, high concentration of chromatic substrates may decrease the transmittance of the reaction suspension as well as scatter the irradiation, intercepting photons before they reach the catalyst surface.

Wang et al. observed that the MO degradation rate increased when the initial concentration of MO elevated from 5 to 10 mg/L and then decreased over 10 mg/L. This was because as the initial MO concentration increased, the MO adsorption on Ag/AgBr surface was enhanced while the light absorption of Ag/AgBr paticles was curbed due to the worse transmittance of the MO solution. When the initial MO concentration increased from 5 to 10 mg/L, the adsorption of MO on Ag/AgBr surface dominated its degradation; while when the concentration was over 10 mg/L, the transmittance of MO solution became more powerful. [62]

The intermediates produced during photocatalysis may also occupy part of the limited adsorption and catalytic sites on the catalyst, as indicated by Li et al., where the degradation efficiency of RhB and MO over BiOI nanosheets both reduced as their initial concentrations rose [63]. A similar phenomenon was also found when a dual Z-scheme $BiVO_4/Ag/Cu_2O$ nanocomposite was used to decompose TC [30].

C-6 Catalyst Dosage

Catalyst dosage plays an important role in semiconductor-based photocatalysis for water decontamination, primarily owing to its close relation with cost. Same as initial substrate concentration, there is usually an optimal catalyst dosage under a given reaction environment. When the dosage increases at a low level, the amount of photo-sensitive and active sites would be increased. The former facilitates light absorption and thus charge carrier production while the latter provides more places for substrate adoption and degradation [26]. However, as the catalyst dosage rises up continuously, collision of catalyst particles would occur, reducing the photo-sensitive and active sites [64]. In addition, photocatalyst overdose may also engender a screening effect. This is because excessive catalyst particles improves the turbidity while reducing the transparency of the

suspension system, shortening the penetrating path of photons, accompanied by more scattering of incident radiation, and thus a poor photon absorption [47].

Bechambi et al. found the increase in C-doped ZnO loading was beneficial to the production of photogenerated charge carriers and other reactive oxygen species that were responsible for the BPA degradation, while the excessive catalyst caused particle agglomeration and a reduced specific surface area, resulting in a depressed photocatalytic activity [49]. Malathi et al. investigated the influence of $BiFeWO_6$/BiOI dosage on RhB photocatalytic decomposition. Results exhibited an improved efficiency as the catalyst amount increased from 0.25 g/L up to 0.75 g/L, and after that the degradation attained constant, which was attributed to the increased turbidity and the consequent decrease of light penetration. [9] Similarly, a retarded photocatalytic activity was also observed during the degradation of RR120 over ZnO nanocrystal when the catalyst loading exceeded 4 g/L, as shown in Figure C-3, which was explained as the aggregation of catalyst and its screening effect [65].

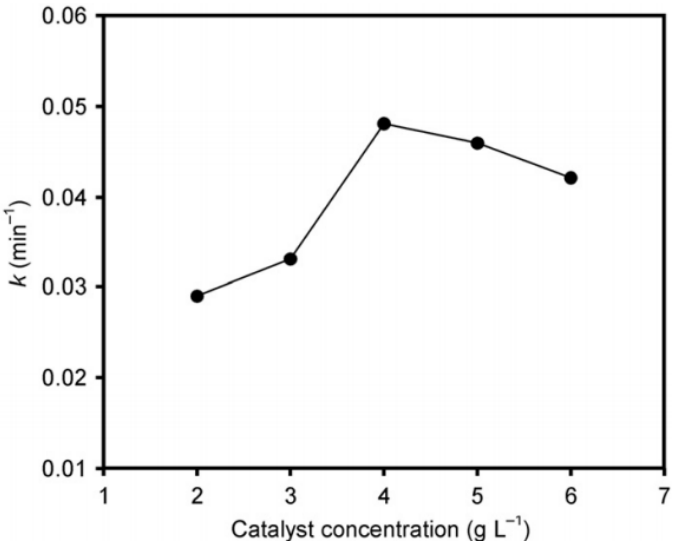

Figure C- 3 Effect of catalyst concentration: dye concentration=2×10^{-4} M, pH=5, airflow rate =8.1 mL/s and irradiation time = 30 min. Reprinted with permission from [65]. Copyright (2010) Elsevier.

C-7 Additional Oxidants

The consumption of CB electrons and VB holes is expected to proceed simultaneously during photocatalysis, but in fact, the former is much slower than the latter [66]. Considering that electrons and holes are equally generated, electrons will accumulate at CB and thus a great possibility of

recombination will be caused. Therefore, it is essential to introduce appropriate electron acceptors in order to consume the redundant electrons and produce more reactive species as well [54]. The most common oxidants that have been proven to reach this goal include O_2, O_3, H_2O_2, Fenton reagent ($Fe^{2+} + H_2O_2$) [67–70], etc.. Considering that O_3 and H_2O_2 applied to water decontamination are AOP strategies as well, the combination of photocatalysis and ozonation or hydrogen peroxide are deemed as incorporations of two AOP approaches, which will be elaborated in Appendix D-2 and D-1, respectively.

Dissolved oxygen (O_2) has been found to either support or hinder the photodegradation process depending on the degradation pathway/mechanism of a given substrate [71]. Its primary function is to capture electrons, producing $O_2^{\bullet-}$ and retarding recombination. Plus, O_2 in a slurry system, which is common in heterogeneous photocatalysis, also provides sufficient buoyant force for the suspension of catalyst particles [35]. By means of investigating the influence of oxygen partial pressure in the photocatalytic mineralization of 2- 2-CB in aqueous TiO_2 suspensions, Wang and Hong proposed that a higher O_2 partial pressure resulted in a faster rate of 2-CB transformation, which might due to the involvement of molecular oxygen in the cleavage of aromatic ring through decomposing the hydroxyl by-products, as indicated by the distribution profiles of aromatic intermediates. [72] However, dissolved oxygen molecules may have detrimental impacts as well, as proven by Shirayama et al. that O_2 weakened the UV irradiation intensity due to its absorption bands at 185 and 254 nm [73].

The mixture of ferrous ion (Fe(II)) and hydroxyl peroxide (H_2O_2) is called Fenton reagent, and if ferrous ions are replaced by ferric ions (Fe(III)) [68] or other metal ions [69], it is called Fenton-like reagent [61]. A conventional Fenton process without irradiation produces •OH following Equation (C.4). In the presence of light, the produced Fe^{3+} would be reduced back to Fe^{2+} and produce •OH as well, as indicated by Equation (C.5). On the other hand, photolysis of H_2O_2 would also occur under UV irradiation following Equation (C.6).

$$Fe^{2+} + H_2O_2 \rightarrow Fe^{3+} + OH^- + \bullet OH \quad \text{(C.24)}$$

$$Fe^{3+} + H_2O + h\nu \rightarrow Fe^{2+} + H^+ + \bullet OH \quad \text{(C.5)}$$

$$H_2O_2 + h\nu \rightarrow 2\bullet OH \quad \text{(C.6)}$$

In photocatalysis, Fenton-like reagent are more commonly used for the reduction of Fe^{3+} can be realized by photogenerated electrons (Equation (C.7)), which would not only prevent electron/hole recombination, but also enable the catalytic cycle of Fe^{2+}/Fe^{3+} and thus maintain a considerable concentration of Fe^{3+} as an electron acceptor as well as provide more reactive $\bullet OH$, as experimentally proved by Kim et al., in which study an accelerated oxidative degradation of phenol, benzoic acid, and methanol was realized benefiting from a combination of TiO_2 photocatalysis and the Fenton-like reaction under at circumneutral pH. [67] The same efficacy of Fenton-like reagents was also observed in the $WO_3/Fe(III)/H_2O_2$ system employed for the degradation of various probe compounds (benzoic acid, coumarin, and methanol). [74]

$$Fe^{3+} + e^- \rightarrow Fe^{2+} \quad \text{(C.7)}$$

However, iron sludge may also be caused during the above process, preventing the desired reaction from moving on. Therefore, Xu et al. designed a novel Bi_2WO_6/Cu^o composite photocatalyst with the synergistic effect of a Fenton-like oxidation process by immobilizing zero valent copper on the Bi_2WO_6 surface. The production of $\bullet OH$ followed Equations (C.8-9). Electrons generated on the Bi_2WO_6 CB were trapped by the produced Cu^{2+} and Cu^+, regenerating Cu^+ and Cu^o, respectively. This process not only inhibited recombination but prevented Cu^o from leaching as well. As a result, the degradation efficiency of phenol was rose from less than 20% up to nearly 60% and after five runs no significant loss of activity exhibited. [69]

$$Cu^o + H_2O_2 \rightarrow Cu^+ + OH^- + \bullet OH \quad \text{(C.8)}$$

$$Cu^+ + H_2O_2 \rightarrow Cu^{2+} + OH^- + \bullet OH \quad \text{(C.9)}$$

Peroxydisulfate ions ($S_2O_8{}^{2-}$) have been found possessing higher oxidization than H_2O_2 and thereby have been drawing greater attention recently. The reason is that the sulfate radical anions ($SO_4{}^{\bullet-}$) produced from $S_2O_8{}^{2-}$ decomposition, either thermally (Equation (C.10)) or photolytically (Equation (C.11)), are capable of capturing the excessive electrons and thus hindering recombination (Equation (C.12)) and producing high-reactive $\bullet OH$ (Equation (C.13)), as well as oxidizing substrates and intermediates directly (Equation (C.14)). Shang et al. investigated the effect of $S_2O_8{}^{2-}$ on the mineralization of a complex mixture of 10 commercial

pesticides. Results exhibited a highly promoted TOC removal rate while a greatly decreased energy consumption compared to in the case of no $S_2O_8^{2-}$ applied. [75]

$$S_2O_8^{2-} + e_{CB}^{-} \rightarrow SO_4^{2-} + SO_4^{\bullet-} \quad \text{(C.10)}$$

$$S_2O_8^{2-} + h\nu \rightarrow 2SO_4^{\bullet-} \quad \text{(C.11)}$$

$$SO_4^{\bullet-} + e_{CB}^{-} \rightarrow SO_4^{2-} \quad \text{(C.12)}$$

$$SO_4^{\bullet-} + H_2O \rightarrow SO_4^{2-} + \bullet OH + H^+ \quad \text{(C.13)}$$

$$SO_4^{\bullet-} + RH \rightarrow \text{Intermediates or,}$$

$$SO_4^{\bullet-} + \text{Intermediates} \rightarrow CO_2 + H_2O + \text{Mineralization products} \quad \text{(C.14)}$$

Peroxymonosulfuric ions (HSO_5^{-}) have been reported to provide $SO_4^{\bullet-}$ via both photolysis (Equation (C.15)) and trapping electrons (Equation (C.16)). The former process produces not only reactive species $\bullet OH$, but also $SO_4^{\bullet-}$ ions, which can scavenge photogenerated electrons and produce more $\bullet OH$ as indicated by Equation (C.12) and (C.13), respectively. However, excessive HSO_5^{-} may waste the reactive $\bullet OH$. Through analyzing the effect of HSO_5^{-} on the photocatalytic degradation of RR120 with ZnO nanocrystal, the degradation efficiency for 30 min irradiation was promoted from 76.9% to 99.8%, which was attributed to the immediate trapping of photogenerated electrons by HSO_5^{-} and the subsequent production of $\bullet OH$ [65].

$$HSO_5^{-} + h\nu \rightarrow SO_4^{\bullet-} + \bullet OH \quad \text{(C.15)}$$

$$HSO_5^{-} + e_{CB}^{-} \rightarrow OH^{-} + SO_4^{\bullet-} \quad \text{(C.16)}$$

$$HSO_5^{-} + e_{CB}^{-} \rightarrow \bullet OH + SO_4^{2-} \quad \text{(C.17)}$$

$$HSO_5^{-} + \bullet OH \rightarrow SO_5^{\bullet-} + H_2O \quad \text{(C.18)}$$

Sun et al. did a comparative study of $S_2O_8^{2-}$, HSO_5^{-}, and H_2O_2 on the photocatalytic oxidation of MB over rGO modified TiO_2 under visible light. Results suggested that H_2O_2 intensely improved the MB degradation activity, and HSO_5^{-} was able to increase MB removal rate as well.

However, $S_2O_8^{2-}$ showed a slightly negative effect. The different effects of the oxidants might result from their distinct photolysis behaviors. Specifically, the photolysis of one mole of H_2O_2 produces two moles of $\bullet OH$, while one for HSO_5^-, and zero for $S_2O_8^{2-}$, as manifested by Equations (C.6), (C.15), and (C.11), respectively. [76]

Some other oxidants are also found to have influences. Selvam et al. reported different facilitating effects of various inorganic anion oxidants on the degradation of 4-fluorophenol, which were in the order of $IO_4^- > BrO_3^- > S_2O_8^{2-} > H_2O_2 > ClO_3^-$ in both UV/TiO_2 and UV/ZnO systems. It is obvious that the most effective oxidant is IO_4^- in this case. The higher reactivity of the $UV/TiO_2/IO_4^-$ system was due to the production of highly reactive intermediate radicals such as $IO_3\bullet$ (Equation (C.19)), $\bullet OH$ (Equation (C.20)), and $IO_4\bullet$ (Equation (C.21)). [77]

$$IO_4^- + h\nu \rightarrow IO_3\bullet + O^{\bullet -} \quad \text{(C.19)}$$

$$O^{\bullet -} + H^+ \rightarrow \bullet OH \quad \text{(C.20)}$$

$$\bullet OH + IO_4^- \rightarrow OH^{\bullet -} + IO_4\bullet \quad \text{(C.21)}$$

The effects of a certain additional oxidant may variou in different systems, and may not always be favorable in some cases. For example, Sobana et al. found hydrogen peroxides inhered the degradation of AR 18 on ZnO due to the poor adsorption of H_2O_2 molecules on the semiconductor surface [78].

C-8 Other Ions

Since inorganic ions, such as NO_3^-, HCO_3^-, Cl^-, SO_4^{2-}, Na^+, Ca^{2+} and Mg^{2+}, are naturally present in water [79], it is necessary to take their influences into consideration when investigating photocatalytic water decontamination.

Carbonate (CO_3^{2-}) and bicarbonate (HCO_3^-) are most considered. Both CO_3^{2-} and HCO_3^- scavenge hydroxyl radicals, producing carbonate radicals ($CO_3^{\bullet -}$), an oxidant with higher selectivity but lower reactivity compared to $\bullet OH$, according to the following reactions:

$$CO_3^{2-} + \bullet OH \rightarrow CO_3^{\bullet -} + OH^- \quad \text{(C.22)}$$

$$HCO_3^- + \bullet OH \rightarrow CO_3^{\bullet -} + H_2O \quad (C.23)$$

Behnajady et al. observed a significantly decreased decolorization of C.I. Acid Yellow 23 over ZnO photocatalyst by increasing the concentration of CO_3^{2-} and HCO_3^-, which was mainly due to their scavenging effect. The blockage of active sites on the ZnO surface was also speculated to be a reason for the reduced photocatalytic performance. [47] Some studies also reported enhanced photocatalysis in the presence of carbonate and bicarbonate ions. For example, the photocatalytic transformation of norfloxacin (NOR) on $BiOBr/Fe_3O_4$ composites was promoted in the presence of HCO_3^-, which was related to the molecular structure of NOR. NOR has two aromatic aniline's structures bearing electron-donating substituents and structures similar to amino acids, which ware easily oxidized [80]. Studies have found that carbonate radicals reacted rapidly with compounds possessing the above structures, which makes them significant reactants in the oxidation of sulfur-containing compounds [80] . The complexes of bicarbonate on $BiOBr/Fe_3O_4$ surface was also speculated as one of the reasons for the degradation enhancement. [79]

Nitrate (NO_3^-) was the major precursor of $\bullet OH$ under solar light, as indicated and proven by Guo's work. The degradation of NOR photocatalyzed by $BiOBr/Fe_3O_4$ composites was slightly enhanced at low concentration (<1.0 mM) while inhibited in the concentration range of 2.0-10.0 mM, which was contributed to the excessively adsorbed NO_3^- ions competing for active sites on the catalyst surface with the substrate. [79]

Some other inorganic anions, such as halogens, are also been found to influence photocatalysis, which is usually related to the generation of weak oxidative halogen species oxidized by holes [81]. Liang et al. has reported the contribution of Cl^o clusters on the photocatalytic degradation of RhB under visible light, produced from the hole-oxidization of Cl- came from the slightly dissolved AgCl. [82] The same effect was also found in Br^- [62].

Metal cations may also have impacts on the photocatalytic decomposition of organic substrates. Noble metal ions are the most commonly studies, for they can be reduced by electrons, producing noble metal NPs, which may inhibit the LSPR effect to facilitate photocatalysis, as interpreted in Section 2.3.3. Yet, the excessive metal ions may be jeopardized instead. Natarajan noticed an evidently thwarted adsorption and degradation of RhB on TiO_2 photocatalyst in the presence of various metal ions (Zn^{2+}, Ag^+, Fe^{3+}, Cu^{2+} and Cd^{2+}) at the concentration of 100 μM, which was

attributed on the blockage of active sites on the catalyst surface as a result of the overdose of the employed metal ions [4]. Ferrous (Fe^{2+}) and ferric (Fe^{3+}) ions influences the photocatalytic activity by forming a respective Fenton or Fenton-like reagent with H_2O_2 under irradiation, which was mentioned in Appendix C-7.

References:

[1] T. Wu, X. Zhou, H. Zhang, X. Zhong, Bi2S3 nanostructures: A new photocatalyst, Nano Res. 3 (2010) 379–386. doi:10.1007/s12274-010-1042-0.

[2] S.G. Kumar, L.G. Devi, Review on Modified TiO2 Photocatalysis under UV/ Visible Light: Selected Results and Related Mechanisms on Interfacial Charge Carrier Transfer Dynamics, Phys. Chem. A. 115 (2011) 13211–13241. doi:10.1021/jp204364a.

[3] V. Kumar, A. Govind, R. Nagarajan, Optical and photocatalytic properties of heavily F--doped SnO2 nanocrystals by a novel single-source precursor approach, Inorg. Chem. 50 (2011) 5637–5645. doi:10.1021/ic2003436.

[4] T.S. Natarajan, M. Thomas, K. Natarajan, H.C. Bajaj, R.J. Tayade, Study on UV-LED/TiO2 process for degradation of Rhodamine B dye, Chem. Eng. J. 169 (2011) 126–134. doi:10.1016/j.cej.2011.02.066.

[5] L. Kuai, Y. Zhou, W. Tu, P. Li, H. Li, Q. Xu, L. Tang, X. Wang, M. Xiao, Z. Zou, Rational construction of a CdS/reduced graphene oxide/TiO2 core–shell nanostructure as an all-solid-state Z-scheme system for CO2 photoreduction into solar fuels, RSC Adv. 5 (2015) 88409–88413. doi:10.1039/C5RA14374H.

[6] D. Fatta-Kassinos, M.I. Vasquez, K. Kümmerer, K. Kummerer, Transformation products of pharmaceuticals in surface waters and wastewater formed during photolysis and advanced oxidation processes - Degradation, elucidation of byproducts and assessment of their biological potency, Chemosphere. 85 (2011) 693–709. doi:10.1016/j.chemosphere.2011.06.082.

[7] N. Riaz, N. Ela, M.S. Khan, Effect of Photocatalysts Preparation Methods and Light Source on Orange II Photocatalytic Degradation, Sci. Technol. 6 (2011) 112–117.

[8] S. Juntrapirom, D. Tantraviwat, S. Suntalelat, O. Thongsook, S. Phanichphant, B. Inceesungvorn, Visible light photocatalytic performance and mechanism of highly efficient SnS/BiOI heterojunction, J. Colloid Interface Sci. 504 (2017) 711–720. doi:10.1016/j.jcis.2017.06.019.

[9] A. Malathi, P. Arunachalam, A.N. Grace, J. Madhavan, A.M. Al-Mayouf, A robust visible-light driven BiFeWO6/BiOI nanohybrid with efficient photocatalytic and photoelectrochemical performance, Appl. Surf. Sci. 412 (2017) 85–95. doi:10.1016/j.apsusc.2017.03.199.

[10] H. Ming, Z. Ma, Y. Liu, K. Pan, H. Yu, F. Wang, Z. Kang, Large scale electrochemical synthesis of high quality carbon nanodots and their photocatalytic property, Dalt. Trans. 41 (2012) 9526. doi:10.1039/c2dt30985h.

[11] F. Yoshikawa, N. Namiki, Y. Otani, P. Biswas, A titanium dioxide-silica glass granule packed bed reactor for degradation of airborne organic compounds, J. Chem. Eng. Japan. 37 (2004) 503–513. doi:10.1252/jcej.37.503.

[12] W. Choi, J.Y. Ko, H. Park, J.S. Chung, Investigation on TiO2-coated optical fibers for gas-phase photocatalytic oxidation of acetone, Appl. Catal. B Environ. 31 (2001) 209–220. doi:10.1016/S0926-3373(00)00281-2.

[13] P. Du, J.T. Carneiro, J.A. Moulijn, G. Mul, A novel photocatalytic monolith reactor for multiphase heterogeneous photocatalysis, Appl. Catal. A Gen. 334 (2008) 119–128. doi:10.1016/j.apcata.2007.09.045.

[14] N.J. Peill, M.R. Hoffmann, M.M.K. Laboratories, Development and Optimization of a TiO2-Coated Fiber-

Optic Cable Reactor : Photocatalytic Degradation of 4-Chlorophenol Development and Optimization of a Ti02-Coated FiberiOptic Cable Photocatalytic Degradation of 4-Chlorophenol, EnvironSciTechnol. 29 (2002) 2974–2981. doi:10.1021/es00012a013.

[15] R.-D. Sun, A. Nakajima, I. Watanabe, T. Watanabe, K. Hashimoto, TiO2-coated optical fiber bundles used as a photocatalytic filter for decomposition of gaseous organic compounds, J. Photochem. Photobiol. A Chem. 136 (2000) 111–116. doi:10.1016/S1010-6030(00)00330-0.

[16] X. Wang, W. Yu, J. Zhang, J. Aldana, X. Peng, M. Xiao, Photoluminescence upconversion in colloidal CdTe quantum dots, Phys. Rev. B. 68 (2003) 1–6. doi:10.1103/PhysRevB.68.125318.

[17] D.H. Chen, X. Ye, K. Li, Oxidation of PCE with a UV LED Photocatalytic Reactor, Chem. Eng. Technol. 28 (2005) 95–97. doi:10.1002/ceat.200407012.

[18] J.L. Shie, C.H. Lee, C.S. Chiou, C.T. Chang, C.C. Chang, C.Y. Chang, Photodegradation kinetics of formaldehyde using light sources of UVA, UVC and UVLED in the presence of composed silver titanium oxide photocatalyst, J. Hazard. Mater. 155 (2008) 164–172. doi:10.1016/j.jhazmat.2007.11.043.

[19] J. Fu, B. Chang, Y. Tian, F. Xi, X. Dong, Novel C3N4–CdS composite photocatalysts with organic–inorganic heterojunctions: in situ synthesis, exceptional activity, high stability and photocatalytic mechanism, J. Mater. Chem. A. 1 (2013) 3083. doi:10.1039/c2ta00672c.

[20] Y. Bessekhouad, N. Chaoui, M. Trzpit, N. Ghazzal, D. Robert, J. V. Weber, UV-vis versus visible degradation of Acid Orange II in a coupled CdS/TiO2 semiconductors suspension, J. Photochem. Photobiol. A Chem. 183 (2006) 218–224. doi:10.1016/j.jphotochem.2006.03.025.

[21] L. Ye, J. Liu, Z. Jiang, T. Peng, L. Zan, Facets coupling of BiOBr-g-C3N4 composite photocatalyst for enhanced visible-light-driven photocatalytic activity, Appl. Catal. B Environ. 142–143 (2013) 1–7. doi:10.1016/j.apcatb.2013.04.058.

[22] J. Tang, Z. Zou, J. Yin, J. Ye, Photocatalytic degradation of methylene blue on CaIn2O4 under visible light irradiation, Chem. Phys. Lett. 382 (2003) 175–179. doi:10.1016/j.cplett.2003.10.062.

[23] D. Wang, L. Guo, Y. Zhen, L. Yue, G. Xue, F. Fu, AgBr quantum dots decorated mesoporous Bi2WO6 architectures with enhanced photocatalytic activities for methylene blue, J. Mater. Chem. A. 2 (2014) 11716. doi:10.1039/C4TA01444H.

[24] G.H. Jiang, X. Li, Z. Wei, T.T. Jiang, X.X. Du, W.X. Chen, Effects of N and/or S doping on structure and photocatalytic properties of BiOBr crystals, Acta Metall. Sin. (English Lett. 28 (2015) 460–466. doi:10.1007/s40195-015-0220-1.

[25] L. Liu, Y. Qi, J. Yang, W. Cui, X. Li, Z. Zhang, An AgI@g-C3N4 hybrid core@shell structure: Stable and enhanced photocatalytic degradation, Appl. Surf. Sci. 358 (2015) 319–327. doi:10.1016/j.apsusc.2015.07.212.

[26] Y. Liang, H. Wang, L. Liu, P. Wu, W. Cui, J.G. McEvoy, Z. Zhang, Microwave-assisted synthesis of a superfine Ag/AgI photocatalyst with high activity and excellent durability, J. Mater. Sci. 50 (2015) 6935–6946. doi:10.1007/s10853-015-9245-0.

[27] J. Huang, S. Liu, L. Kuang, Y. Zhao, T. Jiang, S. Liu, X. Xu, Enhanced photocatalytic activity of quantum-dot-sensitized one-dimensionally-ordered ZnO nanorod photocatalyst, J. Environ. Sci. (China). 25 (2013) 2487–2491. doi:10.1016/S1001-0742(12)60330-1.

[28] K. Dai, L. Lu, J. Dong, Z. Ji, G. Zhu, Q. Liu, Z. Liu, Y. Zhang, D. Li, C. Liang, Facile synthesis of a surface plasmon resonance-enhanced Ag/AgBr heterostructure and its photocatalytic performance with 450 nm LED illumination, Dalton Trans. 42 (2013) 4657–62. doi:10.1039/c3dt32813a.

[29] P. Wang, Y. Tang, Z. Dong, Z. Chen, T.-T. Lim, Ag–AgBr/TiO2/RGO nanocomposite for visible-light photocatalytic degradation of penicillin G, J. Mater. Chem. A. 1 (2013) 4718. doi:10.1039/c3ta01042b.

[30] Y. Deng, L. Tang, G. Zeng, C. Feng, H. Dong, J. Wang, H. Feng, Y. Liu, Y. Zhou, Y. Pang, Plasmonic resonance excited dual Z-scheme BiVO4/Ag/Cu2O nanocomposite: synthesis and mechanism for enhanced photocatalytic performance in recalcitrant antibiotic degradation, Environ. Sci. Nano. 4 (2017) 1494–1511. doi:10.1039/C7EN00237H.

[31] X. Lin, T. Huang, F. Huang, W. Wang, J. Shi, Photocatalytic activity of a Bi-based oxychloride Bi4NbO8Cl, J. Mater. Chem. 17 (2007) 2145–2150. doi:10.1039/b615903f.

[32] T. Welderfael, O.P. Yadav, A.M. Taddesse, J. Kaushal, Synthesis, characterization and photocatalytic activities of Ag-N-codoped ZnO nanoparticles for degradation of methyl red, Bull. Chem. Soc. Ethiop. 27 (2013) 221–232. doi:10.4314/bcse.v27i2.7.

[33] S. Ahmed, M.G. Rasul, W.N. Martens, R. Brown, M.A. Hashib, Heterogeneous photocatalytic degradation of phenols in wastewater: A review on current status and developments, Desalination. 261 (2010) 3–18. doi:10.1016/j.desal.2010.04.062.

[34] S. Chakrabarti, B.K. Dutta, Photocatalytic degradation of model textile dyes in wastewater using ZnO as semiconductor catalyst, J. Hazard. Mater. 112 (2004) 269–278. doi:10.1016/j.jhazmat.2004.05.013.

[35] M.N. Chong, B. Jin, C.W.K. Chow, C. Saint, Recent developments in photocatalytic water treatment technology: A review, Water Res. 44 (2010) 2997–3027. doi:10.1016/j.watres.2010.02.039.

[36] A.F. Alkaim, T.A. Kandiel, F.H. Hussein, R. Dillert, D.W. Bahnemann, Enhancing the photocatalytic activity of TiO2 by pH control: a case study for the degradation of EDTA, Catal. Sci. Technol. 3 (2013) 3216. doi:10.1039/c3cy00494e.

[37] S. Sakthivel, B. Neppolian, M. V Shankar, B. Arabindoo, M. Palanichamy, V. Murugesan, Solar photocatalytic degradation of azo dye: comparison of photocatalytic efficiency of ZnO and TiO2, Sol. Energy Mater. Sol. Cells. 77 (2003) 65–82. doi:10.1016/S0927-0248(02)00255-6.

[38] N.J. Peill, M.R. Hoffmann, Chemical and physical characterization of a TiO2-coated fiber optic cable reactor, Environ. Sci. Technol. 30 (1996) 2806–2812. doi:10.1021/es960047d.

[39] T. Van Gerven, G. Mul, J. Moulijn, A. Stankiewicz, A review of intensification of photocatalytic processes, Chem. Eng. Process. Process Intensif. 46 (2007) 781–789. doi:10.1016/j.cep.2007.05.012.

[40] W.Y. Wang, Y. Ku, Photocatalytic degradation of Reactive Red 22 in aqueous solution by UV-LED radiation, Water Res. 40 (2006) 2249–2258. doi:10.1016/j.watres.2006.04.041.

[41] K.J. Buechler, C.H. Nam, T.M. Zawistowski, Design and Evaluation of a Novel-Controlled Periodic Illumination Reactor To Study Photocatalysis, Ind. Eng. Chem. Res. 38 (1999) 1258–1263. doi:10.1021/ie9806139.

[42] W. Xu, D. Raftery, J.S. Francisco, Effect of irradiation sources and oxygen concentration on the photocatalytic oxidation of 2-propanol and acetone studied by in situ FTIR, J. Phys. Chem. B. 107 (2003) 4537–4544. doi:10.1021/jp025995h.

[43] A. Houas, H. Lachheb, M. Ksibi, E. Elaloui, C. Guillard, J. Herrmann, Photocatalytic degradation pathway of methylene blue in water, Appl. Catal. B Environ. 31 (2001) 145–157. doi:10.1016/S0926-3373(00)00276-9.

[44] S.K. Kansal, M. Singh, D. Sud, Studies on photodegradation of two commercial dyes in aqueous phase using different photocatalysts, J. Hazard. Mater. 141 (2007) 581–590. doi:10.1016/j.jhazmat.2006.07.035.

[45] M.A. Gondal, M.N. Sayeed, Z.H. Yamani, A.R. Al-Arfaj, Efficient removal of phenol from water using Fe2O3 semiconductor catalyst under UV laser irradiation, J. Environ. Sci. Heal. Part a-Toxic/Hazardous Subst. Environ. Eng. 44 (2009) 515–521. doi:10.1080/10934520902720033.

[46] J. Gamage McEvoy, W. Cui, Z. Zhang, Synthesis and characterization of Ag/AgCl–activated carbon composites for enhanced visible light photocatalysis, Appl. Catal. B Environ. 144 (2014) 702–712. doi:10.1016/j.apcatb.2013.07.062.

[47] M.A. Behnajady, N. Modirshahla, R. Hamzavi, Kinetic study on photocatalytic degradation of C.I. Acid Yellow 23 by ZnO photocatalyst, J. Hazard. Mater. 133 (2006) 226–232. doi:10.1016/j.jhazmat.2005.10.022.

[48] L. Bharadwaj, M. Bhardwaj, M.K. Sharma, An analysis of Fe2O3 assisted photocatalytic degradation of Congo Red dye, Toxicol. Environ. Health Sci. 4 (2012) 62–69. doi:10.1007/s13530-011-0102-5.

[49] O. Bechambi, S. Sayadi, W. Najjar, Photocatalytic degradation of bisphenol A in the presence of C-doped ZnO: Effect of operational parameters and photodegradation mechanism, J. Ind. Eng. Chem. 32 (2015) 201–210. doi:10.1016/j.jiec.2015.08.017.

[50] N.R. Khalid, E. Ahmed, Z. Hong, L. Sana, M. Ahmed, Enhanced photocatalytic activity of graphene-TiO2 composite under visible light irradiation, Curr. Appl. Phys. 13 (2013) 659–663. doi:10.1016/j.cap.2012.11.003.

[51] R. Tang, H. Su, Y. Sun, X. Zhang, L. Li, C. Liu, S. Zeng, D. Sun, Enhanced photocatalytic performance in Bi2WO6/SnS heterostructures: Facile synthesis, influencing factors and mechanism of the photocatalytic process, J. Colloid Interface Sci. 466 (2016) 388–399. doi:10.1016/j.jcis.2015.12.054.

[52] L. Liu, L. Ding, Y. Liu, W. An, S. Lin, Y. Liang, W. Cui, Enhanced visible light photocatalytic activity by Cu2O-coupled flower-like Bi2WO6 structures, Appl. Surf. Sci. 364 (2016) 505–515. doi:10.1016/j.apsusc.2015.12.170.

[53] L. Yue, S. Wang, G. Shan, W. Wu, L. Qiang, L. Zhu, Novel MWNTs-Bi2WO6 composites with enhanced simulated solar photoactivity toward adsorbed and free tetracycline in water, Appl. Catal. B Environ. 176–177 (2015) 11–19. doi:10.1016/j.apcatb.2015.03.043.

[54] M. Kaneko, I. Okura, Photocatalysis: Science and Technology, 2003rd ed., Springer, Berlin Heidelberg, 2003. doi:10.1016/S1010-6030(03)00234-X.

[55] S. Parra, V. Sarria, S. Malato, P. Péringer, C. Pulgarin, Photochemical versus coupled photochemical-biological flow system for the treatment of two biorecalcitrant herbicides: Metobromuron and isoproturon, Appl. Catal. B Environ. 27 (2000) 153–168. doi:10.1016/S0926-3373(00)00151-X.

[56] Y. Akama, A. Tong, M. Ito, S. Tanaka, The study of the partitioning mechanism of methyl orange in an aqueous two-phase system, Talanta. 48 (1999) 1133–1137. doi:10.1016/S0039-9140(98)00331-2.

[57] U.I. Gaya, Heterogeneous Photocatalysis Using Inorganic Semiconductor Solids, Springer Netherlands, Dordrecht, 2014. doi:10.1007/978-94-007-7775-0.

[58] A. Chithambararaj, N.S. Sanjini, S. Velmathi, A. Chandra Bose, Preparation of h-MoO3 and α-MoO3 nanocrystals: comparative study on photocatalytic degradation of methylene blue under visible light irradiation, Phys. Chem. Chem. Phys. 15 (2013) 14761. doi:10.1039/c3cp51796a.

[59] Y. Wang, H. Sun, H.M. Ang, M.O. Tade, S. Wang, Facile Synthesis of Hierarchically Structured Magnetic MnO2/ZnFe2O4 Hybrid Materials and Their Performance in Heterogeneous Activation of Peroxymonosulfate, ACS Appl. Mater. Interfaces. 6 (2014) 19914−19923. doi:10.1021/am505309b.

[60] K. Zhu, J. Wang, Y. Wang, C. Jin, A.S. Ganeshraja, Visible-light-induced photocatalysis and peroxymonosulfate activation over ZnFe2O4fine nanoparticles for degradation of Orange II, Catal. Sci. Technol. 6 (2016) 2296–2304. doi:10.1039/c5cy01735a.

[61] S. Malato, P. Fernández-Ibáñez, M.I. Maldonado, J. Blanco, W. Gernjak, Decontamination and disinfection of water by solar photocatalysis: Recent overview and trends, Catal. Today. 147 (2009) 1–59. doi:10.1016/j.cattod.2009.06.018.

[62] D. Wang, Y. Duan, Q. Luo, X. Li, L. Bao, Visible light photocatalytic activities of plasmonic Ag/AgBr particles synthesized by a double jet method, Desalination. 270 (2011) 174–180. doi:10.1016/j.desal.2010.11.042.

[63] S. Li, S. Hu, K. Xu, W. Jiang, J. Liu, Z. Wang, A Novel Heterostructure of BiOI Nanosheets Anchored onto MWCNTs with Excellent Visible-Light Photocatalytic Activity, Nanomaterials. 7 (2017) 22. doi:10.3390/nano7010022.

[64] H. Gülce, V. Eskizeybek, B. Haspulat, F. Sarı, A. Gülce, A. Avcı, Preparation of a New Polyaniline/CdO Nanocomposite and Investigation of Its Photocatalytic Activity: Comparative Study under UV Light and Natural Sunlight Irradiation, Ind. Eng. Chem. Res. 52 (2013) 10924–10934. doi:10.1021/ie401389e.

[65] R. Velmurugan, M. Swaminathan, An efficient nanostructured ZnO for dye sensitized degradation of Reactive Red 120 dye under solar light, Sol. Energy Mater. Sol. Cells. 95 (2011) 942–950. doi:10.1016/j.solmat.2010.11.029.

[66] H. Ehrenreich, D. Turnbull, Advances in Research and Applications: Semiconductor Heterostructures and Nanostructures, Academic Press, London, 1991.

[67] H.E. Kim, J. Lee, H. Lee, C. Lee, Synergistic effects of TiO2 photocatalysis in combination with Fenton-like reactions on oxidation of organic compounds at circumneutral pH, Appl. Catal. B Environ. 115–116 (2012) 219–224. doi:10.1016/j.apcatb.2011.12.027.

[68] T.T. ThanhThuy, H. Feng, Q. Cai, Photocatalytic degradation of pentachlorophenol on ZnSe/TiO2 supported by photo-Fenton system, Chem. Eng. J. 223 (2013) 379–387. doi:10.1016/j.cej.2013.03.025.

[69] J. Xu, W. Wang, E. Gao, J. Ren, L. Wang, Bi2WO6/Cuo: A novel coupled system with enhanced photocatalytic activity by Fenton-like synergistic effect, Catal. Commun. 12 (2011) 834–838. doi:10.1016/j.catcom.2011.01.011.

[70] L. Zou, B. Zhu, The synergistic effect of ozonation and photocatalysis on color removal from reused water, J. Photochem. Photobiol. A Chem. 196 (2008) 24–32. doi:10.1016/j.jphotochem.2007.11.008.

[71] K. Kabra, R. Chaudhary, R.L. Sawhney, R. Kabra, Kavita. Chaudhary, Rubina. Sawhney, K. Kabra, R. Chaudhary, R.L. Sawhney, Treatment of Hazardous Organic and Inorganic Compounds through Aqueous-Phase Photocatalysis: A Review, Ind. Eng. Chem. Res. 43 (2004) 7683–7696. doi:10.1021/ie0498551.

[72] Y. Wang, C.S. Hong, TiO2-mediated photomineralization of 2-chlorobiphenyl: The role of O2, Water Res. 34 (2000) 2791–2797. doi:10.1016/S0043-1354(00)00009-9.

[73] H. Shirayama, Y. Tohezo, S. Taguchi, Photodegradation of chlorinated hydrocarbons in the presence and absence of dissolved oxygen in water, Water Res. 35 (2001) 1941–1950.

[74] H. Lee, J. Choi, S. Lee, S.T. Yun, C. Lee, J. Lee, Kinetic enhancement in photocatalytic oxidation of organic compounds by WO3in the presence of Fenton-like reagent, Appl. Catal. B Environ. 138–139 (2013) 311–317. doi:10.1016/j.apcatb.2013.03.006.

[75] S. Malato, J. Blanco, M.I. Maldonado, P. Fernandez-Ibanez, A. Campos, Optimising solar photocatalytic mineralisation of pesticides by adding inorganic oxidising species; application to the recycling of pesticide containers, Appl. Catal. B Environ. 28 (2000) 163–174. doi:10.1016/S0926-3373(00)00175-2.

[76] H. Sun, S.S. Liu, S.S. Liu, S. Wang, A comparative study of reduced graphene oxide modified TiO2, ZnO and Ta2O5 in visible light photocatalytic/photochemical oxidation of methylene blue, Appl. Catal. B Environ. 146 (2014) 162–168. doi:10.1016/j.apcatb.2013.03.027.

[77] K. Selvam, M. Muruganandham, I. Muthuvel, M. Swaminathan, The influence of inorganic oxidants and metal ions on semiconductor sensitized photodegradation of 4-fluorophenol, Chem. Eng. J. 128 (2007) 51–57. doi:10.1016/j.cej.2006.07.016.

[78] N. Sobana, M. Swaminathan, The effect of operational parameters on the photocatalytic degradation of acid red 18 by ZnO, Sep. Purif. Technol. 56 (2007) 101–107. doi:10.1016/j.seppur.2007.01.032.

[79] C. Guo, S. Gao, J. Lv, S. Hou, Y. Zhang, J. Xu, Assessing the photocatalytic transformation of norfloxacin by BiOBr/iron oxides hybrid photocatalyst: Kinetics, intermediates, and influencing factors, Appl. Catal. B Environ. 205 (2017) 68–77. doi:10.1016/j.apcatb.2016.12.032.

[80] X.H. Wang, A.Y.C. Lin, Phototransformation of cephalosporin antibiotics in an aqueous environment results in higher toxicity, Environ. Sci. Technol. 46 (2012) 12417–12426. doi:10.1021/es301929e.

[81] M.A. Rauf, S.S. Ashraf, Fundamental principles and application of heterogeneous photocatalytic degradation of dyes in solution, Chem. Eng. J. 151 (2009) 10–18. doi:10.1016/j.cej.2009.02.026.

[82] Y. Liang, S. Lin, L. Liu, J. Hu, W. Cui, Oil-in-water self-assembled Ag@AgCl QDs sensitized Bi2WO6: Enhanced photocatalytic degradation under visible light irradiation, Appl. Catal. B Environ. 164 (2015) 192–203. doi:10.1016/j.apcatb.2014.08.048.

Appendix D. Strategies Coupling Photocatalysis with Other Treatment: A Brief Summary

AOPs are based on the generation of hydroxyl radicals, which is such a strong oxidative reagent that it can be deemed as non-selective. Therefore, the combination of two or more AOPs is expected to be more effective than either of them being used separately, which is attributed to the increased amount of generated •OH [1].

D-1 Coupling with Hydrogen Peroxide

Hydrogen peroxide (H_2O_2) is able to decompose to produce •OH radicals both thermally (Equation (D.1-2)) and photochemically (Equation (D.3)) [2–4]. Besides, considering that the oxidation potential of •OH generated from H_2O_2 is stronger than that of $O_2^{\bullet-}$ produced by O_2, hydrogen peroxide is a better electron acceptor compared to oxygen [5]. It should be noticed that there is an optimum concentration range of H_2O_2, and different effects may be presented when it is outranged. Insufficient dosage doubtlessly facilitates the reactions, although not as much as the sufficient dose does. Overdose may have the same effect when the exceeding amount is not too much but plays a counterpart role when it gets too high. This is because at high H_2O_2 concentration, it may decompose to give water and oxygen (Equation (D.4)), or scavenges photogenerated holes (Equation (D.5)) or hydroxyl radicals (Equation (D.6)), producing oxidants that are much weaker than the desired hydroxyl radicals. By introducing 0.25 mL of H_2O_2 into the photoreaction suspension containing RhB and PANI/$BiVO_4$ composites, the degradation activity was increased about 18-fold compared to that of the without-H_2O_2 system [6]. In the investigation of photocatalytic activity of C-doped ZnO under visble light, the degradation and mineralization rates of BPA was promoted as the H_2O_2 concentration increased from 10^{-3} to 5×10^{-3} M, which was attributed to the photocatalytic election scavenging and thus inhibited recombination. When the H_2O_2 concentration increased to 10^{-2} M, however, the excessive H_2O_2 molecules consumed • OH and formed HO_2 • following Equation (D.6), and thus suppressed the photocatalytic effect. [7]

$$H_2O_2 + e_{CB}^- \rightarrow \bullet OH + OH^- \quad \text{(D.1)}$$

$$H_2O_2 + O_2^{\bullet-} \rightarrow \bullet OH + OH^- + O_2 \quad \text{(D.2)}$$

$$H_2O_2 + h\nu \rightarrow 2\bullet OH \quad \text{(D.3)}$$

$$2H_2O_2 + h\nu \rightarrow 2H_2O + O_2 \quad \text{(D.4)}$$

$$H_2O_2 + h_{VB}^{+} \rightarrow O_2 + 2H^+ \quad \text{(D.5)}$$

$$H_2O_2 + \bullet OH \rightarrow H_2O + HO_2\bullet \quad \text{(D.6)}$$

D-2 Coupling Ozonation

Ozone is a powerful oxidant with an electrochemical oxidation potential of 2.07 eV (vs. NHE) [1], and has been used for dissociating various organics [8]. Under irradiation, an ozone molecule may generate one hydroxyl radical via a direct reaction with water (Equation (D.7)) or two via an indirect reaction (Equation (D.8-9)) [9,10].

$$O_3 + H_2O \xrightarrow{h\nu} \bullet OH + \bullet OOH + O_2 \quad \text{(D.7)}$$

$$O_3 + H_2O \xrightarrow{h\nu} H_2O_2 + O_2 \quad \text{(D.8)}$$

$$H_2O_2 \xrightarrow{h\nu} 2\bullet OH \quad \text{(D.9)}$$

In the presence of semiconductor photocatalysts, O_3 is more often working as the electron sink, which would not only restrain electron/hole recombination, but produce more •OH for the subsequent substrate degradation, as demonstrated by Equation (D.10-12). Zou and Zhu found a nearly 10 time and 1.6 times higher TOC removal efficiency of a O_3/TiO_2 system compared to the pure ozonation and TiO_2 -photocatalysis treatment under UV irradiation [1]. The same mechanism also explained the enhanced catalytic performance of WO_3 towards the degradation of IBP under visible light [11]. By means of introducing ozone into the reaction system, Mahmoodi rose the decomposition activity of RR 198 RR120 over $CuFe_2O_4$ to 1.48 and 1.74 times higher, respectively, under UV irradiation [12].

$$O_3 + e^- \rightarrow O_3^{\bullet-} \quad \text{(D.10)}$$

$$O_3^{\bullet-} + H^+ \rightarrow HO_3\bullet \quad \text{(D.11)}$$

$$HO_3\bullet \rightarrow O_2 + \bullet OH \quad \text{(D.12)}$$

Kopf et al. claimed another theory. They indicated that it was O_2 instead of O_3 that trapped electrons. The produced $O_2^{\bullet-}$ reduced O_3 to $O_3^{\bullet-}$ (Equation (D.13)), which took part in the next steps same as Equation (D.10-12). In addition to the strongly enhanced degradation efficiency of monochloroacetic acid and pyridine compared with ozonation and photocatalysis worked separately, the specific energy consumption was also greatly reduced as shown in Table D-1. [13]

$$O_3 + O_2^{\bullet-} \rightarrow O_3^{\bullet-} + O_2 \quad \text{(D.13)}$$

Table D- 1 Comparison of specific energy consumption among the three systems. Adapted with permission from [13]. Copyright (2000) Elsevier.

Substrate	Pure Photocatalysis	Pure Ozonation	Combination
Monochloroacetic Acid	19	110	5.4
Pyridine	120	73	11

Unit of specific energy consumption: $kWh/g\ DOC - reduction$

D-3 Coupling with Other Treatments

The synergistic effect of photocatalysis and other AOP treatments, such as sonolysis- [14,15] and microwave- irradiation [16,17], have also been researched.

Berberidou et al. investigated MG degradation in water in the presence of TiO_2 under ultrasound irradiation. The superior sonophotocatalytic efficiency was attributed to the enhanced production of • OH. [14] Similarly, the simultaneous application of ultraviolet and ultrasound irradiation to photocatalytic degradation of RB5 resulted in an improved efficiency compared to photocatalysis and sonolysis operated separately, as well as the additive effect of the two processes, suggesting the synergistic effect between them [15].

Zhang et al. found a facilitated catalytic degradation of X-3B at high concentration on TiO_2 using microwave electrodeless lamp as the light source, which was benefited from the enhanced • OH

generation [17]. Another research focusing on the decomposition of 4-CP by a microwave assisted photocatalysis method found that in addition to produce $\bullet OH$, microwave likely generated additional defect sites on the TiO_2 surface, which inhibited electron/hole recombination, resulting a more effective photocatalytic process [16].

References:

[1] L. Zou, B. Zhu, The synergistic effect of ozonation and photocatalysis on color removal from reused water, J. Photochem. Photobiol. A Chem. 196 (2008) 24–32. doi:10.1016/j.jphotochem.2007.11.008.

[2] K. Selvam, M. Muruganandham, I. Muthuvel, M. Swaminathan, The influence of inorganic oxidants and metal ions on semiconductor sensitized photodegradation of 4-fluorophenol, Chem. Eng. J. 128 (2007) 51–57. doi:10.1016/j.cej.2006.07.016.

[3] S. Malato, J. Blanco, C. Richter, B. Braun, M.I. Maldonado, Enhancement of the rate of solar photocatalytic mineralization of organic pollutants by inorganic oxidizing species, Appl. Catal. B Environ. 17 (1998) 347–356. doi:10.1016/S0926-3373(98)00019-8.

[4] E. Evgenidou, K. Fytianos, I. Poulios, Photocatalytic oxidation of dimethoate in aqueous solutions, J. Photochem. Photobiol. A Chem. 175 (2005) 29–38. doi:10.1016/j.jphotochem.2005.04.021.

[5] S.R. Cater, M.I. Stefan, J.R. Bolton, A.S. Amiri, UV/H2O2 Treatment of Methyl, Environ. Sci. Technol. 34 (2000) 659–662.

[6] M. Shang, W. Wang, S. Sun, J. Ren, L. Zhou, L. Zhang, Efficient Visible Light-Induced Photocatalytic Degradation of Contaminant by Spindle-like PANI/BiVO4, J. Phys. Chem. C. 113 (2009) 20228–20233. doi:10.1021/jp9067729.

[7] O. Bechambi, S. Sayadi, W. Najjar, Photocatalytic degradation of bisphenol A in the presence of C-doped ZnO: Effect of operational parameters and photodegradation mechanism, J. Ind. Eng. Chem. 32 (2015) 201–210. doi:10.1016/j.jiec.2015.08.017.

[8] T.E. Agustina, H.M. Ang, V.K. Vareek, A review of synergistic effect of photocatalysis and ozonation on wastewater treatment, J. Photochem. Photobiol. C Photochem. Rev. 6 (2005) 264–273. doi:10.1016/j.jphotochemrev.2005.12.003.

[9] J. Villaseñor, P. Reyes, G. Pecchi, Catalytic and photocatalytic ozonation of phenol on MnO2 supported catalysts, Catal. Today. 76 (2002) 121–131. doi:10.1016/S0920-5861(02)00212-2.

[10] S. Anandan, G.J. Lee, P.K. Chen, C. Fan, J.J. Wu, Removal of Orange II dye in water by visible light assisted photocatalytic ozonation using Bi2O3 and Au/Bi2O3 nanorods, Ind. Eng. Chem. Res. 49 (2010) 9729–9737. doi:10.1021/ie101361c.

[11] A. Rey, E. Mena, A.M. Chávez, F.J. Beltrán, F. Medina, Influence of structural properties on the activity of WO3 catalysts for visible light photocatalytic ozonation, Chem. Eng. Sci. 126 (2015) 80–90. doi:10.1016/j.ces.2014.12.016.

[12] N.M. Mahmoodi, Photocatalytic ozonation of dyes using copper ferrite nanoparticle prepared by co-precipitation method, Desalination. 279 (2011) 332–337. doi:10.1016/j.desal.2011.06.027.

[13] P. Kopf, E. Gilbert, S.H. Eberle, TiO2 photocatalytic oxidation of monochloroacetic acid and pyridine: influence of ozone, J. Photochem. Photobiol. A Chem. 136 (2000) 163–168. doi:10.1016/S1010-6030(00)00331-2.

[14] C. Berberidou, I. Poulios, N.P. Xekoukoulotakis, D. Mantzavinos, Sonolytic, photocatalytic and sonophotocatalytic degradation of malachite green in aqueous solutions, Appl. Catal. B Environ. 74 (2007) 63–72. doi:10.1016/j.apcatb.2007.01.013.

[15] D.E. Kritikos, N.P. Xekoukoulotakis, E. Psillakis, D. Mantzavinos, Photocatalytic degradation of reactive black 5 in aqueous solutions: Effect of operating conditions and coupling with ultrasound irradiation, Water Res. 41 (2007) 2236–2246. doi:10.1016/j.watres.2007.01.048.

[16] Z. Ai, P. Yang, X. Lu, Degradation of 4-chlorophenol by a microwave assisted photocatalysis method, J. Hazard. Mater. 124 (2005) 147–152. doi:10.1016/j.jhazmat.2005.04.027.

[17] X. Zhang, G. Li, Y. Wang, Microwave assisted photocatalytic degradation of high concentration azo dye Reactive Brilliant Red X-3B with microwave electrodeless lamp as light source, Dye. Pigment. 74 (2007) 536–544. doi:10.1016/j.dyepig.2006.03.012.

Appendix E. Recent Development in Photoreactor Design: A Brief Summary

E-1 Introduction

Although photocatalytic water decontamination has been attracting extensive attention, most of them are concentrating on catalyst modification and design and operating parameter optimization, industrial practices are still limited due to scaling-up problems and the difficulties and complexity with regard to reactor design. The primary challenges concentrate on photon transfer limitation and mass transfer limitation [1,2].

Photon transfer limitation results from photon loss during transmission from the light source to catalyst particles, as well as non-uniform illumination distribution throughout the reaction system [3]. The former can be addressed by modifying or exploring novel light sources; the latter may be addressed by increasing the distance between the light source and the reaction system or increasing the amount of lamps around the reactor when artificial light sources are used. Yet, poor light absorption efficiency or high energy consumption may be caused. [4]

Another major barrier to photoreactor development is the relatively slow reaction rate due to the low concentration levels of pollutant substrates, which can be further deteriorated by mass transfer limitation [2]. Except for maximizing the specific surface area of catalyst particles, increasing Reynolds numbers by improving the turbidity of the fluid and thus the collision between substrate and catalyst is also effective [4,5].

E-2 laboratory UV-Activated Photoreactor Design

Among the existing photocatalytic reactor configurations, slurry and suspension systems are most applied, taking the advantage of a strong interaction between react agents and catalysts with a large specific surface area. However, after-use separation of catalysts and non-uniform illumination distribution lead to high operation costs and poor energy efficiency, and thus restrict the industrialization and commercialization of these devices [1].

Alternative reactor configurations include fixed- and fluidized-bed reactors. In conventional fixed-bed reactors, catalyst particles are coated on reactor walls, on solid-supported matrixes, or around the casing of the light source, in the form of thin films or sheets, in order to keep an effective access for substrates to catalyst surface [3,6]. Whereas, the thickness of a porous film- or sheet-supported by catalysts would impact the internal mass transfer process since some substrates may not be able to reach the photocatalysts in the proximity of the support-catalyst interface [1]. Meanwhile, photon loss induced by irradiation scattering and small catalyst specific surface area are also notable barriers for the films or sheets to be applied to industries [7]. The above factors will result in a reduction in the photocatalytic performance of immobilization reactors compared to in the case of slurry reactors [1]. A comparative study of photocatalytic degradation of formic acid was proceeded among a traditional suspended system, an immobilized system with catalysts coated on the tube wall and another immobilized systems packed with coated glass beads. Results exhibited comparable quantum yields for the three systems, and only the second one suffered from mass transfer limitation [8]. Moreover, immobilized systems are not suitable for high catalyst loading because of the potential "screening effect", which is adverse to photon absorption [6]. Instead of fixing catalysts, Ollis and Marinangeli focused irradiation onto the polished tip of optical fibers through a bi-convex lens, and realized the remote delivery of photon energy to reactive sites on the catalyst surface [9]. This strategy has been applied in numbers of novel photoreactors [3,10–12] as the main development for quantum efficiency improvement [4]. Hofstadler et al. investigated the degradation of 4-cCP in a multifiber photocatalytic reactor, and obtained a 1.6 times higher reaction rate compared to a conventional slurry reactor using a 400-W high-pressure Hg lamp working as the light source under comparable conditions [13]. Yet, optical fibers may suffer from exponentially light intensity decays along the axial direction of the coated fibers and requires deeper investigations. [10–12,14].

Fluidized-bed reactor is deemed as a reactor type between slurry and fixed ones, where the catalysts are confined but move freely inside the reactor so that not only the after-separation process can be avoided, sufficient contact between catalyst and substrates is garuanteed as well. However, the non-uniform illumination distribution is still unsolved [15], and the loss or "drifting" of photocatalysts is also inevitable [4]. Moreover, a continuously high feed flow rate to maintain turbulence is indispensable, which requires a large volume of input and thus a high power consumption.

From the above discussions, the two central problems with respect to photocatalytic reactor design can be extracted as needing a sufficiently high specific surface area of catalysts and a uniform distribution of illumination across the reaction system [1]. Efforts focusing on both issues have been carried out. A well-known example is the development of a thin film reactor based on slurry systems with a turbulent flow. In these reactors, there is only a thin water film between the light source and the catalysts, so that photon loss through absorption can be diminished [16]. For instance, a thin-film, slurry reactor was firstly devised by Ollis et al., which implemented an efficient photocatalyst excitation due to the superior light absorption of the slurry suspension, as well as a very large illumination area and thus a minimal mass transfer limitation [17]. On this basis, Puma and Yue devised a novel "fountain" photoreactor operated in a continuous flow (Figure E-1). With this configuration, photons emitted from the lamp could be absorbed by the reaction suspension in the water fountain. On the other hand, since the water fountain was thin, the photons could go through it and reflected by the baffle, and then reach the water fountain and take part in the reaction again, which prolonged the photon lifetime and inhibited photon losses. This design successfully avoided filming and sealing problems and breakage risks that were typical in reactor configurations where photons enter the reactor through a transparent window. [18,19]

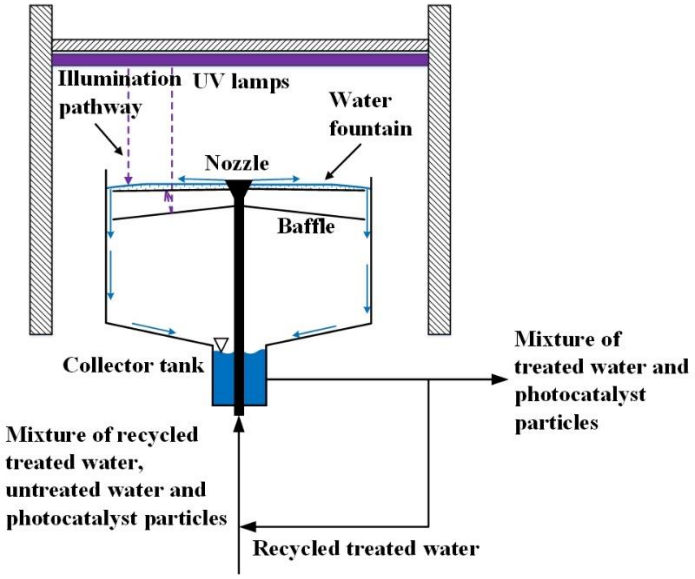

Figure E- 1 Schematic of the fountain photocatalytic reactor operated in continuous flow with external recycle. Adapted with permission from [18,19]. Copyright (2000) Elsevier and Copyright (2001) Elsevier, respectively.

Some thin-film photoreactors are also devised in the form of falling flow reactors [20]. In order to overcome the after-use problem exiting in regular slurry system, they are usually proposed based

on fixed-bed reactors [21]. Catalyst-immobilized falling film reactors and rotating disk reactors are the two most commonly used configurations. In immobilized falling flow reactors, instead of operating at turbulence, there are three dimensionless velocity profiles at steady state: falling film laminar flow, plug flow, and slit flow [22]. A falling film closed loop step photoreactor was found to be valid for describing the degradation pathway and kinetics of chlorotoluron and metolachlor, respectively [21]. In 2000, the first rotating disk photocatalytic reactor operating in a falling film continuous flow mode was developed with immobilized TiO_2. The configuration is shown in Figure E-2. Its performance was tested by the photocatalytic degradation of 4-chlorobenzoic acid with a decent mass transfer efficiency. [23,24] Subsequently, a comparative study between a photon-effective rotating disk photocatalytic reactor and a rotating drum reactor revealed that an approximate 1.73-times-higher maximum initial photonic efficiency was reached in the former compared to the latter. An 11.2% increment in the amount of absorbed photons was also found in the rotating disk reactor due to the recapture of reflected photons realized by its corrugated surface [16]. Another comparison carried out between a rotating disk reactor and a conventional annular reactor achieved a 3 times higher average photonic efficiency and a 2 times larger maximum surface reaction rate in the former, suggesting that the former was significantly more efficient in light energy conversion and under the reaction condition the rate limiting step (either the oxygen adsorption of oxygen on catalyst surface or the electron transfer from the catalyst to the oxygen) was overcome to some degree, respectively [25].

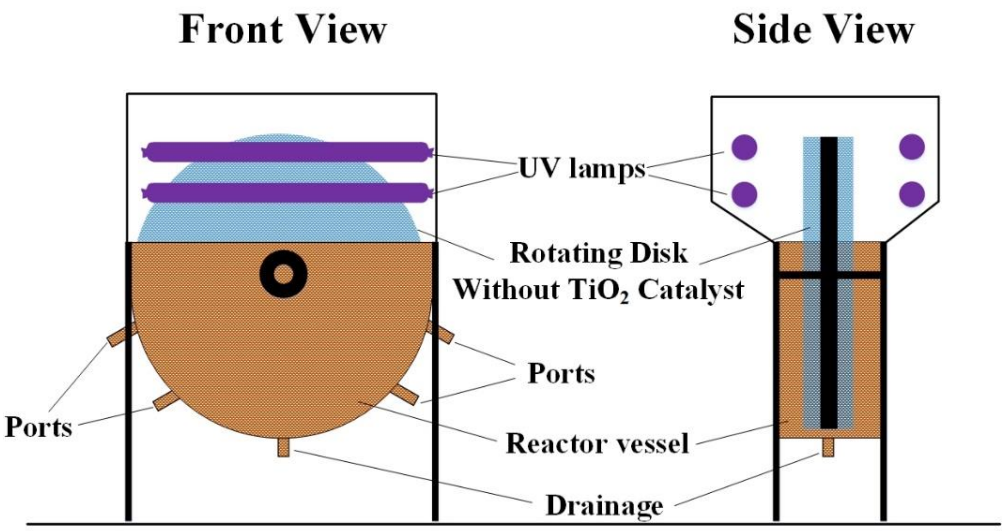

Figure E- 2 Schematic of rotating disk photocatalytic reactor. Adapted with permission from [23]. Copyright (2000) Elsevier.

Based on fixed-bed reactors, multiple-tube reactors with catalysts immobilized on the tube walls have also been devised. Ray and Beenackers proposed a distributive-type fixed-bed reactor system consisting of hollow tubes coated on its outside surface deposited with catalysts. These tubes functioned as both the light conductor and catalyst distributor. An approximately 4.5 times higher photocatalytic activity compared to in the case of a classical annular reactor was observed. The schematic is shown in Figure E-3. [2]

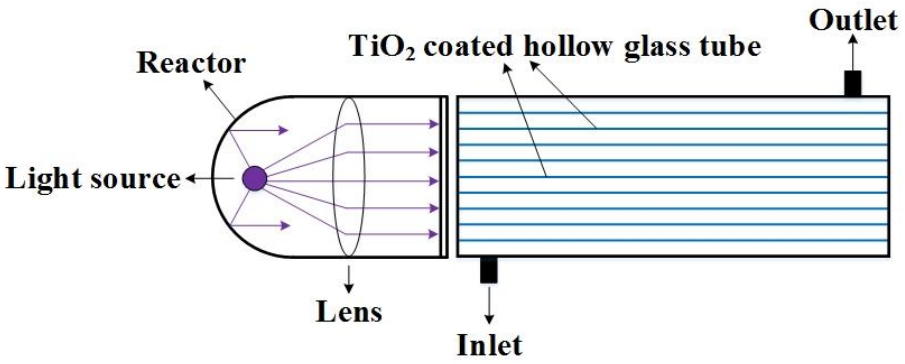

Figure E- 3 Schematic of multiple tube reactor. Adapted with permission from [2]. Copyright (1998) Elsevier.

In order to overcome the mass transfer limitation tubular reactors suffer from, Damodar and Swaminathan combined thin-film and tubular reactors in a continuous immobilized rotating tube reactor (Figure E-4), giving a zigzag flow path for liquid in the reactor. A color removal rate of 90-99.99% and the TOC removal of 55-70% towards a reactive red dye ($C_{18}H_{11}N_8O_{10}S_3ClNa_3$) was realized, and flow rate was found to be significant on color removal and energy consumption. [26]

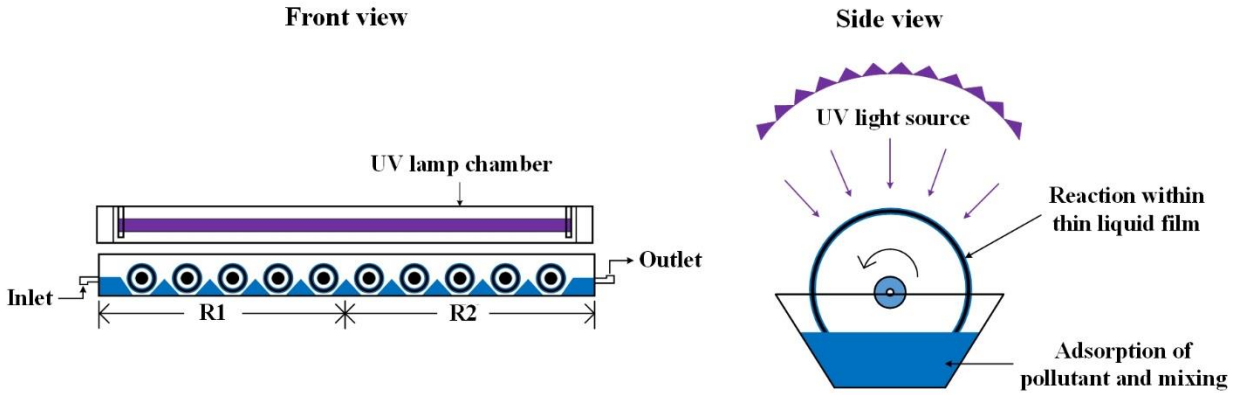

Figure E- 4 Schematic of immobilized rotating tube photocatalytic reactor. Adapted with permission from [26]. Copyright (2008) Elsevier.

Li et al. developed a novel double-cylindrical-shell (DCS) photoreactor immobilized with TiO_2-coated silica gel beads. Two concentric columns were sandwiched with the beads. The inner one was inserted with an UV black light lamp in the center and the outer was covered with aluminum foil to reflect black UV light into the reactor. The reactor was equipped with a peristaltic that allowed continuous circulation of the reaction suspension through the photocatalytic system. Its performance was applied to the degradation of RhB and MO, exhibiting a superior catalytic efficiency with a low energy consumption, as well as an excellent repetitive operation performance. [27] Zhang et al. devised a novel capillary array photocatalytic reactor. Two trtrafluoroethylene tubes inserted with capillaries were fixed on two brackets up and down. An 11 W UV lamp was inserted at the center of the two brackets providing irradiation source. Its success was disclosed by the enhanced photocatalytic degradation efficiency towards RhB and MO compared to the conventional batch reactor with P-25 TiO_2 powder and TiO_2 film as photocatalyst. [28] Rao et al. came up with a pebble bed photoreactor with TiO_2 coated on silica-rich white pebbles distributing in an orderly arrangement in a horizontal or inclined trough. The pebbles positioned in the horizontal direction performed a higher efficiency due to the lower degree of water by-passing and the better contact between the TiO_2-coated pebbles and contaminated water, compared to the case of the inclined trough. The primary advantage of this reactor type was the low cost of catalyst supporter, and the only constraint for its industrial application might be the availability of space for sunlight collection. [29]

E-3 Industrial Solar Collectors

Although lots of efforts have been made with respect to optimizing and exploring novel photocatalytic reactors radiated by UV, outdoor industrial reactors under solar illumination still remain scarce. It is because scaling up photocatalytic reactors is a complex process with multiple interacting factors, such as the distribution and transfer of substrates and photocatalysts, reaction kinetics, irradiation characteristics, etc. [1]. It was suggested that the primary unit costs predominated the overall treatment cost under a satisfactory technical premise [30]. In industrial-scale reactors, substituting natural solar irradiation for artificial UV lamps as the light source for photocatalysis will dramatically reduce the total cost of the treatment system. Therefore, solar thermal collectors have been modified to accommodate for solar photocatalytic reactors. Different from laboratory reaction systems usually operating at a constant temperature, industrial solar

collectors are often exposed to a natural temperature without a strict control due to financial consideration and that temperature has only a slight effect on the aqueous phase photoreactor. [31]

A typical solar collector consists of an aperture plane, an absorber (usually in a tubular shape), and other support structures. The first two are most significant.

The aperture plane is made of special materials that can reflect solar irradiation to the absorber as much as possible, and the aperture material determines the radiation intensity [32]. Traditional silver-coated mirrors have very poor reflectivity in the UV spectrum, and therefore is not suitable for photocatalytic applications [33]. Aluminum-coated materials is the only one that has high and stable reflectance in this case, and is no doubt the best option [34]. However, a freshly deposited aluminum surface would be so fragile that needs to be protected. Although the conventional glass cover does have resistance to weathering and abrasion, it also filters UV light significantly and the oxide layer formed naturally grows increasingly thicker, which would drastically curb UV reflectance. [35] Therefore, electropolished anodized aluminum and organic plastic films with aluminum coatings are considered as the most suitable surface at present [33].

Absorbers in a solar collector for photocatalysis not only work for absorbing photons, but act as the reactor for the substrate degradation as well. Materials suitable for an absorber should have strong light absorbance and be inert to the catalysts, substrates, by-products during the reactions, as well as aggressive radicals (e.g., hydroxyl radicals and superoxide radicals). Resistance to low pH (inorganic acids are common in both by- and end-products in photocatalytic degradation) and high temperature of around 60-70 ℃ (due to the absorption of heat from solar irradiation) are also necessary. [33]

Materials such as fluoropolymers, acrylic transmissions and some low iron-containing glasses have been proven to meet the requirements. Fluoropolymers can be deployed as films attributed to their excellent tear resistance at low pressure. However, at high pressure, thick walls would be necessary due to their fragility in the radical direction. [35] Quartz, on the other hand, is unfeasible because of high price, although their properties are suitable [36].

Since most research studying solar collectors for photocatalysis are carried out in the presence of TiO_2, the catalysts involved in the following discussion are TiO_2 unless stated otherwise.

E-3.1 Concentrating Collector

The first industrial-scale outdoor solar-activated photocatalytic reactor was a converted solar thermal parabolic-trough collector, in which the absorber/glazing-tube combination was replaced by a simple Pyrex glass tube through which the contaminated water could flow [37]. Original photoreactor designs for photocatalysis are based on line-focus parabolic-trough concentrators (PTCs) [35]. It is the most promising and mature type of concentrating solar collectors that have been proven as effective for wastewater treatment [32]. A PTC has one or two motors controlled by the solar tracking system on one or two axes, respectively, keeping the aperture plane perpendicular to the solar rays, so that all available direct solar radiation can be reflected and concentrated on the absorber tube. The construction of a two-axes concentrating collector is shown in Figure E-5(a). The shape of apertures should be precise to ensure that the absorber locates right on the focal line of the aperture so that reflected sunlight can be focused on the absorber (Figure E-5(b), (c)).

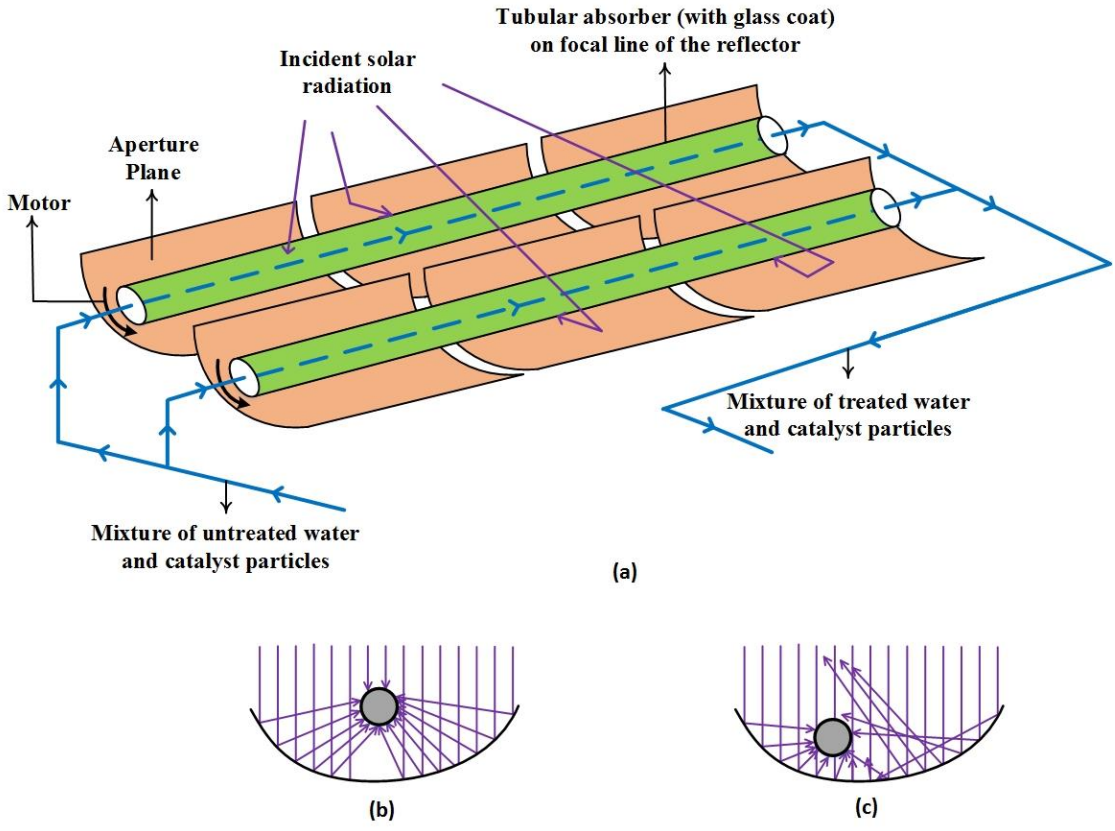

Figure E- 5 (a) Schematic of parabolic trough with two axes, (b) absorber locates on the focal line of the absorber, and (c) absorber does not locate on the focal line of the absorber.

Concentrating collectors usually have small size and length while receiving a large amount of energy per unit volume, and thus a high energy utilization efficiency would be carried out. A turbulent flow with less or no mass transfer limitation inside the reaction system is also easy to be maintained, and also, volatile compounds do not evaporate, which makes the handling and control of the inlet simple and cheap. [6,38]

Yet, concentrating systems can only use direct solar radiation. In the wavelength range of solar radiation reaching the earth's surface that can be absorbed by TiO_2, the direct and diffusion portions are almost equal. Therefore, only half of the incident irradiation can be used at most. [39] Additionally, both optical and quantum efficiency of concentrating collectors are pretty low [40], which can be explained by the square root rather than linear dependence of the reaction rate on the light flux [41,42]. Furthermore, the potential overheating may lead to leaks and corrosion of the reactor bodies [40]. This kind of reactors are usually expensive as well [41].

E-3.2 Non-concentrating Collector

In order to avoid the aforementioned defects of concentrating collectors, especially to realize high efficiencies and low costs, non-concentrating collectors have been proposed (Figure E-6). A non-concentrating solar collector usually consists of an immobilized flat plate orienting towards the equator at a specific inclination, depending on the latitude it locates. There is no solar tracking mechanism in non-concentrating devices, so that the difficulty and cost to build up such a system are both reduced. [32] In fact, tubes are widely used in non-concentrating collectors, but they are still regarded as a flat plate arrangement since the tubes are laid closely and side by side [33]. Also, the most significant difference between concentrating and non-concentrating collectors is that the latter makes use of both direct and diffuse solar radiation and no concentrating structure is needed [33,35,38]. Therefore, non-concentrating collectors have better optical efficiency and the quantum efficiency is not reduced by factors associated with solar tracking and concentrating as in concentrating collectors [37].

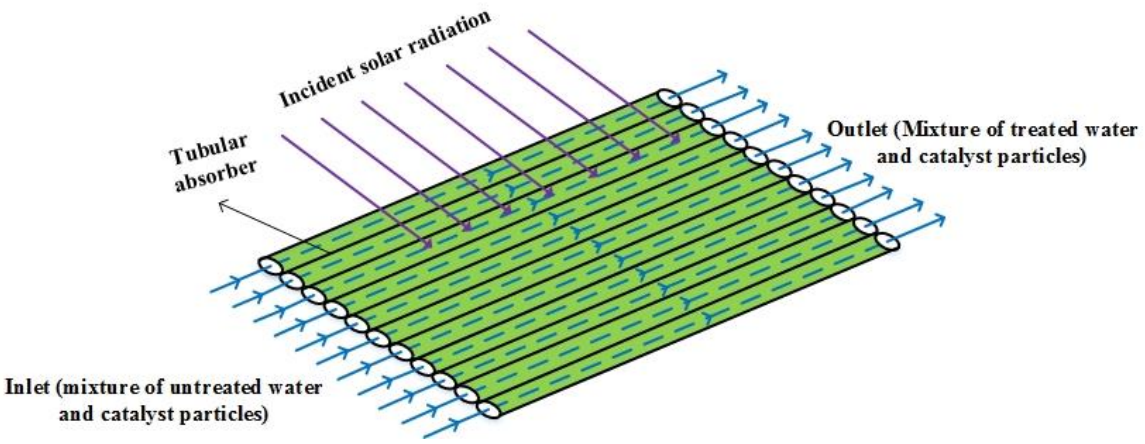

Figure E- 6 Schematic of a non-concentrating collector.

Although non-concentrating collectors possess important advantages, scrupulous design of a robust sun-concentrating photoreactor is not trivial, since they must be weather-resistant, chemically inert and UV-transmissive [6]. In addition, the inlet is usually laminar, which may lead to mass transfer limitation problems, as well as reactant vaporization [33]. Furthermore, non-concentrating systems require significantly large photoreactor surface and must be able to support high operating pressures in order to pump the fluid [32]. It is also more difficult to pipe the fluid into non-concentrating designs compared to in the case of parabolic troughs [6].

E-3.3 Compound Parabolic Collector

From the discussions above, it can be summarized that concentrating solar collectors are more efficient in energy conversion, while non-concentrating collectors bring about higher optical and quantum efficiencies. As a result, a successful attempt combining the advantages exhibited by both of the two collectors have been approached, which is the so-called compound parabolic collector (CPC) [6,32,43]. CPCs come under the category of non-concentrating solar collectors and are considered to be the most efficient and mature design in industrial-scale photochemical applications [6,32]. It is because CPC reactors provide the best optic properties for low-concentration systems and can be designed with a concentration ratio close to one, benefiting from their ingenious design [44]. A CPC is made of two halves of a parabola with closely located focal points and their axes inclined to each other. As such, both direct and diffuse incident solar radiation within the angle between the two axes (i.e., acceptance angle of the CPC) can be reflected with

single or multiple reflections towards the absorber and so that be available for photocatalysis [6,32,33,43].

The concentration factor (C_{CPC}) of a two-dimensional CPC collector is given by Equation (E.1):

$$C_{CPC} = 1/\mathrm{Sin}\theta \qquad \text{(E.1)}$$

where θ is the acceptance semi-angle, which is normally between 60 and 90° for photocatalytic applications; when it reaches 90°, a non-concentrating collector system would be obtained [43].

Based on the geometric configuration of absorber, CPCs are divided into four types: flat, tube, fin, and vee [45]. Yet, only the first two types are suitable for photocatalytic applications. Their cross section schematics are given by Figure E-7 (a) (flat) and (b) (tubular) [6,32,43]. CPCs with flat absorbers have a high optical transmission due to their large shape factors for direct radiation [46]. Same as regular non-concentrating solar collectors, the flat absorber in such a CPC is actually an array of tubes set side by side. In CPCs with tubular absorbers, on the other hand, light reflected by the CPC is distributed around the tubular absorber so that its complete perimeter, rather than just the "front" as in conventional non-concentrating collectors would be illuminated [33,43,47]. Thereby, only half as much absorber material would be required, resulting in lower material cost, smaller conductive loss to the back, and gains in performance due to the improved transient response [45]. Higher concentration ratios and light captivity efficiencies with a smaller aperture area were also observed. However, in tubular absorber CPCs, incident photons are uniformly distributed, while the absorbed irradiation intensity is not, which is attributed to the photon loss during multiple reflections. This would cause high radiation intensity areas and thus hot spots on the absorber surface, resulting in a poor working efficiency and potential overheat areas eventually. [48] In order to minimize the radiation thermal loss from the absorber, Khonkar and Sayigh modified the absorber surface by introducing tiny cavities at the circumferential area with relatively high solar intensities. The contact area between the absorber and the fluid inside was increased as well. [47]

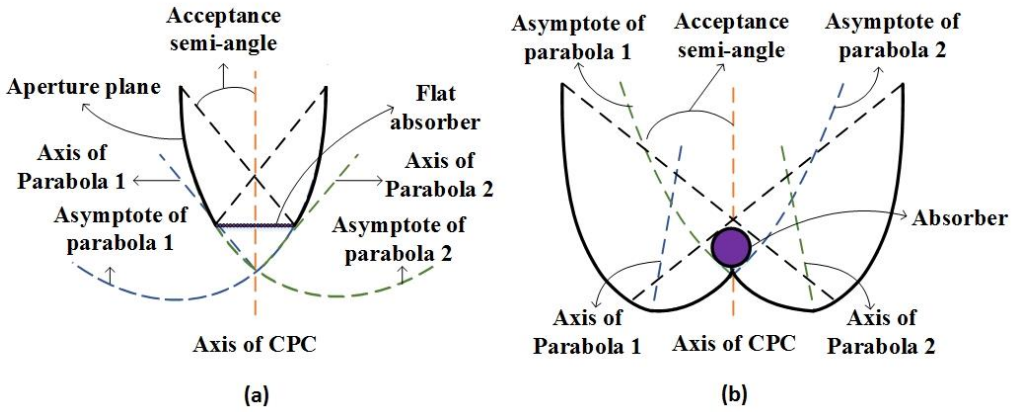

Figure E- 7 Cross section schematics of CPCs with (a) flat absorber, and (b) tubular absorber.

CPCs take advantages of turbulent flow conditions, making use of both direct and diffuse solar radiation, low prices, avoiding vaporization of volatile compounds and thus high optical and quantum efficiencies [32,33,43] However, CPCs have not been widely applied in industries due to insufficient evidence in the commercial scale. Factors inhibiting its performance at commercial scale include slow overall rates, low quantum yields, low-order dependence of rates on light intensity, poisoning and fouling of the catalyst, and scavenging of active oxidizing agents by spectator species. Solar energy experiences cycle diurnally and annually, and vary with weather patterns , which makes its industrial performance hard to be precisely predicted. Also, the inlet may contain chemicals that can block the critical wavelengths necessary for photoactivity and may require pre- or post-treatment. [42]

Except for technological and economical requirements, climate conditions are important in outdoor operations as well. A comparative study of the photocatalytic oxidation of 2,4-Dichlorophenol using TiO2 suspensions under natural solar radiation at pilot-plant scale between PTC and CPC exhibited a comparative effect when operated on clear days but an obvious better performance under cloudy conditions [49].

References:

[1] C. McCullagh, N. Skillen, M. Adams, P.K.J. Robertson, Photocatalytic reactors for environmental remediation: A review, J. Chem. Technol. Biotechnol. 86 (2011) 1002–1017. doi:10.1002/jctb.2650.

[2] A.K. Ray, A.A.C.M. Beenackers, Development of a new photocatalytic reactor for water purification, Catal. Today. 40 (1998) 73–83. doi:10.1016/S0920-5861(97)00123-5.

[3] P. Du, J.T. Carneiro, J.A. Moulijn, G. Mul, A novel photocatalytic monolith reactor for multiphase heterogeneous photocatalysis, Appl. Catal. A Gen. 334 (2008) 119–128. doi:10.1016/j.apcata.2007.09.045.

[4] T. Van Gerven, G. Mul, J. Moulijn, A. Stankiewicz, A review of intensification of photocatalytic processes, Chem. Eng. Process. Process Intensif. 46 (2007) 781–789. doi:10.1016/j.cep.2007.05.012.

[5] H. Lin, K.T. Valsaraj, Development of an optical fiber monolith reactor for photocatalytic wastewater treatment, J. Appl. Electrochem. 52 (2006) 2271–2280. doi:10.1002/aic.10823.

[6] S. Malato, J. Blanco, A. Vidal, C. Richter, Photocatalysis with solar energy at a pilot-plant scale: An overview, Appl. Catal. B Environ. 37 (2002) 1–15. doi:10.1016/S0926-3373(01)00315-0.

[7] M.F.J. Dijkstra, H. Buwalda, A.W.F. De Jong, A. Michorius, J.G.M. Winkelman, A.A.C.M. Beenackers, Experimental comparison of three reactor designs for photocatalytic water purification, Chem. Eng. Sci. 56 (2001) 547–555. doi:10.1016/S0009-2509(00)00259-1.

[8] M.F.J. Dijkstra, H. Buwalda, A.W.F. De Jong, A. Michorius, J.G.M. Winkelman, A.A.C.M. Beenackers, M. Dijsktra, H. Buwalda, A.W.F. De Jong, A. Michorius, M. Benackers, A. Winkelman, Experimental comparison of three reactor designs for photocatalyitic water purification, Chem. Eng. Sci. 56 (2001) 547–555. doi:10.1016/S0009-2509(00)00259-1.

[9] F. Yoshikawa, N. Namiki, Y. Otani, P. Biswas, A titanium dioxide-silica glass granule packed bed reactor for degradation of airborne organic compounds, J. Chem. Eng. Japan. 37 (2004) 503–513. doi:10.1252/jcej.37.503.

[10] W. Choi, J.Y. Ko, H. Park, J.S. Chung, Investigation on TiO2-coated optical fibers for gas-phase photocatalytic oxidation of acetone, Appl. Catal. B Environ. 31 (2001) 209–220. doi:10.1016/S0926-3373(00)00281-2.

[11] N.J. Peill, M.R. Hoffmann, M.M.K. Laboratories, Development and Optimization of a TiO2-Coated Fiber-Optic Cable Reactor : Photocatalytic Degradation of 4-Chlorophenol Development and Optimization of a Ti02-Coated FiberiOptic Cable Photocatalytic Degradation of 4-Chlorophenol, EnvironSciTechnol. 29 (2002) 2974–2981. doi:10.1021/es00012a013.

[12] R.-D. Sun, A. Nakajima, I. Watanabe, T. Watanabe, K. Hashimoto, TiO2-coated optical fiber bundles used as a photocatalytic filter for decomposition of gaseous organic compounds, J. Photochem. Photobiol. A Chem. 136 (2000) 111–116. doi:10.1016/S1010-6030(00)00330-0.

[13] K. Hofstadler, R. Bauer, S. Novalic, G. Heisler, New Reactor Design for Photocatalytic Waste-Water Treatment With TiO2 Immobilized on Fused-Silica Glass-Fibers: Photomineralization of 4-Chlorophenol, Environ. Sci. Technol. 28 (1994) 670–674. doi:10.1021/es00053a021.

[14] W. Wang, Y. Ku, The light transmission and distribution in an optical fiber coated with TiO2 particles, Chemosphere. 50 (2003) 999–1006. doi:10.1016/S0045-6535(02)00641-0.

[15] P.S. Mukherjee, A.K. Ray, Major challenges in the design of a large-scale photocatalytic reactor for water treatment, Chem. Eng. Technol. 22 (1999) 253–260. doi:Doi 10.1002/(Sici)1521-4125(199903)22:3<253::Aid-Ceat253>3.3.Co;2-O.

[16] L. Zhang, W.A. Anderson, Z. (Jason) Zhang, Development and modeling of a rotating disc photocatalytic reactor for wastewater treatment, Chem. Eng. J. 121 (2006) 125–134. doi:10.1016/j.cej.2006.05.011.

[17] D.F. Ollis, E. Pelizzetti, N. Serpone, Heterogeneous photocatalysis in the environment: Application to water purification., in: N. Serpone, E. Pelizzetti (Eds.), Photocatal. Fundam. Appl., Wiley, New York, 1989. doi:10.1017/CBO9781107415324.004.

[18] G. Li Puma, P.L. Yue, A novel fountain photocatalytic reactor: model development and experimental validation, Chem. Eng. Sci. 56 (2001) 2733–2744. doi:10.1016/S0009-2509(00)00528-5.

[19] G.L. Puma, P.L. Yue, The modeling of a fountain photocatalytic reactor with a parabolic profile, Chem. Eng. Sci. 56 (2001) 721–726. doi:10.1016/S0009-2509(00)00281-5.

[20] G. Li Puma, P.L. Yue, Enhanced Photocatalysis in a Pilot Laminar Falling Film Slurry Reactor, Ind. Eng. Chem. Res. 38 (1999) 3246–3254. doi:10.1021/ie9807607.

[21] B. Stephan, L. Ludovic, W. Dominique, Modelling of a falling thin film deposited photocatalytic step reactor for water purification: Pesticide treatment, Chem. Eng. J. 169 (2011) 216–225. doi:10.1016/j.cej.2011.03.016.

[22] G. Li Puma, P.L. Yue, Modelling and design of thin-film slurry photocatalytic reactors for water purification, Chem. Eng. Sci. 58 (2003) 2269–2281. doi:10.1016/S0009-2509(03)00086-1.

[23] D. Dionysiou, Rotating disk photocatalytic reactor: development, characterization, and evaluation for the destruction of organic pollutants in water, Water Res. 34 (2000) 2927–2940. doi:10.1016/S0043-1354(00)00022-1.

[24] H.C. Yatmaz, C. Wallis, C.R. Howarth, The spinning disc reactor - studies on a novel {TiO}_2 photocatalytic reactor, Chemosphere. 42 (2001) 397–403. doi:10.1016/S0045-6535(00)00088-6.

[25] I. Boiarkina, S. Norris, D.A. Patterson, The case for the photocatalytic spinning disc reactor as a process intensification technology: Comparison to an annular reactor for the degradation of methylene blue, Chem. Eng. J. 225 (2013) 752–765. doi:10.1016/j.cej.2013.03.125.

[26] R.A. Damodar, T. Swaminathan, Performance evaluation of a continuous flow immobilized rotating tube photocatalytic reactor (IRTPR) immobilized with TiO2 catalyst for azo dye degradation, Chem. Eng. J. 144 (2008) 59–66. doi:10.1016/j.cej.2008.01.014.

[27] D. Li, H. Zheng, Q. Wang, X. Wang, W. Jiang, Z. Zhang, Y. Yang, A novel double-cylindrical-shell photoreactor immobilized with monolayer TiO2-coated silica gel beads for photocatalytic degradation of Rhodamine B and Methyl Orange in aqueous solution, Sep. Purif. Technol. 123 (2014) 130–138. doi:10.1016/j.seppur.2013.12.029.

[28] Z. Zhang, H. Wu, Y. Yuan, Y. Fang, L. Jin, Development of a novel capillary array photocatalytic reactor and application for degradation of azo dye, Chem. Eng. J. 184 (2012) 9–15. doi:10.1016/j.cej.2011.02.057.

[29] N.N. Rao, V. Chaturvedi, G. Li Puma, Novel pebble bed photocatalytic reactor for solar treatment of textile wastewater, Chem. Eng. J. 184 (2012) 90–97. doi:10.1016/j.cej.2012.01.004.

[30] J.I. Ajona, A. Vidal, V. A, The use of CPC collectors for detoxification of contaminated water: Design, construction and preliminary results, Sol. Energy. 68 (2000) 109. doi:10.1016/S0038-092X(99)00047-X.

[31] D. Yogi, M. Daniel, Cleaning up with sunshine, Sol. Energy. 118 (1996) 56–59.

[32] M. Tanveer, G. Tezcanli Guyer, Solar assisted photo degradation of wastewater by compound parabolic collectors: Review of design and operational parameters, Renew. Sustain. Energy Rev. 24 (2013) 534–543. doi:10.1016/j.rser.2013.03.053.

[33] S.M. Rodríguez, J.B. Gálvez, M.I.M. Rubio, P.F. Ibáñez, D.A. Padilla, M.C. Pereira, J.F. Mendes, J.C. De Oliveira, Engineering of solar photocatalytic collectors, Sol. Energy. 77 (2004) 513–524. doi:10.1016/j.solener.2004.03.020.

[34] G.J. Jorgensen, R. Govindarajan, Ultraviolet Reflector Materials for Solar Detoxification of Hazardous Waste, in: C.M. Lampert, C.G. Granqvist (Eds.), Proc. SPIE 1536, 1991: pp. 194–205.

doi:10.1117/12.49224.

[35] S. Malato, P. Fernández-Ibáñez, M.I. Maldonado, J. Blanco, W. Gernjak, Decontamination and disinfection of water by solar photocatalysis: Recent overview and trends, Catal. Today. 147 (2009) 1–59. doi:10.1016/j.cattod.2009.06.018.

[36] D.M. Blake, K. Magrini-bair, E. Woifrum, E.K. May, E. Wolfrum, E.K. May, Materials issues in solar detoxification of air and water, in: C.M. Lampert, C.G. Granqvist, M. Graetzel, S.K. Deb (Eds.), Proc. SPIE 3138, 1997: pp. 154–162. doi:10.1117/12.290206.

[37] D.Y.Goswami, A Review of Engineering Developments of Aqueous Phase Solar Photocatalytic Detoxification and Disinfection Processes, J. Sol. Energy Eng. 119 (1997) 101. doi:10.1115/1.2887886.

[38] K. Kabra, R. Chaudhary, R.L. Sawhney, R. Kabra, Kavita. Chaudhary, Rubina. Sawhney, K. Kabra, R. Chaudhary, R.L. Sawhney, Treatment of Hazardous Organic and Inorganic Compounds through Aqueous-Phase Photocatalysis: A Review, Ind. Eng. Chem. Res. 43 (2004) 7683–7696. doi:10.1021/ie0498551.

[39] R.E. Bird, R.L. Hulstrom, L.J. Lewis, Terrestrial solar spectral data sets, Sol. Energy. 30 (1983) 563–573. doi:10.1016/0038-092X(83)90068-3.

[40] D. Bockelmann, D. Weichgrebe, R. Goslich, D. Bahnemann, Concentrating versus non-concentrating reactors for solar water detoxification, Sol. Energy Mater. Sol. Cells. 38 (1995) 441–451. doi:10.1016/0927-0248(95)00005-4.

[41] D.F. Ollis, Solar-assisted photocatalysis for water purification: issues, data, questions, Kluwer Academic Publishers, 1991. doi:10.1017/CBO9781107415324.004.

[42] Y. Parent, D. Blake, K. Magrini-Bair, C. Lyons, C. Turchi, A. Watt, E. Wolfrum, M. Prairie, Solar photocatalytic processes for the purification of water: State of development and barriers to commercialization, Sol. Energy. 56 (1996) 429–437. doi:10.1016/0038-092X(96)81767-1.

[43] S. Malato, P. Fernández-Ibáñez, M.I. Maldonado, J.J.J. Blanco, W. Gernjak, D.C. Alarcón, M.I. Maldonado, P. Fernández-Ibáñez, W. Gernjak, D.C. Alarcon, M.I. Maldonado, P. Fernandez-Ibanez, W. Gernjak, D.C. Alarcón, M.I. Maldonado, P. Fernández-Ibáñez, W. Gernjak, Photocatalytic decontamination and disinfection of water with solar collectors, Catal. Today. 122 (2007) 137–149. doi:10.1016/j.cattod.2007.01.034.

[44] J. Blanco, S. Malato, B. Milow, M.I. Maldonado, H. Fallmann, T. Krutzler, R. Bauer, T. Ciema, P.S. De Almeria, C. Senes, Techno-economical assessment of solar detoxification systems with compound parabolic collectors, J. Phys. 9 (1999) 259–264.

[45] A. Rabl, N.. Goodman, R. Winston, Practical design considerations for CPC solar collectors, Sol. Energy. 22 (1979) 373–381. doi:http://dx.doi.org/10.1016/0038-092X(79)90192-0.

[46] R. Siegel, J. Howel, Thermal radiation heat transfer, McGraw-Hill, New York, 1972.

[47] H.E.I.Khonkar, A.A.M.Sayigh, Optimization of the tubular absorber using a compound parabolic concentrator, Renew. Energy. 6 (1995) 17–21.

[48] R.W. Matthews, Photo-oxidation of organic material in aqueous suspensions of titanium dioxide, Water Res. 20 (1986) 569–578. doi:10.1016/0043-1354(86)90020-5.

[49] S. Malato, J. Blanco, C. Richter, D. Curcó, J. Giménez, Low-concentration CPC collectors for photocatalytic water detoxification: Comparison with a medium concentrating solar collector, Water Sci. Technol. 35 (1997) 157–164. doi:10.1016/S0273-1223(97)00021-8.

Appendix F. Previously Failed System

F-1 Carbon Quantum Dots Deposited on Ag/AgBr Surface

F-1.1 Principles and Theories

Different from inorganic semiconductor quantum dots, carbon-containing quantum dots (CCQDs) refer to zero-dimensional carbon-containing nanoparticles with the size of generally several nanometers [1]. The mostly researched CCQDs so far is carbon quantum dots (CQDs). Other than the general functions such as accepting electrons, facilitating charge separation, increasing surface area, and providing active sites as inorganic carbon-containing materials do [1], [2], [3], the most significant application of CCQDs is to sensitize semiconductors with their extraordinary upconverted luinescence property. Specifically, after absorbing one photon from NIR or IR light, multiple electrons can be generated in OQDs and their recombination with holes emits visible light or UV, which in turn triggers the semiconductor particles to process conventional photocatalytic reactions [4], [5], [6]. The upconversion property of QDs is strongly size-dependent: as size increased, E_g decreases, and the emissionn spectrum has a blue shift. This makes the CCQDs/semiconductor composites be capable of effectively using the full spectrum of sunlight and thus extensively promote the photocatalytic efficiency [5]. The superior conductivity of CQDs have also been reported [7], which facilitated electron/hole separation of the photocatalyst it deposited on.

Silver bromide (AgBr) has attracted much attention in the recent years for its visible-light-responsivity due to narrow bandgap (ca. 2.6 eV). However, AgBr photocatalysts are not stable considering Ag^+ would be easy reduced by the photogenerated electrons. On the other hand, the produced Ag nanoparticles (NPs) produced on the AgBr surface under UV or visible irradiation exhibit the localized surface plasmon resonance (LSPR) effect, which is able to extensively enhance photocatalytic performance of the semiconductor it deposited on. So far, three functioning mechanisms of the LSPR effect have been proposed: near-field electromagnetic enhancement, LSPR sensitization, and photon scattering [8]. When there is an overlap between the illumination source spectrum, semiconductor absorbance spectrum and metal NPs LSPR spectrum, the LSPR-

induced electromagnetic field of the metal NPs will form at the metal/semiconductor interface, which has the intensity of up to 100-10000 times higher than that of the incident electric field of the semiconductor, and more electron s and holes would be produced as a result [9]. The formed electromagnetic field also polarized the nonpolar substrate and attract charged and polarized substrates due to Coulomb's force, which enhances substrate adsorption, as well as heats up the surrounding environment and thus further facilitating the photoredox reactions [10], [11]. On the other hand, as the decay of the optically excited plasmons, electrons in the electron cloud from the plasmon metal NPs would be released. If the electrons are able to overcome the Schottky barrier at the metal/semiconductor interface, they would be injected to the semiconductor conduction band and sensitize the semiconductor as a result [12], [13]. Otherwise, they can oxidize substrates in an aqueous solution due to their mild oxidation potential [14]. WIth the NP size rises, incident photos may be scattered by reflection before reaching the semiconductor surface, leading to an improved light absorption efficiency [15].

F-1.2 Expected Effects

Based on the theories and the reported mechanisms of enhanced photocatalytic performance involved with CQDs and Ag/AgBr, the photocatalytic activity of Ag/AgBr was expected to be promoted with the deposition of CQDs on the surface by either converting the NIR and IR irradiation into the visible and UV region accomplishing a higher light absorption efficiency of Ag/AgBr; or accepting the photogenerated electrons from the AgBr conduction band and hence realizing a sufficient charge carrier separation as well as enhancing the photostability of AgBr.

F-1.3 Experiment

F-1.3.1 Photocatalyst Preparation

Synthesis of carbon quantum dots. The CQDs were synthesized by a facile electrochemical etching method. Two graphite rods (99.99%, 0.242in dia x 6in long, Alfa Aesar) with a distance of ca. 7.5 cm were inserted into an aqueous solution containing 199 ml deionized water (DDW), 1 ml ethanol (99%, Fisher Scientific) and 0.3587g NaOH (99%, Sigma-Aldrich). A direct current of ca. 0.7 A was applied on the above system. After reacting for 7 h, the obtained brown solution was

neutralized by 1M HNO_3 aqueous solution and dialyzed with a dialysis cassette (2K MWCO, Fisher Scientific) for 48h. Then, the diluted solution was centrifuged at 6000 rpm for 60 min. The supernatant was refrigerated in a brown glass vial.

Synthesis of CQDs-deposited Ag/AgBr. To deposit CQDs onto AgBr surface, two methods have been tried.

i) **Hydrothermal method.** At first, 0.2g of Polyvinylpyrrolidone (PVP, 95%, Fisher Scientific) was dissolved in 40 ml mixture of CQDs solution and DDW, and then 0.357g KBr (99%, Sigma-Aldrich) and labeled as solution A. In the meanwhile, 0.3825g $AgNO_3$ (99%, Fisher Scientific) was dissolved in 40 ml DDW and labeled as solution B. After magnetically stirred for 30 min, solution B was dropwisely added into solution A. After stirring for another 30 min, the precursor was poured into a 100 ml Teflon-lined stainless-steel autoclave and kept at 120 ^{0}C for 12h. After being centrifuged and washed with DDW and ethanol for 3 times, respectively, the pale yellow precipitate was redispersed in 30 ml DDW and magnetically stirred under visible light irradiation (300W tungsten halide bulb (Ushio) equipped with a cutoff (Kenko Zeta, transmittance > 90%, λ > 410 nm)) for 30 min. The as-obtained grey particles were centrifuged and dried at 60 ^{0}C overnight. Pure Ag/AgBr was prepared without the addition of the CQDs solution. The influence of the amout of CQD solution, the time to add CQD solution into the precursor, the reaction time and temperature of the AgBr precursor were investigated.

ii) **Facile wet-impregnation method.** The CQDs and pure AgBr were synthesized separately as described above. Then, a designated amount of the as-prepared CQDs and AgBr particles were dispersed into an organic liquid aqueous solution and magnetically stirred in air until evaporation finished. The influence of the amount of CQD solution and AgBr, the reaction time and temperature of the AgBr precursor, the composition and volume of the dispersion media, and the stirring time and temperature were investigated.

F-1.3.2 Photocatalytic Experiment

Same as described in Chapter III.

F-1.4 Result Analysis

No enhancement was observed in terms of RhB degradation on the CQDs-deposited Ag/AgBr compared to the pure Ag/AgBr. There are three possible reasons for the failure:

i) The size of the prepared carbon particles may not reach the quantum level and even though carbon quantum dots were fabricated successfully, they may aggregate in the solution, which prevented the quantum effect from exhibiting.

ii) The CQDs might not successfully deposited onto the AgBr surface, which might be attributed to the inappropriate preparation method.

Due to financial considerations, no characteristic of the prepared sampled were performed.

F-2 N-doped $NaNbO_3$

F-2.1 Principles and Theories

Perovskite sodium niobate ($NaNbO_3$) has emerged as a wide-bandgap semiconductor due to its physical and chemical stability, high crystallinity, low-environmental impact, and low-cost [16]. Its photocatalytic performance has been proved in water splitting [17], water decontamination [18], as well as CO_2 reduction [19] under UV irradiation. Although $NaNbO_3$ does not respond to visible light due to its wide bandgap, it may work as the electron/hole separation center when coupled with a narrow-bandgap-semiconductor, such as Ag_2O [20], BiOI [21], and Cu_2O [22].

Nitrogen, as the most intensively studied non-metal dopant, is usually introduced into oxygen-containing semiconductor lattice by hybridizing O 2p orbital with N 2p orbital, which would elevate the semiconductor valence band and thus improve the light absorption efficiency. [23], [24]

F-2.2 Expected Effects

Although N-doped $NaNbO_3$ has been reported before, it was realized by conventional solid-state reaction [25], [26]. N-doped $NaNbO_3$ with enhanced photocatalytic activity under visible light

irradiation was expected to be realized by hydrothermal preparation.

F-2.3 Experiment

F-2.3.1 Photocatalyst Preparation

Synthesis of $NaNbO_3$. At first, 14g NaOH tablets were dissolved in 30 ml DDW in a 100 ml beaker. After stirring for 30 min, 2g Nb_2O_5 was dispersed in the above concentrated NaOH solution. After magnetically stirring for 2h, the precursor was poured into a 45 ml Teflon-lined stainless steel autoclave and heated to 200 ^{0}C. After reacting for 12 h, the autoclave was taken out of the oven and cooled down naturally to room temperature. The white precipitates were filtered and washed with DDW and ethanol for 3 times, respectively, and then dried at 60 ^{0}C overnight.

Synthesis of N-doped $NaNbO_3$. Nitrogen doping was realized by either adding the nitrogen source in the precursor during of $NaNbO_3$ via a one-pot hydrothermal method, or redispersing the as-prepared $NaNbO_3$ in the solution containing the nitrogen source and hydrothermally treated via a two-step hydrothermal method. Urea (99%, Sigma-Aldrich), Triethanolamine (TEOA, 99%, Fisher Scientific), $NH_3 \bullet H_2O$ (28wt% in H_2O), thiourea (99%, Fisher Scientific), methylamine solution (40wt% in H_2O, Sigma-Aldrich), ethylamine solution (66-72wt% in H_2O, Sigma-Aldrich), hydrazine hydrate solution (24-26wt% in H_2O, Sigma-Aldrich), EG (99%, Fisher Scientific), and ethanol (99%, Fisher Scientific) were employed as the nitrogen source. The influence of type, amount and addition time of nitrogen source, the temperature and time of hydrothermal treatment and calcination have been investigated.

F-2.3.2 Photocatalytic Experiment

Same as described in Chapter III.

F-2.4 Result Analysis

No enhancement was observed in terms of RhB degradation on the N-doped $NaNbO_3$ compared to the pure $NaNbO_3$. There are three possible reasons for the failure:

i) From DRS plot in terms of various nitrogen sources (samples with the strongest absorbance of each nitrogen source was exhibited), no significant enhancement except for the one used TEOA was found in the visible region, indicating the light absorption was not enhanced as expected. This might be attributed to the inappropriate preparation method.

ii) For the sample with TEOA as the nitrogen source, although there was a slight absorption enhancement at ca. 360-500 nm, the photocatalytic performance reduced instead. Also, samples obtained from the two-step hydrothermal method were found to aggregate compared to the pristine $NaNbO_3$. This may because $NaNbO_3$ is not stable in organic environment and high temperature and pressure.

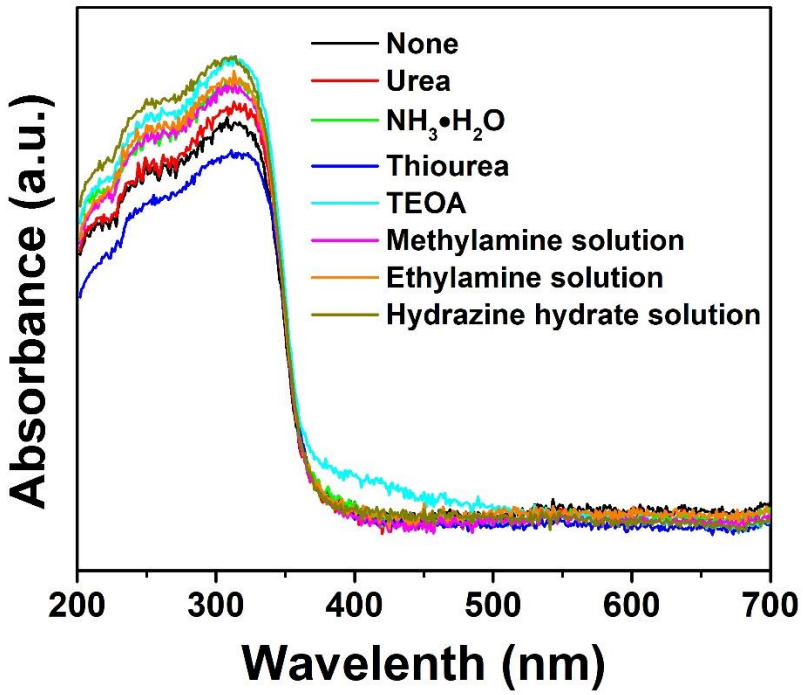

Figure F- 1 DRS spectra of N-doped $NaNbO_3$ samples with various nitrogen sources.

References:

[1] J. Di et al., "Novel visible-light-driven CQDs/Bi2WO6 hybrid materials with enhanced photocatalytic activity toward organic pollutants degradation and mechanism insight," Appl. Catal. B Environ., vol. 168–169, pp. 51–61, 2015.

[2] H. Li et al., "Carbon quantum dots/Cu2O composites with protruding nanostructures and their highly efficient (near) infrared photocatalytic behavior," J. Mater. Chem., vol. 22, no. 34, p. 17470, 2012.

[3] J. Di et al., "The synergistic role of carbon quantum dots for the improved photocatalytic performance of Bi2MoO6," Nanoscale, vol. 7, no. 26, pp. 11433–11443, 2015.

[4] H. Yu et al., “ZnO/carbon quantum dots nanocomposites: one-step fabrication and superior photocatalytic ability for toxic gas degradation under visible light at room temperature,” New J. Chem., vol. 36, no. 4, p. 1031, 2012.

[5] H. Zhang et al., “Carbon quantum dots/Ag3PO4 complex photocatalysts with enhanced photocatalytic activity and stability under visible light,” J. Mater. Chem., vol. 22, no. 21, p. 10501, 2012.

[6] J. Shen, Y. Zhu, C. Chen, X. Yang, and C. Li, “Facile preparation and upconversion luminescence of graphene quantum dots,” Chem. Commun., vol. 47, no. 9, pp. 2580–2582, 2011.

[7] Y. Li, B. P. Zhang, J. X. Zhao, Z. H. Ge, X. K. Zhao, and L. Zou, “ZnO/carbon quantum dots heterostructure with enhanced photocatalytic properties,” Appl. Surf. Sci., vol. 279, pp. 367–373, 2013.

[8] D. B. Ingram, P. Christopher, J. L. Bauer, and S. Linic, “Predictive model for the design of plasmonic metal/semiconductor composite photocatalysts,” ACS Catal., vol. 1, no. 10, pp. 1441–1447, 2011.

[9] M. K. Kumar, S. Krishnamoorthy, L. K. Tan, S. Y. Chiam, S. Tripathy, and H. Gao, “Field effects in plasmonic photocatalyst by precise SiO2 thickness control using atomic layer deposition,” ACS Catal., vol. 1, no. 4, pp. 300–308, 2011.

[10] S. Sun, W. Wang, L. Zhang, M. Shang, and L. Wang, “Ag@C core/shell nanocomposite as a highly efficient plasmonic photocatalyst,” Catal. Commun., vol. 11, no. 4, pp. 290–293, 2009.

[11] X. Zhang, Y. L. Chen, R.-S. Liu, and D. P. Tsai, “Plasmonic photocatalysis,” Reports Prog. Phys., vol. 76, no. 4, p. 46401, 2013.

[12] P. Christopher, H. Xin, and S. Linic, “Visible-light-enhanced catalytic oxidation reactions on plasmonic silver nanostructures,” Nat. Chem., vol. 3, no. May, 2011.

[13] X. Lin, F. Rong, D. Fu, and C. Yuan, “Enhanced photocatalytic activity of fluorine doped TiO2 by loaded with Ag for degradation of organic pollutants,” Powder Technol., vol. 219, pp. 173–178, 2012.

[14] D. Tsukamoto, Y. Shiraishi, Y. Sugano, S. Ichikawa, S. Tanaka, and T. Hirai, “Gold nanoparticles located at the interface of anatase/rutile TiO 2 particles as active plasmonic photocatalysts for aerobic oxidation,” J. Am. Chem. Soc., vol. 134, no. 14, pp. 6309–6315, 2012.

[15] J. J. Mock, D. R. Smith, and S. Schultz, “Local Refractive Index Dependence of Plasmon Resonance Spectra from Individual Nanoparticles,” Nano Lett., vol. 3, no. 4, pp. 485–491, Apr. 2003.

[16] S. Kumar, S. Khanchandani, M. Thirumal, and A. K. Ganguli, “Achieving enhanced visible-light-driven photocatalysis using type-II NaNbO3/CdS core/shell heterostructures,” ACS Appl. Mater. Interfaces, vol. 6, no. 15, pp. 13221–13233, 2014.

[17] D. Zhang, J. Cheng, F. Shi, Z. Cheng, X. Yang, and M. Cao, “Low-temperature synthesis of ribbon-like orthorhombic NaNbO3 fibers and their photocatalytic activities for H2 evolution,” RSC Adv., vol. 5, no. 42, pp. 33001–33007, 2015.

[18] L. Wang et al., “Scale synthesized cubic NaNbO3 nanoparticles with recoverable adsorption and photodegradation for prompt removal of methylene blue,” J. Alloys Compd., vol. 695, pp. 599–606, 2017.

[19] F. Fresno, P. Jana, P. Reñones, J. M. Coronado, D. P. Serrano, and V. A. de la Peña O’Shea, “CO2 reduction over NaNbO3 and NaTaO3 perovskite photocatalysts,” Photochem. Photobiol. Sci., vol. 16, no. 1, pp. 17–23, 2017.

[20] B. Zhang et al., “Synthesis of Ag2O/NaNbO3p-n junction photocatalysts with improved visible light photocatalytic activities,” Sep. Purif. Technol., vol. 178, pp. 130–137, 2017.

[21] M. Sun et al., “Facile fabrication of BiOI decorated NaNbO3cubes: A p–n junction photocatalyst with improved visible-light activity,” Appl. Surf. Sci., vol. 416, pp. 288–295, 2017.

[22] M. Fan et al., “Excellent visible-light-driven photocatalytic performance of Cu 2 O sensitized NaNbO 3 heterostructures,” New J. Chem., vol. 39, no. 8, pp. 6171–6177, 2015.

[23] G. Tan, L. Zhang, H. Ren, J. Huang, W. Yang, and A. Xia, “Microwave hydrothermal synthesis of N-doped BiVO4 nanoplates with exposed (040) facets and enhanced visible-light photocatalytic properties,” Ceram.

Int., vol. 40, no. 7 PART A, pp. 9541–9547, 2014.

[24] B. Hu and Y. Liu, “Nitrogen-doped Nb2O5 nanobelt quasi-arrays for visible light photocatalysis,” J. Alloys Compd., vol. 635, pp. 1–4, 2015.

[25] G. Li, N. Yang, W. Wang, and W. F. Zhang, “Synthesis, photophysical and photocatalytic properties of N-doped sodium niobate sensitized by carbon nitride,” J. Phys. Chem. C, vol. 113, no. 33, pp. 14829–14833, 2009.

[26] H. Shi, X. Li, H. Iwai, Z. Zou, and J. Ye, “2-Propanol photodegradation over nitrogen-doped NaNbO3powders under visible-light irradiation,” J. Phys. Chem. Solids, vol. 70, no. 6, pp. 931–935, 2009.